Water Level Modelling of the Mekong River Based on Multi-Mission Altimetry

Dissertation
von

Eva Susanne Ilona Börgens

Deutsches Geodätisches Forschungsinstitut und Lehrstuhl für Geodätische Geodynamik

Ingenieurfakultät Bau Geo Umwelt, Technische Universität München

Ingenieurfakultät Bau Geo Umwelt

Deutsches Geodätisches Forschungsinstitut und Lehrstuhl für Geodätische Geodynamik

Water Level Modelling of the Mekong River Based on Multi-Mission Altimetry

Eva Susanne Ilona Börgens

Vollständiger Abdruck der von der Ingenieurfakultät Bau Geo Umwelt der Technischen Universität München zur Erlangung des akademischen Grades eines

Doktor-Ingenieurs

genehmigten Dissertation.

Vorsitzende: Prof. Dr. Xiaoxiang Zhu

Prüfer der Dissertation: 1. Prof. Dr. Florian Seitz

2. Prof. Dr. Nico Sneeuw
   Universität Stuttgart

3. Prof. Per Knudsen, Ph.D.
   Danmarks Tekniske Universitet

Die Dissertation wurde am 4. April 2018 bei der Technischen Universität München eingereicht und durch die Ingenieurfakultät Bau Geo Umwelt am 29. Juni 2018 angenommen.

Abstract

Half of the global drinking water is extracted from rivers which are nowadays stressed by both the climate change and human development. In order to evaluate the impact of these changes for the riparian societies, monitoring of the rivers is essential. Nonetheless, the number of in situ observations is declining globally, leaving an observational gap most prominent in developing countries.

This thesis aimed at developing and improving methods for the observation and modelling of the river flow based on satellite altimetry. For this, the Lower Mekong River Basin in South-East Asia was chosen as case study. The diverse topography of the Lower Mekong River Basin allowed to test the altimetry methods under several different environments while the available in situ data allowed for validations.

While satellite altimetry is by now established for the water level observation of large rivers, observing small rivers is still challenging. These challenges include land contamination of the altimetric measurements, identification of the water observations, or off-nadir measurements. In this thesis, new methods were proposed to solve the latter two problems, while for the first problem existing methods, called retrackers, were employed.

Pulse limited altimetry, which was e. g. on board of the Envisat satellite, is prone to off-nadir measurements before and after the crossing of a water body such as a river. These off-nadir measurements form a distinct parabolic shape in the along-track collection of the heights and are called hooking effect. It was shown in this work that by using these observations rather than discarding them, the accuracy of water level estimations was improved over rivers with widths of less than 500 m.

Another problem facing inland altimetry is the identification of the water observations in the data set. Especially for small rivers, land-water-masks are often too inaccurate for the data selection. In this thesis, a classification method was proposed to identify the water observations in CryoSat-2 Synthetic Aperture Radar (SAR) data. Compared to pulse limited altimetry, SAR altimetry is expected to provide more accurate water levels for small rivers due to its higher along-track resolution. The classification method employed the unsupervised k-means algorithm with features derived from the SAR and Range Integrated Power (RIP) waveforms. The altimetry observations classified as water were used to estimate water levels at each crossing of the satellite

with a river in the basin. The validation of these water levels showed the improvement of the classification compared to both water levels from CryoSat-2 data extracted with a land-water-mask and water levels from Envisat. The main advantage of the classification lied in the upstream region with its small rivers, whereas for wider rivers in the middle stream region the land-water-mask results were similar to the classification results.

As long as only one satellite altimetry mission is used to observe the river, both the spatial and temporal resolution is limited; the orbit constellation governs the distance between the satellite tracks and the repeat time. However, the combination of data of several altimeter missions can improve the spatial and temporal resolution. Here, the geostatistical method of spatio-temporal kriging was applied for the combination of single-mission altimetry to multi-mission altimetry. Kriging required a covariance model between the observations that mirrored the flow of the river and that was estimated from the empirical covariances between the data.

To this end, two kriging methods were employed for the data combination. First, Ordinary Kriging was used and tested to combine data of satellite altimetry missions with a short-repeat orbit along the main stream of the Mekong River. Ordinary Kriging is the simplest kriging method but the data needed to be reduced by their spatial mean, i. e. the mean water level at each station. The combination was tested with two covariance models: a stationary and a non-stationary. With this, it was possible to predict water levels at any location along the river with a temporal resolution of a few days. Time series predicted at the location of gauging stations were validated against the in situ data which showed the ability of this multi-mission approach to predict reliable water level time series.

The second multi-mission approach of this thesis was an enhancement of the first one and employed Universal Kriging. In this approach all available data in the whole river network were used which included data along tributaries and from long or non-repeat orbit satellite missions. Universal Kriging allowed the incorporation of the latter data set as the mean water level did not need to be reduced which would not be feasible for long or non-repeat orbit satellite missions. The non-stationary covariance model from before allowed incorporating the tributaries as well. In the predicted water level time series the interannual flood behaviour of the river was well depicted. Especially, the floods of 2008 and 2011 were nicely observed with this multi-mission approach. However, even with all available altimetry data, the resolution was still to coarse to observe small local and short-term peaks in the water level caused by flash floods.

Zusammenfassung

Weltweit wird ungefähr die Hälfte des Trinkwassers aus Flüssen entnommen, die heute sowohl durch den Klimawandel als auch durch menschengemachte Veränderungen unter Stress stehen. Da diese Veränderungen die Gesellschaften der Flussanrainer beeinflussen, ist es nötig, Flüsse durchgehend zu beobachten. Trotz allem sinkt global die Anzahl der verfügbaren In-situ-Beobachtungen, was vor allem in Entwicklungsländern zu einer Beobachtungslücke führt.

Diese Doktorarbeit zielte darauf, Flüsse zu beobachten und zu modellieren, basierend auf unabhängigen Wasserstandbeobachtungen gemessen mit Satellitenaltimetrie. Der Mekong in Südostasien wurde dafür als Testgebiet verwendet. Die sehr unterschiedliche Topographie des Einzugsgebietes erlaubte es, die Methoden zur Altimetriedatenauswertung unter unterschiedlichen Gegebenheiten zu testen. Außerdem waren für den Mekong In-Situ-Daten vorhanden, sodass die Ergebnisse validiert werden konnten.

Obwohl Satellitenaltimetrie mittlerweile gängige Praxis für die Beobachtung von Wasserständen großer Flüsse ist, sind kleine Flüsse mit einer Breite von weniger als 500 m immer noch schwierig zu vermessen. Die Herausforderungen umfassen zum einen Einfluss von nicht mit Wasser bedeckten Flächen auf die altimetrischen Messungen, zum anderen aber auch die Identifikation der Wasserbeobachtungen und "off-nadir"-Beobachtungen. In dieser Arbeit wurden für die beiden letztgenannten Herausforderungen Lösungen vorgestellt. Für die Erstgenannte wurde auf bereits vorhandene Methoden, sogenannte "Retracker", zurückgegriffen.

"Pulse limited"-Altimetrie, wie sie zum Beispiel an Bord von Envisat zu finden war, ist anfällig für "off-nadir"-Beobachtungen vor und nach dem Überflug eines Flusses. Wenn entlang der Bodenspur aufgetragen, zeigen sich diese Beobachtungen in einer typischen Parabelform in den gemessenen Höhen. Dieses Phänomen wird als "Hooking Effect" bezeichnet. In dieser Arbeit wurde gezeigt, dass diese Messungen genutzt werden können, um die Schätzung der Wasserhöhe von kleinen Flüssen zu verbessern anstatt sie wie bisher zu verwerfen.

Ein weiteres Problem der Inlandaltimetrie ist die Identifikation der Wasserbeobachtungen in den Altimetriedaten. Vor allem bei kleineren Flüssen sind die üblichen Land-Wasser-Masken nicht genau genug für die Datenauswahl. Stattdessen wurde ei-

ne Klassifizierungsmethode vorgeschlagen, die Wasserbeobachtungen in CryoSat-2-
"*S*ynthetic *A*perture *R*adar"-Daten (dt. Radar mit synthetischer Apertur, SAR) findet.
Im Vergleich zur "pulse limited"-Altimetrie, ist die erwartete Genauigkeit von SAR-
Altimetrie aufgrund der höheren Auflösung entlang der Spur besser. Für die Klassi-
fikation wurde die nichtüberwachte "k-means"-Methode verwendet mit Merkmalen,
die aus der SAR und "*R*ange *I*ntegrated *P*ower Waveform" (dt. entfernungsintegrierte
Leistung, RIP) abgeleitet wurden. Die als Wasser klassifizierten Beobachtungen wur-
den anschließend genutzt, um für jeden Kreuzungspunkt eine Wasserhöhe zu schät-
zen. Die Validierung zeigte die Verbesserung der Genauigkeit der Wasserhöhen im
Vergleich zu EnvisatDaten und CryoSat-2-Daten, die mit einer Land-Wasser-Maske
bestimmt wurden. Vor allem im Oberlauf des Flusssystems, wo die Flüsse besonders
klein sind, war der Vorteil der Klassifizierung sichtbar. Im Mittelteil des Flusses hinge-
gen war der Unterschied zwischen der Klassifizierung und der Maske nicht sehr groß.

Solange nur eine Satellitenmission verwendet wird, um die Wasserstände eines Flus-
ses zu beobachten, ist die räumliche und zeitliche Auflösung limitiert. Die Satelliten-
orbits bestimmen die Entfernung zwischen den Bodenspuren und die zeitliche Auf-
lösung. Werden jedoch mehrere Missionen sowie alle Kreuzungspunkte verwendet,
verbessert sich die Auflösung sowohl in räumlicher als auch zeitlicher Hinsicht stark.
In dieser Doktorarbeit wurde die geostatistische Krigingmethode verwendet um die
Daten zu einem Multimissions-Datensatz zu verknüpfen. Kriging basiert auf den em-
pirisch geschätzten Kovarianzen zwischen den Beobachtungen, die den Verlauf des
Flusses beschreiben.

Zwei Krigingmethoden wurden für die Datenkombination angewendet. Als Erstes
wurde Ordinary Kriging genutzt und getestet um die Daten von Satellitenaltimetrie-
missionen mit einer kurzen Wiederholzeit und nur entlang des Hauptstroms des Me-
kongs zu verknüpfen. Ordinary Kriging ist die einfachste der Krigingmethoden aber
die Daten mussten um ihren räumlichen Mittelwert, d. h. um den mittleren Wasser-
stand, reduziert werden. Die Kombination wurde mit zwei verschiedenen Kovarianz-
modellen getestet: einem stationäres und einem nicht-stationäres. Damit konnte an je-
dem Ort entlang des Flusses eine Wasserstandszeitreihe mit einer zeitlichen Auflösung
von ein paar Tagen prädiziert werden. Zeitreihen, die am Ort von Pegelstationen prä-
diziert wurden, wurden mit diesen Pegeldaten validiert, womit gezeigt werden konnte,
dass die Methode eine zuverlässige Schätzung von Wasserstandszeitreihen zulässt.

Der zweite Ansatz der Multimissionsaltimetrie war eine Weiterentwicklung des ers-
ten und verwendete Universal Kriging. In diesem Ansatz wurden alle verfügbaren Da-
ten des gesamten Flusssystems verwendet, was sowohl Daten entlang der Nebenflüsse
als auch von Missionen mit langer Wiederholzeit einschloss. Universal Kriging erlaub-
te die Einbindung des letztgenannten Datensatzes da eine Reduktion um den mittleren

Wasserstand nicht mehr notwendig ist. Das bereits angewendete nicht-stationäre Kovarianzmodell war in der Lage, auch Nebenflüsse mit einzubeziehen. Die prädizierten Zeitreihen konnten das jährlich schwankende Flutverhalten mit hinreichender Genauigkeit abbilden. Vor allem die großen Überflutungen in den Jahren 2008 und 2011 sind gut beobachtet. Zur Beobachtung kürzerer und räumlich begrenzter Springfluten reichte jedoch selbst die zeitliche Auflösung mit Multimissionsaltimetrie nicht aus.

Preface

The following papers are the basis for this publication-based dissertation:

P-1:   E. Boergens, D. Dettmering, C. Schwatke, and F. Seitz (2016): **Treating the Hooking Effect in Satellite Altimetry data: A Case Study along the Mekong River and Its Tributaries**. In: *Remote Sensing* 8.2, pp. 1–22

P-2:   E. Boergens, S. Buhl, D. Dettmering, C. Klüppelberg, and F. Seitz (2017a): **Combination of multi-mission altimetry data along the Mekong River with spatio-temporal kriging**. In: *Journal of Geodesy* 91.5, pp. 519–534

P-3:   E. Boergens, K. Nielsen, O. B. Andersen, D. Dettmering, and F. Seitz (2017b): **River Levels Derived with CryoSat-2 SAR Data Classification—A Case Study in the Mekong River Basin**. In: *Remote Sensing* 9.12, pp. 1–21

P-4:   E. Boergens, D. Dettmering, and F. Seitz (2018): **Observing Water Level Extremes in the Mekong River with Multi-Mission Altimetry**. In: *Remote Sensing*. in review

The publications are cited in this thesis with P (for publication) and an Arabic number, indicating the chronological order of the publications.

The main body of this thesis describes the background of the four publications and where they fit into the overall context. An introduction to the topic of river altimetry with problem statement and introduction of the study area is given. Both the theoretical background of satellite altimetry and its application to river observation and the theoretical background of the multi-mission altimetry approach are provided. The main part of the thesis closes with a conclusion of the work and an outlook to further studies. The publications are each included as a section in the chapters but only the abstract is given in the main part of the thesis.

In the appendix, for each of the four publications a one-page summary, a description of the authors' contributions to the publication, and the full original publication are given.

Additionally to the first-authored publications, the following co-authored publications supplement the results of this dissertation:

CP-1:   C. Schwatke, D. Dettmering, E. Börgens, and W. Bosch (2015a): **Potential of SARAL/ AltiKa for Inland Water Applications**. In: *Marine Geodesy* 38.sup1, pp. 626–643

CP-2:   D. Dettmering, C. Schwatke, E. Boergens, and F. Seitz (2016): **Potential of ENVISAT Radar Altimetry for Water Level Monitoring in the Pantanal Wetland**. In: *Remote Sensing* 8.7, pp. 1–21

CP-3:   A. Zlinszky, E. Boergens, P. Glira, and N. Pfeifer (2017): **Airborne Laser Scanning for calibration and validation of inshore satellite altimetry: A proof of concept**. In: *Remote Sensing of Environment* 197, pp. 35–42

CP-4:   M. Passaro, S. K. Rose, O. B. Andersen, E. Boergens, F. M. Calafat, D. Dettmering, and J. Benveniste (2018): **ALES+: Adapting a homogenous ocean retracker for satellite altimetry to sea ice leads, coastal and inland waters**. In: *Remote Sensing of Environment* 211, pp. 456–471

These publications are cited in the thesis in the usual citation style.

Table of Contents

1 Introduction

1.1 Problem Statement and Background

Only 0.006% of the global fresh water is stored in rivers but around half of the global drinking water is extracted from rivers or river reservoirs (Gleick, 1996). Although rivers contribute only a fraction of the global water they amount for a large part of the global water flow with their short turnover time which make them an important part of the hydrological cycle (Gleick, 1993). However, the short turnover time also make river systems more sensitive to climate change or climate variations (Nijssen et al., 2001). For example, the climate variation of El Niño can be detected in water level variations of large rivers in South America (Maheu et al., 2003) as well as in South-East Asia (Räsänen and Kummu, 2013). Due to climate change the amount of precipitation is changing with, generally speaking, an increase of precipitation in the tropics but a decrease inside the large land masses and mid-latitudes (Trenberth, 2011). As the precipitation is highly correlated with the river runoff, the change of the former will induce a change in the river flow (T. Jiang et al., 2007). Additionally, the climate change affects the water flow of snow and glacier fed rivers, i. e. most of the large Asian river systems. Warmer temperatures can lead to shrinking glaciers and a decrease of snowfall in winter with earlier snowmelt in spring which decreases the river flow in summer (Barnett et al., 2005). In nearly all of the Asian river systems the changes in river flow due to changes in precipitation and snowmelt happen at the same time but affect the river flow differently.

At the same time, for many countries the water of rivers is essential for the life of the people who use the river water for drinking water, irrigation, transportation, or industry. For example, in the Mekong River Basin 98% of the agricultural area is irrigated by water extracted from the river which equals to 13% of the total river runoff (Mekong River Commission, 2010). The annual flood of the river is used to overflow paddy fields in the downstream lowlands and the deposed sediments fertilise the fields. However, floodings can destroy agricultural areas and infrastructure whereas droughts destroy the crops during the following dry season (Mekong River Commission, 2009; Adamson et al., 2009). Additionally to climate change, human development along the river changes the river flow, sometimes even significantly (Lauri et al., 2012). For

many major rivers, dams have been built during the last years or are planned in the coming years. Also in the Mekong River Basin several dams are in operation or under construction (International Centre for Enviromental Management, 2010). Not only engineering structures, but population growth increases the demand of fresh water from the river which can alter the flow as well (Vörösmarty et al., 2000). In many global river networks, including the Mekong River Basin, the climate related changes of the river flow are superimposed to man made changes (Vörösmarty et al., 2000).

All this calls for a continuous monitoring of the river network but the availability of global in situ data is declining since the 1980s (Global Runoff Data Center, 2013). Especially, rivers in developing countries are less well observed with in situ gauges, partly due to infrastructural neglect, but for many countries information on water availability is treated as a state secret. For the Mekong River Basin, for some 20 in situ stations data are available during the flood seasons of the last years from the *M*ekong *R*iver *C*ommission (MRC)[1].

Satellite altimetry can be used to close the data gap of in situ river observations with the measurement of the water surface height below the satellite. Due to a repeat orbit of the satellite missions of usually a few days, a time series of water level observations at a fixed location are possible. Though originally designed for ocean observations, satellite altimetry is by now applied to observe inland water bodies such as rivers. The surface area observed by the altimeter has a diameter of up to 10 km which leads to problems with the observation of rivers; the problems increase the smaller the river gets. Thus, the first topic of this thesis addresses the satellite altimetry over rivers with a focus on small rivers with its key questions:

> ### Water level observation with satellite altimetry
>
> - Which altimetric observation should be used to estimate the water level?
> - What is the size of a river that can be observed with satellite altimetry?
> - Do novel altimeter techniques improve the derived water levels?

Even though altimetry allows observing rivers over a longer time span, the spatial and temporal resolution of the water level time series depend on the orbit of the different altimeter missions. Many hydrological events of a river, like floodings, have a shorter time span than the repeat time of the altimeter missions and therefore, can often not be observed with satellite altimetry. At the same time, the distance along the river between two observations of the same satellite can be significantly larger than 100 km due to the shape and meandering of the river. If all available satellite altimetry data

---

[1]   `http://ffw.mrcmekong.org/historical_rec.htm`

are combined, a denser spatial and temporal observation of the river is possible. But to combine the data along the river, its flow behaviour has to be considered. This leads to the second topic of this thesis and its key questions:

Combination methods for multi-mission altimetry

- What is an appropriate method for the combination?

- How can the flow of the river be statistically modelled?

- Is multi-mission altimetry capable of observing extreme river flood events?

1.2 Study Area

This thesis used the Lower Mekong River Basin as case study. The Mekong River in South-East Asia is one of the largest rivers worldwide and the basin is densely populated. The basin includes six countries: China, where the river source lies on the Tibetan Plateau; Myanmar; Laos, with many of the tributaries contributing large discharge; Thailand; Cambodia with the Tonle Sap system; and Vietnam with the Mekong Delta. **??** shows a map of the Lower Mekong River Basin.

The landscape surrounding the river changes during its flow to the ocean. North of Vientiane the main river flows through a mountainous area with steep river gorges; here the river is only a few hundred meters wide. South of Vientiane the main river flows over the Khorat Plateau with its gently sloping landscape up to the Mekong Falls south of Pakse. In this stretch the river width reaches already one kilometre. From there on the river widens to one–five kilometres and is surrounded by flat terrain and seasonal wetlands. In Phnom Penh the Tonle Sap River merges with the Mekong River and the river opens up to the delta with many shifting channels and islands. In the delta the river is under tidal influence. Most of the tributaries flow through hilly or mountainous topography, including the important left bank tributaries in Laos. Only the right bank tributaries originating on the Khorat Plateau and the tributaries of the downstream flat lands flow through smooth landscape.

The hydrology of the Mekong River has two major compartments (Mekong River Commission, 2005; Adamson et al., 2009): The first compartment is called the Yunnan compartment. The snowmelt on the Tibetan Plateau causes the variations of this compartment. Its discharge governs the flow of the river up to Vientiane and makes up to 30% of the average dry season flow of the Mekong River. Its main flood occurs in August and September. South of Vientiane, the South-Eastern monsoon compartment is the governing driver of the hydrology. The major left bank tributaries in Laos are solely governed by the monsoon and provide 50% of the overall runoff of the Mekong

Figure 1.1: Map of the Lower Mekong River Basin

River Basin. The monsoon lasts from mid-May to mid-October which defines the annual flood season during June and November with its main peak in precipitation and water level in August. The central region around Pakse and the left bank tributaries see an annual average of 2000 mm precipitation with 500 mm on average only in August.

The two separated hydrological compartments, though normally in phase, can cause a so-called hydrological discontinuity. This means that the amplitude of the flood upstream of Vientiane can be different from the amplitude downstream of Vientiane. Therefore, it is even possible that in the same flood season the upstream reach sees a flooding while the downstream reaches experience a drought; this happened in the flood season of 2008.

The anomalous hydrology of the Tonle Sap Lake and River should be mentioned here as well: During the dry season, the Tonle Sap drains in Phnom Penh into the Mekong River. But during the flood season, the water of the Mekong River presses into the Tonle Sap River and cause a flow reversal which fills the Tonle Sap Lake with water. The lake more than triples its size during the flood every year.

Despite the dense population along the river, compared to other large global river systems the Lower Mekong River Basin is still rather natural in its flow with only dams for hydro-electrical power plants and flood regulation along minor tributaries. The location of the dams which were built and put in operation before 2016 are shown as well in **??**. For the next years more dams are planned in the Lower Mekong River Basin, even along the main stream (Mekong River Commission, 2010, chap. 4.2). In the Upper Mekong River Basin in China, several dams have been in operation along the main stream for the last few years with even more planned. Simulation studies estimate that the operation of the main stream dams will increase the dry season and decrease the wet season discharge (Lauri et al., 2012) and a recent study indicates that this effect is already caused by the Chinese dams (Liu et al., 2016). The dams along the tributaries have only a very regional influence and do not alter the main river flow (Mekong River Commission, 2010, chap. 3.1)

In this thesis not the whole basin is investigated but only the Lower Mekong River Basin, which are the main river and all its tributaries south of the Chinese border near Chiang Saen and north of the confluence with the Tonle Sap River. In the northern reach in China, the narrow river gorges often shadow the river for the altimeter. In the South, the confluence with the Tonle Sap builds the border of the study area. From here on, tidal influence corrections would be necessary but are not available. Rivers upstream of dams are also not considered; if dams were erected during the time frame considered in this thesis, only data prior to the finalisation are used.

The Mekong River has been chosen as a study area for this thesis because of its importance for the large local population as well as its diverse topography. It allowed investigating the influence of the topography on satellite altimetry in one basin. The hydrology of the Mekong is so far stable, yet interesting and expected to change due to climate change. At the same time, the river is well described and observed by the MRC which allowed for validation of the methods. The transferability of this thesis' methods to other river basins will be discussed in the outlook in **??**.
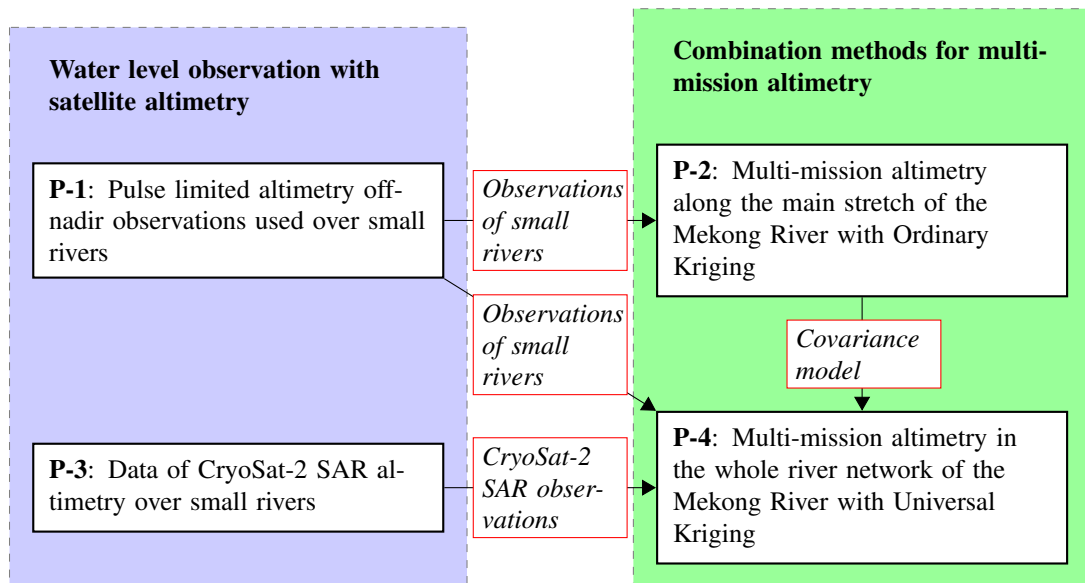
1.3 Outline of this Thesis

Figure 1.2: Relation of the four publications of this thesis to each other: The publications can be divided into two groups, data related and combination related. The arrows show the results that are transferred between the publications.

This thesis includes the four publications:

P-1:   E. Boergens, D. Dettmering, C. Schwatke, and F. Seitz (2016): **Treating the Hooking Effect in Satellite Altimetry data: A Case Study along the Mekong River and Its Tributaries**. In: *Remote Sensing* 8.2, pp. 1–22

P-2:   E. Boergens, S. Buhl, D. Dettmering, C. Klüppelberg, and F. Seitz (2017a): **Combination of multi-mission altimetry data along the Mekong River with spatio-temporal kriging**. In: *Journal of Geodesy* 91.5, pp. 519–534

P-3:   E. Boergens, K. Nielsen, O. B. Andersen, D. Dettmering, and F. Seitz (2017b): **River Levels Derived with CryoSat-2 SAR Data Classification—A Case Study in the Mekong River Basin**. In: *Remote Sensing* 9.12, pp. 1–21

P-4:   E. Boergens, D. Dettmering, and F. Seitz (2018): **Observing Water Level Extremes in the Mekong River with Multi-Mission Altimetry**. In: *Remote Sensing*. in review

These four publications lead the way from single-mission satellite altimetry observations of small rivers to a river basin wide multi-mission altimetry model. The publications can be divided into two groups, a data related group and a part dedicated to multi-mission altimetry (see **??**). The relation between the different publications are

indicated in **??** as well. The data part consists of the publications P-1 and P-3 while the multi-mission altimetry part consists of P-2 and P-4. In P-1 a method was developed to retrieve water level observations for small rivers from pulse limited altimetry. The method was tested on *Envi*ronmental *Sat*ellite (Envisat), *S*atellite with *Ar*gos and *Al*tiKa (SARAL), and *E*uropean *R*emote *S*ensing Satellite-2 (ERS-2) data. P-3 focused then on *S*ynthetic *A*perture *R*adar (SAR) altimetry for water levels in the whole Lower Mekong River Basin and used to this end CryoSat-2 data. In P-2 the first approach was made to combine different altimeter observations from different satellite missions to multi-mission altimetry along the main stream of the Mekong River. This approach was based on *O*rdinary *K*riging (OK) and two covariance functions to model the rivers flow. In this publication only data were used from the *s*hort-*r*epeat *o*rbit (SRO) missions Envisat, SARAL, and Jason-2 as well as Envisat EM with a drifting *n*on-*r*epeat *o*rbit (NRO). Here, the data of the small upstream rivers were processed with the method introduced in P-1. P-4 extended the multi-mission approach of P-2 to incorporate data from all missions, SRO, *l*ong-*r*epeat *o*rbit (LRO) as well as NRO missions, and data over the main stream and over tributaries. To this end, the method applied was *U*niversal *K*riging (UK) with the covariance function developed in P-2. Both the data processing methods of P-1 and P-3 were used for the data of this publication. With this method it was possible to quantify the extremes of the flood season.

?? introduces the different satellite altimetry missions and the basic principles of pulse limited and SAR altimetry. For both pulse limited and SAR altimetry an overview of the state of the art is provided and the two related publications are given in **??** and **??**. **??** is dedicated to multi-mission altimetry with a short outline of the state of the art in this field. The theoretical mathematical background of OK and UK is given with the results presented in **??** and **??**, respectively. The thesis closes with conclusion and outlook in **??**.

2 Satellite Altimetry over Rivers

This chapter addresses the issue of deriving river water level observations from satellite altimetry measurements. Satellite altimetry was originally designed for the observation of the open oceans but has been applied in recent years for the observation of inland water bodies such as lakes, reservoirs, and rivers, too. In the two publications, P-1 and P-3, methods for water level estimations especially designed for small rivers are presented and tested for pulse limited and SAR altimetry, respectively. Today, satellite altimetry can be divided into two groups either by their type of instrument (pulse limited or SAR altimetry) or their orbit configuration (short or long/non-repeat time). Throughout this chapter the former division is employed.

First, a brief overview will be provided of the satellite altimetry missions which will be used or mentioned in this thesis. Second, an introduction to the theoretical background of pulse limited and SAR altimetry and their differences is given. Afterwards, for both techniques the problems of river and inland altimetry are explained and how they can be resolved. P-1 for pulse limited and P-3 for SAR altimetry present a solution of one of the river altimetry problems.

2.1 Satellite Altimetry Missions

Here, a short overview is given over the past, current, and planed satellite altimetry missions. The timeline of the missions is shown in **??** with the missions used in each of the publications indicated; in **??** a summary of all missions is presented.

The first satellite altimeters on board of Seasat (1978) and Geosat (1985–1990) were designed and used for the observation of the ocean surface. With the launch of TOPEX/Poseidon in 1992 the first altimetry satellite which could observe inland water bodies was in orbit. TOPEX/Poseidon measured with the Poseidon-1 Ku-band altimeter and its orbit had a repeat time of 10 days with an inter-track distance of 315 km at the equator. The satellite was in a shifted interleave orbit since 2002 before the satellite's last measurement was recorded in October 2005 and its decommissioning in 2006. Jason-1 was TOPEX/Poseidon's successor on the same original orbit and was equipped with a similar instrument, Poseidon-2. It was launched in 2001, shifted to an
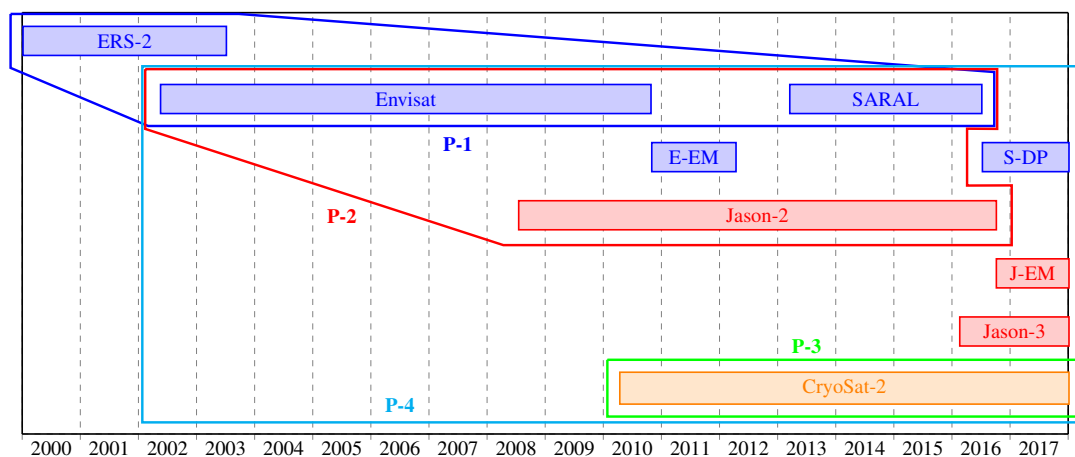
Figure 2.1: Satellite missions that are used in this work with their temporal availability. The start of ERS-2 in May 1995 is cut off due to space limitation. All missions before that are not shown. For each of the four publications the missions used are indicated.

interleave orbit in 2009 and to a geodetic NRO in 2012. Its decommissioning was in 2013. Jason-1 was followed by Jason-2 (launched 2008) with the Poseidon-3 altimeter and Jason-3 (launched Feburary 2016) with Poseidon-3B. Jason-2 was shifted to an interleave orbit after the launch of its successor which leaves Jason-3 currently on the original TOPEX/Poseidon orbit. Since July 2017, Jason-2 is on a LRO due to gyroscope failure. The TOPEX mission and the following Jason missions were and are all jointly operated by *N*ational *A*eronautics and *S*pace *A*dministration (NASA) and *C*entre *n*ational d'*é*tudes *s*patiales (CNES). For Jason-2 and Jason-3, *N*ational *O*ceanic and *A*tmospheric *A*dministration (NOAA) and *Eu*ropean Organisation for the Exploitation of *Met*eorological *Sat*ellites (EUMETSAT) joined the operational team. The altimeter missions of TOPEX/Poseidon, Jason-1, Jason-2, and Jason-3 all measure with a radar bandwidth of 320 MHz (AVISO). The bandwidth governs the temporal resolution and thus the range resolution of the receiving signal; a smaller bandwidth leads to a coarser resolution (see **??**).

The first *E*uropean *S*pace *A*gency (ESA) operated altimeter mission was *E*uropean *R*emote *S*ensing Satellite-1 (ERS-1) launched in 1991 followed by ERS-2 in 1995. Both missions have a repeat time of 35 days and also a Ku band altimeter. The intertrack distance is about 80 km at the equator. ERS-1 was decommissioned in 2000. ERS-2 was officially decommissioned in 2011 but with data gaps since 2003 due to a failure of the onboard tape drive. The ESA mission Envisat was launched in 2002 and had the same orbit as ERS-2 with a repeat time of 35 days. Again its RA-2 altimeter measured in Ku band. Envisat measured in three modes with different bandwidth and accordingly with different bin sizes: over oceans with 320 MHz, over land with 80 MHZ, and over mountainous areas with 20 MHZ (Resti et al., 1999). In October 2010, Envisat was shifted to a NRO with a subcycle of 30 days, i.e. it nearly passed

over the same location again after 30 days. The mission ended in April 2012. For data continuity, the SARAL mission, launched April 2013, had the same orbit as Envisat. In July 2016, a technical problem made it impossible to hold the satellite on a repeat orbit; since then SARAL has a NRO. For the first time, a Ka band altimeter AltiKa is used on this mission which leads to a higher spatial resolution yet also a higher sensitivity to atmospheric water content. The mission is jointly operated by CNES and *I*ndian *S*pace *R*esearch *O*rganisation (ISRO). SARAL has a larger bandwidth, compared to Envisat, with 500 MHz (Bronner et al., 2016).

Since 2010, the ESA mission CryoSat-2 is the first altimeter mission equipped with a Delay-Doppler or SAR altimeter with two antennas and measures in the three modes *L*ow *R*esolution *M*ode (LRM), SAR, and *SAR In*terferometric (SARIn), for which the two antennas are necessary (ESRIN-ESA, 2012). In LRM the CryoSat-2 altimeter operates as a pulse limited altimeter. The altimeter switches between the three different modes according to a mode mask which is updated once in a while[2]. Unlike the other missions so far, CryoSat-2 has been operated since the start on a LRO with a repeat time of 369 days, with a subcycle of 30 days, leading to an intertrack spacing of only 7.5 km at the equator. The altimeter measures with Ku band as well as a bandwidth of 320 MHz. In 2016, ESA launched its second SAR altimeter on board of Sentinel-3A which has a repeat time of 27 days. The altimeter is again a Ku band altimeter but the bandwidth is increased to 350 MHz (ESA, 2015).

The twin satellite to Sentinel-3A, Sentinel-3B, is planned to be launched 2018. Its orbit will be phase shifted by $\pm140°$ to Sentinel-3A. Sentinel-3C and Sentinel-3D are planned to continue the missions into the 2030s for data continuity. Jason-CS/ Sentinel-6 is a European/US American joint mission to be launched in 2020. The planned orbit is the nominal TOPEX orbit but the instrument will be a SAR altimeter. NASA, CNES, *C*anadian *S*pace *A*gency (CSA), and *U*nited *K*ingdom *S*pace *A*gency (UKSA) plan the *S*urface *W*ater and *O*cean *T*opography (SWOT) mission for 2021. The altimeter of this mission will no longer measure the height of a point on the Earth's surface but a 120 km wide swath.

---

[2]   https://earth.esa.int/web/guest/-/geographical-mode-mask-7107

Table 2.1: Overview of the past, current and future satellite altimetry missions

Name	Lifetime	Orbit Repeat time	Orbit Distance equator	Measuring mode	Radar band	Bandwidth	Bin size	Operators	Notes
Past missions									
TOPEX/ Poseidon	1992–2002	10 days	315 km	pulse limited	Ku band	320 MHz	3.125 ns	NASA, CNES	
EM	2002–2005								interleave orbit
Jason-1	2001–2009	10 days	315 km	pulse limited	Ku band	320 MHz	3.125 ns	NASA, CNES	TOPEX orbit
EM	2009–2012								interleave orbit
GM	2012–2013	406 days	8 km						geodetic orbit
Jason-2	2008–2016	10 days	315 km	pulse limited	Ku band	320 MHz	3.125 ns	NASA, CNES, NOAA, EU-METSAT	TOPEX orbit
EM	2016–2017								interleave orbit
ERS-1	1991–2000	35 days	75 km	pulse limited	Ku band	330 MHz; 82.5 MHz	3.03 ns; 12.12 ns	ESA	
ERS-2	1995–2011	35 days	75 km	pulse limited	Ku band	330 MHz; 82.5 MHz	3.03 ns; 12.12 ns	ESA	since 2003 data gaps, ERS-1 orbit
Envisat	2002–2010	35 days	75 km	pulse limited	Ku band	320 MHz; 80 MHz; 20 MHz	3.125 ns; 6.25 ns; 12.5 ns	ESA	ERS-1 orbit
EM	2010–2012		-						drifting orbit
SARAL	2013–2016	35 days	75 km	pulse limited	Ka band	500 MHz	2 ns	CNES, ISRO	ERS-1 orbit
Current missions									
CryoSat-2	2010–	369 days	7.5 km	pulse limited, SAR, SARin	Ku band			ESA	
SARAL DP	2016–	-	-	pulse limited	Ka band	500 MHz	2 ns	CNES, ISRO	drifting orbit
Jason-3	2016–	10 days	315 km	pulse limited	Ku band	320 MHz	3.125 ns	NASA, CNES, NOAA, EU-METSAT	TOPEX orbit
Sentinel-3A	2016–	27 days	104 km	SAR	Ku band	350 MHz	2.86 ns	ESA	
Jason-2 GM	2017–		8 km	pulse limited	Ku band	320 MHz	3.125 ns	NASA, CNES, NOAA, EU-METSAT	geodetic orbit
Future missions									
Sentinel-3B	planned 2018	27 days	104 km	SAR	Ku Band	350 MHz	2.86 ns	ESA	Sentinel-3 orbit 140° phase shifted
Jason-CS/ Sentinel-6	planned 2020	10 days	315 km	SAR	Ku band	320 MHz	3.125 ns	NASA, ESA, NOAA, CNES, EUMETSAT	TOPEX orbit
SWOT	planned 2021	21 days		wide-swath interferometric altimeter	Ka band	200 MHz	5 ns	NASA, CNES, CSA, UKSA	

2.2 Pulse Limited and SAR Altimetry: Theoretical Background

The basic principle of satellite altimetry, pulse limited and SAR likewise, is the measurement of the distance between the satellite and the surface of the Earth. In **??**, the basic geometrical principle of altimetry is shown. With a known ellipsoidal altitude H_{sat} of the satellite and the assumption that the range R is observed in nadir of the satellite, the ellipsoidal height h_e of the Earth's surface is

$$h_e = H_{sat} - R. \tag{2.1}$$

In most applications, not ellipsoidal heights but geoid heights are needed, thus the geoid height at the location of the observation has to be considered. Additionally, the measured range R is subject to geophysical distortions which have to be corrected as well. The geophysical corrections include atmospheric corrections (wet and dry troposphere and ionosphere) as well as corrections for the surface deformation due to Earth and pole tides. Over the oceans, also corrections for ocean tides and the inverse barometric effect have to be considered. The geoid correction is usually summarised with all other corrections. The height of the surface above the geoid h_g is then

$$h_g = H_{sat} - (R + \text{corrections}). \tag{2.2}$$

The range R is measured as the two way travel time of a radar impulse between the satellite and the surface. The difference between pulse limited and SAR altimetry lies in the acquisition of R.
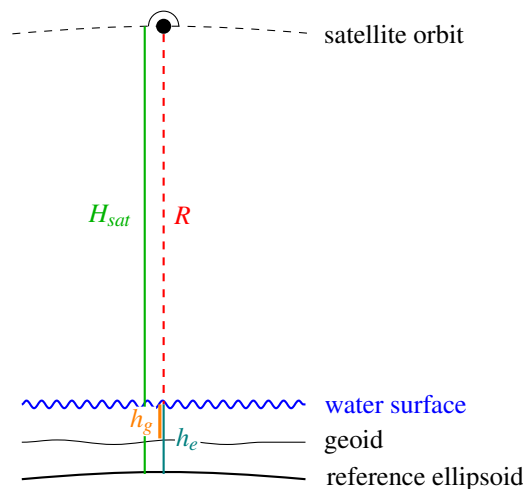

Figure 2.2: Geometric principle of altimetry

2.2.1 Pulse Limited Altimetry

The pulse limited altimeter emits a short radar pulse which propagates spherically towards the Earth's surface, as can be seen in **??**, and whose reflection is observed. The reflection of the signal depends on the reflective surface area which is why first the illuminated area in dependence of time is regarded under the assumption of a planar surface and diffuse reflection. Before the leading edge of the radar crest reaches the ocean surface no area is illuminated (**??** (a)). As soon as the leading edge of the pulse reaches the water, the illuminated area increases linearly with time and the radar pulse is reflected by the surface (**??** (b) and (c)). When the trailing edge of the radar pulse intersects with the surface in nadir the illuminated area is only an annulus with constant area (**??** (d)). The whole area that is illuminated by the radar pulse during a measurement is called the footprint of the altimeter.

Instead of a diffuse reflecting planar surface, waves of different wave heights modulate the water surface. The waves smooth the area function: the smaller the wave heights the steeper the area function rises (see for details on the wave influence Chelton et al. (2000)).

The returned power is recorded over time in a so-called waveform (**??** fourth row). The reflected power of the radar signal is linearly dependent on the reflective area (Chelton et al., 1989) which is why the detected power shows a similar shape to the area (compare **??**, third and fourth row). The fourth row of **??** shows a real waveform over the Pacific Ocean. The part of the waveform with rising power is called leading edge. The opposite trailing edge shows declining power. Though, the illuminated surface area is constant in this part, the surface reflects less well further away from nadir due to waves. The water surface height is assumed to correspond to the half power point of the leading edge.

The altimeter can only detect the returning power with some discretisation called "bins" or "gates". The bin size in seconds depends on the radars bandwidth f_{radar} by $bs = \frac{1.0\,s}{f_{radar}}$ (Chelton et al., 1989) (see **??** for the bandwidth and bin sizes of the different altimeter missions). The size of the footprint, i.e. the maximum illuminated area, depends on the radar bandwidth, the satellite altitude, and the wave height. In general the size of the area ranges between 6 km for SARAL and 10 km for the Jason missions.

The theoretical shape of an ocean waveform has been described by Brown (1977) and Hayne (1980) which is why such waveforms are called Brown-like or ocean-like waveforms. The analytical formula describing the waveform function can be found e.g. in Gommenginger et al. (2011). All satellite altimetry missions have an onboard tracker fitting the Brown-model to the received waveform and most importantly estimate the delay time τ, i.e. difference between the midpoint of the leading edge

and the nominal tracking gate, from which the water surface height is calculated (see details in **??**). Over inland waters the returned waveform deviates from this theoretical shape due to land contamination in the footprint. This will be discussed in **??**.
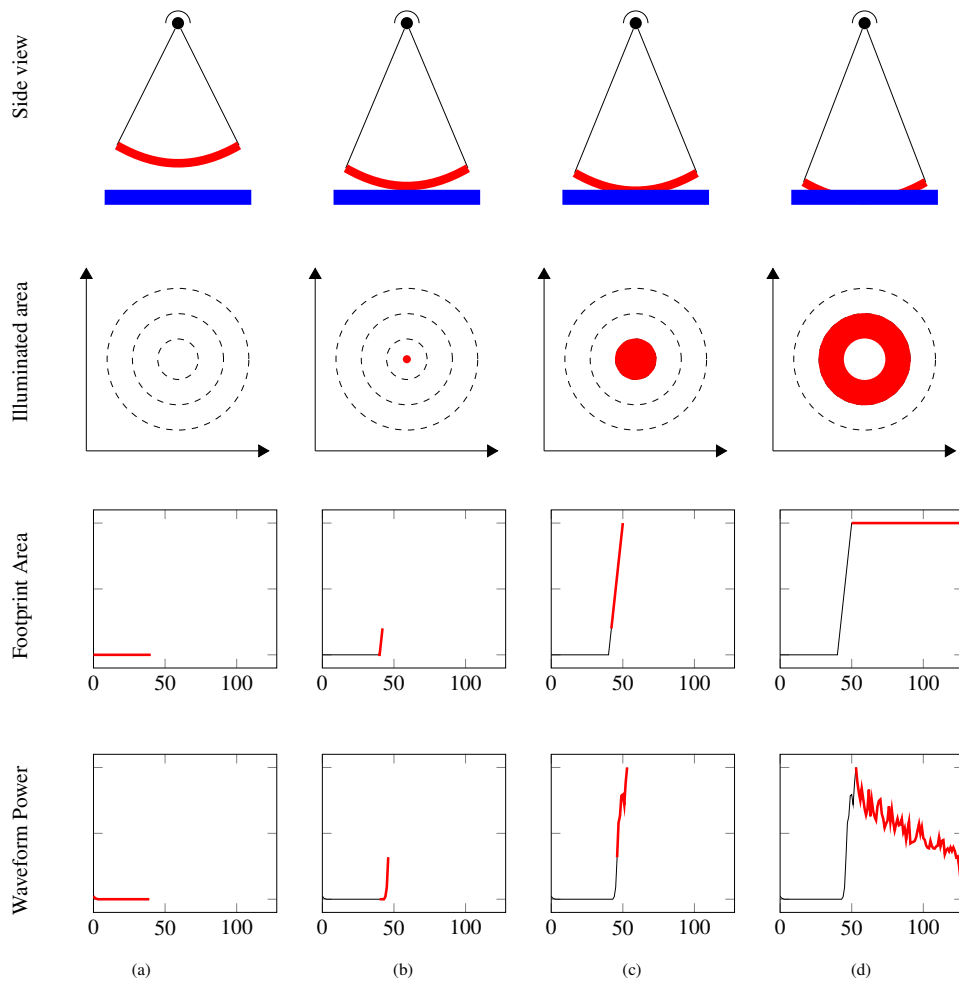
Figure 2.3: Theoretical propagation of the radar impulse and its reflection on a water surface: The first row shows the side view of the altimeter with the emitted radar pulse; the second row shows the top view on the water surface and which part is illuminated by the radar; the third row displays the theoretical illuminated area by the altimeter; the last row shows a real waveform which is reflected by a wave rippled water surface. Each column is a time step. Figure inspired by Chelton et al. (2000).

2.2.2 SAR Altimetry

The concept of Delay-Doppler or SAR altimetry has been originally developed by Raney (1998). In **??** the propagation of the radar impulse for a SAR altimeter is shown similar to **??**. The main difference between pulse limited and SAR altimetry is the along-track discretisation of the returned signal according to across-track "stripes" of the footprint.

The forward motion of the satellite induces a Doppler frequency modulation of the radar signal in the along-track dimension. This frequency shift can be used to recognise the location of the reflection in along-track direction. For this a coherency within one pulse burst of the altimeter is necessary which is ensured with the transmission pattern (Raney, 1998). For example, Sentinel-3 emits in SAR mode four bursts consisting of 64 coherent pulses, whereas in pulse limited mode 95 uncorrelated pulses are emitted for one $20\,\mathrm{Hz}$ waveform (Le Roy et al., 2007). The selected higher pulse repetition frequency of $17.8\,\mathrm{kHz}$ for SAR, compared to $1970\,\mathrm{Hz}$ for pulse limited, has to be larger than the Doppler bandwidth to satisfy the Nyquist criteria (Phalippou et al., 2001). The length of one burst, $12.5\,\mathrm{ms}$ for Sentinel-3, determines the along-track altimeter resolution (Nielsen et al., 2014).

The along-track discretisation of the SAR altimetry divides the radar footprint in said across-track stripes which are shown in **??**, second row. For each of the stripes a returned waveform is recorded in the altimeter but the theoretical shape of it differs from the pulse limited waveform. To understand the difference again the illuminated area is regarded first: Due to the discretisation of the footprint the illuminated area does not increase linearly after the radar pulse reaches the surface but with the square root (**??** (b) and (c) third row). After the trailing edge of the radar pulse intersects with the surface the area does not remain constant but declines with the square root (**??** (d)). Hence, the waveform has a steeper trailing edge. The last row of **??** shows a real waveform collected over the Pacific Ocean, too. Compared to the waveform in **??**, the steeper trailing edge is well visible. The theoretical shape of the waveform has been described by Ray et al. (2015).

For pulse limited altimetry, the returned signal is only detected one-dimensionally in the time domain which corresponds to the increasing radius of the footprint. In contrast, for SAR altimetry the returned signal is detected in a two-dimensional domain with distance along-track and time across-track. This implies that at each location of the satellite orbit, a number of positions on the Earth's surface are measured, or vice versa, that each point on the Earth's surface below the satellites track is measured a number of times under different looking angles. Each of these looks produces a so-called single-look waveform. Usually the data are organised in such a way that

all single-look waveforms of the same location are stacked together (Wingham et al., 2006). To get only one waveform for each location, the mean of the single-look waveforms is taken, which is then called multi-look or SAR waveform. In some applications, the overall power of each single-look waveforms, the *R*ange *I*ntegrated *P*ower (RIP), is considered and collected in the RIP waveform.

In comparison to pulse limited altimetry, SAR altimetry has a higher along-track resolution due to the smaller along-track footprint size, approximately 300 m for the current SAR altimeter missions. The signal-to-noise ratio is reduced compared to conventional pulse limited altimetry and the range accuracy is improved by a factor of up to two (Phalippou and Enjolras, 2007).
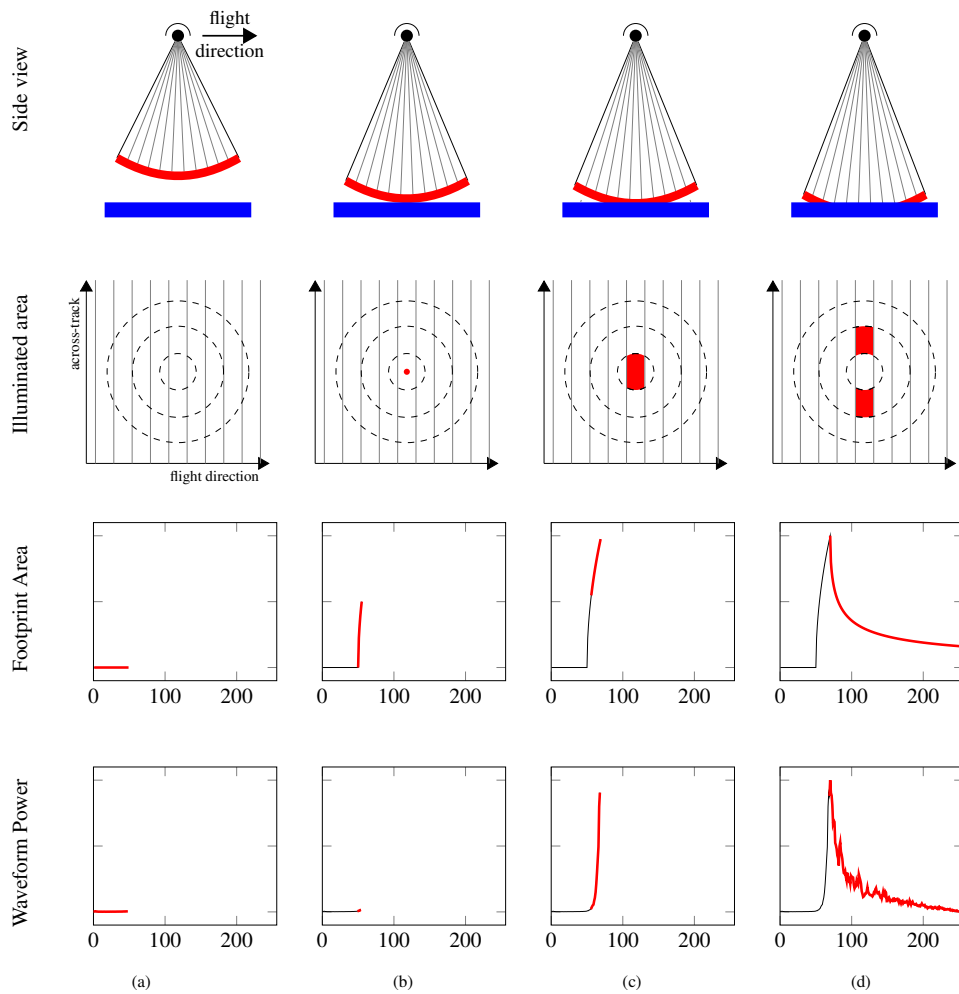

Figure 2.4: Theoretical propagation of the SAR radar impulse and its reflection on a water surface: The first row shows the side view of the altimeter with the emitted radar pulse, the vertical lines indicate the along-track discretisation. The second row shows the top view on the water surface and which part is illuminated by the radar. The footprint of a pulse limited altimeter is shown as well for better comparison. The third row displays the theoretical illuminated area by the altimeter. The last row shows a real waveform which is reflected by a wave rippled water surface. Each column is a time step. Figure inspired by Raney (1998).

2.3 Pulse Limited Altimetry over Rivers

Pulse limited altimetry over inland waters and especially rivers faces problems unknown in ocean altimetry: Due to the land influence the returned waveform deviates from the ideal shape of a Brown-like waveform. This problem is tackled by the use of retrackers which will be described in **??** where also more details on the shape of disturbed waveforms will be given. A second problem of river altimetry is that only very few altimetry observations are collected over a river and these have to be identified in order to derive correct river water levels. To this end, land-water identification approaches are used, the state of the art of these approaches is presented in **??**. The third problem, most immanent over small rivers, are off-nadir measurements called hooking effect. The background of this effect and how it can be treated is described in P-1.

By now, a large number of studies have been published which used satellite altimetry to observe river water levels. In the early years of river altimetry, mostly large rivers like the Amazon River have been observed (e. g. Birkett, 1998; De Oliveira Campos et al., 2001; Birkett et al., 2002; Berry et al., 2005; Frappart et al., 2006). Over large rivers the land contamination is less pronounced and thus, the waveforms appear more ocean-like. Besides, the Amazon River flows in West-East direction which leads to nearly perpendicular intersections between satellite track and river improving the estimation of water levels.

With enhanced algorithms it is possible to improve the results, to reduce the size of the observed rivers, and to automatise the process. For example, Schwatke et al. (2015b) have built the global water level data base *Da*tabase for *H*ydrolog*i*cal *T*ime Series of *I*nland Waters (DAHITI) for both lakes and rivers. The water levels over rivers have been derived with a throughout along-track data selection based on along-track standard deviation combined with waveform classification (Schwatke: personal communication). The Zambezi River has been successfully observed with Envisat in Michailovsky et al. (2012). The Mekong River and its discharge estimated from satellite altimetry have been investigated in Birkinshaw et al. (2010). The São Francisco River in Brazil, which is in some parts only 50 m wide, has been observed in Maillard et al. (2015) with Envisat and SARAL. The water levels have been obtained with the correction of the hooking effect similar to P-1. Indonesian rivers as narrow as 40 m have been observed in Sulistioadi et al. (2015) with Envisat altimetry data. Biancamaria et al. (2016) have measured the 200 m wide Garonne River with Envisat and Jason-2. After an approximate data selection based on Google Earth the precise selection have applied, besides others, a correction of the hooking effect (see again P-1).

The SARAL mission with its smaller footprint due to the Ka band altimeter (instead of a Ku band altimeter in all former missions, see **??**) provides water levels with an improved accuracy over rivers (Frappart et al., 2015) which comes at the price of a higher sensitivity to atmospheric water content (Schwatke et al., 2015a). The sensitivity to atmospheric water content limits the use of SARAL for global river monitoring as many large rivers cannot be observed reliably during the rainy season.

Most of the aforementioned studies use the concept of *Virtual Station* (VS). The VS collects the time series of water level observations for the location of the crossing point of a satellite's track and the river. The temporal resolution of the VS depends on the altimetry mission: 35 days for ERS-2, Envisat, and SARAL or 10 days for TOPEX/Poseidon, Jason-2, and Jason-3. The concept of the VS only works for SRO missions.

2.3.1 Retracking the Pulse Limited Waveform

In **??** and **??**, the theoretical shape of the waveform over the open ocean is introduced. Over inland waters the waveform deviates from this ideal shape because of land present in the altimeter footprint. The footprint size varies between the different altimeter missions due to differing orbit altitude or radar bandwidth and even for the same mission caused by different wave heights (see **??**); as rule of thumb, an upper bound of 10 km footprint size can be used. This leads to land contamination of nearly every waveform measured over a river. In **??**, two exemplary river waveforms measured by Envisat are displayed. The first one, on the left hand side, is a waveform recorded over a 2 km wide river section in the downstream region of the Mekong River and shows peaky disturbances on the trailing edge. Such peaks can be on both the leading and the trailing edge. Land surface has reflective properties different from water, usually it reflects the radar less well than water. At the same time, land surrounding a river is always higher in altitude than the river itself which is why off-nadir land surface can cause a peak before the leading edge. Along many rivers sandbanks or concrete from settlements are very bright reflectors which also cause peaks in the waveform. Thus, in the footprint multiple reflective surfaces are present at different heights which lead to a signal mixture.

The waveform on the right hand side in **??** is a specular or peaky waveform most often found over small rivers with an approximate width of 500 m. The river over which this waveform was measured is only 200 m wide and lies in the upstream region of the Mekong River. Small rivers often have a smooth surface that only reflects the radar pulse in near nadir direction but there very well. This leads to peaky and narrow waveforms with an overall higher maximum power.
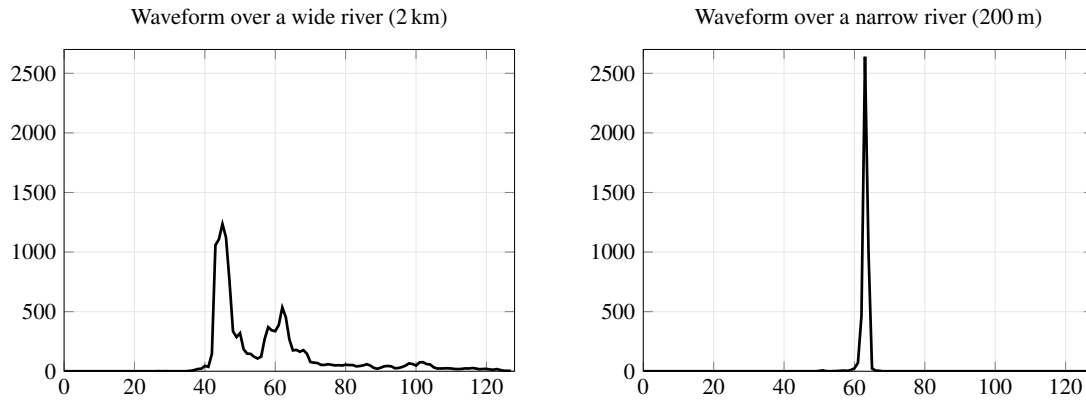
Waveform over a wide river (2 km)   Waveform over a narrow river (200 m)

Figure 2.5: Two waveforms measured over a wide and a narrow river.

Both of the shown waveforms could not be fitted to a Brown-model described in **??**. Nonetheless, the position of the leading edge is sought for the water level estimation. To this end, special algorithms, called retrackers, are used. Retrackers are not only used for inland water bodies such as rivers but also for coastal or sea ice areas. In fact, most retrackers have been originally designed for the latter two applications and then proved to be useful for inland altimetry as well. At first, an introduction to the most important, commonly used, or interesting retrackers is given here, followed by details of the retrackers used in this thesis. In the latter, the way from estimated leading edge position to water level height is described as well.

The retracking algorithms can be divided into three groups: the empirical, the physically-based, and multi-waveform retrackers. Empirical retrackers find the leading edge based only on statistics of the waveform without describing the physical properties behind the waveform. The *O*ffset *C*entre *o*f *G*ravity (OCOG) Retracker (Wingham et al., 1986) is a robust retracker yet its accuracy can be poor. The retracker estimates the centre of gravity of the waveform based on the waveform amplitude and width. Due to its robustness, it is often used as a first retracker to get initial values for a parameter estimation of other retrackers but also for inland applications. The OCOG retracker is e. g. applied for one of the Envisat height data sets, the Ice-1, which is often used for inland water altimetry studies.

In the *T*hreshold *R*etracker (TR), the leading edge is defined as the point of the waveform where the power exceeds a given threshold for the first time (Davis, 1995; Davis, 1997). The threshold is calculated by a percentage of the waveform's amplitude. The TR is independent of distortions of the waveform but does not give any other information than the position of the leading edge. The TR is refined to the *I*mproved *T*hreshold *R*etracker (ITR) which is a TR based on subwaveforms. The ITR is used in this work and will be explained in detail after this general introduction to retrackers.

In contrast to empirical retrackers, physically-based ones provide physically meaningful parameters. The most prominent physically-based retracker is the Brown-Haynes retracker (Gommenginger et al., 2011) which fits the Brown-model to the waveform. This retracker is commonly used on board of the satellites to estimate the water heights. As this retracker does not work well over inland waters, no further detail will be given here.

Passaro et al. (2014) have developed the retracker *A*daptive *L*eading *E*dge *S*ubwaveform (ALES), a physically-based subwaveform retracker for coastal regions. In this retracker, the Brown-model is only fitted to the subwaveform around the leading edge allowing for noisier waveforms on the trailing edge. Passaro et al. (2018) have improved the retracker to ALES+ to be more fitting for ice leads and inland waters. A first test over the Mekong River has shown comparable performance for ALES+ and ITR.

Enjolras and Rodriguez (2009) have developed a waveform model based on remote sensing data from *Mod*erate-resolution *I*maging *S*pectroradiometer (MODIS), Landsat, and *S*huttle *R*adar *T*opography *M*ission *D*igital *E*levation *M*odel (SRTM DEM). The model output is a land contaminated waveform that is expected at a given location. This model waveform has been fitted to the measured waveform to derive the position of the leading edge. This retracker has proved suitable for lakes and rivers though it is dependent on the remote sensing data and requires a larger computational load. A Brown-model with peaks on the leading or trailing edge has been fitted in the retracker by Uebbing et al. (2015). The retracker has shown good results for inland lakes in Africa but it is computationally expensive.

In the last group of retrackers, the multi-waveform retrackers, instead of the single waveform a succession of several waveforms is considered. For coastal areas or larger lakes it can be assumed that adjacent altimetry observations measure the same water level. One example of such a retracker is Sandwell and Smith (2005). As these retrackers cannot be used for rivers, the group of multi-waveform retrackers is just mentioned here for the sake of completeness.

This introduction to retracking algorithms cannot be exhaustive as many studies develop specific retrackers for the aim of their study which are not used in another context afterwards. It should be noted that each retracker might introduce its own offset to the water surface heights which is why one should use a consistent retracker for different data processing in the same application.

Two retrackers have been used in the work of this thesis: The first one is the ITR of Hwang et al. (2006); the second one has been developed in P-1 and is called the *M*ulti-*S*ubwaveform *R*etracker (MSR). The latter is an enhancement of the ITR.

The ITR belongs to the class of empirical retrackers and is thus equally well suited for peaky or specular waveforms like the ones shown in **??**. In its first step, the waveform is separated into subwaveforms. From each of these subwaveforms the leading edge can be found with a Threshold Retracker. In this, the leading edge is defined as the point where the subwaveform reaches a given threshold defined as percentage of the maximum amplitude of the subwaveform.

With the position of the leading edge determined, the range R and thus the height in **??** can be calculated. To this end, the bin size and the position of the reference bin as well as the range associated to the reference bin are needed. The latter is provided by the mission operating agencies in the data as raw range R_{raw}. The bin size bs in known due to the radar bandwidth and the reference bin B_{ref} is usually given in the handbook of the data product provided by the mission operators. The conversion of the bin size in time to distance is done with the speed of light c. Combining these, we estimate the range as

$$R = R_{\mathrm{raw}} + \frac{bs \cdot c}{2}(B_l - B_{\mathrm{ref}}). \tag{2.3}$$

So far, the ITR provides a set of subwaveforms of which each defines a water level, but it has to be decided which one of these subwaveforms is corresponding to the water reflection and thus provides the correct water level. Here, several possibilities arise: Hwang et al. (2006) have used the ITR for coastal zones and use the subwaveform describing the water level closest to the water level of the previous measurement (approaching the land from the open ocean). This approach is not feasible for inland waters as no reliable previous observation is available. A second approach used more often for inland waters is always to take the first subwaveform. The third approach is to use the "best" subwaveform, where "best" can be defined as the subwaveform with the highest amplitude, the longest subwaveform, or the highest integrated power. In P-3 as well as in the data preparation for P-2 and P-4 the ITR with the highest amplitude subwaveform is used.

The MSR developed in P-1 uses the same subwaveform detection algorithm as ITR. The set of the subwaveforms is then used in two different manners. In the first approach, not a single subwaveform is chosen; instead all subwaveforms are used to determine water levels. This set of water levels is later used with water level sets of adjacent measurements to find the common water level. This approach is only feasible if a second advanced water level finding algorithm is applied afterwards. In P-1 this is used to identify the off-nadir observations that form the hooking effect. The second option of the MSR is a new definition of the 'best' subwaveform. Here, the best subwaveform is the one with the highest integrated power. It is found that this definition

of the best subwaveform most often identifies the subwaveform originating from the off-nadir observation and thus, this has improved the hooking effect treatment in P-1. The MSR has also been used in the data processing of Zlinszky et al. (2017).

2.3.2 Land Water Identification of Pulse Limited Observations

The identification of water observations in the altimetry data is the second big issue for river altimetry after retracking. Mainly, there are two ways of water identification, either by a land-water-mask or by waveform classification.

The use of a land-water-mask to identify water returns is widespread. These masks can be either provided as auxiliary data, such as the masks by the CIA World Data Bank II[3] or by the World Wildlife Fund[4], or retrieved from remote sensing images. Masks have been used e. g. by Berry et al. (2005) for global lakes and the Amazon River. The main drawback of these masks is the deficiency in mapping the temporal change. Either the mask maps the high water extent which leads to the inclusion of land observations during the dry season, or it maps the low water extent in which case valid water returns during high water season are missed.

In recent years, the availability of high resolution remote sensing images allowed to derive improved masks. With the high temporal sequence of images the seasonal variability can be mapped to a land-water-mask. Both optical and SAR images are used for this water identification. In general, optical images have a higher spatial resolution but cannot look through cloud cover. This cloud cover is a prominent problem in the tropics where during the rain and high water season most days are overcast. Unfortunately, also the global major river systems are located in the tropics. SAR images are independent of cloud cover but used to have a lower spatial resolution which changed with the launch of Sentinel-1 in 2014. Nonetheless, SAR images were used before but only for large major rivers. For example, Frappart et al. (2005) have used JERS-SAR images to detect rivers in the Rio Negro Basin. In regions without the cloud problem, Landsat images could be used to detect water surfaces; such an approach has been chosen in Kouraev et al. (2004) for the Ob River and TOPEX/Poseidon altimetry data. With better image processing algorithms of recent years, it is also possible to decrease the size of the detected rivers. Marshall and Deng (2016) have showed this with Landsat data for the Fly River and its surrounding wetlands in Papua New Guinea. Global land-water data sets derived from Landsat are by now available (Pekel et al., 2016).

Besides land-water-masks, waveform classification is used to identify water and land observations. Deng and Featherstone (2006) have used a waveform classification scheme in the coastal areas where each waveform is assigned to a waveform shape

---

[3]   https://www.evl.uic.edu/pape/data/WDB/
[4]   https://www.worldwildlife.org/pages/global-lakes-and-wetlands-database

class. Due to the higher backscatter of water compared to land the waveform backscatter coefficient can be used for discriminating land and water observations with a threshold level for the coefficient (e.g. Ghosh et al., 2015). This approach does not require further computation as the backscatter coefficient is included in the official data product and the approach is suitable for smaller lakes. Dettmering et al. (2016) have tested both the backscatter classification approach and a classification with waveform-derived peakiness in the Pantanal wetland. Peakiness is a measure for the specular shape of the waveform. Similar to the backscatter classification, all waveforms with a peakiness above a certain threshold are considered as water returns.

SARAL and Jason-2 data have been classified over the Brahmaputra in Desai et al. (2015) based on the shape of the waveform and the number of its peaks. With this, the waveforms are grouped as water, land, or land-water transition and retracked accordingly. Sulistioadi et al. (2015) have classified Envisat waveform shapes and used only Brown-like, specular, and flat-patch waveforms for the water level estimation along Indonesian Rivers.

Schwatke et al. (2015c, and personal communication) have used the waveform derived parameters skewness, kurtosis, peakiness, maximum power, and signal-to-noise-ratio to classify the observations in different single peak, ocean-like, and noisy waveform classes. The classes which should be used depend on the application: single peak (or specular) waveforms should be used for rivers; whereas ocean-like should be used for larger lakes. In Schwatke and Dettmering (2017, and personal communication) the fit of different waveform functions has been used to distinguish between single peak, ocean-like, or noisy waveforms. Similar to Schwatke et al. (2015c), the classes used for each application can differ.

Many authors do not use either a land-water-mask or a waveform classification but a combination of both approaches. For example, already Birkett (1998) have used the Operational Navigation Charts together with the backscatter coefficient to identify the water returns in TOPEX/Poseidon data. Berry et al. (2005) have employed both the CIA World Data Bank II and classify the waveform according to their shape for lakes and the Amazon River. The combination of Landsat derived land-water-mask and the backscatter coefficient have been used in Michailovsky et al. (2012) over the Zambezi River.

In the work of this thesis, the classification of Schwatke and Dettmering (2017) is used for parts of the data processing of the LRO or NRO missions in P-4. P-2 and P-4 use altimetry data processed in DAHITI in which the same classification method is applied for the water level retrieval. In the study of P-1, a land-water identification is not necessary as not only data over the river but also off-nadir observations besides the river are used.

2.3.3 Off-nadir Effects in Pulse Limited Altimetry

The off-nadir observations called hooking effect are described and corrected over small rivers in the Mekong River Basin in the following publication:

E. Boergens, D. Dettmering, C. Schwatke, and F. Seitz (2016): **Treating the Hooking Effect in Satellite Altimetry data: A Case Study along the Mekong River and Its Tributaries**. In: *Remote Sensing* 8.2, pp. 1–22

Abstract: This study investigates the potential of satellite altimetry for water level time series estimation of smaller inland waters where only very few measurements above the water surface are available. A new method was developed using off-nadir measurements to estimate the parabola generated by the hooking effect. For this purpose, a new waveform retracker was used as well as an adopted version of the RANdom SAmple Consensus (RANSAC) algorithm. The method is applied to compute time series of the water levels height of the Mekong River and some of its tributaries from Envisat high-frequency data. Reliable time series can be obtained from river crossings with widths of less than 500 m and without direct nadir measurements over the water. The expected annual variations are clearly depicted and the time series well agree with available *in situ* gauging data. The mean RMS value is 1.22 m between the resulting time series and *in situ* data, the best result is 0.34 m, the worst 2.26 m, and 80% of the time series have an RMS below 1.5 m.

2.4 SAR Altimetry over Rivers

The main difference between pulse limited and SAR altimetry is the smaller footprint dimension in the along-track direction (see **??**). This improves the water level accuracy, especially of smaller inland waters like rivers. Due to the reduced along-track footprint size, the hooking effect as described for pulse limited altimetry in P-1 does not affect SAR altimetry in such a significant way. Still across-track off-nadir measurements, called snagging, are still possible for SAR altimetry data and cannot be removed as easily as the hooking effect.

So far, merely a limited number of studies have been published using SAR altimetry data over inland waters and in particular over rivers. Up to now, only two missions carry a SAR altimeter, CryoSat-2 and Sentinel-3A. The long-repeat time of CryoSat-2 hinders the VS concept along rivers, while Sentinel-3A has a repeat time of 27 days but only two years of available data. Additionally, CryoSat-2 is measuring only few rivers, or parts of them, in SAR mode: the Mekong River, the Ganges-Bramaputra River system, the Amazon River, the Mississippi, the Po River, and the Yellow River.

Nevertheless, some authors have used CryoSat-2 data for inland waters: Water levels of lakes around the world with varying size have been investigated in Nielsen et al. (2015) and Nielsen et al. (2017). They have applied a new statistical model to identify the water level which does not need any land-water identification (except a rough outline) or outlier detection. Göttl et al. (2016) have used CryoSat-2 SAR data over lakes as well but identified the lake level observations with an unsupervised waveform classification. CryoSat-2 LRM, SAR, and SARIn data have been used in L. Jiang et al. (2017) to monitor Chinese lakes and rivers. Unfortunately, of all Chinese rivers only the downstream reach of the Yellow River is measured in SAR mode.

CryoSat-2 SAR data have been used by Bercher et al. (2013) over the Amazon River. Villadsen et al. (2015) have employed SAR data to observe the water level variations in the Ganges-Bramaputra basin. To build water level time series, the river slope has been approximated by simple polynomial functions which have been estimated from CryoSat-2 and Envisat water levels. CryoSat-2 data, both LRM and SAR, have been used in Tourian et al. (2016) over the Po River together with altimetry data of other missions in a multi-mission altimetry approach. To date, only in Bogning et al. (2018) Sentinel-3 data have been used for river altimetry to study the Ogooué River in West-Africa.

Similar to pulse limited altimetry, SAR altimetry data need special post-processing over inland waters, namely retracking. In **??** new and different retracking methods specifically designed for SAR altimetry will be introduced while in P-3 the land-water classification of SAR data is treated.

SAR altimetry data contain additional information with the stack data (see **??**) which can be used for improving a land-water classification as it is done in P-3. But, the stack data can also be used to improve the waveform: Over small inland waters, the specular reflection of the water surface yields only returned power near nadir. This is visible in the stack data with high-power in the single-look waveforms adjacent to the nadir-looking one. Figure 3 of P-3 displays two stack matrices over a small river and a lake. All other single-look waveforms contain only noise. By selecting only these high-power single-look waveforms for the multi-look SAR waveform, the waveform gets less noisy.

A small test of this has been conducted at some locations along the Mekong River. Two different methods have been tested to identify the high-power single-look waveforms: first, an exponential peak function has been fitted through the RIP waveform and only those single-look waveforms have been taken where this function was above a certain threshold for the multi-look waveform. Second, every single-look waveform has been used to estimate a height from it. From these heights, all single-looks which measured the same height have been identified and used for a multi-look waveform. It has been found that with both approaches the waveform gets less noisy; even better with the second approach at the cost of a high computational effort. However, the height estimation has not significantly improved by this.

2.4.1 Retracking the SAR Waveform

Similar to pulse-limited altimetry, SAR altimetry needs retracking over rivers and lakes. Some authors use pulse limited altimetry retrackers for SAR altimetry as well, e. g. Göttl et al. (2016) use the ITR for CryoSat-2 SAR data.

Nevertheless, the different shape of the SAR waveform makes specific SAR retrackers advantageous. Ray et al. (2015) have developed a mathematical model similar to the Brown-model for pulse limited altimetry which can be fitted to the observed SAR waveforms. The corresponding retracker is called the *S*AR *A*ltimetry *Mo*de *S*tudies and *A*pplications over Ocean, Coastal Zones and Inland Waters (SAMOSA) retracker. SAMOSA3 is a simplified version of the SAMOSA retracker assuming Gaussian ocean statistics; SAMOSA+ is another version of the SAMOSA retracker specifically designed for inland waters and coastal areas (Dinardo et al., 2017). The SAMOSA retrackers are used in the *G*rid-*P*rocessing *O*n *D*emand *SAR V*ersatile *A*ltimetric *T*oolkit for *O*cean *Re*search & Exploitation (GPOD SARvatore) database, which disseminate CryoSat-2 and Sentinel-3 data including the stack data[5].

Besides physically based retrackers, empirical retrackers have been developed for SAR altimetry, too, which are often better suited for inland waters. The *Primary Peak Retracker* (PPR) has been developed by Jain et al. (2015). Thought originally designed for ice leads, it can be used for river as they show a similar behaviour with specular peaky waveforms. PPR is a subwaveform retracker similar to the ITR but with slightly different thresholds. The first subwaveform is taken and the leading edge is either found with the OCOG retracker applied to the subwaveform or with a TR; in the latter case it is called the *Narrow Primary Peak Retracker* (NPPR). Villadsen et al. (2015) have found a threshold of 80% most suitable for the NPPR over the Ganges-Bramaputra River.

Villadsen et al. (2016) developed the multi-waveform retracker *Multiple Waveform Persistent Peak Retracker* (MWaPPR) for lakes and rivers. An averaged waveform of the height aligned adjacent waveforms is used to identify the primary peak of the waveform. This peak is retracked with a TR to determine the position of the leading edge.

In P-3, an ITR is applied with a threshold of 50%. Usually, it is advisable to use the same retracker for data of different satellite missions in one application. However, this does not apply if both pulse limited and SAR data are combined because of the different physical properties of the waveform. The retracking bias has to be removed by other means.

2.4.2 Land Water Identification of SAR Altimetry Observations

The land-water classification of CryoSat-2 SAR data is subject of the following publication:

E. Boergens, K. Nielsen, O. B. Andersen, D. Dettmering, and F. Seitz (2017b): **River Levels Derived with CryoSat-2 SAR Data Classification—A Case Study in the Mekong River Basin**. In: *Remote Sensing* 9.12, pp. 1–21

Abstract: In this study we use CryoSat-2 SAR (Delay-Doppler Synthetic Aperture Radar) data in the Mekong River Basin to estimate water levels. Compared to classical pulse limited radar altimetry, medium and small sized inland waters can be observed with CryoSat-2 SAR data with a higher accuracy due to the smaller along-track footprint. However, even with this SAR data the estimation of water levels over medium sized river (width less than 500 m) is still challenging with only very few consecutive observations over the water. The target identification with land-water-masks tends to fail as the river becomes smaller. Therefore, we developed a classification approach to divide the observations into water and land returns based solely on the data. The classification is done with an unsupervised classification algorithm, and it is based on features derived from the SAR and RIP (Range Integrated Power) waveforms. After the classification, classes representing water and land are identified. Better results are obtained when the Mekong River Basin is divided in different geographical regions: upstream, middle stream and downstream. The measurements classified as water are used in a next step to estimate water levels for each crossing over a river in the Mekong River network. The resulting water levels are validated and compared to gauge data, Envisat data and CryoSat-2 water levels derived with a land-water-mask. The CryoSat-2 water levels derived with the classification lead to more valid observations with less outliers in the upstream region than with a land-water-mask (1700 with 2% outliers vs. 1500 with 7% outliers). The median of the annual differences that is used in the validation, is in all test regions smaller for the CryoSat-2 classification results than for Envisat or CryoSat-2 land-water-mask results (for the entire study area: 0.76m vs 0.96m vs. 0.83m). Overall, in the upstream region with small and medium sized rivers the classification approach is more effective for deriving reliable water level observations than in the middle stream region with wider rivers.

3 Altimetry Data Combination

In this chapter, the combination of different altimeter missions and passes to a new multi-mission altimetry time series along rivers is introduced. Altimetric water level time series are limited by the temporal and spatial resolution of the different satellite altimetry missions. To overcome the resolution limitations, a combination of the single-mission altimetry is done. First, state of the art of multi-mission altimetry over lakes and along rivers is introduced. The first multi-mission approach of this thesis is based on *O*rdinary *K*riging (OK); in **??**, the theoretical background of OK is explained and in P-2, the results of this approach are presented. In the second approach altimetry data not only along the main stream of the Mekong River but along the tributaries as well are incorporated. Additionally, data of LRO and NRO missions, most importantly CryoSat-2 data, are included in this approach. To this end, it is necessary to use *U*niversal *K*riging (UK) whose theoretical background is introduced in **??**. The results of this are then shown in P-4.

3.1 Multi-Mission Altimetry—State of the Art

The combination of multi-mission altimetry over lakes and reservoirs has been done by several groups in the last years. The lake surface theoretically describes the same equipotential surface and thus all altimetric observations should observe the same water level at the same time regardless of the mission and their pass location over the lake. As a consequence, the same water level variations are observed everywhere over the lake. In reality, some biases between the observations occur and have to be corrected in order to combine multiple passes and altimeter missions to one common water level time series. These biases can be caused by geoid models which cannot reflect small spatial variations or inter-mission biases.

Two of the global databases providing altimetric water level time series use multi-mission altimetry over lakes and reservoirs: Hydroweb[6], developed by *L*aboratoire d'*E*tudes en *G*éophysique et *O*céanographie *S*patiales (LEGOS), and DAHITI[7] developed by *D*eutsches *G*eodätisches *F*orschungsinstitut der *T*echnischen *U*niversität *M*ünchen (DGFI-TUM).

---

[6]   http://hydroweb.theia-land.fr/
[7]   http://dahiti.dgfi.tum.de

In Hydroweb, for each mission and each pass over the lake a water level time series is computed individually. In the temporal overlap between the time series the offset between them is estimated and the time series are reduced by this offset to a common basis (Crétaux et al., 2011). With this approach, the inter-mission offsets are removed and the geoid variations can be reduced. In DAHITI, the inter-mission biases are reduced beforehand by the offsets provided by Bosch et al. (2014) as well as by using a common retracking method for all data. After an outlier detection in the first step, the water level observations are combined with a Kalman filter (Schwatke et al., 2015b). The Kalman filter approach allows introducing the water level observations of different missions and tracks with varying accuracies. For larger lakes, the Kalman filter can be processed on a grid to allow for surface variability.

For rivers, the combination of multi-mission altimetry data proves to be more complicated. Here, the water surface is sloped along the river and the amplitude of the water level variations depends on the topography and topology of the river. Narrow gorges cause a higher amplitude of the water level time series and inflowing tributaries can alter the flood behaviour. Nonetheless, beside the work of this thesis a few studies addressing multi-mission altimetry along rivers have been published.

Tourian et al. (2016) have densified altimetric water level observations of Jason-2, Envisat, SARAL, and CryoSat-2 along the Po River. Data combination has been achieved with the flow velocity between the water level observations. At each VS the flow velocity has been estimated by using the river slope, approximated at four in situ stations, and the river width, derived from Landsat 7 images. Tourian et al. (2017) have used multi-mission altimetry along the Niger River and two major tributaries to estimates river basin wide discharge instead of water level time series. The discharge has been estimated from the altimetry data via a rating curve at the gauging stations. Only the missions Jason-2, Envisat, and SARAL have been used here. The link between the discharge at the VSs has been done with a Kalman filter.

The spatial coverage of simulated SWOT data along the Tennessee River has been improved with a local space-temporal kriging in Yoon et al. (2013). The method is based on an OK with an adapted variogram model that allows for the flood time lag between different locations.

Though no multi-mission approach in a strict sense, two studies have investigated the combination of CryoSat-2 data along a river to yield water level time series; these methods could also be used to combine multi-mission altimetry. Villadsen et al. (2015) have reduced the topography of the Ganges and the Brahmaputra River with a simple polynomial function estimated from CryoSat-2 and Envisat data which allowed to connect the CryoSat-2 data. Bercher et al. (2013) have used a simple topography model of the Amazon River to combine CryoSat-2 data.

3.2 Spatio-Temporal Kriging Approach for Multi-Mission Altimetry

Kriging is an optimal geostatistical interpolation method based on scattered data with a known covariance function. It was developed by Krige (1952), originally only for spatial data. The kriging interpolation is optimal in the sense that it is an unbiased estimator optimal with respect to the mean-squared interpolation error. The word interpolation and prediction can be used interchangeably in the kriging context.

Altimetry data $\{Z(\boldsymbol{s}_1, t_1), \ldots, Z(\boldsymbol{s}_n, t_n)\}$ are observed at the spatial location $\{\boldsymbol{s}_1 \ldots \boldsymbol{s}_n\}$ with $\boldsymbol{s} \in \mathbb{R}^2$ and the time $\{t_1, \ldots, t_n\}$ with $t \in [0, \infty)$; the number of observations is n. Each tuple of $(\boldsymbol{s}_i, t_i)$ is unique but not every location $\boldsymbol{s}_i$ or time t_i needs to be unique.

For all kriging methods, the prediction $\mathrm{p}(\boldsymbol{s}_0, t_0)$ at the location $(\boldsymbol{s}_0, t_0)$ is the weighted mean of all observations $Z(\boldsymbol{s}_i, t_i)$, i.e. for weights $\lambda_i \in \mathbb{R}$, $(i = 1, \ldots, n)$,

$$\mathrm{p}(\boldsymbol{s}_0, t_0) = \sum_{i=1}^{n} \lambda_i Z(\boldsymbol{s}_i, t_i). \tag{3.1}$$

The expected value of the prediction is equal to the expected value of the true value $Z(\boldsymbol{s}_0, t_0)$, thus $E\{\mathrm{p}(\boldsymbol{s}_0, t_0)\} = E\{Z(\boldsymbol{s}_0, t_0)\}$.

The weights λ_i are estimated based on the dependencies between the observations which are modelled with covariances. The estimation of the weights $\boldsymbol{\lambda} = [\lambda_1, \ldots, \lambda_n]$ differs between the different kriging methods which will be explained in more detail in the following sections.

3.2.1 Introduction to Ordinary Kriging

*O*rdinary *K*riging (OK) is the most common sub-method in kriging and was employed in P-2. All observations are assumed to be a realisation of the model

$$Z(\boldsymbol{s}, t) = \mu + \delta(\boldsymbol{s}, t) \tag{3.2}$$

where μ is the deterministic part of the signal and an unknown constant mean while $\delta(\boldsymbol{s}, t)$ is the stochastic signal, i.e. the water level variations. OK is based on the model assumption that μ is constant for all observations which requires that for altimetric water level observations the mean water level, or topography, has to be reduced. Thus, it can only be used for altimetry data of SRO missions where the mean water level of the time series can be computed.

The estimation of the λ_i, and thus the prediction $p(s_0, t_0)$ for $Z(s_0, t_0)$, should be optimal under the constraint $\sum_{i=1}^{n} \lambda_i = 1$ which ensures the unbiasedness of the prediction:

$$E\left\{\left(Z(s_0, t_0) - \sum_{i=1}^{n} \lambda_i Z(s_i, t_i)\right)^2\right\} - 2m\left(\sum_{i=1}^{n} \lambda_i - 1\right) \rightarrow \min \tag{3.3}$$

w.r.t. $\boldsymbol{\lambda} = [\lambda_1, \ldots, \lambda_n]$ and the Lagrange multiplier for the constraint m. With the condition $\sum_{i=1}^{n} \lambda_i = 1$, the first summand of **??** can be reformulated as

$$E\left\{\left(Z(s_0, t_0) - \sum_{i=1}^{n} \lambda_i Z(s_i, t_i)\right)^2\right\} = \underbrace{E\left\{(Z(s_0, t_0) - \mu)^2\right\}}_{C(\mathbf{0}, 0)}$$

$$+ \sum_{i=1}^{n}\sum_{j=1}^{n} \lambda_i \lambda_j \underbrace{E\left\{(Z(s_i, t_i) - \mu)(Z(s_j, t_j) - \mu)\right\}}_{C((s_i, t_i), (s_j, t_j))}$$

$$- 2\sum_{i=1}^{n} \lambda_i \underbrace{E\left\{(Z(s_0, t_0) - \mu)(Z(s_i, t_i) - \mu)\right\}}_{C((s_0, t_0), (s_i, t_i))}. \tag{3.4}$$

Under the assumption that $\delta(s, t)$ is a zero-mean process, the covariances C can be introduced in **??** and **??** becomes

$$C(\mathbf{0}, 0) + \sum_{i=1}^{n}\sum_{j=1}^{n} \lambda_i \lambda_j C((s_i, t_i), (s_j, t_j)) - 2\sum_{i=1}^{n} \lambda_i C((s_0, t_0), (s_i, t_i))$$

$$- 2m\left(\sum_{i=1}^{n} \lambda_i - 1\right) \rightarrow \min. \tag{3.5}$$

To find the minimum of **??**, it is differentiated w.r.t. $\lambda_1, \ldots, \lambda_n$ and m and equated to zero:

$$\sum_{j=1}^{n} \left(\lambda_j C((s_i, t_i), (s_j, t_j))\right) - C((s_0, t_0), (s_i, t_i)) - m = 0, \text{ for } i = 1, \ldots, n. \tag{3.6}$$

Thus, the optimal parameters are:

$$\boldsymbol{\lambda}_{OK} = \boldsymbol{\Sigma}_{OK}^{-1} \mathbf{c}_{OK} \tag{3.7}$$

with

$$\boldsymbol{\lambda}_{OK} = [\lambda_1, \ldots, \lambda_n, m]^\top, \tag{3.8}$$

$$\mathbf{c}_{OK} = [C((s_0, t_0), (s_1, t_1)), \ldots, C((s_0, t_0), (s_n, t_n)), 1]^\top \tag{3.9}$$

$$\Sigma_{OK} = \begin{cases} C((\boldsymbol{s}_i, t_i), (\boldsymbol{s}_j, t_j)), & i, j = 1, \ldots, n \\ 1, & i = n+1, j = 1, \ldots, n \\ 1, & i = 1, \ldots, n, j = n+1 \\ 0, & i = n+1, j = n+1. \end{cases} \tag{3.10}$$

$C((\boldsymbol{s}_i, t_i), (\boldsymbol{s}_j, t_j))$ is the covariance between the two observations at the points $(\boldsymbol{s}_i, t_i)$ and $(\boldsymbol{s}_j, t_j)$. From **??** the separate estimation of the parameter groups can be obtained with:

$$\boldsymbol{\lambda} = [\lambda_1, \ldots, \lambda_n] = (\boldsymbol{c} + \mathbf{1} \frac{(1 - \mathbf{1}^\top \boldsymbol{\Sigma}^{-1} \boldsymbol{c})}{\mathbf{1}^\top \boldsymbol{\Sigma}^{-1} \mathbf{1}})^\top \boldsymbol{\Sigma}^{-1}, \tag{3.11}$$

where $\mathbf{1} = [1, \ldots, 1]^\top$, $\boldsymbol{c} = \boldsymbol{c}_{OK}[1:n]$ and $\boldsymbol{\Sigma} = \boldsymbol{\Sigma}_{OK}[1:n, 1:n]$.

So far, a constant $C(\mathbf{0}, 0)$ has been assumed in the data which equates to the same uncertainties for all observations. For altimetric water level observations along a river network this does not hold.

Let's assume that the uncertainties ε_i of the water level observations are non-systematic, i.e. $E\{\varepsilon_i\} = 0$; uncorrelated between each other, i.e. $cov(\varepsilon_i, \varepsilon_j) = 0, \forall i \neq j$; uncorrelated to the observation, i.e. $cov(\varepsilon_i, Z(x)) = 0$; and the variance factor for each observation σ_i^2 is known (De Marsily, 1986). Then, in **??** the second summand is extended to

$$\sum_{i=1}^n \sum_{j=1}^n \lambda_i \lambda_j C((\boldsymbol{s}_i, t_i), (\boldsymbol{s}_j, t_j)) + \sum_{i=1}^n \lambda_i^2 \sigma_i^2. \tag{3.12}$$

This leads in **??** to

$$\sum_{j=1}^n \left(\lambda_j C((\boldsymbol{s}_i, t_i), (\boldsymbol{s}_j, t_j)) \right) + \lambda_i \sigma_i^2 - C((\boldsymbol{s}_0, t_0), (\boldsymbol{s}_i, t_i)) - m = 0, \text{ for } i = 1, \ldots, n. \tag{3.13}$$

Accordingly, **??** becomes

$$\boldsymbol{\lambda} = [\lambda_1, \ldots, \lambda_n] = (\boldsymbol{c} + \mathbf{1} \frac{(1 - \mathbf{1}^\top \boldsymbol{\Sigma}^{-1} \boldsymbol{c})}{\mathbf{1}^\top \boldsymbol{\Sigma}^{-1} \mathbf{1}})^\top (\boldsymbol{\Sigma} + \boldsymbol{\Sigma}_{\text{alti}})^{-1} \tag{3.14}$$

with $\boldsymbol{\Sigma}_{\text{alti}}[i, i] = \sigma_i^2$. The absolute variance σ_i^2 is not always known in the application but the weighting factors between the different observations are. Without changing the result it is possible to exchange in **??** $\boldsymbol{\Sigma}$ and $\boldsymbol{\Sigma}_{\text{alti}}$ with weight matrices under the condition of a common variance factor σ_0.

In most literature treating kriging, it is assumed for OK that the data are stationary, i. e. the statistical moments of the data do not depend on the location of the data. But, in fact it is irrelevant for the kriging equations if the data is stationary as long as the covariance model can mirror the non-stationarity. Stationarity simplifies the estimation of the covariance function. Similarly, it does not matter in the kriging equation if the data distribution is only spatial or spatio-temporal. The differences between the spatial and the temporal domains are handled by the covariances. The OK approach has been tested with data only along the main stretch of the Mekong River with two different covariance models which are given in detail in P-2. The results of the OK are given there as well.

3.2.2 Multi-Mission Altimetry with Ordinary Kriging

The *O*rdinary *K*riging approach is tested along the main stretch of the Mekong River in the following publication:

E. Boergens, S. Buhl, D. Dettmering, C. Klüppelberg, and F. Seitz (2017a): **Combination of multi-mission altimetry data along the Mekong River with spatio-temporal kriging**. In: *Journal of Geodesy* 91.5, pp. 519–534

Abstract: River water-level time series at fixed geographical locations, so-called virtual stations, have been computed from single altimeter crossings for many years. Their temporal resolution is limited by the repeat cycle of the individual altimetry missions. The combination of all altimetry measurements along a river enables computing a water-level time series with improved temporal and spatial resolutions. This study uses the geostatistical method of spatio-temporal Ordinary Kriging to link multi-mission altimetry data along the Mekong River. The required covariance models reflecting the water flow are estimated based on empirical covariance values between altimetry observations at various locations. In this study, two covariance models are developed and tested in the case of the Mekong River: a stationary and a non-stationary covariance model. The proposed approach predicts water-level time series at different locations along the Mekong River with a temporal resolution of five days. Validation is performed against in situ data from four gauging stations, yielding RMS differences between 0.82 and 1.29 m and squared correlation coefficients between 0.89 and 0.94. Both models produce comparable results when used for combining data from Envisat, Jason-2, and SARAL for the time period between 2002 and 2015. The quality of the predicted time series turns out to be robust against a possibly decreasing availability of altimetry mission data. This demonstrates that our method is able to close the data gap between the end of the Envisat and the launch of the SARAL mission with interpolated time series.

3.2.3 Introduction to Universal Kriging

*U*niversal *K*riging (UK) is a more general approach than *O*rdinary *K*riging as it loosens the constraint of constant mean in the data domain. This allows to incorporate data of LRO and NRO altimeter missions as well where the mean water level is unknown and, thus, cannot be reduced. In contrast to **??** the underlying data model in UK is

$$Z(\boldsymbol{s},t) = \mu(\boldsymbol{s},t) + \delta(\boldsymbol{s},t) = \sum_{j=0}^{l} f_j(\boldsymbol{s},t)\beta_j + \delta(\boldsymbol{s},t). \tag{3.15}$$

$\delta(\boldsymbol{s},t)$ is again the zero-mean random process with covariance $C(\cdot)$ describing the water level variation. The deterministic signal is no longer a constant mean μ but is replaced by $\mu(\boldsymbol{s},t)$, the mean water level depending on location and time. $\mu(\boldsymbol{s},t)$ can be reformulated with an unknown linear combination of known functions $\{f_0(\boldsymbol{s},t),\ldots, f_l(\boldsymbol{s},t)\}$; the vector $\boldsymbol{\beta} = [\beta_0,\ldots,\beta_l]^\top$ is the unknown parameter vector. From **??** follows for all data points

$$\mathbf{Z} = \mathbf{F}\boldsymbol{\beta} + \boldsymbol{\delta}, \tag{3.16}$$

where $\mathbf{F}[j,i] = f_j(\boldsymbol{s}_i,t_i)$, $\mathbf{Z} = [Z(\boldsymbol{s}_1,t_1),\ldots,Z(\boldsymbol{s}_n,t_n)]^\top$, $\boldsymbol{\delta} = [\delta(\boldsymbol{s}_1,t_1),\ldots,\delta(\boldsymbol{s}_n,t_n)]^\top$. The true value at the prediction location is following **??**

$$Z(\boldsymbol{s}_0,t_0) = \mathbf{f}^\top\boldsymbol{\beta} + \delta(\boldsymbol{s}_0,t_0), \tag{3.17}$$

with $\mathbf{f} = [f_0(\boldsymbol{s}_0,t_0),\ldots,f_l(\boldsymbol{s}_0,t_0)]^\top$.

The expected value of the predictor again needs to be equal to the expected value of $Z(\boldsymbol{s}_0,t_0)$ which is necessary and sufficient for the unbiased predictor. I. e. $E\{p(\boldsymbol{s}_0,t_0)\} = E\{\boldsymbol{\lambda}^\top\mathbf{Z}\} = \boldsymbol{\lambda}^\top\mathbf{F}\boldsymbol{\beta}$ have to be equal to $E\{Z(\boldsymbol{s}_0,t_0)\} = \mathbf{f}^\top\boldsymbol{\beta}$. From this, the UK prediction constrain $\boldsymbol{\lambda}^\top\mathbf{F} = \mathbf{f}^\top$ is derived to ensure unbiasedness. The constraint of $\sum_{i=1}^{n}\lambda_i = 1$ still applies and is realised by $f_0(\boldsymbol{s},t) = 1$.

Similar to OK, the mean-squared prediction error has to be minimised under these constraints:

$$E\left\{\left(Z(\boldsymbol{s}_0,t_0) - \sum_{i=1}^{n}\lambda_i Z(\boldsymbol{s}_i,t_i)\right)^2\right\} - 2\sum_{j=0}^{l} m_j\left(\sum_{i=1}^{n}\lambda_i f_j(\boldsymbol{s}_i,t_i) - f_j(\boldsymbol{s}_0,t_0)\right) \to \min,$$
$$\tag{3.18}$$

w.r.t. $\boldsymbol{\lambda} = [\lambda_1,\ldots,\lambda_n]$ and $\boldsymbol{m} = [m_1,\ldots,m_l]$. The derivation of the resulting equations is equivalent to the OK equations, and therefore not shown here.

It leads to the estimation of $\boldsymbol{\lambda}$ with

$$\boldsymbol{\lambda} = \left(\mathbf{c} + \mathbf{F}(\mathbf{F}^\top \boldsymbol{\Sigma}^{-1} \mathbf{F})^{-1} (\mathbf{f} - \mathbf{F}^\top \boldsymbol{\Sigma}^{-1} \mathbf{c}) \right)^\top \boldsymbol{\Sigma}^{-1}. \tag{3.19}$$

The choice of the basis functions $f_j(\boldsymbol{s}, t)$ is essential for the UK approach. To this end, B-Splines of degree 3 have been chosen which will be introduced in more detail in **??**. For offsets between data sets of different altimeter missions (see **??**), another parameter β_{l+k} is introduced for each mission k with the function $f_{l+k} = 1$.

The different uncertainties of the observations can be included in **??** similar to **??** with

$$\boldsymbol{\lambda} = \left(\mathbf{c} + \mathbf{F}(\mathbf{F}^\top \boldsymbol{\Sigma}^{-1} \mathbf{F})^{-1} (\mathbf{f} - \mathbf{F}^\top \boldsymbol{\Sigma}^{-1} \mathbf{c}) \right)^\top (\boldsymbol{\Sigma} + \boldsymbol{\Sigma}_{alti})^{-1}. \tag{3.20}$$

The covariance model used in the UK approach is again the non-stationary model described in P-2. To incorporate tributaries in the UK approach and the covariance model, the relative river location of two observations needs to be known, most importantly if they are flow connected or not. The spatial relations can be modelled by a river topology which is introduced in the following **??**. The UK approach has been tested on water level data in the Mekong River Basin for the observation of extreme events in P-4.

3.2.3.1 River Topology

The river topology should mirror the spatial relations of the different tributaries to each other, i.e. if they are flow connected or not. Additionally, it should be possible to transform two dimensional longitude and latitude coordinates along the rivers to the topology space and vice versa.

To this end, the river network as it is provided as a river polygon by the MRC is mapped to a directed graph. In the first step, the polygon is skeletonised (B. Jiang et al., 2011). In the resulting graph, each confluence of two rivers is represented by a vertex with two possible predecessors (upstream) and one successor (downstream). The upstream end of a tributary and the downstream endpoint of the river are also represented by a vertex. Each edges between two vertices gets a section or tributary number. **??** shows the principle of this topology in an easy example. This representation allows for the spatial relations between the different tributaries but not for the transformation between real world coordinates and the topology.

To be able to transform real world coordinates into the topology, and vice versa, each edge is discretised into vertices with less than 1 km distance originating in the river polygon's skeleton. Each of these vertices represents a real world point of the

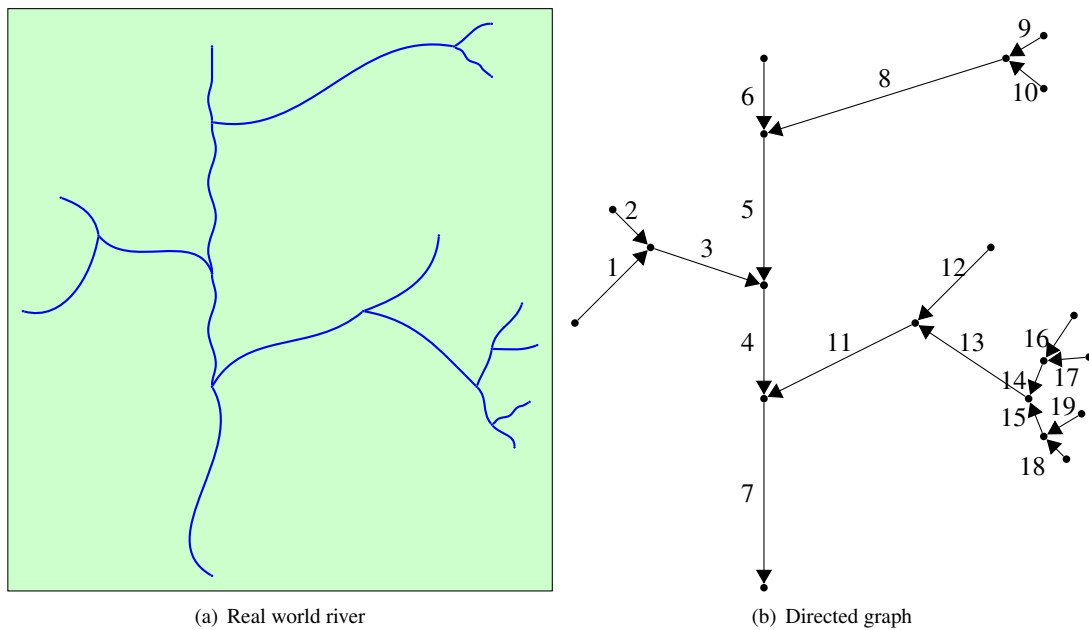(a) Real world river

(b) Directed graph

Figure 3.1: From real world river to topology: The river on the left side is transferred to the directed graph on the right side. The arrows indicate the flow direction and the numbers are the given tributary numbers.

river. This leads to a topology composed of a set of points where each point has a corresponding real world coordinate and between zero and two predecessors (upstream) and zero or one successor (downstream). The distance along the river to the river mouth as well as the tributary it belongs to is associated with each vertex.

In order to transform any given coordinate along the river to the topology, the closest topology vertex is sought. For the back transformation, the associated coordinates of the closest topology vertex are used. This is not an exact transformation between coordinates and topology but with a vertex distance of less than 1 km the transformation error is neglectable.

With this topology it is possible for two given points along the river to determine if they are flow connected and in case they are, if they are on the same river section and their distance from each other along the river.

3.2.3.2 B-Splines for River Topography

The functions $f_j(\boldsymbol{s},t)$ used in the UK approach have to be suitable to model the topography or mean water level along the river. It is assumed that the topography is constant over the study time. Thus, the temporal dependencies of $f_j(\boldsymbol{s},t)$ can be neglected. The function of the unknown sum of the functions $g(\boldsymbol{s}) = \sum_{j=0}^{l} f_j(\boldsymbol{s})\beta_j$ needs to be continuous and semi-monotonically increasing to represent the mean water level along the river. At the same time, the topography is too complicated to be represented by a sum

of simple polynomial functions. The altimetry data are not equally distributed along the river and its tributaries which can lead to instability of the function's estimation as well. *Polynomial B-splines* have been found to be best fitting for the basis functions f_j under the aforementioned conditions. Only the semi-monotonic increase is not ensured with B-Splines but in the realisation in the Mekong River Basin the function $g(\boldsymbol{s})$ is monotonically increasing.

Polynomial B-Splines of degree m are piece-wise polynomial functions of degree $m-1$ which have a local support (Stollnitz et al., 1995; Schmidt et al., 2015). They are defined over locations which are called knots t_j with $j = 0, \ldots, m+k+1$, with t_j non-decreasing. The number of B-Splines that can be defined by a given set of knots and a given degree is k. The B-spline B_i^m (the ith of degree m) is recursively defined by:

$$B_i^0(x) = \begin{cases} 1 & \text{if } t_i \leq x < t_{i+1} \\ 0 & \text{otherwise,} \end{cases}$$

$$B_i^r(x) = \frac{x - t_i}{t_{i+r} - t_i} N_i^{r-1}(x) + \frac{x_{i+r+1} - x}{x_{i+r+1} - x_{i+1}} N_{i+1}^{r-1}(x) \qquad (3.21)$$

with $i = 0, \ldots, k$ and $r = 1, \ldots, m$. The knots do not need to be equally distributed in the spatial domain but in order to be able to interpolate the end points as well, the first and last knot are m-times duplicated, $t_0 = t_1 = \ldots = t_{m+1}$ and $t_{k+1} = \ldots = t_{m+k+1}$. Such B-Splines are called *endpoint-interpolating B-Splines*. The B-Splines are the basis of a function space which has $m-1$ continuous derivatives in the interior knots $\{t_{m+1}, \ldots, t_k\}$. **??** displays some exemplary endpoint-interpolating B-Splines in the space $[0, 10]$ with irregularly spaced knots, $B_3^3(x)$ in red.
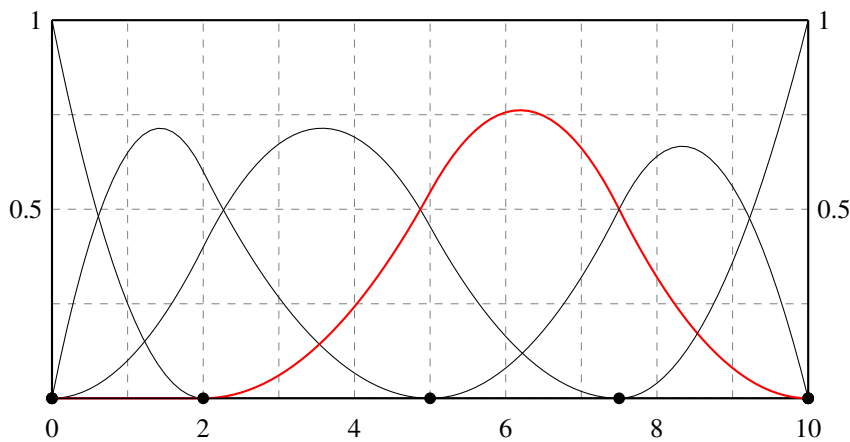

Figure 3.2: Example of endpoint-interpolating B-Splines of degree 3 with irregularly spaced knots in the space $[0, 10]$; the B-Spline $B_3^3(x)$ is marked in red.

For the functions f_j in the UK approach, B-Splines of degree 3 have been chosen. The knot distribution is not straightforward for the river network application. In **??** and **??**, the B-Splines and their knots are only defined on a one-dimensional space but the river network is two-dimensional. One solution for this problem is to define the B-Splines in two dimensions which raises the problem of the very sparse data coverage only along the rivers. Another solution is to transform the two-dimensional coordinates of latitude and longitude to a one-dimensional river length coordinate. The second approach has been chosen since it is the more feasible one. As long as only the main river is considered, the placement of the knots is straightforward. They can either be placed equidistant or in relation to the density of water level observations along the river. To include the tributaries as well, the river topology is needed from **??**.

The difficulties of this approach arise at the confluence of two rivers. The topography modelled by the B-Spline have to be continuous for both the main river and the tributary upstream of a confluence. A B-Spline downstream of the confluence "reaches" upstream beyond the confluence. Vice versa, a B-Spline upstream can reach downstream of the confluence. As can be seen in **??**, the width of a B-Spline depends on the distance between the knots. Thus, the distance for knots placed on the upstream sections to knots placed on the downstream section needs to be equal for both upstream sections. This leads to the following distribution of the B-Spline knots t_j:

- at the confluences of two rivers,
- at the downstream end point of the river duplicated for endpoint-interpolating B-Splines,
- at all upstream ends of all tributaries, duplicated as well,
- along all topology river sections, equidistant starting from the most downstream knot.

The last point guarantees the symmetry at the confluences. In **??**, one confluence or furcation with exemplary knots and B-Splines is shown. The B-splines do not distinguish the order of the river (main or tributary) at a furcation.
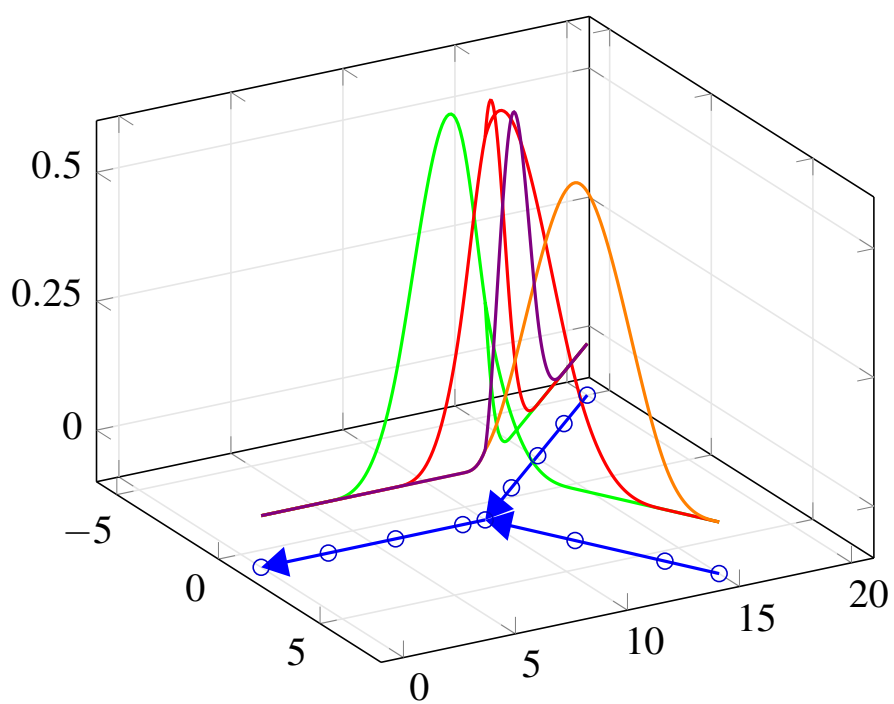
Figure 3.3: Schematic example of B-Splines on a furcation, schematic river in blue.

3.2.4 Multi-Mission Altimetry with Universal Kriging

Data of all available altimeter missions, SRO, LRO, and NRO missions along the main river and its tributaries, are combined with *U*niversal *K*riging in the following publication:

   E. Boergens, D. Dettmering, and F. Seitz (2018): **Observing Water Level Extremes in the Mekong River with Multi-Mission Altimetry**. In: *Remote Sensing*. in review

Abstract: Single-mission altimetric water level observations of rivers are spatial and temporally limited, and are often unable to quantify the full extent of extreme flood events. Combining data from multiple altimeter missions into a multi-mission product increases the spatial and temporal resolution of the data. In this study, we combined water level data from multiple altimeter missions in the Mekong River Basin between 2008 and 2016 into one multi-mission water level time series with universal kriging. Universal kriging allowed the incorporation of altimetry data from long or non-repeat orbit missions, such as CryoSat-2. The covariance model used in universal kriging also enabled inclusion of data both from the main stream and tributaries. The multi-mission time series adequately reflected the general inter-annual flood behaviour and extreme floodings in 2008 and 2011. However, flash floods remained undetectable with multi-mission data. We also used universal kriging to forecast water levels. We tested this application with different lead times for two stations, Chiang Saen and Stung Treng. For a number of years, predicted water levels reached accuracies close to those of the official Mekong forecasts. However, our forecast was unable to predict details of the flood.

4 Conclusion and Outlook

4.1 Conclusion

In this thesis, methods were developed to monitor water level observations of rivers with satellite altimetry and to combine these observations along the river network. The Mekong River Basin in South-East Asia was chosen as case study for these methods because of its divers topography and available in situ data for validations. The work had two main topics: The observation of the water levels in the river basin with new methods designed for small rivers and the combination of these data to basin-wide multi-mission altimetry. In the introduction, key questions to these topics were raised which have been answered in this thesis:

Water level observation with satellite altimetry

- Which altimetric observation should be used to estimate the water level?

In the two publications dedicated to the water level observation, P-1 and P-3, different answers to this questions were presented. In P-1, not only the observations directly above the river were used but additionally all measurements that observe the water body off-nadir. These off-nadir observations, called hooking effect, are only collected with pulse limited altimetry. The hooking effect forms a distinct parabolic shape in the along-track set of heights which is identified with a *Ran*dom *Sa*mple *C*onsensus (RANSAC) algorithm. The vertex of the hooking parabola is equivalent to the water level height of the observed river. In fact, it was not necessary that any altimetry observation was directly above the river in this approach as even a part of the parabola was sufficient to estimate the water levels. Thus, no exact location of the river was needed in this approach and it was independent from inaccurate land-water-masks.

On the other side, in P-3, a classification approach was applied to identify water observations in CryoSat-2 *S*ynthetic *A*perture *R*adar (SAR) data. As the hooking effect did not occur in SAR altimetry, only observations above the river could be used for the water level estimation. However, land-water-masks are often too inaccurate for this task, especially for small rivers. An approach was presented based on the unsupervised k-mean clustering with features derived from the SAR and the *R*ange *I*ntegrated *P*ower (RIP) waveform. The latter is only available for SAR data and holds valuable

additional information about the reflective surface of the river. The altimetry observations classified as water were then used to estimate the water level. However, the classification was not able to distinguish between water reflections originating from the river and reflections from surrounding wetlands. Thus, in regions with surrounding (seasonal) wetland, the classification failed to identify the observations which should be used for the river water level estimation.

- What is the size of a river that can be observed with satellite altimetry?

The answer to this question depends on the altimeter technique used for the water level observation and the method applied for the water level estimation. The hooking approach from P-1 allowed for pulse limited altimetry to observe water levels of rivers with a width as small as 90 m, although most of the observed rivers had a width between 200 m to 500 m. Theoretically, the hooking approach would allow to observe even smaller rivers but such rivers can have too limited reflective surfaces in the altimeter footprint to observe their reflection in the waveform. This depended on the surrounding land as well: the less well it reflected the radar signal the more likely it was to observe the river. The topography had an influence as well: Mountainous terrain can shadow part of the radar signal and thus, complicated the observation of small rivers.

SAR altimetry has a major advantage for observing small rivers: the smaller along-track footprint size compared to pulse limited altimetry. With this, it was possible in P-3 to observe rivers as narrow as 20 m, but most of the observed rivers were only as small as 100 m. SAR altimetry can also be influenced by the surrounding topography similar to pulse limited altimetry. However, as only nadir observations were used in SAR altimetry for the water level estimation, the shadowing of mountainous terrain had less influence.

- Do novel altimeter techniques improve the derived water levels?

This question aimed at both the SAR altimetry, on CryoSat-2, and Ka band altimetry, on *S*atellite with *Ar*gos and *Al*tiKa (SARAL). In P-3, levels derived from CryoSat-2 SAR altimetry have been compared to pulse limited altimetry observed by *Envir*onmental *Sat*ellite (Envisat). It turned out that under the chosen comparison, the SAR water levels had a higher quality than those observed by Envisat. The smaller along-track footprint was improving the quality of the water levels. Also the number of usable water level observations over small rivers was larger for CryoSat-2 SAR than for Envisat, which could also be seen in the size of the data sets used in P-4. Thus, the SAR altimetry technique is improving the observation's quality of small rivers.

The Ka band pulse limited altimeter on SARAL has a smaller footprint compared to the Ku band pulse limited altimeters of all other missions. Thus, it should be more suitable for inland water observations. The potential of the Ka band altimeter on SARAL was investigated in Schwatke et al. (2015a). It was found that the higher sensitivity of the Ka band towards atmospheric water content deteriorates the resulting water levels, especially during the rain and high flood season. Not only individual water level observations were missing in the SARAL data but sometimes even a whole *Virtual Station* (VS) could not be used in the data sets of both P-2 and P-4. Therefore, Ka band altimetry does not improve the water levels of rivers, at least not in a region with a (seasonal) high atmospheric water content.

Combination methods for multi-mission altimetry

- What is an appropriate method for the combination?

In this thesis, two kriging methods were presented for the combination of altimetry data along the Mekong River. Kriging in general produces a statistically optimal estimation with respect to the mean-squared prediction error. It was suitable for the combination of altimetry data as it was flexible enough to combine data with different accuracies both across the time and the spatial domain. The two kriging approaches of this thesis, *Ordinary Kriging* (OK) presented in P-2 and *Universal Kriging* (UK) in P-4, have different advantages and disadvantages:

In P-2, the OK method was applied to combine data of the *short-repeat orbit* (SRO) missions Envisat, SARAL, and Jason-2. Only these missions, as well as any other SRO mission, could be used with OK as the method required a constant mean value in the whole data set. This implied that the mean water level of each time series had to be reduced before the multi-mission combination. As this was only feasible for SRO missions which allow the VS concept, *long-repeat orbit* (LRO) and *non-repeat orbit* (NRO) missions could not be combined with the OK approach. On the other hand, the approach was numerically stable.

The UK approach was introduced in P-4 and allowed combining data of all altimeter missions, regardless of their orbit constellation. In this kriging approach the mean water level did not need to be reduced but was modelled in the approach itself with an estimated combination of basis functions. The advantage of this was its flexibility to incorporate all kind of altimetry data, but to be numerically stable the data needed to be more equally distributed in the study area. UK with only data of SRO missions was not possible as the topography, or mean water level, along the river could not be successfully modelled with only the sparse spatial data coverage. Also the setup of the basis function—B-splines in P-4—along a river network was challenging. In

conclusion, the answer to the question which of the two methods, OK or UK, is more appropriate for the multi-mission combinations strongly depends on the data that are used.

- How can the flow of the river be statistically modelled?

The kriging methods for the multi-mission combinations required a statistical modelling of the river. In this thesis, this modelling was done by means of covariances. In P-2, two spatio-temporal covariance models were introduced. In both models the temporal part was assumed to be stationary and thus, the temporal covariance between two observations only depended on the time distance between the two. In the first model the spatial part was also assumed stationary, therefore it was termed stationary model. The second, more advanced model, was non-stationary in space, termed the non-stationary model. The stationary model was far easier to implement as fewer parameters needed to be estimated from empirical covariances. At the same time, it showed comparably good results in P-2 despite ignoring the changing flow along the course of the river.

The non-stationary covariance model included the non-stationary covariance along the river between two observations but also the relation between their sub-catchments. However, for this model more parameter needed to be estimated. Its big advantage over the stationary model was the twofold ability to incorporate tributaries as well. As long as only the main stream of the Mekong River was involved, the flow behaviour did not change significantly. Thus, ignoring the changing flow of the river in the covariance model could be acceptable. However, the tributaries showed significantly changing flood behaviour. Therefore, for the inclusion of tributary data a non-stationary model was needed that can represent the flow connection, too. Thus, in P-4, only the non-stationary model was applied.

Hence, the choice of the covariance model depends again on the data to combine. As long as only main river data are combined and the river has no large changes in the flow, the stationary covariance model can be sufficient. Including tributaries or rivers with complicated flow behaviour, a non-stationary covariance model is more appropriate.

- Is multi-mission altimetry sufficient to observe extreme river flood events?

This question was addressed in P-4 for the years 2008 to 2016. The multi-mission time series was able to observe the interannual flood behaviour with exceptionally high and low floods. This was not possible with only single-mission altimetry. Especially the floodings in 2008 and 2011 were well observed by the multi-mission time series basin wide, whereas the low floods in 2015 and 2016 were less well observed. However,

even the combination of all available altimetric water levels was not dense enough do observe local flash floods. Sometimes even the main peak of the flood was not observed by any close by measurement and thus, the multi-mission time series could not observe every flood peak.

4.2 Outlook

In this thesis, only data until the end of 2016 were used, but no Sentinel-3A data though this mission was launched in February 2016. The Sentinel-3A satellite carries a SAR altimeter and the orbit has a short repeat time of 27 days. In 2018, the launch of its twin Sentinel-3B is planned with the same, but phase shifted, orbit. Incorporating data of these two missions will probably improve and stabilise the multi-mission approach presented in this thesis. The water level data of the other missions should and will then be updated as well.

In 2021, the launch of the *S*urface *W*ater and *O*cean *T*opography (SWOT) mission is planned which carries a new altimeter to observe the Earth's surface with a 120 km wide swath. This allows comprehensive observation of surface water. Thus, observations of the water surface will no longer be point-wise and conventional processing methods have to be adapted for the SWOT data. The combination of the SWOT data with older data sets will require combination methods similar to the kriging approaches.

A problem arising in the Mekong Basin in the next years is the commissioning of several dams along the main stream of the river. So far, most dams in the basins were along minor tributaries which allowed to neglect data upstream of dams as the multi-mission approach fails at dams until now. In order to further use the multi-mission approach, it needs to be adapted to allow for dams along the main stream. The easiest possibility to do so would be to cut the river model at the dams into different parts and only consider multi-mission data between the dams in one combination. This would ignore the fact that even across a dam the water level observations upstream and downstream are correlated. Hence, a more satisfying solution is to adapt the covariance model to mirror the correlation across dams which will be done in future work.

Kriging methods can be used to forecast water levels into the near future but the available data so far is not sufficient to provide reliable flood forecasts based on altimetry data only. Still, the kriging method allows to introduce auxiliary data in the combination system via *Co-K*riging (CoK). In CoK other data sets can be introduced as secondary variable if their correlation to the primary variable, i. e. the water level observations, are known. Thus, it is possible to combine the altimetry data with other data sets such as in situ gauges, precipitation, or total water storage. In situ gauges are

not available in every river basin but could be used to densify the temporal resolution of the data set if available. As precipitation is one of the main drivers of the river discharge, and thus also of the water level, combining observations of water levels and precipitation should improve the accuracy of the river stage prediction and forecasting. To this end, the statistical relation between the two measures has to be found and incorporated into the covariance model. Total water storage, as measured by the *G*ravity *R*ecovery *A*nd *C*limate *E*xperiment (GRACE) satellite mission, observes not only the surface water but the groundwater and soil moisture as well. This data set can help to observe the river system basin-wide but at a significantly lower spatial resolution. The ability of GRACE to observe a river basin strongly depends on the size and shape of the basin. Again, the relation between water levels of the river and the total water storage needs to be established for the covariance model in order to combine the data sets with a CoK approach. The combination of all these data sets is planned for future work to improve the forecast of water levels of the river.

So far, only the Mekong River Basin has been used as a case study for all methods of this thesis. The Mekong River is fairly well-monitored and has a reliable forecasting system, which allowed to validate the methods. However, globally many major river systems are poorly monitored. Satellite altimetry based water level observations can be used in such basins among others for understanding the hydrology or development of safety precautions. Altimetry based water level forecast and flood warnings would help the people along these unmonitored river. Thus, the transferability of the methods to other river networks will be tested.

List of Abbreviations and Nomenclature

List of Figures and Tables

Figures

Tables

Bibliography

Adamson P. T., Rutherfurd I. D., Peel M. C., and Conlan I. A. (2009): **The Hydrology of the Mekong River**. In: *The Mekong. Biophysical Environment of an International River Basin*. Ed. by I. C. Campbell. Elsevier, pp. 53–76. DOI: 10.1016/B978-0-12-374026-7.00004-8.

AVISO: **Poseidon altimeters**. visited on 01/19/2018: https://www.aviso.altimetry.fr/en/missions/past-missions/topexposeidon/instruments/poseidon-1.html, https://www.aviso.altimetry.fr/en/missions/past-missions/jason-1/instruments/poseidon-2.html, https://www.aviso.altimetry.fr/en/missions/current-missions/jason-2/instruments/poseidon-3.html, https://www.aviso.altimetry.fr/en/missions/current-missions/jason-3/instruments/poseidon-3b.html.

Barnett T. P., Adam J. C., and Lettenmaier D. P. (2005): **Potential impacts of a warming climate on water availability in snow-dominated regions.** In: *Nature* 438.7066, pp. 303–309. DOI: 10.1038/nature04141.

Bercher N., Dinardo S., Lucas B. M., Fleury S., and Picot N. (2013): **A review of Cryosat-2/Siral applications for the monitoring of river water levels**. In: *ESA Living Planet 2013*. Ed. by ESA.

Berry P. A. M., Garlick J. D., Freeman J. A., and Mathers E. L. (2005): **Global inland water monitoring from multi-mission altimetry**. In: *Geophysical Research Letters* 32.16, pp. 1–4. DOI: 10.1029/2005GL022814.

Biancamaria S., Frappart F., Leleu A.-S., Marieu V., Blumstein D., Desjonquères J.-D., Boy F., Sottolichio A., and Valle-Levinson A. (2016): **Satellite radar altimetry water elevations performance over a 200m wide river: Evaluation over the Garonne River**. In: *Advances in Space Research* 59.1, pp. 1–19. DOI: 10.1016/j.asr.2016.10.008.

Birkett C. M. (1998): **Contribution of the TOPEX NASA radar altimeter to the global monitoring of large rivers and wetlands**. In: *Water Resources Research* 34.5, pp. 1223–1239. DOI: 10.1029/98WR00124.

Birkett C. M., Mertes L. A. K., Dunne T., Costa M. H., and Jasinski M. J. (2002): **Surface water dynamics in the Amazon Basin: Application of satellite radar altimetry**. In: *Journal of Geophysical Research* 107.D20, p. 8059. DOI: 10.1029/2001JD000609.

Birkinshaw S. J., O'Donnell G. M., Moore P., Kilsby C. G., Fowler H. J., and Berry P. A. M. (2010): **Using satellite altimetry data to augment flow estimation techniques on the Mekong River**. In: *Hydrological Processes* 24.26, pp. 3811–3825. DOI: 10.1002/hyp.7811.

Boergens E., Buhl S., Dettmering D., Klüppelberg C., and Seitz F. (2017a): **Combination of multi-mission altimetry data along the Mekong River with spatio-temporal kriging**. In: *Journal of Geodesy* 91.5, pp. 519–534. DOI: 10.1007/s00190-016-0980-z.

Boergens E., Dettmering D., Schwatke C., and Seitz F. (2016): **Treating the Hooking Effect in Satellite Altimetry data: A Case Study along the Mekong River and Its Tributaries**. In: *Remote Sensing* 8.2, pp. 1–22. DOI: 10.3390/rs8020091.

Boergens E., Dettmering D., and Seitz F. (2018): **Observing Water Level Extremes in the Mekong River with Multi-Mission Altimetry**. In: *Remote Sensing*. in review.

Boergens E., Nielsen K., Andersen O. B., Dettmering D., and Seitz F. (2017b): **River Levels Derived with CryoSat-2 SAR Data Classification—A Case Study in the Mekong River Basin**. In: *Remote Sensing* 9.12, pp. 1–21. DOI: `10.3390/rs9121238`.

Bogning S., Frappart F., Blarel F., Niño F., Mahé G., Bricquet J.-P., Seyler F., Onguéné R., Etamé J., Paiz M.-C., and Braun J.-J. (2018): **Monitoring Water Levels and Discharges Using Radar Altimetry in an Ungauged River Basin: The Case of the Ogooué**. In: *Remote Sensing* 10.2. DOI: `10.3390/rs10020350`.

Bosch W., Dettmering D., and Schwatke C. (2014): **Multi-mission cross-calibration of satellite altimeters: Constructing a long-term data record for global and regional sea level change studies**. In: *Remote Sensing* 6.3, pp. 2255–2281. DOI: `10.3390/rs6032255`.

Bronner E., Guillot A., and Picot N. (2016): **SARAL / AltiKa Products Handbook**. Tech. rep., p. 76.

Brown G. (1977): **The average impulse response of a rough surface and its applications**. In: *IEEE transactions on antennas and propagation* 25.1, pp. 67–74.

Chelton D. B., Ries J. C., Haines B. J., Fu L.-L., and Callahan P. S. (2000): **Satellite Altimetry**. In: *Satellite Altimetry and Earth Sciences: A Handbook of Techniques and Applications*. Ed. by L.-L. Fu and A. Cazenave. Academic Press, pp. 1–131. DOI: `10.1016/S0074-6142(01)80146-7`.

Chelton D. B., Walsh E. J., and MacArthur J. L. (1989): **Pulse Compression and Sea Level Tracking in Satellite Altimetry**. In: *Journal of Atmospheric and Oceanic Technology* 6.3, pp. 407–438. DOI: `10.1175/1520-0426(1989)006<0407:PCASLT>2.0.CO;2`.

Crétaux J.-F., Jelinski W., Calmant S., Kouraev A., Vuglinski V., Bergé-Nguyen M., Gennero M.-C., Nino F., Del Rio R. A., and Cazenave A. (2011): **SOLS: A lake database to monitor in the Near Real Time water level and storage variations from remote sensing data**. In: *Advances in Space Research* 47.9, pp. 1497–1507. DOI: `10.1016/j.asr.2011.01.004`.

Davis C. H. (1995): **Growth of the Greenland Ice Sheet: A Performance Assessment of Altimeter Retracking Algorithms**. In: *IEEE Transactions on Geoscience and Remote Sensing* 33.5, pp. 1108–1116. DOI: `10.1109/36.469474`.

Davis C. H. (1997): **A robust threshold retracking algorithm for measuring ice-sheet surface elevation change from satellite radar altimeters**. In: *IEEE Transactions on Geoscience and Remote Sensing* 35.4, pp. 974–979. DOI: `10.1109/36.602540`.

De Marsily G. (1986): **Geostatistic and Stochastic Approach in Hydrogeology**. In: *Quantitative hydrogeology*. Academic Press, Inc.,Orlando, FL.

De Oliveira Campos I., Mercier F., Maheu C., Cochonneau G., Kosuth P., Blitzkow D., and Cazenave A. (2001): **Temporal variations of river basin waters from Topex/Poseidon satellite altimetry. Application to the Amazon basin**. In: *Comptes Rendus de l'Académie des Sciences-Series IIA-Earth and Planetary Science* 333.10, pp. 633–643. DOI: `10.1016/S1251-8050(01)01688-3`.

Deng X. and Featherstone W. E. (2006): **A coastal retracking system for satellite radar altimeter waveforms: Application to ERS-2 around Australia**. In: *Journal of Geophysical Research: Oceans* 111.May 2005, pp. 1–16. DOI: `10.1029/2005JC003039`.

Desai S., Chander S., Ganguly D., Chauhan P., Lele P., and James M. (2015): **Waveform Classification and Water-Land Transition over the Brahmaputra River using SARAL/AltiKa & Jason-2 Altimeter**. In: *Journal of the Indian Society of Remote Sensing* 43.3, pp. 475–485. DOI: `10.1007/s12524-014-0428-y`.

Dettmering D., Schwatke C., Boergens E., and Seitz F. (2016): **Potential of ENVISAT Radar Altimetry for Water Level Monitoring in the Pantanal Wetland**. In: *Remote Sensing* 8.7, pp. 1–21. DOI: `10.3390/rs8070596`.

Dinardo S., Fenoglio-Marc L., Buchhaupt C., Becker M., Scharroo R., Fernandes M. J., and Benveniste J. (2017): **Coastal SAR and PLRM altimetry in German Bight and West Baltic Sea**. In: *Advances in Space Research*. DOI: `https://doi.org/10.1016/j.asr.2017.12.018`.

Enjolras V. and Rodriguez E. (2009): **Using altimetry waveform data and ancillary information from SRTM, landsat, and MODIS to retrieve river characteristics**. In: *IEEE Transactions on Geoscience and Remote Sensing* 47.6, pp. 1869–1881. DOI: `10.1109/TGRS.2008.2006365`.

ESA (2015): **Sentinel-3, User Handbook**. Tech. rep., p. 157.

ESRIN-ESA (2012): **CryoSat Product Handbook**. Tech. rep., p. 90.

Frappart F., Calmant S., Cauhopé M., Seyler F., and Cazenave A. (2006): **Preliminary results of ENVISAT RA-2-derived water levels validation over the Amazon basin**. In: *Remote Sensing of Environment* 100.2, pp. 252–264. DOI: `10.1016/j.rse.2005.10.027`.

Frappart F., Papa F., Marieu V., Malbeteau Y., Jordy F., Calmant S., Durand F., and Bala S. (2015): **Preliminary Assessment of SARAL/AltiKa Observations over the Ganges-Brahmaputra and Irrawaddy Rivers**. In: *Marine Geodesy* 38.sup1, pp. 568–580. DOI: `10.1080/01490419.2014.990591`.

Frappart F., Seyler F., Martinez J. M., León J. G., and Cazenave A. (2005): **Floodplain water storage in the Negro River basin estimated from microwave remote sensing of inundation area and water levels**. In: *Remote Sensing of Environment* 99.4, pp. 387–399. DOI: `10.1016/j.rse.2005.08.016`.

Ghosh S., Kumar Thakur P., Garg V., Nandy S., Aggarwal S., Saha S. K., Sharma R., and Bhattacharyya S. (2015): **SARAL/AltiKa Waveform Analysis to Monitor Inland Water Levels: A Case Study of Maithon Reservoir, Jharkhand, India**. In: *Marine Geodesy* 38.sup1, pp. 597–613. DOI: `10.1080/01490419.2015.1039680`.

Gleick P. H. (1993): **Water in crisis a guide to the world's fresh water resources**. Oxford University Press. DOI: `10.2307/2623756`.

Gleick P. H. (1996): **Water resources**. In: *Encyclopedia of Climate and Weather*. Ed. by S. H. Schneider and F. K. Hare. Oxford university press New York.

Global Runoff Data Center (2013): **Long-term mean monthly discharges and annual characteristics of GRDC stations**. Tech. rep. Federal Institute of Hydrology.

Gommenginger C., Thibaut P., Fenoglio-Marc L., Quartly G., Deng X., Gómez-Enri J., Challenor P., and Gao Y. (2011): **Retracking altimeter waveforms near the coasts**. In: *Coastal altimetry*. Ed. by J. Benveniste, P. Cipollini, A. G. Kostianoy, and S. Vignudelli. Springer. DOI: `10.1007/978-3-642-12796-0`.

Göttl F., Dettmering D., Müller F. L., and Schwatke C. (2016): **Lake level estimation based on CryoSat-2 SAR altimetry and multi-looked waveform classification**. In: *Remote Sensing* 8.11, pp. 1–16. DOI: `10.3390/rs8110885`.

Hayne G. S. (1980): **Radar Altimeter Mean Return Waveforms from Near-Normal-Incidence Ocean Surface Scattering**. In: *IEEE Transactions on Antennas and Propagation* 28.5, pp. 687–692. DOI: `10.1109/TAP.1980.1142398`.

Hwang C., Guo J., Deng X., Hsu H. Y., and Liu Y. (2006): **Coastal gravity anomalies from retracked Geosat/GM altimetry: Improvement, limitation and the role of airborne gravity data**. In: *Journal of Geodesy* 80.4, pp. 204–216. DOI: `10.1007/s00190-006-0052-x`.

International Centre for Enviromental Management (2010): **Strategic Enviromental Assessment of Hydropower on the Mekong Mainstream**. Tech. rep. October. DOI: 10.1115/1.802915.ch1.

Jain M., Andersen O. B., Dall J., and Stenseng L. (2015): **Sea surface height determination in the Arctic using Cryosat-2 SAR data from primary peak empirical retrackers**. In: *Advances in Space Research* 55.1, pp. 40–50. DOI: 10.1016/j.asr.2014.09.006.

Jiang B., Xie Z., Wu X., Wu L., and Zhou L. (2011): **Topology constrain for river dimension-reducing generalization in land-use map**. In: *Proceedings - 2011 19th International Conference on Geoinformatics*. Ed. by IEEE.

Jiang L., Nielsen K., Andersen O. B., and Bauer-Gottwein P. (2017): **CryoSat-2 radar altimetry for monitoring freshwater resources of China**. In: *Remote Sensing of Environment* 200, pp. 125–139. DOI: 10.1016/j.rse.2017.08.015.

Jiang T., Su B., and Hartmann H. (2007): **Temporal and spatial trends of precipitation and river flow in the Yangtze River Basin, 1961-2000**. In: *Geomorphology* 85.3-4, pp. 143–154. DOI: 10.1016/j.geomorph.2006.03.015.

Kouraev A. V., Zakharova E. A., Samain O., Mognard N. M., and Cazenave A. (2004): **Ob' river discharge from TOPEX/Poseidon satellite altimetry (1992-2002)**. In: *Remote Sensing of Environment* 93.1-2, pp. 238–245. DOI: 10.1016/j.rse.2004.07.007.

Krige D. G. (1952): **A statistical analysis of some of the borehole values in the Orange Free State goldfield**. In: *Journal of the Chemical, Metallurgical and Mining Society of South Africa* 53.3, pp. 47–70.

Lauri H., De Moel H., Ward P. J., Räsänen T. A., Keskinen M., and Kummu M. (2012): **Future changes in Mekong River hydrology: Impact of climate change and reservoir operation on discharge**. In: *Hydrology and Earth System Sciences* 16.12, pp. 4603–4619. DOI: 10.5194/hess-16-4603-2012.

Le Roy Y., Deschaux-Beaume M., Mavrocordatos C., Aguirre M., and Heliere F. (2007): **SRAL SAR radar altimeter for sentinel-3 mission**. In: *Geoscience and Remote Sensing Symposium, 2007. IGARSS 2007. IEEE International*. IEEE, pp. 219–222. DOI: 10.1109/IGARSS.2007.4422769.

Liu K.-T., Tseng K.-H., Shum C. K., Liu C.-Y., Kuo C.-Y., Liu G., Jia Y., and Shang K. (2016): **Assessment of the Impact of Reservoirs in the Upper Mekong River Using Satellite Radar Altimetry and Remote Sensing Imageries**. In: *Remote Sensing* 8.5, p. 367. DOI: 10.3390/rs8050367.

Maheu C., Cazenave A., and Mechoso C. (2003): **Water level fluctuations in the Plata Basin (South America) from Topex/Poseidon Satellite Altimetry**. In: *Geophysical Research Letters* 30.3, pp. 41–43. DOI: 10.1029/2002GL016033.

Maillard P., Bercher N., and Calmant S. (2015): **New processing approaches on the retrieval of water levels in ENVISAT and SARAL radar altimetry over rivers: A case study of the São Francisco River, Brazil**. In: *Remote Sensing of Environment* 156, pp. 226–241. DOI: 10.1016/j.rse.2014.09.027.

Marshall A. and Deng X. (2016): **Image Analysis for Altimetry Waveform Selection over Heterogeneous Inland Waters**. In: *IEEE Geoscience and Remote Sensing Letters* 13.8, pp. 1198–1202. DOI: 10.1109/LGRS.2016.2575068.

Mekong River Commission (2005): **Overview of the Hydrology of the Mekong Basin**. Mekong River Commission.

Mekong River Commission (2009): **Annual Mekong Flood Report 2008**. Tech. rep.

Mekong River Commission (2010): **Mekong River Commission, State of the Basin Report 2010**. Tech. rep., pp. 1–24. DOI: 10.1017/CBO9781107415324.004.

Michailovsky C. I., McEnnis S., Berry P. A. M., Smith R., and Bauer-Gottwein P. (2012): **River monitoring from satellite radar altimetry in the Zambezi River basin**. In: *Hydrology and Earth System Sciences* 16.7, pp. 2181–2192. DOI: `10.5194/hess-16-2181-2012`.

Nielsen K., Andersen O. B., Jain M., Villadsen H., Stenseng L., Knudsen P., Berry P. A. M., Egido A., and Caparrini M. (2014): **D2 . 1 : State of the art review of SAR mode over land**. Tech. rep.

Nielsen K., Stenseng L., Andersen O. B., and Knudsen P. (2017): **The performance and potentials of the CryoSat-2 SAR and SARIn modes for lake level estimation**. In: *Water* 9.6, pp. 1–13. DOI: `10.3390/w9060374`.

Nielsen K., Stenseng L., Andersen O. B., and Villadsen H. (2015): **Validation of CryoSat-2 SAR mode based lake levels**. In: *Remote Sensing of Environment* 171, pp. 162–170. DOI: `10.1016/j.rse.2015.10.023`.

Nijssen B., O'Donnell G. M., Hamlet A. F., and Lettenmaier D. P. (2001): **Hydrologic sensitivity of global rivers to climate change**. In: *Climatic Change* 50.1-2, pp. 143–175. DOI: `10.1023/A:1010616428763`.

Passaro M., Cipollini P., Vignudelli S., Quartly G. D., and Snaith H. M. (2014): **ALES: A multi-mission adaptive subwaveform retracker for coastal and open ocean altimetry**. In: *Remote Sensing of Environment* 145, pp. 173–189. DOI: `10.1016/j.rse.2014.02.008`.

Passaro M., Rose S. K., Andersen O. B., Boergens E., Calafat F. M., Dettmering D., and Benveniste J. (2018): **ALES+: Adapting a homogenous ocean retracker for satellite altimetry to sea ice leads, coastal and inland waters**. In: *Remote Sensing of Environment* 211, pp. 456–471. DOI: `https://doi.org/10.1016/j.rse.2018.02.074`.

Pekel J.-F., Cottam A., Gorelick N., and Belward A. S. (2016): **High-resolution mapping of global surface water and its long-term changes**. In: *Nature* 540.7633, pp. 418–422. DOI: `10.1038/nature20584`.

Phalippou L. and Enjolras V. (2007): **Re-tracking of SAR altimeter ocean power-waveforms and related accuracies of the retrieved sea surface height, significant wave height and wind speed**. In: *International Geoscience and Remote Sensing Symposium (IGARSS)*. Ed. by IEEE.

Phalippou L., Rey L., Chateau-Thierry P. D., Thouvenot E., Steunou N., Mavrocordator C., and Francis R. (2001): **Overview of the performances and tracking design of the SIRAL altimeter for the CryoSat mission**. In: *IGARSS 2001. Scanning the Present and Resolving the Future, International Geoscience and Remote Sensing Symposium*. Ed. by IEEE.

Raney R. K. (1998): **The delay/doppler radar altimeter**. In: *IEEE Transactions on Geoscience and Remote Sensing* 36.5 PART 1, pp. 1578–1588. DOI: `10.1109/36.718861`.

Räsänen T. A. and Kummu M. (2013): **Spatiotemporal influences of ENSO on precipitation and flood pulse in the Mekong River Basin**. In: *Journal of Hydrology* 476, pp. 154–168. DOI: `10.1016/j.jhydrol.2012.10.028`.

Ray C., Martin-Puig C., Clarizia M. P., Ruffini G., Dinardo S., Gommenginger C., and Benveniste J. (2015): **SAR altimeter backscattered waveform model**. In: *IEEE Transactions on Geoscience and Remote Sensing* 53.2, pp. 911–919. DOI: `10.1109/TGRS.2014.2330423`.

Resti A., Benveniste J., Roca M., Levrini G., and Johannessen J. (1999): **The Envisat Radar Altimeter system (RA-2)**. Tech. rep. 98, pp. 94–101.

Sandwell D. T. and Smith W. H. (2005): **Retracking ERS-1 altimeter waveforms for optimal gravity field recovery**. In: *Geophysical Journal International* 163.1, pp. 79–89. DOI: `10.1111/j.1365-246X.2005.02724.x`.

Schmidt M., Dettmering D., and Seitz F. (2015): **Using B-Spline expansions for ionosphere modeling**. In: *Handbook of Geomathematics: Second Edition*, pp. 939–983. DOI: 10.1007/978-3-642-54551-1_80.

Schwatke C. and Dettmering D. (2017): **Mission-Independent Classification of Altimeter Waveforms for Applications in the Open Ocean, at the Coastal Zone and Over Land**. In: *10th Costal Altimetry Workshop*.

Schwatke C., Dettmering D., Börgens E., and Bosch W. (2015a): **Potential of SARAL/ AltiKa for Inland Water Applications**. In: *Marine Geodesy* 38.sup1, pp. 626–643. DOI: 10.1080/01490419.2015.1008710.

Schwatke C., Dettmering D., Bosch W., and Seitz F. (2015b): **DAHITI - an innovative approach for estimating water level time series over inland waters using multi-mission satellite altimetry**. In: *Hydrology and Earth System Sciences* 19.10, pp. 4345–4364. DOI: 10.5194/hess-19-4345-2015.

Schwatke C., Dettmering D., and Göttl F. (2015c): **Classification of Altimeter Waveforms for an Improved Estimation of Water Level Time Series over Inland Water**. In: *9th Costal Altimetry Workshop*.

Stollnitz E. J., DeRose T. D., and Salesin D. H. (1995): **Wavelets for Computer Graphics : A Primer Part 2**. In: *Computer* 15.July, pp. 75–85. DOI: 10.1109/38.376616.

Sulistioadi Y. B., Tseng K. H., Shum C. K., Hidayat H., Sumaryono M., Suhardiman A., Setiawan F., and Sunarso S. (2015): **Satellite radar altimetry for monitoring small rivers and lakes in Indonesia**. In: *Hydrology and Earth System Sciences* 19.1, pp. 341–359. DOI: 10.5194/hess-19-341-2015.

Tourian M. J., Schwatke C., and Sneeuw N. (2017): **River discharge estimation at daily resolution from satellite altimetry over an entire river basin**. In: *Journal of Hydrology* 546, pp. 230–247. DOI: 10.1016/j.jhydrol.2017.01.009.

Tourian M. J., Tarpanelli A., Elmi O., Qin T., Brocca L., Moramarco T., and Sneeuw N. (2016): **Spatiotemporal densification of river water level time series by multimission satellite altimetry**. In: *Water Resources Research* 52.2, pp. 1140–1159. DOI: 10.1002/2015WR017654.

Trenberth K. E. (2011): **Changes in precipitation with climate change**. In: *Climate Research* 47.1-2, pp. 123–138. DOI: 10.3354/cr00953.

Uebbing B., Kusche J., and Forootan E. (2015): **Waveform Retracking for Improving Level Estimations From TOPEX/Poseidon, Jason-1, and Jason-2 Altimetry Observations Over African Lakes**. In: *IEEE Transactions on Geoscience and Remote Sensing* 53.4, pp. 2211–2224. DOI: 10.1109/TGRS.2014.2357893.

Villadsen H., Andersen O. B., Stenseng L., Nielsen K., and Knudsen P. (2015): **CryoSat-2 altimetry for river level monitoring—Evaluation in the Ganges–Brahmaputra River basin**. In: *Remote Sensing of Environment* 168, pp. 80–89. DOI: 10.1016/j.rse.2015.05.025.

Villadsen H., Deng X., Andersen O. B., Stenseng L., Nielsen K., and Knudsen P. (2016): **Improved inland water levels from SAR altimetry using novel empirical and physical retrackers**. In: *Journal of Hydrology* 537, pp. 234–247. DOI: 10.1016/j.jhydrol.2016.03.051.

Vörösmarty C. J., Green P., Salisbury J., and Lammers R. B. (2000): **Global water resources: vulnerability from climate change and population growth.** In: *Science (New York, N.Y.)* 289.5477, pp. 284–8. DOI: 10.1126/science.289.5477.284.

Wingham D. J., Francis C. R., Baker S., Bouzinac C., Brockley D., Cullen R., Chateau-Thierry P. de, Laxon S. W., Mallow U., Mavrocordatos C., Phalippou L., Ratier G., Rey L., Rostan F., Viau P., and Wallis D. W. (2006): **CryoSat: A mission to determine the fluctuations in Earth's land and marine ice fields**. In: *Advances in Space Research* 37.4, pp. 841–871. DOI: 10.1016/j.asr.2005.07.027.

Wingham D. J., Rapley C. G., and Griffiths H. (1986): **New Techniques in Satellite Altimeter Tracking Systems**. In: *Proceedings of IGARSS 86*. Ed. by ESA.

Yoon Y., Durand M., Merry C. J., and Rodriguez E. (2013): **Improving temporal coverage of the SWOT mission using spatiotemporal kriging**. In: *IEEE Journal of Selected Topics in Applied Earth Observations and Remote Sensing* 6.3, pp. 1719–1729. DOI: 10.1109/JSTARS.2013.2257697.

Zlinszky A., Boergens E., Glira P., and Pfeifer N. (2017): **Airborne Laser Scanning for calibration and validation of inshore satellite altimetry: A proof of concept**. In: *Remote Sensing of Environment* 197, pp. 35–42. DOI: 10.1016/j.rse.2017.04.027.

Acknowledgements

This thesis would not have been possible without the support and help of many people whom I want to thank.

Foremost, I want to thank my doctoral supervisor, Professor Dr. Florian Seitz, for his guidance through this thesis. The challenging discussions with him helped me to develop and improve new research ideas. I also want to express heartfelt thanks to my mentor, Dr. Denise Dettmering, who had always an open ear for my ideas and problems. Without her, the writing of the four publications would have been a lot more painful and I would have lost sight of the bigger framework frequently.

Without the altimetry working group at the DGFI, I would not have been able to do this research. Many thanks go to Denise Dettmering, Christian Schwatke, Felix Müller, Marcello Passaro, Franziska Göttl, Wolfgang Bosch, and Gaia Piccioni. They were, at our weekly altimeter rounds, the most challenging and critical, yet constructive, reviewers I could get for my work. I always knew that all of them would help me with a problem. Especially Christian helped me to find my way into inland water altimetry at the beginning and I really enjoyed the smaller or larger discussions we had.

I am thankful that I had the opportunity to stay for three months with Karina Nielsen and Ole B. Andersen at the Danish Technical University in Lyngby. I learned a lot about CryoSat-2 processing from the Danish colleagues and really enjoyed my time there.

I was fortunate to conduct this research as part of the REWAP project inside the International Graduate School of Science and Engineering (IGSSE). The collaborative work with Dr. Sven Buhl and Professor Dr. Claudia Klüppelberg from the Chair of Mathematical Statistics led me to the multi-mission altimetry work done in this thesis. Working together with Sven challenged me to be more mathematically precise while I learned a lot about statistics. I also want to thank the administrative staff of IGSSE who are very helpful and just great.

I want to thank all colleagues at the DGFI who provided a very pleasant working environment for me these last years. Discussions across the border of the working groups were always enriching. But I also enjoyed the social events in the institute and with colleagues, be it the daily coffee break, the rafting on the Isar, or the numerous other activities.

Finally, I want to thank my parents Sylvia and Manfred Börgens who always supported me along my academic path. And I want to thank my boyfriend Daniel Rotter who always cheered me up when I was down and tired after work and who helped with one or another LaTeX crisis.

Appendices

A. 1 Publications

This appendix contains the four first-authored publications of this thesis. For each publication a one-page summary is provided and the authors' contributions are outlined, followed by the full publication. For P-1 and P-3 the publications are open access and could be provided as published; P-2 is given as an author's pre-print; P-4 is submitted to the journal and is included in its present form. For the four co-authored publications supplementing the results of this thesis a short summary and authors' contributions are provided as well.

?? gives an overview of the contributions of Eva Börgens for each of the publications. The contributions are separated into idea, realisation, analysis and discussion, figure compilation, and manuscript writing. The stated overall contribution is the mean of the aforementioned contribution parts.

Table A.1: Contributions to the first-authored publications P-1 to P-4: The contributions are broken down to idea, realisation, analysis and discussion and manuscript writing.

Publication	Idea	Realisation	Analysis and Discussion	Figure Compilation	Manuscript Writing	Overall Contribution
P-1	85%	95%	80%	100%	90%	90%
P-2	50%	70%	80%	95%	70%	73%
P-3	85%	100%	85%	100%	90%	92%
P-4	95%	95%	85%	100%	95%	94%

P-1: Treating the Hooking Effect in Satellite Altimetry Data: A Case Study along the Mekong River and Its Tributaries

E. Boergens, D. Dettmering, C. Schwatke, and F. Seitz (2016): **Treating the Hooking Effect in Satellite Altimetry data: A Case Study along the Mekong River and Its Tributaries**. In: *Remote Sensing* 8.2, pp. 1–22

Copyright

This work is published in Remote Sensing, an open access MDPI journal, under the creative commons license. The copyright remains with the authors.

Summary of content

Satellite altimetry has proved to be valuable to observe water level of inland waters, especially rivers. However, small rivers are only measured by few consecutive observations which hinder reliable water level estimation. At the same time, the altimeter tends to collect off-nadir measurements in the vicinity of water bodies. This study used these off-nadir measurements, called hooking effect, to enhance the water level determination of small rivers in the Mekong River Basin.

The off-nadir observations form a distinct parabola in the along-track heights whose vertex is identical with the water level of the water body. This study introduced a new method to identify the parabola shape with a *Ran*dom *Sa*mple *C*onsensus (RANSAC) algorithm in the data. The RANSAC algorithm can be used to find any geometric shape in a point cloud with outliers; except for the information about the geometric shape no further information is needed. The RANSAC algorithm is a randomised iterative algorithm: In each iteration the number of points necessary to define the geometry is drawn from all points and the geometric shape is estimated from these. Afterwards it is checked how well all other points fit to the so defined shape. After a given number of iterations the shape is selected with the most matching points. The amount of expected outliers in the data set is used to estimate the required number of iterations. With the best parabola found, its vertex could be used as the estimated water level.

This study also introduced a new retracking method for multi-peak waveforms, the *M*ulti-*S*ubwaveform *R*etracker (MSR). The retracker identified the most powerful sub-waveform which was most likely the returning signal from the water body.

The described algorithm was tested with *Envi*ronmental *Sat*ellite (Envisat), *S*atellite with *Ar*gos and *Al*tiKa (SARAL), and *E*uropean *R*emote *S*ensing Satellite-2 (ERS-2) data on several locations along the Mekong River and some of its tributaries and validated against in situ gauge data. The resulting time series of water levels showed good

agreement with the in situ data. The validation was extended to both *Da*tabase for *H*ydrolog*i*cal *T*ime Series of *I*nland Waters (DAHITI) water level time series and water level time series gained with a land-water-mask. The hooking approach performed better than both other data sets. Additionally, the study showed the multitude effects of different topography on the altimetric observations: First, the more acute angled the satellite track crossed the river the less satisfying the results tended to be; second, in very narrow and steep river gorges multi-path effects can occur; and third, the amplitude of the annual water level signal can change rapidly over the river course due to changes in the river valley.

Declaration of contribution

In a discussion in the altimeter working group at DGFI, namely with Christian Schwatke, the idea to use the hooking effect over small rivers came up. Eva Börgens introduced the RANSAC algorithm for the identification of the off-nadir observations. She also developed the idea for the new retracker which was developed and implemented with the help of Christian Schwatke. The implementation of the hooking method was mostly done by Eva Börgens as well as the manuscript writing and figure compilation. Denise Dettmering supported the discussion and analysis of the manuscript. All co-authors help with writing and linguistic improvement of the publication. The overall own contribution of Eva Börgens is estimated to be **90%**.

Treating the Hooking Effect in Satellite Altimetry Data: A Case Study along the Mekong River and Its Tributaries

Eva Boergens *, Denise Dettmering, Christian Schwatke and Florian Seitz

Deutsches Geodätisches Forschungsinstitut, Technische Universität München, Arcisstraße 21, 80333 Munich, Germany; denise.dettmering@tum.de (D.D.); christian.schwatke@tum.de (C.S.); florian.seitz@tum.de (F.S.)

*   Correspondence: eva.boergens@tum.de; Tel.: +49-89-23031-1263

Abstract: This study investigates the potential of satellite altimetry for water level time series estimation of smaller inland waters where only very few measurements above the water surface are available. A new method was developed using off-nadir measurements to estimate the parabola generated by the hooking effect. For this purpose, a new waveform retracker was used as well as an adopted version of the RANdom SAmple Consensus (RANSAC) algorithm. The method is applied to compute time series of the water levels height of the Mekong River and some of its tributaries from Envisat high-frequency data. Reliable time series can be obtained from river crossings with widths of less than 500 m and without direct nadir measurements over the water. The expected annual variations are clearly depicted and the time series well agree with available *in situ* gauging data. The mean RMS value is 1.22 m between the resulting time series and *in situ* data, the best result is 0.34 m, the worst 2.26 m, and 80% of the time series have an RMS below 1.5 m.

---

1. Introduction

A prerequesite for an accurate description of the global water cycle, is the assessment of water storage of inland water bodies. In particular, long-term changes in water storage are important for the risk assessment of floods and drought and for water availability. However, the number of *in situ* gauges along inland waters has been declining worldwide since the 1980s. The number of available gauges at the Global Runoff Data Center (GRDC) decreased from 7300 in 1978 to 1000 today [1]. Especially in Asia and Africa, almost no *in situ* data are available.

More recently, satellite altimetry has begun to close this data gap for inland waters. Altimetry data are especially advantageous for inland waters because they are obtainable even in remote regions. Satellite altimetry was originally designed for sea surface observations, but with the development of new data processing strategies, altimetry measurements may now be used over inland water bodies such as lakes, reservoirs, rivers, and wetlands. For example, using Geosat data, Morris and Gill [2] obtained time series of the levels of the Great Lakes in North America. With the launch of the ERS-1 mission in 1991 and the Topex/Poseidon mission in 1992, more inland waters became observable (e.g., [3–6]). The ERS-1 mission was succeeded by ERS-2, Envisat, and SARAL/AltiKa in the same orbit; similarly, the Topex/Poseidon mission was succeeded by Jason-1 and Jason-2. Currently, we can access more than 20 years of continuous altimetry time series.

However, altimetry data collected over inland water bodies are more difficult to process than open ocean data. The over-land footprint size of Envisat's Ku-band radar echo is between 2 and 16 km [7], which limits the use of standard Geophysical Data Record (GDR) products for inland

water applications. The waveforms returned from complex surfaces differ from the Brown-like ocean waveforms on which the standard processing algorithms are based [8]. For reliable results over smaller water bodies, we require specific retracking algorithms, such as β-5 Retracker, Threshold Retracker, or Improved Threshold Retracker [8].

Reflecting the importance of inland water altimetry, four inland water altimetry databases have now been established: Hydroweb, developed by Laboratoire d'Etudes en Géophysique et Océanographie Spatiales (LEGOS) [9]; the River and Lake database provided by the European Space Agency (ESA) [10]; the Global Reservoir and Lake Monitor (GRLM), maintained by the Foreign Agricultural Service of the United States Department of Agriculture (USDA) [11]; and the Database for Hydrological Time Series over Inland Water (DAHITI), developed by the Deutsches Geodätisches Forschungsinstitut der Technischen Universität München (DGFI-TUM) [12].

To date, most of the small-river studies have focused on the Amazon basin (e.g., [13–15]) or on other rivers surrounded by flat topography (e.g., [16,17]). Flat topography is desirable, as it does not shadow the water body in the altimetric footprint, reducing the risk of the altimeter losing lock.

Off-nadir measurements are also problematic over inland water bodies. Because water reflects more strongly than the surrounding land, the altimeter instrument measures the slant distance to the water surface even when not in nadir. Such off-nadir measurements lead to a parabolic shape of the track-height profile, called the hooking effect (Figure 1). Frappart *et al.* [13] were the first ones who described this effect for inland waters. They corrected the effect using a migration method which integrated the energy over such a parabolic feature. Calmant *et al.* [18] addressed the hooking effect as one major issue which affects the altimetry of inland water bodies. In Santos da Silva *et al.* [15] the geometry behind the hooking effect is explained in more detail and the effect is corrected for some of the presented time series over the Amazon basin. Later works, such as Santos da Silva *et al.* [19] or Frappart *et al.* [20], corrected the hooking effect as well. Maillard *et al.* [17] developed a new method to correct the hooking effect by comparing the theoretical shape of the hooking parabola with the measured data profile. All of these studies, including the study presented in this paper, were conducted with conventional radar altimetry. SAR altimetry data, like Crysosat-2 data, is less prone to the hooking effect and does not require its correction.

In this study, we introduce a new method that derives reliable water-level time series over smaller rivers using measurements affected by the hooking effect. This method can even be used when no nadir data over the river is available at all but only parts of the hooking parabola. In contrast to the above mentioned studies by Frappart *et al.* [13], Santos da Silva *et al.* [15], or Maillard *et al.* [17], the presented method is almost fully automatic and enables a fast and reliable processing of almost all river crossings, even for very small rivers. We developed a special retracker in order to ensure that all off-nadir measurements can be used and the parabola is well represented in the data set. To identify off-nadir measurements and thus estimate the parabola, we employ the RANSAC algorithm [21]. RANSAC is commonly used in computer vision, for example, in image registration (e.g., [22–24]) and feature extractions from LiDAR data (e.g., [25,26]).

The method is trialed in a case study, namely the derivation of water-level time series along the Mekong River in South-East Asia and some of its tributaries. In terms of discharge and length, the Mekong River ranks among the 10 largest rivers in the world. Using satellite altimetry, Frappart *et al.* [27] have already investigated the lowest part of the Mekong basin south of Krong Stung Treng, where the river width exceeds 2 km. Birkinshaw *et al.* [28] studied the entire lower Mekong basin (the same region is investigated in the present study) using Envisat and ERS-2 data. They focused on the area south of Vientiane and one station further in the North, where the river is less than 500 m wide.
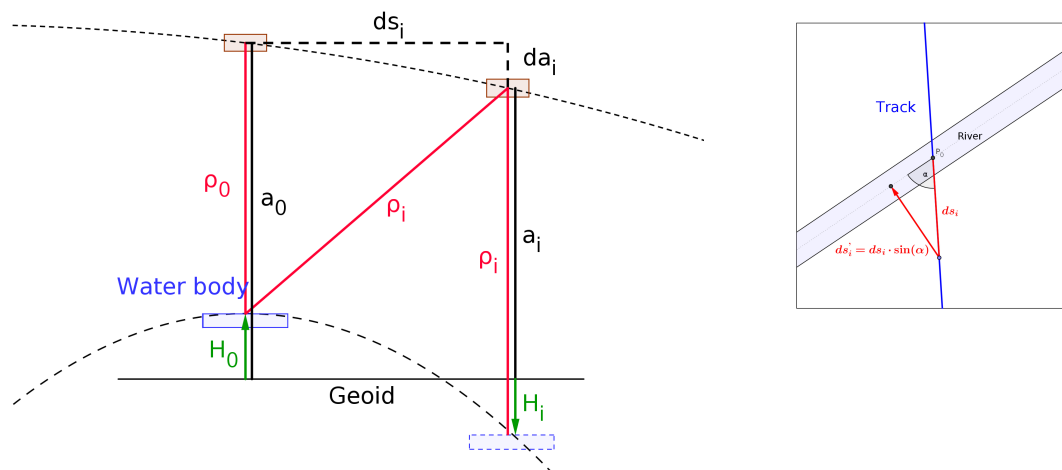
Figure 1. Off-nadir measurement of the slant distance to the water body (ρ_i) generates a parabolic profile of the heights above the geoid. The vertex of this parabola is the height H_0 at the nadir position. On the right side the situation of non-perpendicular intersection is shown.

2. Study Area

The Mekong River is one of the longest rivers in the world (approximately 4500 km). From the Tibetan Plateau, it flows through six countries in South East Asia: China, Myanmar, Laos, Thailand, Cambodia, and Vietnam. The present paper focuses on the lower Mekong basin, downstream of the South of the mountainous regions in China, and the triangle of Myanmar, Laos, and Thailand. From there, it flows 2600 km south and outflows into the South China Sea in Vietnam. This area is inhabited by roughly 60 million people who are provided with water from the Mekong River. At the beginning of the lower basin, the Mekong River is less than 500 m wide, but widens to more than 2 km at the beginning of the delta. Most of the tributaries and the main stream north of Vientiane are less than 1 km wide. North of Vientiane, the Mekong River not only narrows to below 500 m but is also surrounded by mountainous and hilly topography. Figure 2 displays the lower Mekong region. During the summer months (mid-May to early September), the climate in the lower Mekong basin is dominated by the yearly south-eastern monsoon [29], which can raise the water level of the Mekong to more than 10 m [28].

3. Data

3.1. Altimetry Data

This study uses the high-frequency altimetry data of the Envisat/RA-2, ERS-2 and SARAL/AltiKa satellite missions, focusing on Envisat data. Envisat had a 35 day-repeat orbit with an inclination of 98.55° and height of approximately 770 km. Envisat's orbit is a continuation of the ERS-1 and ERS-2 orbits. The mission started in March 2002 and was shifted to a new orbit in October 2010. Only data prior to October 2010 is used in this study, cycle 006 to 094. The altimeter instrument measures ranges between the satellite and the surface. The heights H are obtained by subtracting the observed ranges ρ from the satellite height H_{sat}, and are corrected for the atmospheric delay caused by the ionosphere (*iono*) and the dry and wet troposphere (*dry* and *wet*, respectively), the crustal motions caused by pole tides (*pt*) and solid earth tides (*et*), a geoid correction (*geoid*) and the radial bias between different altimeter missions (*oerr*). Thus, the physical heights are calculated as

$$H = H_{sat} - \rho - (iono + dry + wet + pt + et + geoid + oerr).\tag{1}$$

Table 1 summarizes the corrections applied to the data. For a proper comparison among altimeter missions, we adopted correction models that were available over the entire time period of the altimetry data. In addition to these corrections, the ranges ρ were retracked over the inland water bodies to obtain more reliable heights. The retracking process will be detailed in Section 5.1.

Table 1. Corrections applied to the altimeter measurements.

Correction	Model/Source	Reference
ionosphere	NOAA Ionosphere Climatology 2009 (NIC09)	Scharroo and Smith [30]
dry troposphere	ECMWF (2.5° × 2.0°) for Vienna Mapping Functions 1	Boehm *et al.* [31]
wet troposphere	ECMWF (2.5° × 2.0°) for Vienna Mapping Functions 1	Boehm *et al.* [31]
polar tides	IERS Conventions 2003	McCarthy and Petit [32]
earth tides	IERS Conventions 2003	McCarthy and Petit [32]
geoid	EIGEN-6C3stat	Förste *et al.* [33]
oerr	MMXO14	Bosch *et al.* [34]

Envisat's RA-2 instrument measures high-resolution data in the Ku- and S-bands with a frequency of 18 Hz, corresponding to a distance of approximately 365 m between two consecutive measurements. This study employs the Sensor Geophysical Data Record (SGDR) v2.1 data. In the study region, the bandwidth of the RA-2 instrument switches among 320 MHz, 80 MHz, and 20 MHz depending on the roughness of the topography [35]. Over rougher terrain the bandwidth is lowered which increases the tracking window of the altimeter. This prevents the altimeter to lose lock over rapidly changing heights. According to the smaller bandwidth the size of each bin is increasing and thereby the height resolution is decreasing. The different bandwidth are also called measuring modes.

The Envisat satellite mission was preceded by ERS-2 (1995–2011) and succeeded by SARAL/AltiKa (2013 onward) in the same orbit. ERS-2 was measuring in two different bandwidth like Envisat. SARAL/AltiKa does not change measuring bandwidth. For ERS-2 we used the cycles 000 till 085 (REAPER) and for SARAL/AltiKa the cycles 001 till 020 (GDR-T patch 2).

3.2. In-Situ Gauging Data

The time series derived from the altimetry data is validated by comparisons with *in situ* gauging data. The *Mekong River Commission* (http://ffw.mrcmekong.org/) maintains several gauging stations along the lower Mekong River and its tributaries. Among the 27 available time series of gauging-station data, we selected those satisfying the following criteria: First, because this study focuses on smaller rivers, we selected only the gauging stations upstream of Vientiane and along the tributaries, where the river width is about 1 km or less. The only exception is the Mukdahan station, where specific topographic influences can be studied. Second, we excluded gauging stations with large data gaps or unexplained jumps in their time series. Third, we filtered out all gauging stations with no usable close-by altimetry data. The nine remaining stations were located 15–80 km distant from the investigated virtual stations, *i.e.*, the crossing points of the altimeter tracks and the rivers. The locations of the gauging and virtual stations are shown in Figure 2.
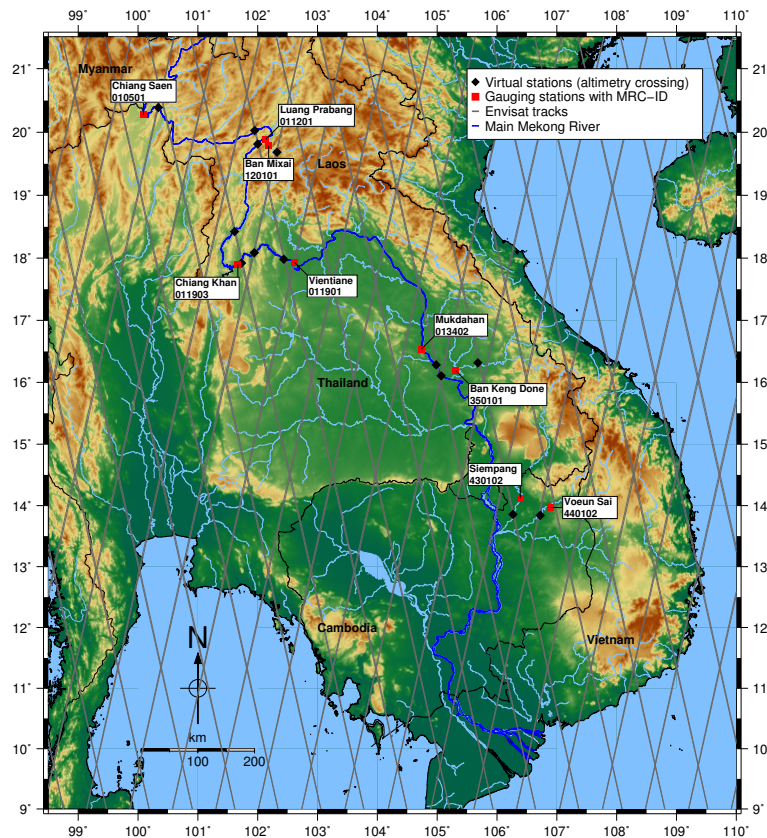
Figure 2. Study area of the lower Mekong River, indicating the gauging stations used in the validation (name of the nearest settlement and ID issued by the Mekong River Commission), the virtual stations, and the Envisat altimetry tracks.

The temporal resolution of the time series of the gauging stations is one day. Gauging data along the main stream cover the entire time frame of the Envisat measurements (until 2010), while those along the tributaries terminate between 2005 and 2007.

4. Hooking Effect

The hooking effect is an off-nadir distortion of altimetry measurements that occurs at the water-land transition. Because the water surface reflects usually more strongly than the surrounding land surface, the altimeter measures the distance to the water surface even when not vertically positioned over the water. The measured off-nadir distances form a parabolic shape in the along-track altimetric height profiles [15]. This can be explained from the relationship between the off-nadir measurements and the heights (Figure 1). The measured range ρ_i at a distance ds_i from the nadir over the water body is given by

$$\rho_i = \sqrt{ds_i^2 + (\rho_0 - da_i)^2}. \tag{2}$$

Here, $da_i = \frac{\partial a}{\partial s} ds_i$ is the height difference of the satellite between the nadir point and the actual measurement points, $\frac{\partial a}{\partial s}$ is the change in satellite altitude along the track, and ρ_0 is the measured nadir range over the water body. Given that the water-level height is $H_i = a_i - \rho_i$, H_i can be expressed as a function of ds_i with

$$H_i = \underbrace{a_0 - da_i}_{a_i} - \rho_0 \sqrt{\left(1 - \frac{da_i}{\rho_0}\right)^2 + \frac{ds_i^2}{\rho_0^2}}. \tag{3}$$

Neglecting the higher-order polynomials, Equation (3) can be rewritten as

$$H_i = H_0 - ds_i^2 \left(\frac{1}{2\rho_0} \right) \left(1 + \left(\frac{\partial a}{\partial s} \right)^2 \right).$$

(4)

Equation (4) shows that H_i follows a parabolic profile with a vertex at H_0, *i.e.*, the water height. The parabola is distorted by the term $\left(\frac{\partial a}{\partial s} \right)^2$, which changes over the water body region. The changes of height over short distances are small (approximately 0.005 $\frac{m}{m}$). For example, over 5 km from a water body away, the height would be distorted by approximately 8 cm, below the accuracy of the altimetry-derived inland water heights (a few decimeters). Therefore, the height distortion can be neglected.

Equation (4) assumes that the along-track distance equals the horizontal distance between the satellite and the water body, *i.e.*, the altimetry track is perpendicular to the water body. In practice, however, the track intersects the river at an angle α. The strongest water return then originates not from the intersection of the altimetry track and the river, but from a closer upstream or downstream position. Assuming a straight river in proximity, the distance between the footprint center and the nearest water body is $ds_i' = ds_i \cdot \sin(\alpha)$ (see Figure 1 right side). Therefore, the hooking parabola is dilated but not distorted.

However, depending on the intersection angle, the altimeter can measure river sections of length 10 km or more. Over a stretch of 10 km, the slope of the river cannot usually be neglected, and the measurements must be corrected accordingly.

Figure 3 shows an altimetry profile over the upper Mekong River, near Luang Prabang (Figure 2). The parabolic shape of the measurements is clearly visible. In this example the hooking effect extends to 10 km from the water body and the error in the parabolic heights is up to 100 m. Not all of the measurements are influenced by the off-nadir returns. The topography of the river and its surroundings can influence the measurements such that no hooking parabola appears in the data. Winding rivers and regions surrounded by mountains that shadow the river are especially prone to this effect. As the exact crossing point of the altimeter track and the river slightly changes (up to 1 km), the hooking parabola may be apparent in some measurements, while others show a completely different characteristic.
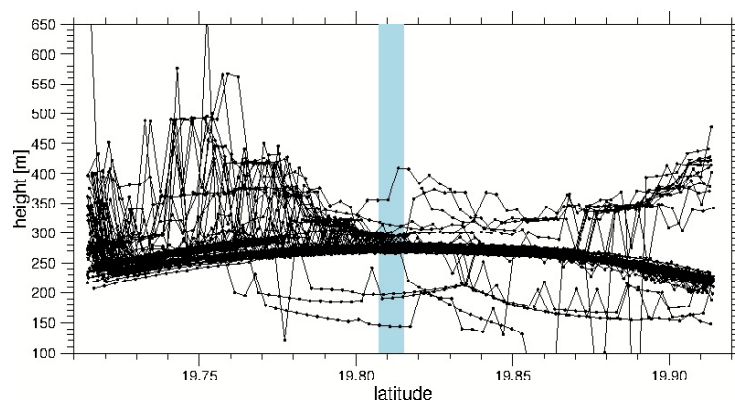

Figure 3. Profile of measured Envisat data over the Mekong River near Luang Prabang (see Figure 2). The figure shows all available passes at this location. The data were retracked beforehand using the Multi-Subwaveform Retracker (MSR) (see Section 5.1). The blue region indicates the actual location of the river.

Most land-water transitions generate a hooking effect in the altimetry data. However, the hooking effect can usually be ignored in water-level estimates of larger water bodies where enough nadir measurements allow for a reliable estimate of the water level. For smaller rivers or lakes, (<1 km) where fewer altimetric measurements over the water body are available, the altimeter instrument can

lose lock due to the rapidly changing topography. In these cases, the hooking parabola can yield more reliable water levels than those obtained solely from measurements over the water body. Especially in the Envisat data, no measurements may exist where the river width is less than 350 m which is the distance between two consecutive measurements of Envisat. If the altimeter loses lock and misses some water surface data, information can be retrieved from distant parts of the hooking parabola. When analyzing the parabola, the water body does not need to be precisely located; indeed, its position might change over time.

The whole hooking effect and its treatment is based on the assumption that water causes the strongest return of all objects in the footprint. However, other objects may cause a strong reflection as well, such as river banks, surrounding rice fields, or urban buildings. If these objects are the strongest reflector over the whole pass they might even form a parabola on their own.

In the Mekong region investigated in this work rice fields have the highest importance of these reflecting objects. However, only a few time series examined in this work are surrounded by rice fields as we focus on the more northern part of the river in hilly and mountainous areas. For some crossings of the altimeter over the river no parabolic shape is visible in the heights which can be caused by water bodies surrounding the river such as rice fields. In these cases, correction the hooking parabola is not applicable.

5. Method

In our approach, the hooking parabola is derived from all measurements during a single pass around the river crossing. Our method can be divided into three main steps. First, we process the data using a newly developed retracker, the Multi-Subwaveform Retracker (MSR), which improves the data along the hooking parabola. The second (and most important) step detects the useful measurements that are influenced by the hooking effect. For this purpose, we adopt the RANSAC algorithm. The final step combines the measurements extracted by the RANSAC algorithm into a model of the hooking parabola, from which the water-level is obtained.

5.1. Multi-Subwaveform Retracker MSR

Our novel retracking method, MSR, was developed to improve the data quality of water-level time series, with special focus on the hooking effect. The method determines the sub-waveforms in Improved Threshold Retracker (ITR) data [8]. As an initial step, we consider here all ITR sub-waveforms, although only the first one is used for determining the water height. Figure 4 shows a typical waveform of a land-water transition, with the identified sub-waveforms marked by different colors. Over the water body itself, the first return and (and therefor the first sub-waveform) is caused by the reflection of the water. As the satellite retreats from the water, the first return signal most likely originates from land reflectance, and later sub-waveforms can be attributed to water returns. Thus, the first sub-waveform in the ITR waveform delivers good results over the water body, but yields no information on the hooking parabola. We assume that in each waveform, one of the sub-waveforms originates from water reflectance, but we cannot know which one. We can only assume that the water return yields the most intense sub-waveform. To find this sub-waveform, we define a weight for each subwaveform.

$$w_j = \sum_i P_i \qquad i = 1 \dots \text{length(subwaveform)} \tag{5}$$

where w_j is the weighting factor of the jth sub-waveform and P_i denotes the return power at gate i of the jth sub-waveform. The number of sub-waveforms j and the number of gates i for each sub-waveform are determined in the MSR. The sub-waveform with the largest weight is assumed as the water-return sub-waveform and is therefor used in the height determination. This factor w_j defines the dominant sub-waveform as the one with the most power and highest amplitude. The weighting factor also defines the accuracy of the heights estimated in further calculations.

Figure 5 shows the MSR results for one crossing. The hooking parabola is clearly visible in the bundle of heights derived from all sub-waveforms (black dots), and the best sub-waveform (red stars) is usually caused by water reflection. The ITR results (green squares) turn out to be less suitable for extracting the hooking parabola.
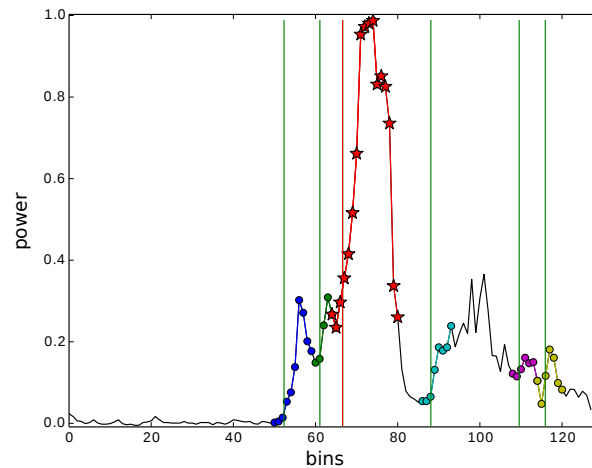

Figure 4. Typical waveform near the water-land transition. The identified sub-waveforms are marked with different colors. The most intense sub-waveform (red stars) is assumed to come from the water surface. The vertical lines indicate the leading edge of each sub-waveform.
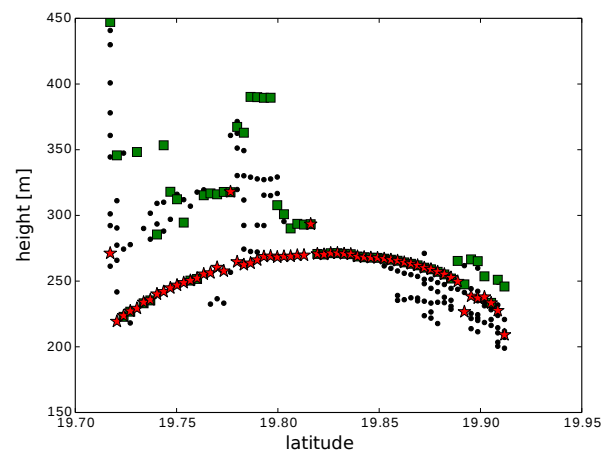

Figure 5. Altimeter profiles obtained by two retrackers during one pass over the Mekong River. The heights obtained from all subwaveforms of the MSR are marked in black dots, the heights of the best waveforms in the MSR and Improved Threshold Retracker (ITR) data are marked as red stars and green squares, respectively.

The analysis of the heights retrieved from all subwaveforms affirms the assumption that the most prominent return is caused by the river. Other objects in the footprint might cause a strong reflection as well (river banks, surrounding rice fields, or urban buildings). However, heights caused by these targets would probably not lie on the hooking parabola, save they are such strong reflectors that they form a parabola on their own. Figure 5 shows clearly that most of the heights derived from the most prominent sub-waveform from a parabolic shape.

Nonetheless, it is possible to use all heights by sub-waveforms in the following algorithm and not only the best. By this, one can be certain that the water return is included. The effects of including all heights and not only the best in the algorithm will be examined in Section 6.

The retracking process is not impaired by the changing mode of the altimeter mentioned in Section 3.1. The nominal tracking gate and bin size are changing with each mode, but both are known for all bandwidths. Therefore, the retracking method can be used regardless of the actual measuring mode.

5.2. RANSAC Algorithm for Hooking Effect Estimation

The off-nadir altimetry returns from the water surface along the hooking parabola are identified by the RANSAC algorithm. This non-deterministic algorithm estimates the model parameters from data with outliers [21]. By virtue of its iterative approach, RANSAC more robustly handles data with outliers than conventional estimation algorithms. The iterative process begins with the best-fitting model within a given uncertainty range. The success of the algorithm depends on the accuracies of the input data. Moreover, it is helpful, but not necessary, to know the approximate number of outliers in the data.

The RANSAC algorithm proceeds through three steps (an example is illustrated in Figure 6):
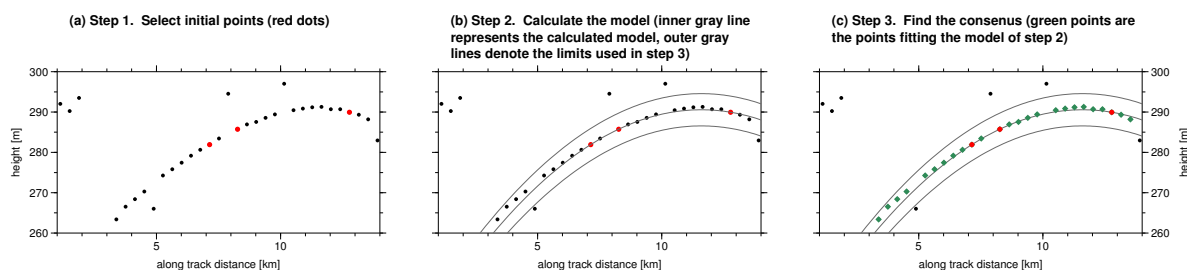

Figure 6. The main steps of the RANdom SAmple Consensus (RANSAC) algorithm.

1. Select the initial values: A sufficient number of points to unambiguously define the model are randomly picked from all data points (e.g., 3 for a parabola and 2 for a line; see Figure 6a).
2. Calculate the a-priori model: This step uses the randomly chosen points from step 1 (See Figure 6b).
3. Find the consensus set:

   (a) The consensus set contains all data points that fit the model within a specified limit, which is determined by the accuracy of the points. Given the uncertainty in the data, if many data points fit the model the randomly picked starting points have probably homed-in on the correct model (See Figure 6c).

   (b) Recalculate the model using all points in the consensus set, and determine and save the new consensus set.

These three steps are repeated N times. The number of repetitions depends on the proportion of outliers and the targeted level of confidence. N can be estimated by

$$N = \frac{\log\left(1 - prob\right)}{\log\left(1 - (1-\epsilon)^s\right)}.$$ (6)

Here ϵ is the relative number of outliers (as a percentage), *prob* denotes the confidence level (e.g., 99%), and s is the number of points required in the model determination. The confidence level defines the probability of finding the correct model. Although the number of outliers needs not be exactly known, an overlyoptimistic assessment reduces the number of repetitions, impeding the estimation of the correct model. If the number of outliers exceeds 60% (as in the present study), N can be 1000 or even larger.

Finally, the algorithm selects the "best" model. In the original RANSAC algorithm, the best model acquires the largest consensus set. We modified the RANSAC algorithm to account for the goodness of

fit of the points to the model. Instead of maximizing the number of points in the consensus set, we seek the model that minimizes the following error function

$$C = \sum_i v(dist(p_i, model)) \tag{7}$$

with

$$v(dist(p_i, model)) = \begin{cases} dist(p_i, model) & : dist(p_i, model) < limit \\ constant & : dist(p_i, model) > limit. \end{cases} \tag{8}$$

In these expressions, $dist(p_i, model)$ denotes the difference between the model and the ith data point, and *limit* defines the threshold below which points are considered to fit the model (*cf.*, Step 3a). The constant can be freely chosen but must be larger than the limit. In this study, we set $constant = 2 * limit$. Different values for the *constant* were tested on their performance in the algorithm, but $constant = 2 * limit$ yielded overall the best results. The proportion of outliers determines whether a model is accepted. If the best model has a smaller consensus set than expected from the outliers, the model is discarded, and no model is returned. Again, it is preferable to overestimate rather than underestimate the outlier proportion.

In our study, the RANSAC algorithm finds the points belonging to the hooking parabola, not the final parameters of the parabola. Two parabola fittings are required, one each for the northern and southern banks of the water. The two half-parabolas are estimated separately because their shapes are influenced by the topography in the footprint (among other factors), which might differ on both sides of the river. Moreover, two half-parabolas might not share a common vertex. To estimate these parabolas, the algorithm requires only points from the northern or southern half of the data (with an additional 10% margin). For wider rivers with more than 500 m width, the algorithm also identifies points along a horizontal line over the river.

Sometimes, parabolic height profiles can result from the topography around the water body. To avoid such profiles, we impose three restrictions on Step 2 of the RANSAC algorithm. First, the hooking parabola is known to open toward the downside. Second, the parabola opening can be roughly estimated from Equation (4) . Third, the water height is roughly known (±25 m) from a topography model. Therefore, models that predict water heights outside of this window are discarded. Under these restrictions, the RANSAC algorithm may not find any model and the height determination may fail in that epoch.

We also found that, in general, models with vertexes close to the middle of the water body yielded superior results.

5.3. Final Parameter Estimation

The RANSAC algorithm outputs up to three sets of points, one set for each of the two parabolas and one set for the line (optional). These models are not necessarily consistent, as they define different water levels. Therefore, to determine which of the models fit together, we use restricted parameter estimation with hypothesis testing [36] (Chapters 3.2 and 4.2). The three models were pairwise-tested if they predicted the same height with a level of confidence of 95% .

In the first step, the points of the two test models are used in a parameter estimation of the water-level height. The second step forces the parameters of both models to predict the same height of the water body. The subsequent hypothesis test evaluates whether the same-height restriction appreciably distorts the models. To this end, it compares the standard deviations of the unrestricted and restricted parameters.

Provided that the models fit together, their points are used in a parameter estimation to determine the water-level height. If none of the models fit together, the model with the smallest standard deviation is selected. The height of the vertex of the estimated hooking parabola is adopted as the final height when composing the time series.

5.4. Post-Processing of the Time Series

5.4.1. Slope Correction

The slope of the river influences the data processing in two ways. First, it influences the altimeter measurements at non-perpendicular intersections as described in Section 4. This influence is corrected in the retracked altimeter heights prior to the main algorithm. The correction is minor and exerts no significant influence on the results.

The second influence is caused by the orbital variation. The crossing location might change as much as 1 km, leading to variable biases in the time series. If the slope is known, the water levels can be corrected to the mean point of the river crossing. The slopes of the main Mekong River are reported in Gupta and Liew [37], but those of the tributaries are unknown. However, this correction improves the root mean square (RMS) (relative to data from a neighboring gauging station) by only a few centimeters, and is therefore a secondary correction. Hence, it is applied only to measurements along the main river.

5.4.2. Outlier Detection

The time series resulting from the final parameter estimation might contain some outliers. Residual outliers are detected with prior information; namely, we expect that an annual signal dominates the time series. To this end, we fit an annual sinusoidal signal to the time series, and detect all points whose residual is outside the 95% quantile of all residuals. However, points outside of this quantile are not necessarily outliers. For instance, the peak of a flood, drought, or some other unusual event would be detected as an outlier. If the neighboring measurements show a similarly large residual, we attribute these points to extreme events in the time series, rather than discarding them as artefacts.

For the absolut standard deviation σ_{h_i} it is neccessary to know the variance factor σ_0:

$$\sigma_{h_i}^2 = \sigma_0^2 \cdot \frac{1}{w_{h_i}}. \tag{9}$$

We assume, that σ_0 is constant for all heights in one time series and for all time series. To derive σ_0 we compare altimeter time series with close by *in situ* gauging data. The RMS is considered to be identical with the standard deviation of the whole time series, which is

$$(RMS)^2 = \sigma_T^2 = \frac{\sum_i^N \sigma_{h_i}^2}{N} = \frac{\sigma_0^2 \cdot \sum_i^N \frac{1}{w_{h_i}}}{N} \quad \text{with } N \text{ number of points in time series.} \tag{10}$$

In a strict sense the accuracies of the corrections and orbit have to be included here on the left hand side. However, as they are assumed constant over both time and the Mekong River region and small compared to the RMS ($\approx$5 cm) their contribution will be absorbed in the variance factor σ_0.

6. Results, Validation and Discussion

This section presents the water-level time series of the Mekong River and its tributaries, and validates them in comparisons with gauging data. For this purpose, we ensured that all virtual stations are close to an existing gauging station. The validation stations have different topographic surroundings and river widths, and thus, represent the diversity of real inland waters.

For the following results we had to set parameters in the RANSAC methods (see Section 5.2). Where Envisat data were measured at the highest resolution with a bandwidth of 320 MHz, we set *limit* = 1 and the outlier proportion to 70%. All virtual stations south of Chiang Khan (latitude 18° N) were measured in this bandwidth. At more northern stations, the bandwidth altered during a single pass and also among passes, increasing the proportion of outliers to 80%. In these cases, we set

$limit = 1$ if most of the measurements remained within the 320 MHz bandwidth; otherwise, we set $limit = 1.5$.

6.1. Results and Validation of the Water-Level Time Series Derived by the Hooking Approach

In this section, we derive the water-level time series from altimetry data using our proposed method, hereafter referred to as the hooking approach. Table 2 compares the results of the virtual stations with those of their nearest gauging stations. To compare the time series derived from our method with that of the gauging station data, we compute the RMS, the coefficient of determination (R^2), and the number of points in the time series and all available Envisat cycles. For both the RMS and R^2 coefficient we remove the long term mean from both the altimetry and gauge time series as the gauge data is not height referenced. The long term mean is only calculated with time points which are in both time series. An interpolation is not needed because of the daily resolution of the gauge data. The hooking approach outputs two values: the first from the time series without outlier detection and the second with outlier detection (see Section 5.4.2).

The hooking approach yields water-level time series for over three-quarters of the available cycles. The exception is the Ban Mixai Station, where the topography is atypical (see Section 6.2). We also identified three sources of missing cycles. First, even when Envisat collects measurements over a complete cycle, data might be missing over a specific region. Accordingly, data from this cycle is missing in all altimetric time series. Second, our algorithm might be unable to fit a parabola or a line to the available data; in this case, it would return no height measurements. Finally, even when the height data are well-fitted to a parabola or line, they might be discarded because they fall outside the specified height window.

The RMS of the time series derived by the hooking approach ranges from 0.34 m to 2.26 m, with a mean of 1.22 m. The RMS is below 1.5 m in 80% of the cases. The R^2 lies between 0.55 and 0.97 with a mean of 0.83 (improving to 0.91 for the main river only). The RMS exceeds 2 m in only one time series (Luang Prabang 1), where the river topography is especially prone to seasonal effects (see Section 6.2). Excluding outliers (at the expense of reducing the number of data points) improves the derived time series in 8 out of 14 cases. In three cases, outlier detection does not change the results; in two cases, it slightly deteriorates the results; and in one case, the RMS decreases but also the correlation.

The quality (R^2) of the gauging-station data is generally poorer along the tributaries of the Mekong River than along the main river. At only one station (Voeun Sai 1), R^2 exceeds 0.8 and the RMS is very low (0.34 m). However, the low R^2 at other stations does not necessarily imply defects in the hooking approach; rather, it depends largely on the quality of the gauging data. Despite our choice of gauging data (see Section 3.2), both the quality and length of the *in situ* data are inferior. As the time series shortens, the determination of R^2 becomes more unstable and more strongly influenced by single outliers. In addition, the amplitudes of the annual variations are smaller along the tributaries (6–11 m) than along the main river (10–18 m). Assuming the same uncertainty in all water levels, smaller signal amplitudes will yield smaller R^2, although the magnitude of the absolute RMS difference is independent of amplitude. Along the tributaries, where the RMS is less sensitive to the signal amplitude, the RMS values are comparable (within the same order of magnitude) to those of the main river.

We also conducted this examinations with using the heights derived by all sub-waveforms and not only the best one (see Section 5.1). With all heights we can be certain to always include the height of the water return which should improve the results. However, we found that in general the results are neither improving nor deteriorating but the computational time is increasing. With an increasing number of points used in the RANSAC algorithm the portion of outliers is increasing as well. With this the number of neccessary iterations of the RANSAC algorithm increases accordingly (see Equation (6)). This lead us to the conclusion that it is not worth using all heights instead of the best. However, it is possible that at other locations at other rivers using all heights prove to be useful.

Table 2. Comparison of results obtained by the hooking approach and the median approach. The MCR code is the code of the gauging station assigned by the Mekong River Commission and the station name is the nearest settlement. The stations above the double lines reside along the main Mekong River; those below the double lines reside along the tributaries. Listed are the pass numbers of the intersecting Envisat track, the location of the intersection, the distance between the gauge and the intersection in kilometer, the intersection length of the water body measured by the altimeter in meter, and the approximate amplitude measured at the gauge in meters. The quality of the results is indicated by three measures: the root mean square error (RMS) in meter between the altimetry time series and the gauging data, the squared correlation coefficient (R^2), and the number of epochs in the time series (compared to the number of all available altimeter epochs).

| | | | | | | | | | Hooking Approach | | | | | | Median Approach | | | |
| | | | | | | | | | *without Outlier Detection* | | | *with Outlier Detection* | | | | | | |
MCR Code	Station Name	Dist.	River Name	Pass	Lon	Lat	Intersect. Length	max. Amplitude	RMS	R^2	# Epochs	RMS	R^2	# Epochs	RMS	R^2	# Epochs	# Avail. Epochs
010501	Chiang Saen	30	Mekong River	294	100.339	20.390	350	10	2.25	0.61	59	1.83	0.84	55	6.04	0.29	50	80
011201	Luang Prabang 1	24	Mekong River	651	101.949	20.027	250	15	2.51	0.94	81	2.26	0.97	77	3.64	0.71	77	81
	Luang Prabang 2	16	Mekong River	651	102.000	19.814	500	15	1.23	0.88	76	1.20	0.91	73	6.96	0.26	76	79
011903	Chiang Khan 1	60	Mekong River	193	101.612	18.424	240	13	0.87	0.94	72	0.86	0.94	72	3.58	0.48	71	80
	Chiang Khan 2	5	Mekong River	193	101.730	17.919	2860	13	1.28	0.86	65	1.08	0.89	62	10.23	0.00	52	80
	Chiang Khan 3	35	Mekong River	666	101.943	18.084	340	13	1.46	0.91	70	1.48	0.90	67	1.96	0.75	73	80
011901	Vientiane	19	Mekong River	651	102.436	17.980	1800	11	1.63	0.76	71	1.22	0.86	69	6.30	0.03	82	82
013402	Mukdahan 1	39	Mekong River	21	104.984	16.283	3220	12	1.35	0.78	71	0.97	0.89	67	4.61	0.25	79	83
	Mukdahan 2	60	Mekong River	952	105.068	16.109	1000	12	0.51	0.97	79	0.50	0.97	77	5.47	0.16	84	86
120101	Ban Mixai	18	Nam Khan	666	102.3240	19.6856	90	4.50	1.79	0.58	46	1.68	0.70	43	3.90	0.32	67	81
350101	Ban Keng Done	42	Xe Bangfai River	479	105.6986	16.3180	180	14	1.44	0.78	74	1.40	0.55	68	6.32	0.25	80	85
440102	Voeun Sai 1	18	Tonle San River	322	106.7130	13.8421	460	7	0.97	0.79	73	0.34	0.88	69	3.44	0.39	82	84
	Voeun Sai 2	16	Tonle San River	937	106.9437	14.0426	320	7	0.98	0.61	63	0.89	0.59	61	3.11	0.30	81	85
430102	Siempang	31	Tonle Kong River	479	106.2653	13.8467	430	10	1.49	0.72	69	1.49	0.72	69	2.29	0.44	84	85

6.2. Effects Influencing the Accuracy of the Water-Level Time Series

The topography of the Mekong River strongly influences the consistency of the altimetry time series and the gauging data. The gauging data are always maintained at settlement sites, where the river valley is usually widened. In contrast, altimetry measurements can be collected upstream or downstream of settlements, where the river is narrower. Consequently, the amplitudes are higher in the altimetry water-level time series than in the gauge time series. The amplitude difference is revealed in the RMS values but not in the determination coefficients (R^2). This effect becomes obvious at the virtual stations of Chiang Saen and Luang Prabang 1.

The time series of the two virtual Luang Prabang stations are compared with that of the gauge station in Figure 7 (for visual clarity, the means of all time series are removed). The virtual station Luang Prabang 1 lies *ca.* 20 km upstream of the gauging station and Luang Prabang 2 *ca.* 5 km downstream. The amplitude of the time series at Luang Prabang 1 is clearly exaggerated during periods of low water, possibly because of the changing river width. The river width at different water levels can be measured from Landsat 7 panchromatic images (data available from http://earthexplorer.usgs.gov/), with a pixel size of 15 m [38]. For this purpose, we used two 2006 images: one from the dry season in March and the other from the flood season in August. The Landsat images of the three locations at both dates are shown in Figure 8. The measured river width is also shown. The Mekong River clearly widens at Luang Prabang 2 and at the gauging station, from 400 m and 240 m during the dry season to 520 m and 450 m, respectively, during the flood season. The wet season covers many sand banks that are visible during the dry season. On the other hand, the river at Luang Prabang 1 is little expanded during the flood season (from 240 to 300 m); instead, the water rises in the valley. This effect is clearly visible in the amplitudes of the three time series.
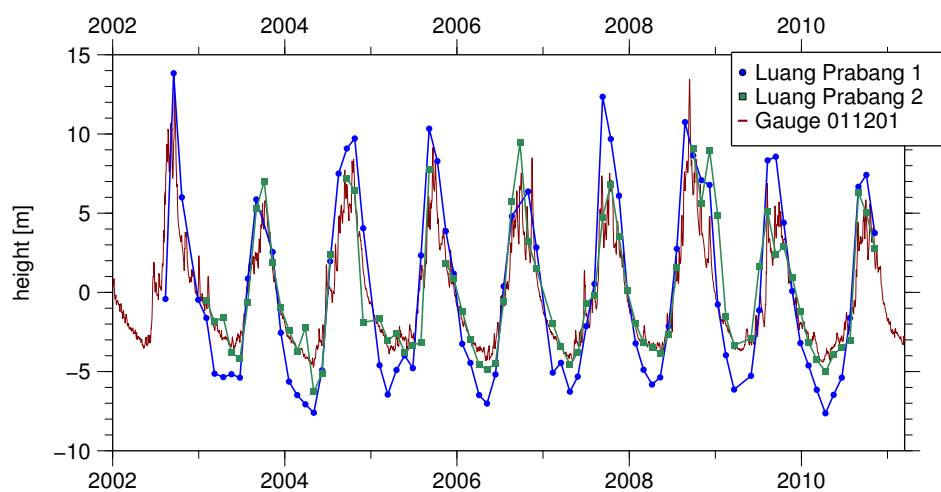

Figure 7. Water-level time series at the stations near Luang Prabang.

The change of river width can be used to estimate the river discharge at the three sites. This parameter should be similar for all three stations at a given time epoch. If assuming a trapezoidal shape of the river intersection, which is clearly a strong simplification, one is able to estimate the discharge variation from the change of intersection area. Furthermore, we assume an identical flow velocity at all locations. For the altimetry height differences we took the measured values closest in time to the Landsat images. Heights from the gauge are taken at the same epoch. For Luang Prabang 1 we obtain a height difference of 9 m and a change of the intersection area of 2430 m^2; for Luang Prabang 2 we find a height difference of 5 m, and area change of 2300 m^2; and for the gauge the height difference is 7 m which leads to an area change of 2450 m^2. Considering the assumption of the simplified river shape and the accuracy of width measurement which of least one pixel on each side of the river and a pixel size of 15 m, no significant difference can be determined.
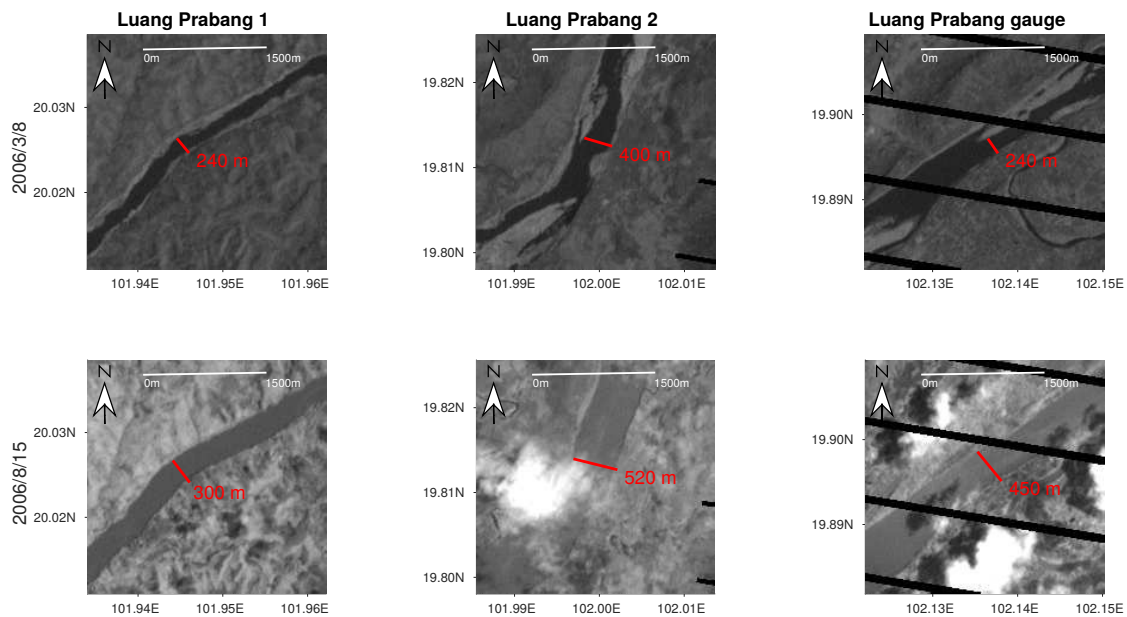
Figure 8. Landsat 7 images at the Luang Prabang sites during the dry season (**top**) and the wet season (**bottom**).

The influence of different topography even between close by stations shows the importance of co-location of the observations. Unfortunately, co-locating the gauge data and altimetry data is not available in most cases which should be keep in mind when gauge data and altimetry data are compared.

Besides the topography surrounding the station, the time series is affected by the angle of intersection between the altimeter track and the river. The two virtual stations at Mukdahan are closely spaced and surrounded by comparable landscape, but yield significantly different time series. These two virtual stations differ only by the angle at which the altimetry track intersects the river. Track 21 (Mukdahan 1 further upstream) intersects very obliquely and passes along the river for several kilometers, whereas track 952 (Mukdahan 2 further downstream) intersects nearly perpendicular to the river. Equivalently, the intersection length is three times longer at Mukdahan 1 than at Mukdahan 2. Reflecting this difference, the time series of Mukdahan 2 has an RMS against the gauge only half the size then the Mukdahan 1 series, and contains more data points. Because of the oblique intersecting angle and long intersection length, the altimetry data at Mukdahan 1 are influenced by the slope in the water surfaces, which can be compensated as described in Section 5.4.1. However, to properly correct this influence one has to know the exact slope, which points are influenced by the slope, and which points are cross track off-nadir measurements from the river. Gupta and Liew [37] provide river slopes for the Mekong. However, Mukdahan is located at the transition of two river units. For the upstream unit a slope of 0.06 $\frac{m}{km}$ is given, and for the downstream unit a slope of 0.2 $\frac{m}{km}$. Using the altimetry data set, we calculate slopes between 0.09 $\frac{m}{km}$ and 0.11 $\frac{m}{km}$, which seems to be realistic and in accordance to Gupta and Liew [37]. The time series of Mukdahan 1 and 2 are compared with that derived from the gauge data in Figure 9. Although neither of the virtual time series properly reproduces the maxima, Mukdahan 2 generates better data overall and a more accurate time series at the minima than Mukdahan 1.

The results are influenced not only by acute intersection angle between the altimetry track and the water body but also by the shape of the river at the intersection. This is exemplified at Chiang Khan 2, where the intersection length seems to not fit the expectations. At Chiang Khan 2, the river makes an s-bend which expands its apparent width under the altimetric track, although the river is only around 300 m wide at this point. The meandering of the river under the track also degrades the quality of the

results, as the measured water-level height can no longer be regarded as constant. Consequently, the time series deteriorates and displays more data gaps.
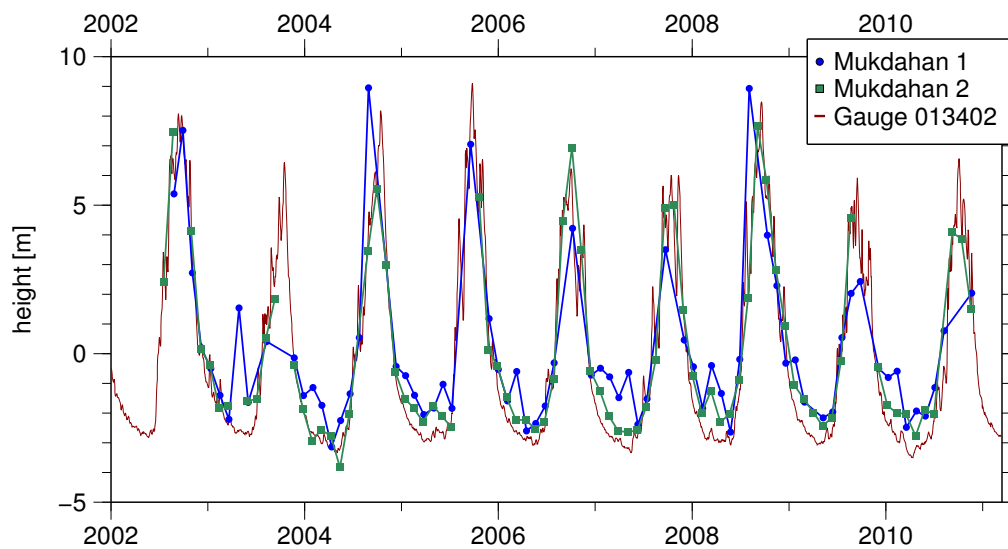

Figure 9. Water-level time series at the stations near Mukdahan.

As discussed above, the differences in the time series derived from the virtual stations and the gauging data depend on the valley width. However, at Ban Mixai station, the valley introduces an additional problem. In this stretch, the river flows through a narrow valley with high and very steep banks (indeed, the Ban Mixai site has the steepest banks among the sites investigated in this study). These steep banks reflect the radar signal multiple times, causing offsets in some of the height measurements. The water levels acquired through one cycle at Ban Mixai are plotted in Figure 10. We show both the results of all sub-waveforms from the MSR and the best one. Clearly, there are two shifted parabolas and partially also a third one. Two similar peaks are visible in the waveforms: the first from the original water reflection and the second from the multiway reflection. The applied retracker detects the dominant peak in either of these parabolas. Because the algorithm cannot distinguish between water returns and multiple reflections, it indiscriminately extracts measurements from either the upper or lower parabola. The two parabolas can be offset by up to 15 m, three times higher than the amplitude of the seasonal signal at Ban Mixai (5 m). Thus, the multireflections preclude a reliable time series at this location as many cycles cannot be used.

In Section 4 we discussed about possible reflections from objects other than the river. In the Mekong region the biggest concern are neighboring paddy fields which might show a strong reflectance as well. However, only a few virtual stations south of Vientiane are surrounded by rice field. In order to investigate these stations for possible non-river influences we can also use the hooking approach. Since it is not only possible to extract the height of the vertex of the hooking parabola but also its along-track position we are able to check whether the vertexes are in a close proximity to the river or not. A vertex further away of the river is probably caused by a reflection not originating from the river. In Figure 11 we show as an example all tracks and the position of the vertex for the two stations near Mukdahan which are surrounded by paddy fields. For both virtual stations all vertexes are in close vicinity to the river. Moreover, the water leverage of rice fields is season-dependent since they are only flooded during the wet season. Therefore, the reflection from the paddy fields would only degrade the measurements during these months, but we do not see any season dependency of the time series quality. Additionally, the consistency of the two parabolas we estimate for each target (see Section 5.3) can be used as indicator, that only desired reflections are included: if both parabolas fit together in height they originate most probably from the same reflector, *i.e.*, the river.
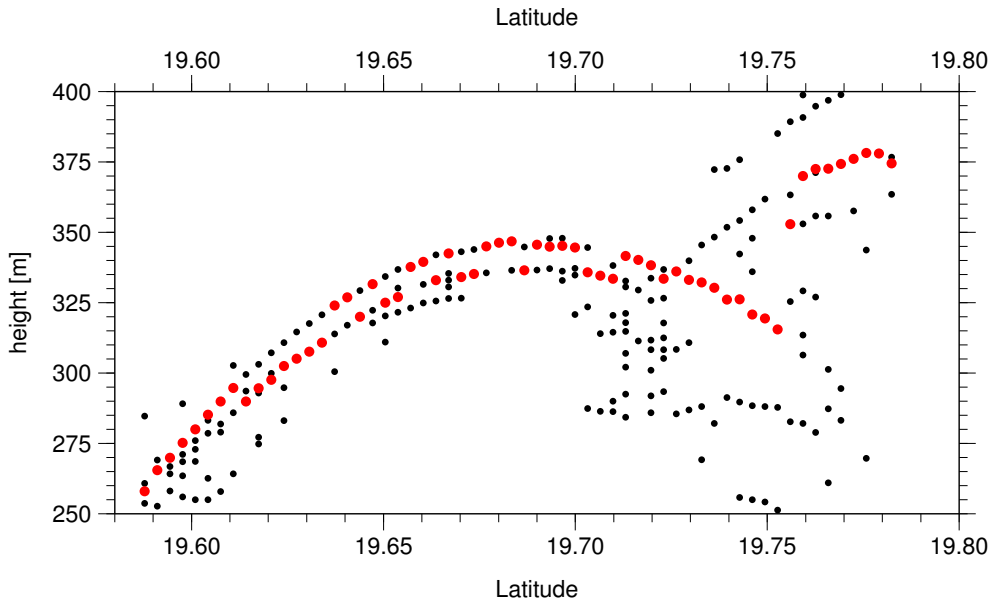
Figure 10. Along-track heights at Ban Mixai, Envisat cycle 16, retracked with MSR, showing all heights of all sub-waveforms in black and the best one in red.
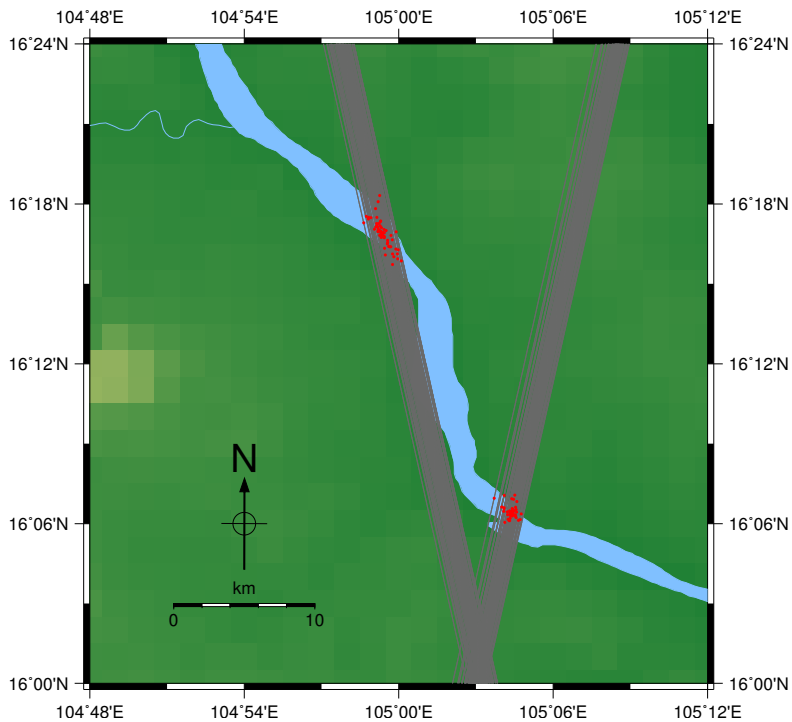

Figure 11. The position of the vertexes along the track for the two virtual stations near Mukdahan.

6.3. Comparison with Other Altimetry Products

This subsection compares the results of the hooking approach with those of an established median approach (e.g., [17]). The median approach uses the median of all MSR retracked altimeter measurements within a 3 km radius around the river center. Similar to our hooking approach, it also discards all heights outside a specified height window. The median approach is the easiest one for deriving the water-level time series of inland waters, requiring only the river location as additional information.

The hooking approach always yields superior results to the median approach for all vriitual stations. The results of the median approach should improve with increasing intersection length; on the contrary, both RMS and R^2 values reduce with increasing intersection length, whereas the results of the hooking approach are independent of intersection length. The median approach yields a meaningful time series only at the Chiang Khan 3 station. At all other stations, the resulting time series are of insufficient quality for further analysis.

Birkinshaw *et al.* [28] published altimetry time series at Luang Prabang 2 and Vientiane and at downstream stations not considered in this study. In their study they use ERS-2 and Envisat data between 1995 and 2003 and 2002 and 2008 respectively. The altimetry data is retracked according to the shape of each waveform (ocean-like, flat patch and two quasi-specular). They adopted two outlier detection methods in their time series determination. Comparing the altimetric and gauging-station time series at Luang Prabang 2, they reported RMS values of 1.99 m and 1.24 m with 22 points and 16 points in the time series, respectively. The hooking approach yieldes an RMS value of 1.23 m and 1.20 m without and with outlier detection and the time series contains 76 and 73 data points of 79 available epochs respectively (see Table 2). Over the same period, the Vientiane station yielded RMS values of 0.41 m and 0.44 m with 29 points and 33 points in the time series, respectively. For the Envisat data between 2002 and 2008 there should be approximately 60 repeats, but due to the retracking scheme and the measurement quality only 25 repeats for Luang Prabang and 37 for Vientiane are available after retracking. Our results for the same station show RMS values of 1.63 m and 1.22 m with 70 and 67 data points of 82 available epochs in the time series. Although the time series obtained by Birkinshaw *et al.* [28] and our hooking approach are comparable in quality measured with the RMS, the former is constructed from fewer data points.

We could not compare our results with data from the GLRM [11] or Hydroweb [9] databases, because no common virtual stations are available. In the ESA River and Lake database [5] two virtual stations near Mukdahan are included. For Mukdahan 1 the ESA time series has an RMS value of 2.42 m and R^2 of 0.76 compared to 0.97 m and 0.89 in our results; the Mukdahan 2 ESA time series has an RMS value of 0.43 m and R^2 of 0.99 compared to 0.50 m and 0.97 in our results.

6.4. Application of the Hooking Approach to Other Missions

The Envisat satellite mission was preceded by ERS-2 and succeeded by SARAL/AltiKa. Therefore, we should consider whether the hooking approach is applicable to data from these satellites, and consequently, whether the time series can be expanded. To this end, we tested the hooking approach on a previously used virtual station, Chiang Khan 1. Although the hooking approach yielded reasonable time series from ERS-2 and SARAL/AltiKa data, the results were limited by inherent defects in the datasets. The ERS-2 data were discontinuous due to lost lock of the altimeter and changing bandwidth of the measurements, which were not properly documented. However, compared with the gauging data, the 1995–2003 time series derived by the hooking approach exhibited an RMS and R^2 of 1.33 m and 0.85, respectively. Given the aforementioned limitations, the quality of these results is comparable to that of the Envisat analysis.

Data gaps also limited the processing of the SARAL/AltiKa data, but in this case, the gaps were caused by weather influence. SARAL/AltiKa measurements are more sensitive to atmospheric water content [39] than the other two missions, and are more degraded during the monsoon season. Nonetheless, the time series of SARAL/AltiKa derived by the hooking approach yielded good statistics (RMS = 0.76 m; R^2 = 0.93 versus the gauging station data). The SARAL/AltiKa measurements should yield better results than Envisat, especially over smaller inland waters, because of the higher repetion rate (40 MHz) and smaller footprint. In fact, the time series derived from SARAL/AltiKa and Envisat were comparable in quality because the SARAL/AltiKa data are degraded by atmospheric water content.

According to these results, the hooking approach is applicable to ERS-2 and SARAL/AltiKa data, as well as to Envisat data. To collate the time series derived from the three altimetry missions, we must

tackle the range biases between the missions. One part of these biases is the radial range error *oerr* between the altimetry mission. This is determinded over the open ocean and interpolated over the continents [34]. The correction of this bias is already included in the generel corrections mentioned in Section 3.1. The other part mostly depends on the retracking algorithm and is not constant for even one retracker. Solutions to the later one are currently being debated. At Chiang Khan, the between-mission bias can be reduced by establishing the long-term mean. This approach enables us to merge the three time series into a single time series of nearly 20 years (see Figure 12). However, if the observed water body has no constant long-term mean, correcting the range biases becomes a complex problem, and is not attempted here.
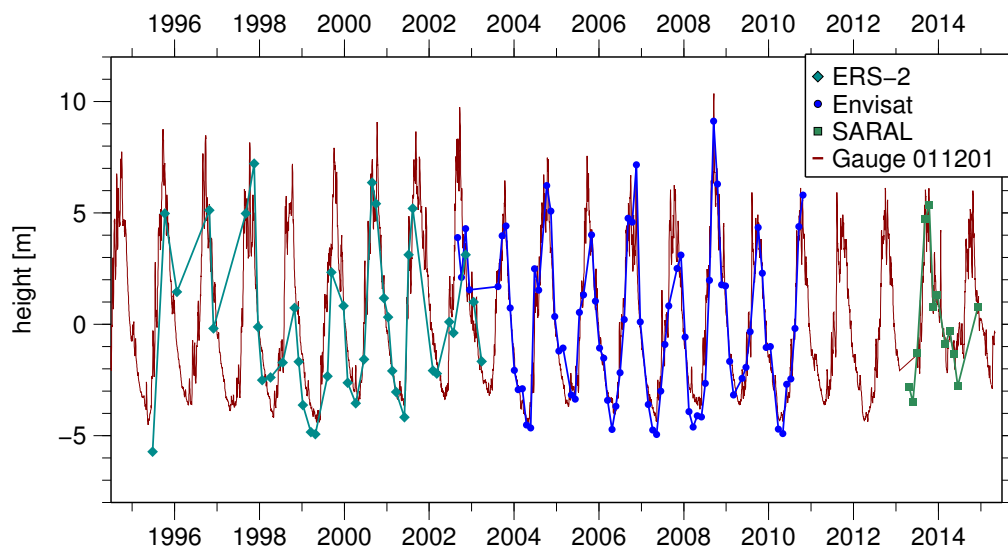

Figure 12. Twenty years multi-mission time series at the station Chiang Khan 1.

7. Conclusions

In this study, we demonstrated a method that derives reliable time series from off-nadir measurements acquired in satellite altimetry over rivers narrower than 500 m. These off-nadir measurements form a parabola in their height profiles whose vertex is the water level. Without further a-priori information, our method identifies the measurements affected by the hooking effect. From these measurements, it derives one water level per epoch. The method of deriving water levels is even applicable if no nadir measurement over the river is available as long as parts of the hooking parabola can be identified in the data.

The off-nadir measurements are detected by the RANSAC algorithm. Because the only additional information is the estimated location of the river, the operation of the algorithm is almost fully automatic. To validate our method, we derived water-level time series along the Mekong River and some of its tributaries, and compared them to the time series acquired by *in situ* gauging stations. The RMS of our time series ranged between 0.34 m and 2.26 m, with a mean of 1.22 m, and the R^2 value ranged between 0.97 and 0.55, with a mean of 0.83 (improving to 0.91 when the tributaries were excluded).

The topography exerted a major influence on the altimetry data in the Mekong region. For example, the amplitude of the time series is increased in narrow valleys. Another influence was the intersection angle between the altimetry track and the river; as the intersection became more oblique, the data quality declined.

Comparing the results of our hooking approach with those of the median approach, we find that the hooking approach clearly outperforms the median approach in the study area. Using the hooking approach, we can measure water-level time series of rivers in the Mekong region even when no nadir

altimetry data are available. The approach is also well-suited to very small rivers (width below 500 m). Over wider rivers, there are usually sufficient altimetric measurements for conventional approaches such as used in DAHITI or other altimetry databases. Due to the automatization of the algorithm we are able to extract a larger number of water level time series in a short time. The hooking approach seems equally applicable to smaller river systems around the globe.

Here, we demonstrated the presence and correction of the hooking effect in data from three satellites: Envisat, ERS-2, and SARAL/AltiKa. After removing the range biases between consecutive missions, we derived a water-level time series over the Mekong River that spans 20 years.

In the next stage of our research, we will combine our hooking approach with the DAHITI database operated by the DGFI-TUM [12] in order to be able to process altimetry data for large and small rivers within one common software. Toward this goal, we are planing to correct the measured altimetric heights of the hooking parabola, providing more data points at the height of the water surface. This correction should yield reliable water-level time series for all kinds of inland water bodies, lakes, reservoirs, and rivers, including very small bodies (width <500 m).

Author Contributions: Eva Boergens developed the method, conducted the data analysis and wrote the majority of the paper. Denise Dettmering and Christian Schwatke helped with discussion of the method and results and writing the manuscript. Florian Seitz supervised the research and contributed to manuscript writing and organization.

Conflicts of Interest: The authors declare no conflict of interest.

References

1. Global Runoff Data Center. *Long-Term Mean Monthly Discharges and Annual Characteristics of GRDC Stations*; Technical Report; Federal Institute of Hydrology: Koblenz, Germany, 2013.

2. Morris, C.S.; Gill, S.K. Variation of Great Lakes water levels derived from Geosat altimetry. *Water Resour. Res.* **1994**, *30*, 1009–1017.

3. Birkett, C. The contribution of TOPEX/POSEIDON to the global monitoring of climatically sensitive lakes. *J. Geophys. Res.: Oceans* **1995**, *100*, 25179–25204.

4. Birkett, C.M. Contribution of the TOPEX NASA radar altimeter to the global monitoring of large rivers and wetlands. *Water Resour. Res.* **1998**, *34*, 1223–1239.

5. Berry, P. Two decades of inland water monitoring using satellite radar altimetry. In Proceedings of the Symposium on 15 Years of Progress in Radar Altimetry, Venice, Italy, 13–18 March 2006; Volume 15.

6. De Oliveira Campos, I.; Mercier, F.; Maheu, C.; Cochonneau, G.; Kosuth, P.; Blitzkow, D.; Cazenave, A. Temporal variations of river basin waters from Topex/[Poseidon satellite altimetry. Application to the Amazon basin. *Comptes Rendus L'Académie Sci.-Ser. IIA-Earth Planet. Sci.* **2001**, *333*, 633–643.

7. Chelton, D.B.; Ries, J.C.; Haines, B.J.; Fu, L.L.; Callahan, P.S. Satellite altimetry. *Int. Geophys.* **2001**, *69*, i–ii.

8. Gommenginger, C.; Thibaut, P.; Fenoglio-Marc, L.; Quartly, G.; Deng, X.; Gómez-Enri, J.; Challenor, P.; Gao, Y. Retracking altimeter waveforms near the coasts. In *Coastal Altimetry*; Benveniste, J., Cipollini, P., Kostianoy, A.G., Vignudelli, S., Eds.; Springer: Berlin, Germany, 2011; pp. 61–101.

9. Crétaux, J.F.; Jelinski, W.; Calmant, S.; Kouraev, A.; Vuglinski, V.; Bergé-Nguyen, M.; Gennero, M.C.; Nino, F.; Del Rio, R.A.; Cazenave, A.; *et al.* SOLS: A lake database to monitor in the Near Real Time water level and storage variations from remote sensing data. *Adv. Space Res.* **2011**, *47*, 1497–1507.

10. Berry, P.; Bracke, H.; Jasper, A. Retracking ERS-1 altimeter waveforms over land for topographic height determination: An expert systems approach. *ESA SP* **1997**, *1*, 403–408.

11. Birkett, C.; Reynolds, C.; Beckley, B.; Doorn, B. From research to operations: The USDA global reservoir and lake monitor. In *Coastal Altimetry*; Springer: Berlin, Germany, 2011; pp. 19–50.

12. Schwatke, C.; Dettmering, D.; Bosch, W.; Seitz, F. DAHITI – an innovative approach for estimating water level time series over inland waters using multi-mission satellite altimetry . *Hydrol. Earth Syst. Sci.* **2015**, *19*, 4345–4364.

13. Frappart, F.; Calmant, S.; Cauhopé, M.; Seyler, F.; Cazenave, A. Preliminary results of ENVISAT RA-2-derived water levels validation over the Amazon basin. *Remote Sens. Environ.* **2006**, *100*, 252–264.

14. Zhang, M.; Lee, H.; Shum, C.; Alsdorf, D.; Schwartz, F.; Tseng, K.H.; Yi, Y.; Kuo, C.Y.; Tseng, H.Z.; Braun, A.; *et al.* Application of retracked satellite altimetry for inland hydrologic studies. *Int. J. Remote Sens.* **2010**, *31*, 3913–3929.

15. Santos da Silva, J.; Calmant, S.; Seyler, F.; Rotunno Filho, O.C.; Cochonneau, G.; Mansur, W.J. Water levels in the Amazon basin derived from the ERS-2 and ENVISAT radar altimetry missions. *Remote Sens. Environ.* **2010**, *114*, 2160–2181.

16. Kuo, C.Y.; Kao, H.C. Retracked Jason-2 altimetry over small water bodies: Case study of Bajhang River, Taiwan. *Mar. Geod.* **2011**, *34*, 382–392.

17. Maillard, P.; Bercher, N.; Calmant, S. New processing approaches on the retrieval of water levels in ENVISAT and SARAL radar altimetry over rivers: A case study of the São Francisco River, Brazil. *Remote Sens. Environ.* **2015**, *156*, 226–241.

18. Calmant, S.; Seyler, F.; Cretaux, J.F. Monitoring continental surface waters by satellite altimetry. *Surv. Geophys.* **2008**, *29*, 247–269.

19. Santos da Silva, J.; Seyler, F.; Calmant, S.; Rotunno Filho, O.C.; Roux, E.; Araújo, A.A.M.; Guyot, J.L. Water level dynamics of Amazon wetlands at the watershed scale by satellite altimetry. *Int. J. Remote Sens.* **2012**, *33*, 3323–3353.

20. Frappart, F.; Papa, F.; Marieu, V.; Malbeteau, Y.; Jordy, F.; Calmant, S.; Durand, F.; Bala, S. Preliminary assessment of SARAL/AltiKa observations over the Ganges-Brahmaputra and Irrawaddy Rivers. *Mar. Geod.* **2015**, *38*, 568–580.

21. Fischler, M.A.; Bolles, R.C. Random sample consensus: A paradigm for model fitting with applications to image analysis and automated cartography. *Commun. ACM* **1981**, *24*, 381–395.

22. Chen, C.S.; Hung, Y.P.; Cheng, J.B. RANSAC-based DARCES: A new approach to fast automatic registration of partially overlapping range images. *IEEE Trans. Pattern Anal. Mach. Intell.* **1999**, *21*, 1229–1234.

23. Kim, T.; Im, Y.J. Automatic satellite image registration by combination of matching and random sample consensus. *IEEE Trans. Geosci. Remote Sens.* **2003**, *41*, 1111–1117.

24. Dung, L.R.; Huang, C.M.; Wu, Y.Y. Implementation of RANSAC algorithm for feature-based image registration. *J. Comput. Commun.* **2013**, *1*, 46–50.

25. Tarsha-Kurdi, F.; Landes, T.; Grussenmeyer, P. Hough-transform and extended ransac algorithms for automatic detection of 3d building roof planes from LiDAR data. In Proceedings of the ISPRS Workshop on Laser Scanning 2007 and SilviLaser 2007, Espoo, Finland, 12–14 September 2007; Volume 36, pp. 407–412.

26. Yan, J.; Jiang, W.; Shan, J. Quality analysis on RANSAC-based roof facets extraction from airborne LiDAR data. *Int. Arch. Photogramm. Remote Sens. Spat. Inf. Sci.* **2012**, *1*, 367–372.

27. Frappart, F.; Do Minh, K.; L'Hermitte, J.; Cazenave, A.; Ramillien, G.; Le Toan, T.; Mognard-Campbell, N. Water volume change in the lower Mekong from satellite altimetry and imagery data. *Geophys. J. Int.* **2006**, *167*, 570–584.

28. Birkinshaw, S.; O'Donnell, G.; Moore, P.; Kilsby, C.; Fowler, H.; Berry, P. Using satellite altimetry data to augment flow estimation techniques on the Mekong River. *Hydrol. Process.* **2010**, *24*, 3811–3825.

29. Mekong River Commission, Ed. *Overview of the Hydrology of the Mekong Basin*; Mekong River Commission: Vientiane, Lao PDR, 2005.

30. Scharroo, R.; Smith, W.H. A global positioning system–based climatology for the total electron content in the ionosphere. *J. Geophys. Res.: Space Phys.* **2010**, *115*, doi:10.1029/2009JA014719.

31. Boehm, J.; Kouba, J.; Schuh, H. Forecast Vienna Mapping Functions 1 for real-time analysis of space geodetic observations. *J. Geod.* **2009**, *83*, 397–401.

32. McCarthy, D.D.; Petit, G. *IERS Conventions (2003)*; Technical Report; Verlag des Bundesamtes für Kartographie und Geodäsie: Frankfurt am Main, Germany, 2004.

33. Förste, C.; Bruinsma, S.; Shako, R.; Abrikosov, O.; Flechtner, F.; Marty, J.C.; Lemoine, J.M.; Dahle, C.; Neumeyer, H.; Barthelmes, F.; *et al.* A new release of EIGEN-6: The latest combined global gravity field model including LAGEOS, GRACE and GOCE data from the collaboration of GFZ Potsdam and GRGS Toulouse. *Geophys. Res. Abstr.* **2012**, *14*, 2821.

34. Bosch, W.; Dettmering, D.; Schwatke, C. Multi-mission cross-calibration of satellite altimeters: Constructing a long-term data record for global and regional sea level change studies. *Remote Sens.* **2014**, *6*, 2255–2281.

35. Benveniste, J.; Baker, S.; Bombaci, O.; Zeli, C.; Venditti, P.; Zanife, O.; Soussi, B.; Dumont, J.; Stum, J.; Milagro-Perez, M. *ENVISAT RA-2/MWR Product Handbook, Issue 2.2*; Technical Report; PO-TN-ESR-RA-0050; European Space Agency: Frascati, Italy, 2007.

36. Koch, K.R. *Parameter Estimation and Hypothesis Testing in Linear Models*; Springer Science & Business Media: Berlin, Germany, 1999.

37. Gupta, A.; Liew, S.C. The Mekong from satellite imagery: A quick look at a large river. *Geomorphology* **2007**, *85*, 259–274.

38. NASA. *Landsat 7 Science Data Users Handbook*; Technical Report; National Aeronautics and Space Administration: Washington DC, USA, 2011.

39. Schwatke, C.; Dettmering, D.; Börgens, E.; Bosch, W. Potential of SARAL/AltiKa for inland water applications. *Mar. Geod.* **2015**, *38*, 626–643.

P-2: Combination of multi-mission altimetry data along the Mekong River with spatio-temporal Kriging

E. Boergens, S. Buhl, D. Dettmering, C. Klüppelberg, and F. Seitz (2017a): **Combination of multi-mission altimetry data along the Mekong River with spatio-temporal kriging**. In: *Journal of Geodesy* 91.5, pp. 519–534

Copyright

Summary of content

The spatial and temporal resolution of altimetry data over rivers is bound by the repeat time and ground track pattern of each altimeter satellite. The common way of river altimetry only regards single satellite water level time series at a fixed crossing point of the satellite ground track and the river, the so-called *V*irtual *S*tation (VS). Their temporal resolutions depend on the used altimeter mission and are usually between 10 and 35 days.

In this study, these spatial and temporal limitations were diminished by combining several VSs of different altimeter missions along the Mekong River. Unlike for lakes, the altimetric water level time series of a river cannot be linked over an equipotential surface. This study proposed the *O*rdinary *K*riging (OK) method together with an appropriate statistical covariance model for the multi-mission altimetry combination. The OK method itself is a simple weighted interpolation method where the weights are based on the covariances between the interpolation point and all other observations, and between the observations themselves. These covariances are estimated by a covariance model.

Here, two covariance models that were specifically designed for the spatial and temporal behaviour of rivers were introduced:

- The first one was a stationary product covariance model:

$$C_{\mathcal{ST}}(h_{\mathcal{S}}, h_{\mathcal{T}}) = C_{\mathcal{S}}(h_{\mathcal{S}}) C_{\mathcal{T}}(h_{\mathcal{T}}). \tag{A.1}$$

  Stationarity implied that the covariance function remain constant over time and along the river. Using a product model allowed to separately estimate the temporal and the spatial covariance. This approach was only applicable as the two domains were uncorrelated in the study area.

- The second covariance model was non-stationary in space but stationary in time and again a product model. The temporal part of the covariance was the same as in the stationary covariance model; the spatial part was a weighted sum of a covariance depending on the flow of the river, C_{riv}, and the dependencies between the sub-basins of the points, C_{euc}:

$$C_{\mathcal{ST}}((\boldsymbol{s}_1, \boldsymbol{s}_2), h_{\mathcal{T}}) = (\pi_{\mathrm{riv}} C_{\mathrm{riv}}(\boldsymbol{s}_1, \boldsymbol{s}_2) + \pi_{\mathrm{euc}} C_{\mathrm{euc}}(\boldsymbol{s}_1, \boldsymbol{s}_2)) C_{\mathcal{T}}(h_{\mathcal{T}}). \tag{A.2}$$

These two covariance models were tested with the OK method for the combination of altimetry data from Jason-2, *Envi*ronmental *Sat*ellite (Envisat), and *S*atellite with *Ar*gos and *Al*tiKa (SARAL) along the main stream of the Mekong River. The combined time series of water levels had a temporal resolution of five days and were validated against in situ gauge data with very good results. The method proofed to be stable despite the change of available data at the end of the Envisat mission in 2011.

Declaration of contribution

Using kriging methods for geodetic observations was introduced by Sven Buhl and Prof. Claudia Klüppelberg of the Chair of Mathematical Statistics in the frame work of the joined IGSSE project REWAP. Eva Börgens and Sven Buhl developed the multi-mission altimetry approach with ordinary kriging. The two different covariance models were jointly discussed; the stationary model was developed primarily by Eva Börgens, the non-stationary by Sven Buhl. Eva Börgens had the lead in the whole project, providing altimetry data and implementing ordinary kriging as well as the analysis of the results and the discussion. Denise Dettmering contributed to the discussion and analysis. The publication was written by Eva Börgens (70%) and Sven Buhl (30%), the figures were compiled by Eva Börgens except one by Sven Buhl. Florian Seitz and Claudia Klüppelberg help improving the manuscript with corrections and comments. The overall own contribution of Eva Börgens is estimated to be **73%**.

Combination of Multi-Mission Altimetry Data Along the Mekong River with Spatio-Temporal Kriging

Eva Boergens · Sven Buhl · Denise Dettmering · Claudia Klüppelberg · Florian Seitz

Abstract River water-level time series at fixed geographical locations, so-called virtual stations, have been computed from single altimeter crossings for many years. Their temporal resolution is limited by the repeat cycle of the individual altimetry missions. The combination of all altimetry measurements along a river enables computing a water-level time series with improved temporal and spatial resolutions. This study uses the geostatistical method of spatio-temporal ordinary kriging to link multi-mission altimetry data along the Mekong River. The required covariance models reflecting the water flow are estimated based on empirical covariance values between altimetry observations at various locations. In this study, two covariance models are developed and tested in the case of the Mekong River: a stationary and a non-stationary covariance model. The proposed approach predicts water-level time series at different locations along the Mekong River with a temporal resolution of five days. Validation is performed against in situ data from four gauging stations, yielding RMS differences between 0.82 and 1.29 m and squared correlation coefficients between 0.89 and 0.94. Both models produce comparable results when used for combining data from Envisat, Jason-1, and SARAL for the time period between 2002 and 2015. The quality of the predicted time series turns out to be robust against a possibly decreasing availability of altimetry mission data. This demonstrates that our

method is able to close the data gap between the end of the Envisat and the launch of the SARAL mission with interpolated time series.

1 Introduction

Describing and modelling the global water cycle relies on the knowledge of water levels of inland water bodies such as rivers, lakes and wetlands. To detect long-term changes in surface water storage, a dense (in space and time) network of monitoring stations is required. However, the number of global in situ measurements of gauges has been declining since the 1980s (GRDC, 2013).

In the last two decades, many studies have shown the great potential of satellite altimetry for measuring water-level time series of larger inland water bodies worldwide to close the data gap of in situ observations (e.g. Birkett, 1995, 1998; Berry, 2006; De Oliveira Campos et al, 2001; Schwatke et al, 2015b). Especially in the last few years, the accuracy of inland altimetryobservations and their availability for even smaller targets have improved (e.g. Maillard et al, 2015; Boergens et al, 2016). The accuracy has reached a few centimetres for lakes and a few dozens of centimetres for rivers (Schwatke et al, 2015b). The onset of SAR altimetry on Cryosat-2 has proven valuable for the observation of small lakes and rivers with high accuracy (Nielsen et al, 2015; Villadsen et al, 2015).

E. Boergens · D. Dettmering · F. Seitz
Deutsches Geodätisches Forschungsinstitut, Technische Universität München, Arcisstr. 21, D-80333 Munich
E-mail: eva.boergens@tum.de

S. Buhl · C. Klüppelberg
Center for Mathematical Sciences, Technische Universität München, Boltzmannstr. 3, D-85748 Garching
E-mail: sven.buhl@tum.de

Today, many inland altimetry time series are publicly available through five operational databases: the Database for Hydrological Time Series over Inland Water (DAHITI), developed by the Deutsches Geodaetisches Forschungsinstitut der Technischen Universitaet Muenchen (DGFI-TUM) (Schwatke et al, 2015b); Hydroweb, developed by the Laboratoire d'Etudes en Geophysique et Oceanographie Spatiales (LEGOS) (Crétaux et al, 2011); the River and Lake database, provided by the European Space Agency (ESA) (Berry et al, 1997); the Global Reservoir and Lake Monitor (GRLM), maintained by the Foreign Agricultural Service of the United States Department of Agriculture (USDA) (Birkett et al, 2011) and the Altimetry for Inland Water (AltWater) by the Technical University of Denmark (Nielsen et al, 2015), which incorporates only Cryosat-2 data so far.

Over lakes and reservoirs, it is often possible to link different altimeter missions and passes into one multi-mission multi-pass time series (e.g. Schwatke et al, 2015b; Calmant et al, 2008). This is possible based on the assumption that the water level of a lake above the geoid remains constant in space. This is true because the water surface forms an equipotential surface if no other effects such as winds or currents are present. By combining different altimetry passes and missions, the temporal resolution of the water-level time series is increased, depending on the number of passes over the water body. Without multi-mission and multi-pass altimetry, the temporal resolution is restricted to 35 days for ERS-1 and 2, Envisat and SARAL measurements, and 10 days for Topex/Poseidon and Jason missions.

Combining altimetry measurements along rivers cannot follow the same approach as that over lakes, as the water surface is not equipotential along the course of the river. The slope of the river, as well as the water flow along the river, hinders the combination of different observations. Besides, slope and flow velocity might change rapidly over the course of the river. Along rivers, an additional problem is spatial resolution. The locations with available altimetry data do not cover the river consistently due to the meanders of the river; some reaches are measured densely, whereas others are not measured at all. Tourian et al (2016) attempted to combine such measurements by estimating flow times between different time series along the Po River. For the estimation of flow velocity or flow time, additional information on the river dynamics is required, since flow velocity is not only changing over the course of the river but also over time, depending on the water level. A different approach for data combination is to assimilate altimetry-derived water levels into hydrological river models (Michailovsky et al, 2013).

In this study, we propose another way of linking altimetry measurements along rivers in order to estimate multi-mission time series for any location of the river with a temporal resolution of a few days. The river flow is described by spatial and temporal statistical dependencies using covariances in spatio-temporal ordinary kriging. The key element of the methodology is the modelling of the dependencies in space and time. We test two spatio-temporal covariance models on the Mekong River: a separable stationary spatio-temporal product covariance model and a non-stationary spatio-temporal covariance model. The estimated covariances are then input in an ordinary spatio-temporal kriging algorithm, which combines the different altimetric measurements along the Mekong River. The main advantage of spatio-temporal kriging for combining multi-mission altimetry data is that it can be used to interpolate water-level time series at any given point in space and time. Another advantage is its stability against erroneous measurements.

Ordinary kriging was originally developed in a spatial context by Krige (1952). It is an interpolation method based on the covariances between the measurement locations and the location to predict. Spatial and spatio-temporal ordinary kriging have been widely applied in recent years (e.g. Cressie and Wikle, 2011; Gräler et al, 2012). Various authors use spatio-temporal kriging for different sets of observations, for example, to predict soil moisture in Heuvelink et al (1997) or Snepvangers et al (2003), as well as top-kriging for river flow (Skøien and Blöschl, 2007). Yoon et al (2013) used spatio-temporal kriging to interpolate synthetic SWOT data along the Tennessee River.

In order to apply the kriging method, it is necessary to know the statistical dependencies between the measurements; the dependencies are modelled with covariances. There are various models for describing spatio-temporal covariances, which have been published with different objectives and applications suitable for different data (e.g. De Iaco et al, 2001; De Cesare et al, 2001; Heuvelink et al, 1997; Snepvangers et al, 2003; Gräler et al, 2012). Rouhani and Myers (1990) has already investigated the problems of modelling spatio-temporal covariances of geohydrological data. Moreover, Cressie and Wikle (2011) summarised a wide variety of spatio-temporal covariance models, including the product model, which separates space and time.

In all the aforementioned covariance models, the spatial locations are points on a 2D plane and the covariance function depends on the Euclidean distance between two points. However, in order to model covariances along river networks appropriately, it is

important to incorporate both the river distance and the Euclidean distance. Due to river meandering, two river locations can be close in terms of their Euclidean distance, but be far apart along the river; thus, the hydrological conditions would differ. Ver Hoef et al (2006) and Ver Hoef and Peterson (2010) introduced non-stationary covariance models for rivers based on the river distance. However, completely disposing of the Euclidean distance can lead to a loss of information. Asadi et al (2015) tackled this problem with a mixed covariance model of river and Euclidean distances. Nevertheless, the temporal component was not taken into account in all the above-mentioned studies.

In this study, we demonstrate, through a case study along the Mekong River, the great potential of spatio-temporal kriging for combining multi-mission altimetry data along a river. By linking different altimetry water-level time series, both the spatial and temporal resolutions are enhanced. Each time series itself has a temporal resolution of 10 to 35 days, but all time series together can have a temporal resolution of up to a few days. The most important part of the methodology is modelling the spatio-temporal dependencies of the river flow using covariances. Appropriate covariance models are the essential part of linking multi-mission altimetry data along a river. The method described in this study allows for both high temporal and spatial resolutions of the combined time series, which can be interpolated at any given location along the river at any given time point.

The rest of the paper is structured as follows. In Section 2, the ordinary spatio-temporal kriging method used in this study is presented. Section 3 introduces the study area and Section 4 the altimetry and in situ data applied in this study. Our spatio-temporal covariance models for altimetry measurements along the Mekong River are described in detail in Section 5. Section 6 presents the results of kriging based on the different models and validates them against in situ gauge measurements. The influence of the different missions on the results is investigated in the same section, and a comparison with previous studies is presented.

2 Spatio-temporal ordinary kriging with uncertain data

Ordinary kriging (hereafter referred to as *kriging*) is a geostatistical interpolation method, which was originally developed for spatial data by Krige (1952). In this study, altimeter measurements along the Mekong River, scattered in space and time (see more on the data distribution in Subsection 4.1), are used to predict the water level at any given location along the river and at any given point in time.

Kriging produces a statistically unbiased estimator that is optimal with respect to the mean-squared prediction error. The predictor is a weighted average of the observed values, where the weights depend on the spatial or spatio-temporal dependence between the observed locations and the predicted location. The dependency is expressed by the covariance $C((\boldsymbol{s}_1, t_1), (\boldsymbol{s}_2, t_2))$ between the water levels at two space-time points $(\boldsymbol{s}_1, t_1)$ and $(\boldsymbol{s}_2, t_2)$. Spatio-temporal kriging includes one dimension more than spatial kriging. In addition, the spatial and temporal domains have to be treated differently. Time has clear and irreversible ordering, which does not hold for space directly. The difference between space and time is treated in more detail in Section 5. Detailed introductions to spatial and spatio-temporal kriging can be found in Cressie (1993) and Cressie and Wikle (2011), respectively. In the following, we only present the basic formulas.

The kriging predictor $p(\boldsymbol{s}_0, t_0)$ (i.e. the prediction of the water-level) at some unobserved location $(\boldsymbol{s}_0, t_0)$ along the river is the weighted average of all available altimetry measurements $\mathcal{Z} := \{Z(\boldsymbol{s}_1, t_1), \ldots, Z(\boldsymbol{s}_n, t_n)\}$:

$$p(\boldsymbol{s}_0, t_0) = \sum_{i=1}^{n} \lambda_i Z(\boldsymbol{s}_i, t_i), \qquad (1)$$

where the weights λ_i should add up to 1 to guarantee an unbiased estimation. Note that there might be several altimetry measurements for the same location or the same time point; i.e. $\boldsymbol{s}_i = \boldsymbol{s}_j$ or $t_k = t_\ell$ for $i \neq j$ or $k \neq \ell$ is possible. Unlike the classical computation of kriging weights (e.g. Cressie, 1993, Chap. 3.2), where all input data are assigned the same accuracy, we assign different accuracy values for the data according to De Marsily (1986, Chap. 11.4.8). The weights are then given by

$$\boldsymbol{\lambda} = (\lambda_1, \ldots, \lambda_n) = \left(\boldsymbol{c} + \boldsymbol{1} \frac{(1 - \boldsymbol{1}^\top \Sigma^{-1} \boldsymbol{c})}{\boldsymbol{1}^\top \Sigma^{-1} \boldsymbol{1}}\right)^\top (\Sigma + \Sigma_{\text{alti}})^{-1}, \qquad (2)$$

where $\boldsymbol{1} = (1, \ldots, 1)^\top$, $\boldsymbol{c} = (C((\boldsymbol{s}_0, t_0), (\boldsymbol{s}_1, t_1)), \ldots, C((\boldsymbol{s}_0, t_0), (\boldsymbol{s}_n, t_n))^\top$ and $\Sigma = (C((\boldsymbol{s}_i, t_i), (\boldsymbol{s}_j, t_j)))_{i,j=1\ldots n}$. Σ_{alti} denotes the diagonal matrix of the accuracies σ_i^2, which are assumed constant for each altimetry mission and are estimated through variance component analysis (Koch, 1999, chap. 3.6). These variances are not absolute accuracies, but relative accuracies between the observations of the different missions. In particular, the jth diagonal entry of Σ_{alti} is σ_i^2 if the observation $(\boldsymbol{s}_j, t_j)$ recorded by the ith altimetry mission.

Fig. 1: Map of the study area

It is obvious from Equation (2) that the setup of the covariance function $C((\boldsymbol{s}_1, t_1), (\boldsymbol{s}_2, t_2))$ is of particular importance. The estimation of an appropriate covariance function for altimetry data along the Mekong River is discussed in Section 5.

3 Study area

This study focuses on the Lower Mekong River in South East Asia, south of the Chinese border, up to the confluence with the Tonle Sap River. North of the Chinese border, the river is not measurable by satellite altimetry due to the small and steep river channel; south of the confluence with the Tonle Sap River, in Phnom Penh, the delta is subject to tidal influence, which needs special handling of the altimetry data. Tributaries are not directly considered in this study, but have an indirect influence on the dependence modelling; the Subsection 5.2. Figure 1 shows the layout of the study area.

The Mekong River is dominated by two hydrological regimes: the precipitation and snow melt on the Tibetan Plateau, the so-called Yunnan Component, and the yearly south-eastern monsoon (MRC, 2005). The upper part of the Lower Mekong basin is mostly governed by the Yunnan Component, whereas the lower part is under the influence of the monsoon. The change in the water level between the seasons can be as high as 10 m (e.g. Boergens et al, 2016).

4 Data

4.1 Water levels from altimetry

In this study, we employ altimetry data recorded by three different satellite missions with repeat orbits: Envisat, SARAL and Jason-2. For Envisat, we use both the repeat orbit phase between 2002 and 2010 and the extended mission from 2010 until 2011 (hereafter Envisat EM). The SARAL mission succeeded the Envisat mission on the same orbit, but commenced in 2013. Jason-2 data are available from 2008 until the present. The repeat time is 35 days for Envisat and SARAL, 30 days for Envisat EM and 10 days for Jason-2. These missions yield data for virtual stations (VSs) at the crossing points with the river, which are processed with the DAHITI database methodology (Schwatke et al, 2015b). The first step of this method is the pre-processing, i.e. retracking the altimeter measurements and outlier detection. In the second step, a Kalman filter is applied to these heights in order to derive time series of the water-level changes. A correction for the Hooking Effect is included in the pre-processing for the upstream regions (Boergens et al, 2016).

We use 22 VSs of Envisat, 17 of SARAL, 12 of Envisat EM and 3 of Jason-2. We have fewer VSs from SARAL than Envisat because we decide to exclude five VSs that give too few data points in the time series. Missing data points appear mostly in the rainy season and are probably caused by the higher sensitivity of SARAL towards atmospheric water (Schwatke et al, 2015a). Jason-2 has overall five crossings with the Mekong River in our study area, but in two out of those, it is impossible to derive reliable time series. The locations of all VSs are displayed in Figure 1. The temporal and spatial distributions of the data along the river are shown in Figure 2. The longest time series with the densest spatial pattern is provided by Envisat. The Envisat and SARAL missions share the same orbit; i.e. they have VSs at the same points. However, two years of data are missing in-between the missions. This gap is only sparsely covered by Envisat EM and Jason-2 data. Figures of the time series used in this study can be found in the supplementary data.

4.2 Preprocessing of water level time series

In order to apply kriging to the altimetry data described in Subsection 4.1, a pre-processing step is necessary to make the data roughly satisfy the assumption required for the ordinary kriging method, i.e. a constant mean (Cressie, 1993, p. 120). In addition, we remove all trends and seasonality in each of the time series according to
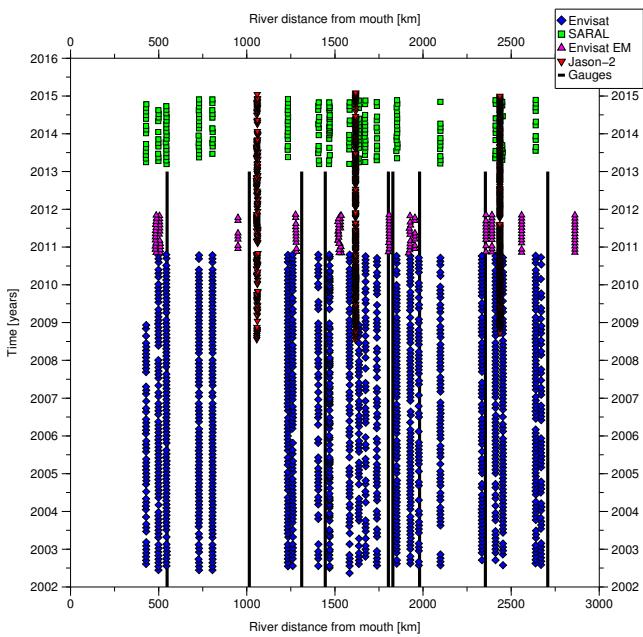
Fig. 2: Spatio-temporal data distribution

Fig. 3: Example of a time series with reduced seasonal signal. The lower panel shows the residuals used for all further computations.

Brockwell and Davis (1997, Section 1.5.2). The seasonality is not modelled with a trigonometric function; instead, we compute and remove the monthly seasonal coefficients for each time series. For the Envisat EM data, with only one year of data, we interpolated the seasonal coefficients from the neighbouring time series. The seasonal coefficients method allows reducing the seasonal signals that do not follow a sinusoidal function Figure 3.

We use the transformed observations as residuals and apply kriging to them. The predictions are then back-transformed, so that they yield interpretable information.

4.3 In-situ data

For validation purposes, we use in situ data from gauging stations. The gauging stations are maintained along the main river and tributaries by the Mekong River Commission (MRC, `http://ffw.mrcmekong.org/`). Nine stations are available for this study, but the records reach only until the end of 2012. The gauging stations appear alongside the virtual stations in Figure 1.

4.4 Auxiliary data

During the study, some auxiliary data are required. In Subsection 5.1, we use the width and slope of the Mekong River provided by Gupta and Liew (2007) to
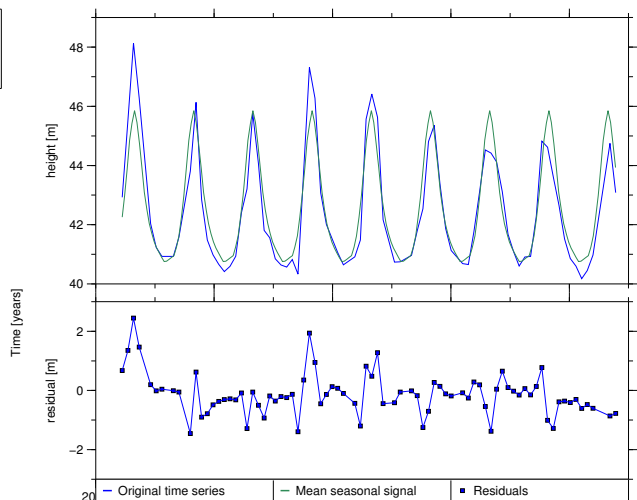
estimate the flow velocity of the river. In Subsection 5.2, we use the Global Precipitation Climatology Centre (GPCC) data of monthly mean precipitation placed on a 0.5° grid (Schneider et al, 2011). A flow direction map from the HydroSHEDS data is used to determine the sub-catchment of each VS in the same section (Lehner et al, 2006). The sub-catchments are in turn used to calculate weights and hydrological locations for the non-stationary covariance model in Subsection 5.2.

5 Spatio-temporal covariance models

A prerequisite for the kriging method (see Section 2), which is used in this study to combine the multi-mission altimetry data, is an appropriate covariance modelling. The covariances have to reflect the changing flow of the river along its course, and can be modelled based on knowledge about the river system or by using empirical covariances obtained from the data. This section introduces the covariance models used for the Mekong River and how they are estimated based on empirical covariances.

We assume that the residuals of the altimetry data (see Subsection 4.2) are a realization of the mean-zero random process $\{Z(\boldsymbol{s},t) : \boldsymbol{s} \in \mathcal{S}, t \in \mathcal{T}\}$ for $\mathcal{S} \times \mathcal{T} \subset \mathbb{R}^2 \times [0, \infty)$. The value $Z(\boldsymbol{s},t)$ can be interpreted as the deviation from the mean seasonal river level at a space-time location $(\boldsymbol{s}, t)$, where $\boldsymbol{s}$ is a location along the Mekong River and t is some time point (a day between 2002 and 2015).

We follow the ideas presented by De Cesare et al (2001, Section 2) and define a valid spatio-temporal covariance model C as the mixture of sums and products of valid spatial and temporal models. For the space-time locations $(\boldsymbol{s}_1, t_1)$ and $(\boldsymbol{s}_2, t_2)$, we define a spatio-temporal covariance model $C_{\mathcal{ST}}$ as

$$
\begin{aligned}
C_{\mathcal{ST}}((\boldsymbol{s}_1, t_1), (\boldsymbol{s}_2, t_2)) = &\, k_1 C_{\mathcal{S}}(\boldsymbol{s}_1, \boldsymbol{s}_2) C_{\mathcal{T}}(t_1, t_2) \\
&+ k_2 C_{\mathcal{S}}(\boldsymbol{s}_1, \boldsymbol{s}_2) + k_3 C_{\mathcal{T}}(t_1, t_2),
\end{aligned}
\tag{3}
$$

where $k_1 > 0$, $k_2, k_3 \geq 0$ and $C_{\mathcal{S}}$ and $C_{\mathcal{T}}$ are valid spatial and temporal covariance models, respectively. We require $Z(\boldsymbol{s}, t)$ to be (second-order) stationary in time; that is, $C_{\mathcal{T}}(t_1, t_2) = C_{\mathcal{T}}(h_{\mathcal{T}})$ can be written only in terms of the temporal lag $h_{\mathcal{T}} = |t_1 - t_2|$. Computing empirical variances of the altimetry data and the correspondent confidence intervals of the estimators, we find that the variance does not vary significantly across the different locations, with most confidence intervals overlapping. Thus, it is reasonable to assume that the spatial variance along the Mekong River is constant; that is, $C_{\mathcal{S}}(\boldsymbol{s}, \boldsymbol{s}) = C_{\mathcal{S}}(\boldsymbol{s}', \boldsymbol{s}')$ for all $\boldsymbol{s}, \boldsymbol{s}' \in \mathcal{S}$. Hence, the spatio-temporal variance $C_{\mathcal{ST}}((\boldsymbol{s}, t), (\boldsymbol{s}, t))$ is also constant over $\mathcal{S} \times \mathcal{T}$. Note that this assumption does not necessarily hold for other river systems.

This assumption is weaker than the one used by De Cesare et al (2001), which requires stationarity in space as well. Validity, i.e. positive definiteness, of the covariance model (3) follows by validity of models $C_{\mathcal{S}}$ and $C_{\mathcal{T}}$ and the requirement of $k_1 > 0$, $k_2, k_3 \geq 0$, see De Iaco et al (2011, Section 4).

There are various valid models for spatial or temporal covariance functions (see for instance Cressie (1993, Section 2.3.1)). As outlined by Ver Hoef, Peterson, and Theobald (2006, Section 1), covariance models that are valid when relying on the Euclidean distance need not yield a valid model of a river network if the Euclidean distance is simply replaced by the river distance.

In Subsection 5.1 and Subsection 5.2, we present two models for the spatial covariance function $C_{\mathcal{S}}$, which are valid for river networks. In Subsection 5.1, we focus on a spatially stationary model applied to observations transformed with respect to flow velocity, whereas Subsection 5.2 deals with a non-stationary approach applied to the original observations.

5.1 Stationary covariance model

In this section, we assume the process $Z(\boldsymbol{s}, t)$ to be second-order stationary in not only time but also space; i.e. we slightly change the notation and write $C_{\mathcal{S}}(\boldsymbol{s}_1, \boldsymbol{s}_2) = C_{\mathcal{S}}(h_{\mathcal{S}})$, where $h_{\mathcal{S}} = |\boldsymbol{s}_1 - \boldsymbol{s}_2|_{\mathrm{riv}}$ is the spatial lag, which is the distance along the river between the two points, expressed as the norm $| \cdot |_{\mathrm{riv}}$. Under this condition, the spatio-temporal covariance model $C_{\mathcal{ST}}$ in (3) can be written only in terms of $h_{\mathcal{S}}$ and $h_{\mathcal{T}}$.

The original altimetry measurements do not fulfil the spatial stationarity assumption in the first place. To make this assumption more feasible, we perform an additional data pre-processing step. We aim for the flow volume between two observed locations on the river within a particular time to be approximately equal whenever the locations are separated by the same river distance. To this end, we transform the observed spatial domain with respect to the estimated flow velocity of the river.

The flow velocity v can be estimated from the slope of the river, its width and the water-level with the Gaukler-Manning-Strickler equation (Jirka, 2007, Chap. 10.3.2); i.e.

$$
v = k_{st} R_h^{2/3} S^{1/2}.
\tag{4}
$$

In this equation, S is the slope of the river, which is approximately known for the reaches of the river from Gupta and Liew (2007). By R_h, we denote the so-called hydraulic radius, which is the proportion between the cross-sectional area and the wetted perimeter. For this hydraulic radius, we assume a constant depth of a river with a rectangular cross-section. The width varies in river reaches, as defined in Gupta and Liew (2007), between 500 and 1500 m. The Strickler coefficient k_{st} measures the roughness of the river channel. Due to missing information on this coefficient for the Mekong River, a constant literature value for large rivers is applied ($k_{st} = 35 \frac{m^{1/3}}{s}$) (Jirka, 2007, Chap. 10.3.2, Tab. 10.2). The transformed distance for each point is then

$$
|\boldsymbol{s} - \boldsymbol{0}|_{\mathrm{riv}}^{new} = \int_0^{|\boldsymbol{s} - \boldsymbol{0}|_{\mathrm{riv}}} \frac{dx}{v(x)},
\tag{5}
$$

where $|\boldsymbol{s} - \boldsymbol{0}|_{\mathrm{riv}}$ is the original river distance for the river mouth to the considered point, $|\boldsymbol{s} - \boldsymbol{0}|_{\mathrm{riv}}^{new}$ is the new river distance and $v(x)$ is the flow velocity at the given point s along the river. In our study, the flow velocity is assumed constant over river reaches, and therefore, the above integral can be transformed to a sum of all reaches downstream of the point. Of course, this representation of the flow velocity is only an approximation. For an exact transformation of water levels along the river, a more sophisticated approach would be necessary, taking for instance time variable slopes into account. However, at this point, the transformation

is carried out to make the assumption of stationarity in space and the use of a stationary spatial covariance model more plausible.

The spatio-temporal covariance is modelled as the product of a valid spatial model $C_{\mathcal{S}}$ and a valid temporal model $C_{\mathcal{T}}$; i.e. we consider the model

$$C_{\mathcal{ST}}(h_{\mathcal{S}}, h_{\mathcal{T}}) = C_{\mathcal{S}}(h_{\mathcal{S}}) C_{\mathcal{T}}(h_{\mathcal{T}}) \qquad (6)$$

for spatial and temporal lags $h_{\mathcal{S}}$ and $h_{\mathcal{T}}$. This corresponds to the special case of (3) obtained for $k_1 = 1$ and $k_2 = k_3 = 0$. This model is a separable model. In particular, it implicitly assumes that there is no interaction between the spatial and temporal parts. The temporal dependence structure is supposed to be location-invariant, and the spatial dependence structure is in turn assumed not to change with time. Spatial invariance of the temporal dependence structure holds approximately for the Mekong River Adamson et al (2009). Temporal invariance of the spatial dependence structure would imply that the course of the river does not change with time. This does not hold for the entire river, especially for the delta, but the part of the river investigated in this study is not exposed to major shifting banks or similar effects.

A first step in fitting the spatio-temporal covariance model $C_{\mathcal{ST}}$ is to obtain an empirical estimate. To this end, we define, for fixed $(h_{\mathcal{S}}, h_{\mathcal{T}})$,

$$
\begin{aligned}
N(h_{\mathcal{S}}, h_{\mathcal{T}}) := \{ & (\boldsymbol{s}_1, t_1, \boldsymbol{s}_2, t_2) \in (\mathcal{S} \times \mathcal{T})^2 : \\
& Z(\boldsymbol{s}_1, t_1) \in \mathcal{Z}, Z(\boldsymbol{s}_2, t_2) \in \mathcal{Z}, \\
& |\boldsymbol{s}_1 - \boldsymbol{s}_2|_{\text{riv}} = h_{\mathcal{S}}, |t_1 - t_2| = h_{\mathcal{T}} \},
\end{aligned}
$$

where $\mathcal{Z}$ denotes again the set of all observations, which in this study are the residuals of the observed altimetry time series without mean water level and seasonal signal.

Under the stationarity assumption, the covariance function C can be estimated by the empirical covariance, which is given by

$$\widehat{C}(h_{\mathcal{S}}, h_{\mathcal{T}}) = \frac{1}{|N(h_{\mathcal{S}}, h_{\mathcal{T}})|} \sum_{\substack{(\boldsymbol{s}_1, t_1, \boldsymbol{s}_2, t_2) \\ \in N(h_{\mathcal{S}}, h_{\mathcal{T}})}} Z(\boldsymbol{s}_1, t_1) Z(\boldsymbol{s}_2, t_2),$$

$$(7)$$

where $|N(h_{\mathcal{S}}, h_{\mathcal{T}})|$ is the cardinality of $N(h_{\mathcal{S}}, h_{\mathcal{T}})$. Since the data are unevenly distributed in space and time, we cluster lags within different tolerance intervals to achieve a reliable estimation of $\widehat{C}$. The cluster sizes are one month for the temporal and $50\,\text{km}$ for the spatial lags. The size of the clusters is a trade-off between the temporal or spatial resolution of the empirical covariance and the reliability of the estimate; the

smaller the clusters are, the more variable the estimate becomes. We modify the cluster size only for the estimation of the cluster with lag 0. For the estimation of temporal covariance with lag 0, we only take measurements that are recorded the same day. We take a tolerance of $5\,\text{km}$ for lag 0 of the spatial covariance estimation due to the slightly shifting orbit of the altimeter satellite. All covariance estimates are tested for a significant difference from zero with a t-test. Empirical covariances failing the test are set equal to zero.

The separability of model (6) allows us to fit a spatial covariance model $C_{\mathcal{S}}$ and a temporal model $C_{\mathcal{T}}$ separately.

For the temporal covariance function, we choose an exponential model with *nugget effect* n_{exp}; i.e.

$$C_{\mathcal{T}}(h_{\mathcal{T}}) = \begin{cases} a_{\text{exp}} + n_{\text{exp}} & \text{if } h_{\mathcal{T}} = 0 \\ a_{\text{exp}} \exp(-b_{\text{exp}} h_{\mathcal{T}}) & \text{if } h_{\mathcal{T}} \neq 0 \end{cases} \qquad (8)$$

and the parameters that need to be estimated are $a_{\text{exp}} > 0$, $b_{\text{exp}} > 0$ and $n_{\text{exp}} \geq 0$. The nugget effect accounts for measurement errors and arises because the estimation is based on lags $h_{\mathcal{T}}$, which are not arbitrarily close to zero. The nugget occurs as a jump or discontinuity in the fitted covariance model at zero.

The spatial covariance is modelled using a linear tent model (c.f Cressie, 1993) with nugget n_{lin}; that is,

$$C_{\mathcal{S}}(h_{\mathcal{S}}) = \begin{cases} a_{\text{lin}} + n_{\text{lin}} & \text{if } h_{\mathcal{S}} = 0 \\ \max\{a_{\text{lin}} - b_{\text{lin}}\, h_{\mathcal{S}}, 0\} & \text{if } h_{\mathcal{S}} \neq 0. \end{cases} \qquad (9)$$

and the parameters to be estimated are $a_{\text{lin}} > 0$, $b_{\text{lin}} > 0$ and $n_{\text{lin}} \geq 0$.

For computational reasons, we fit the correlation function instead of the correspondent covariance model, so that $a_{\text{exp}} + n_{\text{exp}} = a_{\text{lin}} + n_{\text{lin}} = 1$. This reduces the number of parameters to be estimated in both models by one. Figure 4 compares the respective empirical and fitted correlation functions. The approximately exponential and linear decays of the temporal and spatial dependence are visible. Table 1 shows the correspondent model parameter estimates. The nugget effect already accounts for 60% of the covariance decay. After two months, the temporal covariance drops by another 50%. As to the spatial domain, the covariance reaches the 25% level at a lag of $250\,\text{km}$.

An extension of this model would be to divide the river into hydrological reaches and assume stationarity only within each reach, i.e. relax the spatial stationarity constrain. The application of this approach to the Mekong River does not improve the prediction results. When the river is divided into reaches, only data inside

Temporal Correlation

Spatial Correlation
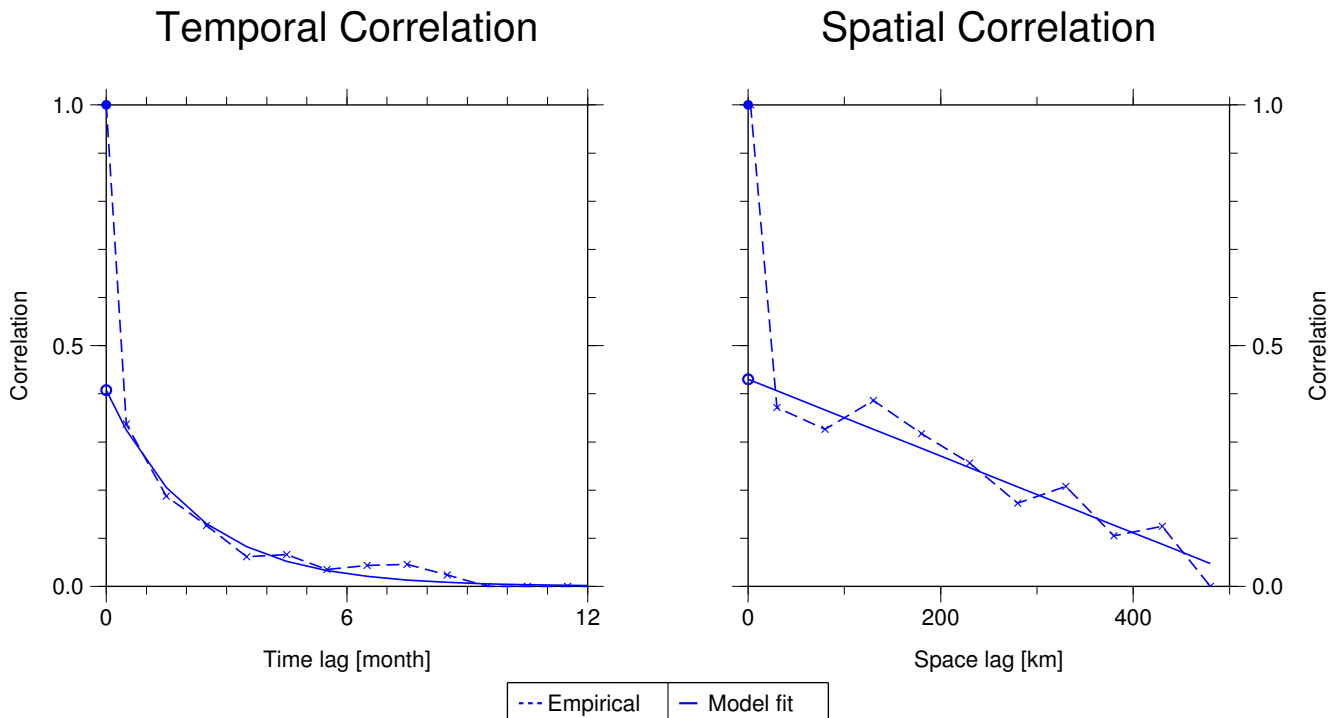

--- Empirical   — Model fit

Fig. 4: Empirical and fitted temporal and spatial covariance functions

Table 1: Parameter estimates for the stationary product covariance model described in Subsection 5.1 fitted to the altimetry data

$a_{\exp}$	$b_{\exp}$	$a_{\lin}$	$b_{\lin}$
0.4078	5.4942	0.4300	0.0008

each reach can be used for fitting the respective covariance and for the kriging prediction. This reduction of data leads to inferior results, which is why we do not pursue the approach further.

5.2 Non-stationary covariance model

The main drawback of the stationary covariance model described above is the implicit assumption of spatial stationarity. Despite working with data transformed with respect to flow velocity, this might lead to predictions with reduced accuracy. In what follows, we propose a new non-stationary covariance model allowing for a changing spatial dependence structure.

We follow Ver Hoef et al (2006) with an "upstream" construction on river networks. A covariance model that is valid for river networks can be defined for $\boldsymbol{s}_1, \boldsymbol{s}_2 \in \mathcal{S}$, where $\boldsymbol{s}_1$ is located downstream of $\boldsymbol{s}_2$, by

$$C_{\mathrm{riv}}(\boldsymbol{s}_1, \boldsymbol{s}_2) = \begin{cases} 0, & \text{if } \boldsymbol{s}_1 \not\leftrightarrow \boldsymbol{s}_2, \\ \tilde{C}_1(0), & \text{if } \boldsymbol{s}_1 = \boldsymbol{s}_2, \\ \prod_{\boldsymbol{s} \in B_{\boldsymbol{s}_1, \boldsymbol{s}_2}} \sqrt{w_{\boldsymbol{s}}} \tilde{C}_1(|\boldsymbol{s}_1 - \boldsymbol{s}_2|_{\mathrm{riv}}), & \begin{array}{l} \text{if } \boldsymbol{s}_1 \leftrightarrow \boldsymbol{s}_2 \\ \text{and } \boldsymbol{s}_1 \neq \boldsymbol{s}_2. \end{array} \end{cases}$$

(10)

Here, the symbols $\leftrightarrow$ and $\not\leftrightarrow$ stand for flow-connectedness and flow-un-connectedness, respectively. The set $B_{\boldsymbol{s}_1, \boldsymbol{s}_2}$ contains the observed measurement locations $\boldsymbol{s}$ between $\boldsymbol{s}_1$ and $\boldsymbol{s}_2$, but excluding $\boldsymbol{s}_1$, and $\tilde{C}_1(\cdot)$ is a stationary covariance model valid in one dimension. We obtain convincing results choosing for $\tilde{C}_1(\cdot)$ again a linear tent model with variance and slope parameters $a_{\mathrm{riv}} > 0$ and $b_{\mathrm{riv}} > 0$, respectively, cf. (9). The factors $w_{\boldsymbol{s}}$ are weights based on the proportion of flow volume contributed by a measurement location $\boldsymbol{s}$ to its next location downstream. This proportion is approximated by integrating the mean monthly precipitation over the sub-catchments of both $\boldsymbol{s}$ and the subsequent location, and then, computing the quotient. The term sub-catchment denotes here the watershed of a location along the river. It consists of all points of the river that drain into this point. Figure 5 shows two examples of sub-catchments in shaded colours corresponding to their VSs (squares). The mean monthly precipitation is obtained using the GPCC data described in Subsection 4.4. Note that
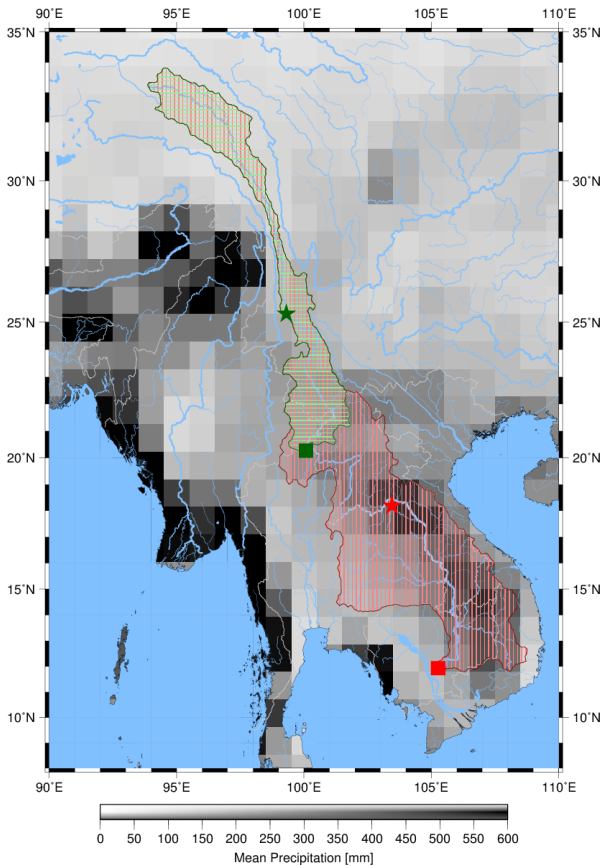
Fig. 5: Hydrological locations for two VSs in their subcatchment. The squares are the locations of the two VSs. The shaded areas indicate the corresponding subcatchments, and the stars are the hydrological locations. The background is the GPCC precipitation map (c.f. Subsection 4.4) used for the hydrological locations.

incorporating evapotranspiration in our computations is negligible, since this yields nearly identical weights for the Mekong River basin.

The flow volume and the weights themselves in Figure 6 reflect the geomorphology of the river with inflowing tributaries. The flow volume is normalized to the value corresponding to the location most downstream. If a major tributary joins the Mekong River between two stations, the flow volume shows a distinct step between the two stations. The same is even better visible in the weights. A smaller weight at some location indicates that, between this location and the next location downstream, a relatively high inflow occurs. In Figure 6, we add the names of the inflowing tributaries to the distinct data points. The most striking peak is caused by two rivers, Mun and Banghiang. One inflow, Nam Ou, is visible well in the weights chart but worse in the flow volume chart. From Equation (10), it is obvious that a higher inflow between two locations along the river

naturally reduces the covariance between them, as they carry less information about each other. Figure 7 shows how the variability in the weights is reflected in the fitted covariance model C_{riv} in comparison with $\tilde{C}_1$, in an example of two locations located downstream and upstream of the confluence of tributary Nam Ngum. Since $\tilde{C}_1$ is a stationary model, the graphs in the left panel overlap. Obvious in the fitted function C_{riv} is the drop in the dependence at the confluence, which shows non-stationarity of the spatial dependence structure.

The difference between model (10) and the "upstream" construction introduced by Ver Hoef et al (2006) is that, in our case, the weights $w_{\boldsymbol{s}}$ are associated with the respective measurement locations $\boldsymbol{s}$ instead of river segments that lie between two locations. This is due to the lack of available observations on all segments of the Mekong River network.

One drawback of model (10) is that it only accounts for isolated river networks. In real data analysis, the Euclidean distance of two measurement locations often plays an important role, since environmental parameters such as precipitation tend to be similar at nearby locations. In the particular case of a river network, it is appropriate not to take into account the Euclidean distance of the measurement locations themselves, but rather the distance of their hydrological locations (Asadi et al, 2015, Section 3.3), which we define as the sub-catchments' mass centres of the monthly precipitation. In Figure 5, we indicate the position of the hydrological location in the sub-catchment for two VSs with a star.

A covariance model based on Euclidean distances is given by

$$C_{\mathrm{euc}}(\boldsymbol{s}_1, \boldsymbol{s}_2) = \tilde{C}_2(\boldsymbol{A}(\boldsymbol{L}(\boldsymbol{s}_1) - \boldsymbol{L}(\boldsymbol{s}_2))), \qquad (11)$$

where $\boldsymbol{L}(\boldsymbol{s})$ is the hydrological location of $\boldsymbol{s}$. The function $\tilde{C}_2$ is a covariance function valid in $\mathbb{R}^2$ and the matrix

$$\boldsymbol{A} = \begin{pmatrix} \cos\alpha & -\sin\alpha \\ a\sin\alpha & a\cos\alpha \end{pmatrix}, \quad a > 0, \quad \alpha \in \left[0, \frac{\pi}{2}\right],$$

allows for spatially anisotropic effects through rotation and dilation. As a model $\tilde{C}_2$ valid in two dimensions, we choose the spherical model (c.f. Cressie, 1993, Section 2.3.1), which is given by

$$\tilde{C}_2(\boldsymbol{h}) = \begin{cases} a_{\mathrm{euc}}\left[1 - \frac{3}{2}b_{\mathrm{euc}}\|\boldsymbol{h}\| + \frac{1}{2}\left(b_{\mathrm{euc}}\|\boldsymbol{h}\|\right)^3\right] & \text{if } 0 \leq \|\boldsymbol{h}\| \leq \frac{1}{b_{\mathrm{euc}}} \\ 0 & \text{if } \frac{1}{b_{\mathrm{euc}}} \leq \|\boldsymbol{h}\|, \end{cases} \qquad (12)$$
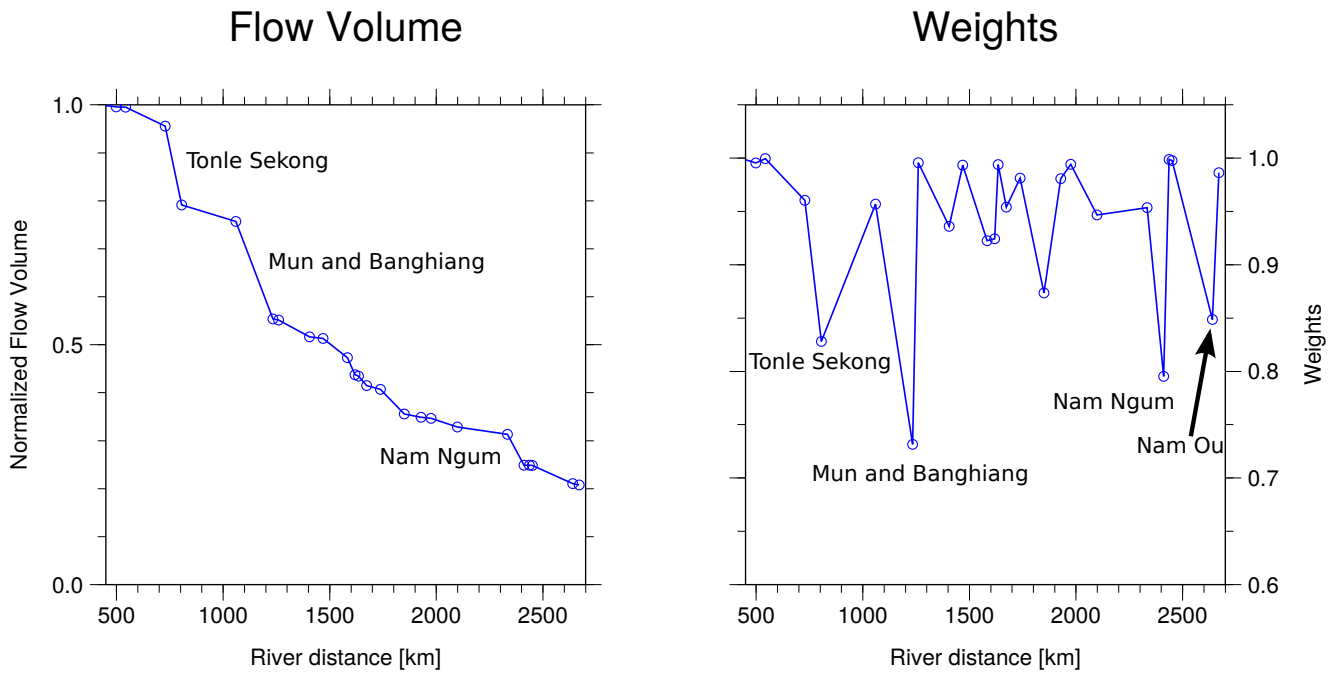
Flow Volume

Weights

Fig. 6: Flow volume and weights used in C_{riv}. The topography of inflowing tributaries is clearly visible. The names of prominent inflowing rivers are indicated.
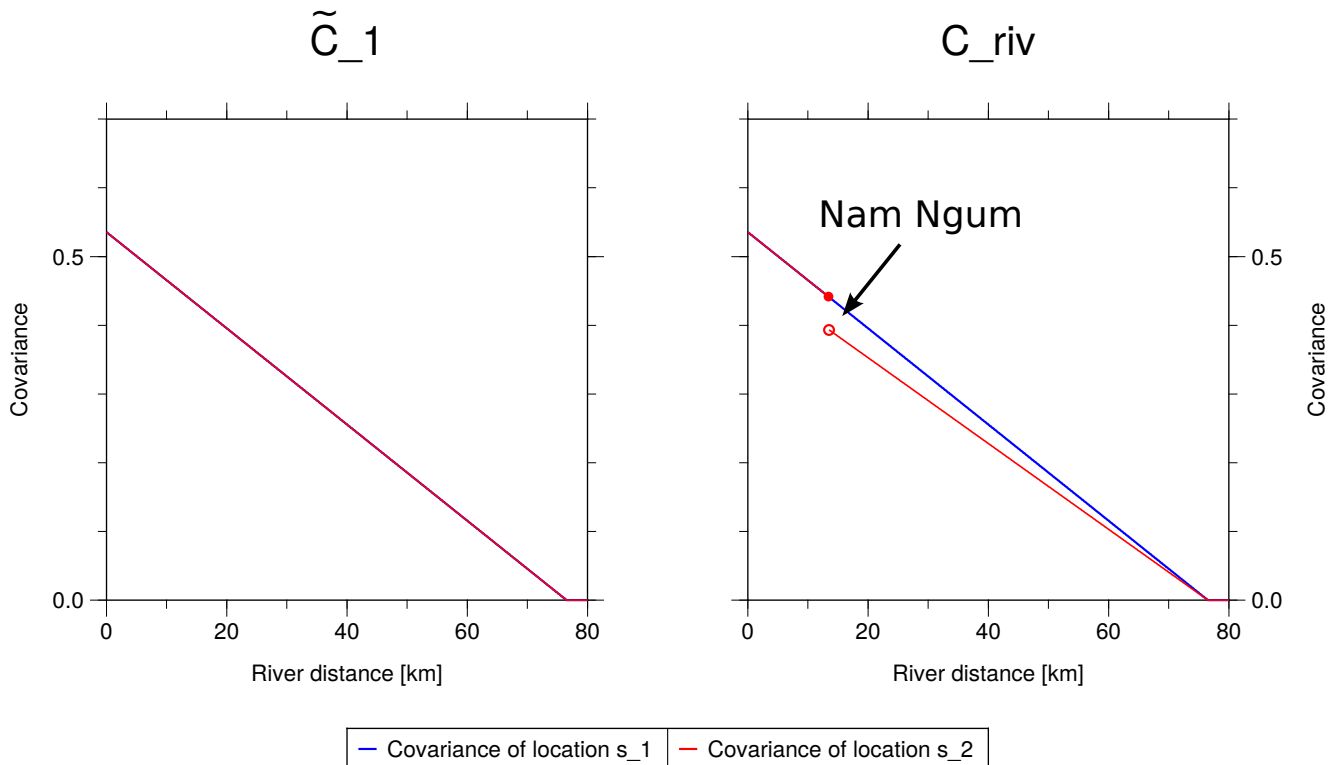
$\widetilde{C}\_1$

C_riv

Fig. 7: Fitted covariance functions $\tilde{C}_1(\cdot)$, $C_{\mathrm{riv}}(\boldsymbol{s}_1, \cdot)$ (red) and $\tilde{C}_1(\cdot)$, $C_{\mathrm{riv}}(\boldsymbol{s}_2, \cdot)$ (blue) for two reference locations $\boldsymbol{s}_1$ and $\boldsymbol{s}_2$ located downstream (at $2320\,\mathrm{km}$ from the river mouth) and upstream (at $2340\,\mathrm{km}$) of the confluence of Nam Ngum. The plots show the respective covariance of the reference locations with locations of up to $80\,\mathrm{km}$ upstream.

where $a_{\text{euc}} > 0$ and $b_{\text{euc}} > 0$ denote the variance and range parameters, respectively. By $\|\cdot\|$, we denote the Euclidean norm.

In the following, we consider an overall spatial covariance model as a weighted sum of (10) and (11); i. e. for $s_1, s_2 \in \mathcal{S}$,

$$C_{\mathcal{S}}(s_1, s_2) = \begin{cases} \pi_{\text{riv}} C_{\text{riv}}(s_1, s_1) + \pi_{\text{euc}} C_{\text{euc}}(s_1, s_1) + n_{\mathcal{S}}, & \text{if } s_1 = s_2 \\ \pi_{\text{riv}} C_{\text{riv}}(s_1, s_2) + \pi_{\text{euc}} C_{\text{euc}}(s_1, s_2), & \text{otherwise,} \end{cases}$$
$$(13)$$

with non-negative weights π_{riv} and π_{euc}. The parameter $n_{\mathcal{S}} \geq 0$ accounts for an additional nugget effect at the origin. Model (13) is non-stationary; indeed, even the notion of stationarity is not clear, since the model is not defined on a Euclidean space (see Asadi et al, 2015, Section 3.4). Note, however, that only one of the parameters π_{riv} and a_{riv} (and likewise π_{euc} and a_{euc}) is statistically identified, since they both appear as a product in (13). Thus, we transform these parameter pairs to single parameters, which we denote again by π_{riv} and π_{euc}. Concerning the temporal covariance model $C_{\mathcal{T}}$, we use, as in Subsection 5.1, a stationary exponential model with variance, scale and nugget parameters $a_{\mathcal{T}} > 0$, $b_{\mathcal{T}} > 0$ and $n_{\mathcal{T}} \geq 0$, see (8).

As an overall spatio-temporal covariance model $C_{\mathcal{ST}}$, we use model (3), i. e.

$$C_{\mathcal{ST}}((s_1, t_1), (s_2, t_2)) = k_1 C_{\mathcal{S}}(s_1, s_2) C_{\mathcal{T}}(|t_1 - t_2|) \\ + k_2 C_{\mathcal{S}}(s_1, s_2) + k_3 C_{\mathcal{T}}(|t_1 - t_2|),$$

for $s_1, s_2 \in \mathcal{S}$, $t_1, t_2 \in \mathcal{T}$. Recall that the coefficients k_1, k_2, k_3 need to satisfy $k_1 > 0$ and $k_2, k_3 \geq 0$ for model (3) to be valid.

Fitting the full model $C_{\mathcal{ST}}$ involves estimating the 13 parameters

$$\{\pi_{\text{riv}}, \pi_{\text{euc}}, b_{\text{riv}}, b_{\text{euc}}, \alpha, a, n_{\mathcal{S}}, a_{\mathcal{T}}, b_{\mathcal{T}}, n_{\mathcal{T}}, k_1, k_2, k_3\}.$$

As opposed to Subsection 5.1, we cannot compute the empirical covariance function as done in (7), since, due to non-stationarity, the true covariance function $C((s_1, t_1), (s_2, t_2))$ does not depend only on the spatio-temporal lag $(|s_1 - s_2|_{\text{riv}}, |t_1 - t_2|)$ but on the space-time locations $(s_1, t_1), (s_2, t_2)$ themselves. However, for each pair of space-time locations (s_1, t_1) and (s_2, t_2), we only have at most one observation to base the estimation on. We, therefore, subdivide the observed temporal domain into K smaller groups, which can be considered approximately independent. Each time group comprises 35 subsequent days $0, \ldots, 34$; the first time group contains the first 35 days, the second group the next 35 days, and so on. Choosing 35 days

makes the temporal independence assumption more realistic, since 35 days is the return time of the Envisat satellite. Additionally, water needs up to four weeks to flow through our study area according to our flow-velocity estimation (cf. Subsection 5.1). In this way, we obtain for each observed pair of space-time locations $(s_1, t_1), (s_2, t_2)$, where t_1 and t_2 each correspond to one (possibly the same) of the 35 days, several associated realizations of $Z(s_1, t_1)$ and $Z(s_2, t_2)$ (roughly one per time group, exceptions are due to missing values). We enumerate the pairs as

$$\{(s_1, t_1)^{(1)}, (s_2, t_2)^{(1)}; \ldots; (s_1, t_1)^{(K)}, (s_2, t_2)^{(K)}\}$$

and compute the empirical covariance as

$$\widehat{C}((s_1, t_1), (s_2, t_2)) = \frac{1}{K} \sum_{j=1}^{K} Z((s_1, t_1)^{(j)}) Z((s_2, t_2)^{(j)}).$$

Model $C_{\mathcal{ST}}$ is then fitted using least squares estimation.

Since the number of parameters in the fully general model is large (13 parameters), we additionally perform the procedure with $k_1 = 1$ and $k_2 = k_3 = 0$, which again yields the simpler separable space-time product model

$$C_{\mathcal{ST}}(s_1, s_2, t_1, t_2) = C_{\mathcal{S}}(s_1, s_2) C_{\mathcal{T}}(|t_1 - t_2|).$$

Additionally, we find that incorporating the spatial nugget effect $n_{\mathcal{S}}$ and the anisotropy parameters α and a downgrades the model fit. Therefore, we fix their values to $n_{\mathcal{S}} = 0$, $a = 1$ and $\alpha = 0$. In this case, there are only seven parameters left for estimation, given by

$$\{\pi_{\text{riv}}, \pi_{\text{euc}}, b_{\text{riv}}, b_{\text{euc}}, a_{\mathcal{T}}, b_{\mathcal{T}}, n_{\mathcal{T}}\}.$$

Due the separability property, it is possible to compute the empirical spatial and temporal covariances separately, similarly as in Subsection 5.1. In our subsequent analyses, kriging with the full (13 parameters) and the simplified model (7 parameters) yield qualitatively comparable results. Hence, for computational reasons, we focus on the latter.

Table 2 shows the least squares parameter estimates for the simplified non-stationary spatio-temporal covariance model. Figure 8 visualizes the latter for two reference locations. Animated versions of the two figures can be found in the supplementary material. They provide an improved three dimensional impression of the content. Sometimes, jumps are visible along the y-axis, i.e. the spatial covariance function of the reference location with the other locations. The jumps appear if a location is further apart from the reference location than the previous one in terms of river length, but the hydrological location is closer to that of the reference location in terms of Euclidean distance. This shows the

Table 2: Parameter estimates of the simplified non-stationary covariance model described in Subsection 5.2 fitted to the altimetry data

π_{riv}	π_{euc}	b_{riv}	b_{euc}	$a_{\mathcal{T}}$	$b_{\mathcal{T}}$	$n_{\mathcal{T}}$
0.536	0.471	0.007	1/2145.247	1.047	5.494	1.168
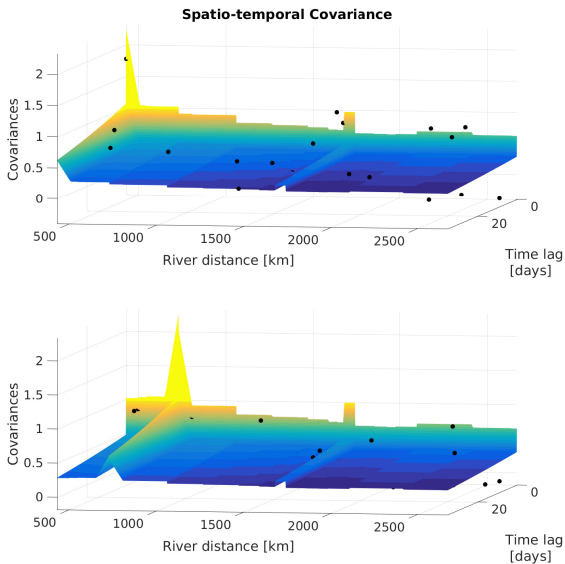
Fig. 8: Fitted non-stationary spatio-temporal covariance functions $C_{\mathcal{ST}}(\boldsymbol{s}, \cdot, 0, \cdot)$ (coloured planes) for two reference locations $\boldsymbol{s}$ in comparison with the correspondent empirical counterparts (black points). The reference locations (visible as green peaks) are 429 km (top) and 729 km (bottom).

influence of the Euclidean covariance part. Recall that by construction the fit of the spatio-temporal covariance function is based on all empirical values, whereof the black dots only constitute a subset. Hence for some fixed reference locations the fitted function seems to give a better fit than for others.

6 Results

In this section, we present the results of the spatio-temporal kriging prediction. We use the term prediction to denote interpolation, which is common with kriging. As the first step, the results based on both the stationary product covariance model described in Subsection 5.1 and the (simplified) non-stationary model explained in Subsection 5.2 are presented and compared to in situ gauging data and to each other. Afterwards, the influence of the available altimeter missions on the

results is investigated. Finally, the results are compared with a previous study on the combination of altimetry data along river networks.

6.1 Validation of the different covariance models against in situ measurements

For validation purposes and in order to verify the goodness of the estimates obtained in Section 5, we use kriging with the two aforementioned covariance models to predict time series with a temporal resolution of five days between 2002 and 2015 at the locations of four gauging stations: Luang Prabang, Nakhon Phanom, Pakse and Kratie (see Figure 1 for the locations). We then compare the predictions with the available in situ measurements. We choose to predict the time series with a five-day resolution based on data availability. In the central part of our study area, between river distance 1000 and 2300 km (see Figure 2), every two or three days, an altimeter measures the water level at some location. Although, in principle, every temporal resolution of the predicted time series is possible with our approach, any higher resolution than these two or three days is useless. Moreover, we reduce the temporal resolution to five days as a compromise, because it is also appropriate for the more upstream or downstream reaches. To predict water levels at a particular location, for the stationary product covariance model, only observations that are recorded either upstream and earlier in time or downstream and later in time are used, in order to take into account the river flow. The non-stationary model described in Subsection 5.2 does not have this limitation, since it is partly based on the Euclidean distance.

The comparison is performed through the *root-mean-square error* (RMS), the *relative RMS* (rRMS), the *coefficient of determination* R^2 and the *Nash-Sutcliff efficiency coefficient* (NSE). The RMS is a measure for the point-wise absolute difference between the predicted time series and the observed gauge time series. The rRMS relates the RMS to the mean water level variation. If the water level variations are larger, then a higher RMS can be acceptable because the variation is still depicted well. The value of R^2, which is the squared correlation coefficient between the two time series, is sensitive to the phase shift of the returning periodic signal between the two time series. The NSE measures the power or quality of the kriging predictions. It is given at a location $\boldsymbol{s} \in \mathcal{S}$ by (Nash and Sutcliffe, 1970)

$$NSE(\boldsymbol{s}) = 1 - \frac{\sum_{t=1}^{T} \left(Z_{\mathrm{g}}(\boldsymbol{s}, t) - p(\boldsymbol{s}, t) \right)^2}{\sum_{t=1}^{T} \left(Z_{\mathrm{g}}(\boldsymbol{s}, t) - \overline{Z_{\mathrm{g}}}(\boldsymbol{s}) \right)^2}. \tag{14}$$

Table 3: Comparison of the results using the different covariance models and the time series of gauging stations at four locations. The panel 'annual signal' presents the results if a mean annual signal is simply used as a predictor. The panel 'Closest VS' shows the results when the values of the closest VSs are used for the prediction; the respective missions are mentioned.

	RMS [m]	rRMS [%]	R^2	NSE
stationary product covariance Model				
Luang Prabang	1.02	11	0.91	0.90
Nakhon Phanom	0.82	10	0.94	0.94
Pakse	0.92	11	0.92	0.92
Kratie	1.29	10	0.92	0.92
Non-Stationary Covariance Model				
Luang Prabang	1.11	12	0.89	0.91
Nakhon Phanom	0.89	10	0.93	0.94
Pakse	0.88	10	0.93	0.93
Kratie	1.15	9	0.94	0.94
Annual Signal				
Luang Prabang	1.50	17	0.81	0.83
Nakhon Phanom	1.25	14	0.85	0.86
Pakse	1.20	14	0.86	0.87
Kratie	1.69	13	0.87	0.88
Closest VS				
Luang Prabang *(E+S)*	1.70	19	0.90	0.87
Nakhon Phanom *(E+S)*	0.39	4	0.96	0.98
Pakse *(J2)*	1.18	14	0.88	0.89
Kratie *(E+S)*	2.04	16	0.83	0.85

$Z_{\mathrm{g}}(\boldsymbol{s},t)$ is the height measured at time t at a gauging location $\boldsymbol{s}$ with a correspondent mean value $\overline{Z_{\mathrm{g}}}(\boldsymbol{s})$, and $p(\boldsymbol{s},t)$ is the predicted height at the same time and location. The NSE ranges from $-\infty$ to 1, where 1 is the optimal value and allocated to perfect predictions. A value of 0 indicates a prediction that is as good as just taking the observed mean value of the time series; values less than 0 indicate even worse predictions.

The results are summarised in Table 3, and the in situ and predicted time series at Luang Prabang are shown in Figure Figure 9. Plots of the time series corresponding to the remaining three stations are provided together with those shown here in the supplementary material. The hydrological profile of the Mekong River exhibits an almost uniform annual signal. Therefore, the mean annual signal is already a good approximation of the true signal. The prediction quality of the mean annual signal is shown along with the results of the kriging predictions in Table 3. The comparison of each gauge with its nearest VS is shown in the last panel of Table 3.

The stationary product covariance model applied to observations transformed with respect to flow velocity yields, at all four stations, satisfying results with RMS

values between 0.82 and 1.29 m. The coefficients of determination are similar for all stations and above 0.90; the same holds for the NSE.

The non-stationary covariance model and the stationary product covariance model provide similar predictions. The RMS lies between 0.88 and 1.15 m. Concerning the coefficient of determination R^2 (0.89–0.94) and NSE (0.91–0.94), the results are not better than those obtained with the stationary covariance model, but equally good. The two downstream stations, Pakse and Kratie, are predicted better with the non-stationary covariance model, whereas the product model performs better for the two upstream stations. In addition, the two stations near the border of our study area, Luang Prabang and Kratie, with less neighbouring data, show inferior results than the other two stations. Nevertheless, we do not have enough results to judge if these differences are random or reflect some difference in the covariance models.

When comparing the kriging results with the measurements at the closest VS, we observe that kriging yields clearly superior results, except for Nakhon Phanom. However, the VS near Nakhon Phanom is one of the best, if not the best, of the VSs used in this study, both in terms of the proximity to a gauge (ca. 15 km distance) and completeness of the time series (no missing data).

The time series of Luang Prabang, as seen in Figure Figure 9, reveals the differences in the two covariance models. For 2007, the rise of the water level is predicted too early with the non-stationary covariance model. On the other hand, the prediction with the non-stationary covariance models shows more small-term variations. It seems that kriging with the non-stationary covariance model results in less smoothing of the result than the stationary product model does. For late 2007, it seems that the correct short-term variation is predicted. However, for 2013, the variations in the low water seem rather unlikely, as in all other years, such variations are not present during low water. Unfortunately, we do not have gauge data for 2013 that could be used to validate this point.

Overall, many short-term variations cannot be detected with satellite altimetry at all. A small peak in water level can occur only locally for a short time frame. If no satellite measures this reach of the river at exactly that time, we cannot gain any information about the variation. Moreover, even if one altimeter measures such a small peak, the kriging tends to even it out, especially with the stationary product covariance model. On the other hand, the kriging method is also robust against outliers in the data and evens them out up to a certain degree.
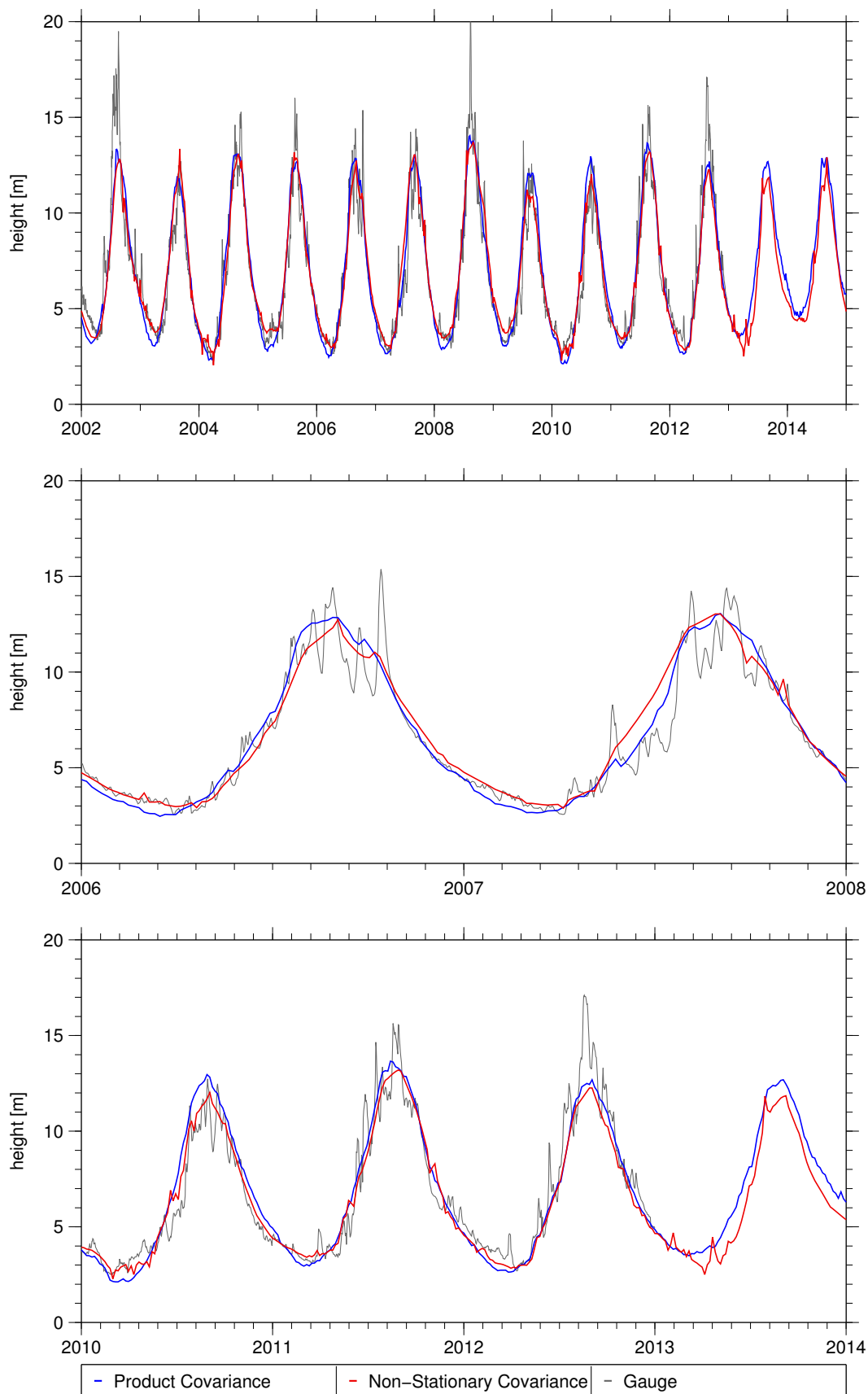
Fig. 9: Comparison of the gauge measurements and the predicted five-day time series at the station of Luang Prabang based on the stationary product and the non-stationary covariance model. The two lower panels are enlargements of the upper panels for the years 2006 until 2008 and 2010 until 2013, respectively. The time series is height-referenced to the gauge data.

6.2 Influence of the altimeter data availability

Between 2011 and 2013, there is a gap in the data due to the end of the Envisat mission. In this time span, only three Jason-2 and (at least partly) a few Envisat EM data points are available (see Figure 2). The Envisat observations are the backbone of our model. For this reason, we are particularly interested in how well the kriging method can handle the change in data availability between the end of 2010 and the beginning of 2013. In the time series in Figure Figure 9, no deterioration during these years is visible. For this reason, we examine the RMS values over the time.

Using kriging, we predict time series of water levels at a 5-day resolution at all available gauging stations in the observation area. To compare the predicted with the observed time series and detect possible changes in the quality of the predictions, we compute the RMS in yearly moving windows. The results are shown in Figure Figure 10 (colour coding is according to their location along the river). The RMS value is chosen for this comparison because, among the analysed coefficients, it shows the largest differences in Table 3. To obtain a clear overview, we present this investigation solely for the stationary product covariance model; the findings are similar for the non-stationary covariance model. The mission lifetimes are indicated at the top of Figure Figure 10. We cannot quantify the influence of the SARAL data, as the gauge time series are only available until the end of 2012.

It is not possible to find any correspondence between the data availability and the variation in the RMS over time. In particular, the RMS does not improve with the start of the Jason-2 mission in 2008, and does not deteriorate in 2012 with the end of Envisat EM. The only pattern visible is the overall smaller RMS in the years 2006 and 2007. We do not have any explanation for this pattern. Still gauging stations at closer distance tend to show more similarity in the RMS over time than those further apart.

6.3 Comparison to other published results

To our knowledge, the only other study combining altimetry data over rivers, so far, has been published by Tourian et al (2016). They conducted their study along the Po, Mississippi, Congo and Danube rivers with a focus on the Po River in Northern Italy. Data from the satellite altimetry missions of Topex/Poseidon, the Topex/Poseidon extended mission, Jason-2, Envisat, the Envisat extended mission, SARAL and Cryosat-2
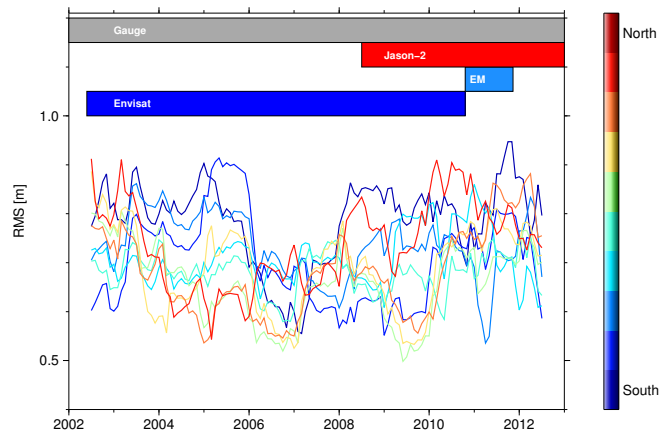

Fig. 10: Moving yearly RMS values at all gauging stations along the Mekong River. The colour indicates the location along the river. Thus, VSs close in space have similar colours.

were used. Their method was based on estimating the flow time between the different VSs with which the stations could be linked.

Despite the differences between the Mekong and the Po River systems, their results can be compared to ours under some limitations. The main limitation is that the annual signal of the Po River is not as strong and regular as that of the Mekong River, which suggests that our prediction is more accurate. Comparing the NSE, in our results, the value is never below 0.89 and ranges up to 0.94, whereas, in the Po River study, this value ranged between 0.2 and 0.6. In addition, there was a larger variance between the different gauging stations than that in our study.

In the Po River study, there were three possible merging processes for the altimetry data: all measurements were treated equally, disregarding the distance between the measurement locations and the predicted location; a three-point moving average with weighting according to their errors; and a three-point moving average with weighting according to the distance between measurement and prediction location. In our study, the observations are weighted according to their distance in space and time from the location to be predicted, which might explain the differences in the results.

7 Conclusion

In this study, we demonstrate the potential of spatio-temporal kriging, together with appropriate covariance modelling, to combine measurements of multi-mission altimetry along rivers over space and time. The essential part of the presented approach is the modelling

of the spatial and temporal dependencies in the data with appropriate covariance models for predicting the river flow. Two covariance models are tested: a simple stationary spatio-temporal stationary product covariance model based on the river distance between locations, but applied to observations transformed with respect to flow velocity, and a non-stationary model, which is designed for river networks and additionally incorporates the Euclidean distance between the centres of the sub-catchments of the locations. These two covariance models are used in the kriging approach to obtain multi-mission time series with a temporal resolution of 5 days. These time series are validated against in situ gauge data. Both models perform equally well, with RMS values between 0.82 and 1.29 m and coefficients of determination above 0.89.

A main advantage of the kriging approach for combining multi-mission altimetry over rivers is its flexibility in both temporal and spatial resolutions. The method can theoretically predict a time series of any given temporal resolution at any point along the river. However, a meaningful result cannot be expected if the temporal resolution of the prediction is higher than that of the altimetry data. Considering measurements and the possibly larger distance between two altimeter measurements closest in time, the temporal resolution should be even lower than the resolution of the altimetry data.

Although the non-stationary model does not yield better results, in this case study along the Mekong River, its advantage is its flexibility to approach more complex river systems and to include measurements along tributaries in the river system. However, this requires further investigation for the Mekong River system. The downside of the non-stationary model is its complexity and the need for additional data such as sub-catchment information. Therefore, the simple stationary product covariance model is sufficient for the rather non-complex main stream of the Mekong River if a spatial transformation according to the flow velocity is used. This transformation is not needed for the non-stationary model, which is again one of its advantages.

We show in this study that using the kriging method, it is not only possible to combine data from different altimeter measurements, but we are also able to bridge data gaps where only a few measurements are available. Particularly, the time between the end of the Envisat mission and the start of the SARAL mission with only three Jason-2 time series was bridged without any apparent decline in the quality of the predictions.

The next steps of this study involve incorporating the data of the long-repeat mission Cryosat-2 (launched 2010), which will densify the observations, especially in the gap between the Envisat and SARAL missions, as well as improve the temporal resolution of the available data. Additionally, the data of the newly launched missions Jason-3 and Sentinel-3 will be incorporated. Furthermore, data along the tributaries of the Mekong River will be included. We will use real-time processed altimetry data with the kriging method to do short-term predictions into the future. The transferability of the multi-mission approach introduced in this study to other river networks will be tested in a future work as well.

References

Adamson PT, Rutherfurd ID, Peel MC, Conlan IA (2009) The Hydrology of the Mekong River. In: The Mekong, Mekong River Commission, pp 53–76, DOI 10.1016/B978-0-12-374026-7.00004-8

Asadi P, Davison AC, Engelke S (2015) Extremes on river networks. The Annals of Applied Statistics 9:1–24

Berry PAM (2006) Two decades of inland water monitoring using satellite radar altimetry. In: Proceedings of the Symposium on 15 Years of Progress in Radar Altimetry, vol 8

Berry PAM, Bracke H, Jasper A (1997) Retracking ERS-1 altimeter waveforms over land for topographic height determination: an expert systems approach. ESA SP 1:403–408

Birkett CM (1995) The contribution of TOPEX/POSEIDON to the global monitoring of climatically sensitive lakes. Journal of Geophysical Research: Oceans (1978–2012) 100(C12):25,179–25,204, DOI 10.1029/95JC02125

Birkett CM (1998) Contribution of the TOPEX NASA radar altimeter to the global monitoring of large rivers and wetlands. Water Resources Research 34(5):1223–1239, DOI 10.1029/98WR00124

Birkett CM, Reynolds C, Beckley B, Doorn B (2011) From research to operations: the USDA global reservoir and lake monitor. In: Coastal altimetry, Springer, pp 19–50, DOI 10.1007/978-3-642-12796-0

Boergens E, Dettmering D, Schwatke C, Seitz F (2016) Treating the Hooking Effect in satellite altimetry data: A case study along the Mekong River and its tributaries. Remote Sensing pp 1–22, DOI 10.3390/rs8020091

Brockwell PJ, Davis RA (1997) Introduction to time series and forecasting. Springer

Calmant S, Seyler F, Cretaux JF (2008) Monitoring continental surface waters by satellite altimetry. Surveys in geophysics 29(4-5):247–269, DOI 10.1007/s10712-008-9051-1

Cressie NAC (1993) Statistics for spatial data. New York : J. Wiley,

Cressie NAC, Wikle CK (2011) Statistics for Spatio-Temporal Data. New York : J. Wiley,

Crétaux JF, Jelinski W, Calmant S, Kouraev A, Vuglinski V, Bergé-Nguyen M, Gennero MC, Nino F, Del Rio RA, Cazenave A (2011) SOLS: A lake database to monitor in the Near Real Time water level and storage variations from remote sensing data. Advances in space research 47(9):1497–1507, DOI 10.1016/j.asr.2011.01.004

De Cesare L, Myers DE, Posa D (2001) Estimating and modeling space-time correlation structures. Statistics and Probability Letters 51(1):9–14, DOI 10.1016/S0167-7152(00)00131-0

De Iaco S, Myers DE, Posa D (2001) Space-time analysis using a general product-sum model. Statistics and Probability Letters 52(1):21–28, DOI 10.1016/S0167-7152(00)00200-5

De Iaco S, Myers DE, Posa D (2011) On strict positive definiteness of product and product-sum covariance models. Journal of Statistical Planning and Inference 141(3):1132–1140, DOI 10.1016/j.jspi.2010.09.014

De Marsily G (1986) Quantitative hydrogeology. Tech. rep., Paris School of Mines, Fontainebleau

De Oliveira Campos I, Mercier F, Maheu C, Cochonneau G, Kosuth P, Blitzkow D, Cazenave A (2001) Temporal variations of river basin waters from Topex/[Poseidon satellite altimetry. Application to the Amazon basin. Comptes Rendus de l'Académie des Sciences-Series IIA-Earth and Planetary Science 333(10):633–643, DOI 10.1016/S1251-8050(01)01688-3

Gräler B, Gerharz L, Pebesma E (2012) Spatio-temporal analysis and interpolation of PM10 measurements in Europe. ETC/ACM Technical Paper 2011/10 1(November 2011):37

GRDC (2013) Long-term mean monthly discharges and annual characteristics of GRDC stations. Tech. rep., Federal Institute of Hydrology, Global Runoff Data Center

Gupta A, Liew SC (2007) The Mekong from satellite imagery: a quick look at a large river. Geomorphology 85(3):259–274

Heuvelink GBM, Musters P, Pebesma EJ, Others (1997) Spatio-temporal kriging of soil water content. Geostatistics Wollongong 96:1020–1030

Jirka GH (2007) Einführung in die Hydromechanik

Koch KR (1999) Parameter estimation and hypothesis testing in linear models. Springer Science & Business Media

Krige DG (1952) A statistical analysis of some of the borehole values in the Orange Free State goldfield. Journal of the Chemical, Metallurgical and Mining Society of South Africa 53:47–70

Lehner B, Verdin K, Jarvis A (2006) HydroSHEDS technical documentation, version 1.0. World Wildlife Fund US, Washington, DC pp 1–27

Maillard P, Bercher N, Calmant S (2015) New processing approaches on the retrieval of water levels in ENVISAT and SARAL radar altimetry over rivers: A case study of the São Francisco River, Brazil. Remote Sensing of Environment 156:226–241, DOI 10.1016/j.rse.2014.09.027

Michailovsky CI, Milzow C, Bauer-Gottwein P (2013) Assimilation of radar altimetry to a routing model of the Brahmaputra River. Water Resources Research 49(8):4807–4816, DOI 10.1002/wrcr.20345, arXiv:1011.1669v3

MRC (ed) (2005) Overview of the Hydrology of the Mekong Basin. Mekong River Commission

Nash JE, Sutcliffe JV (1970) River flow forecasting through conceptual models part I - A discussion of principles. Journal of Hydrology 10(3):282–290, DOI 10.1016/0022-1694(70)90255-6

Nielsen K, Stenseng L, Andersen OB, Villadsen H (2015) Validation of CryoSat-2 SAR mode based lake levels. Remote Sensing of Environment 171:162–170, DOI 10.1016/j.rse.2015.10.023

Rouhani S, Myers DE (1990) Problems in space-time kriging of geohydrological data. Mathematical Geology 22(5):611–623, DOI 10.1007/BF00890508

Schneider U, Becker A, Finger P, Meyer-Christoffer A, Rudolf B, Ziese M (2011) GPCC full data reanalysis version 6.0 at 0.5: monthly land-surface precipitation from rain-gauges built on GTS-based and historic data. doi: 10.5676/DWD_GPCC. FD_M_V6_050

Schwatke C, Dettmering D, Börgens E, Bosch W (2015a) Potential of SARAL/AltiKa for Inland Water Applications. Marine Geodesy (38):0, DOI 10. 1080/01490419.2015.1008710

Schwatke C, Dettmering D, Bosch W, Seitz F (2015b) DAHITI – an innovative approach for estimating water level time series over inland waters using multimission satellite altimetry. Hydrol Earth Syst Sci 19:4345–4364

Skøien JO, Blöschl G (2007) Spatiotemporal topological kriging of runoff time series. Water Resources Research 43(9), DOI 10.1029/2006WR005760

Snepvangers JJJC, Heuvelink GBM, Huisman Ja, a Huisman J (2003) Soil water content interpolation using spatio-temporal kriging with external drift. Geoderma 112(3-4):253–271, DOI 10.1016/S0016-7061(02)00310-5

Tourian MJ, Tarpanelli A, Elmi O, Qin T, Brocca L, Moramarco T, Sneeuw N (2016) Spatiotemporal densification of river water level time series by multimission satellite altimetry. Water Resources Research

Ver Hoef JM, Peterson EE (2010) A Moving Average Approach for Spatial Statistical Models of Stream Networks. Journal of the American Statistical Association 105(489):6–18, DOI 10.1198/jasa.2009.ap08248

Ver Hoef JM, Peterson E, Theobald D (2006) Spatial statistical models that use flow and stream distance. Environmental and Ecological Statistics 13(4):449–464, DOI 10.1007/s10651-006-0022-8

Villadsen H, Andersen OB, Stenseng L, Nielsen K, Knudsen P (2015) CryoSat-2 altimetry for river level monitoring — Evaluation in the Ganges–Brahmaputra River basin. Remote Sensing of Environment 168:80–89, DOI 10.1016/j.rse.2015.05.025

Yoon Y, Durand M, Merry CJ, Rodriguez E (2013) Improving temporal coverage of the SWOT mission using spatiotemporal kriging. IEEE Journal of Selected Topics in Applied Earth Observations and Remote Sensing 6(3):1719–1729, DOI 10.1109/JSTARS.2013. 2257697

P-3: River Levels Derived with CryoSat-2 SAR Data Classification - A Case Study in the Mekong River Basin

E. Boergens, K. Nielsen, O. B. Andersen, D. Dettmering, and F. Seitz (2017b): **River Levels Derived with CryoSat-2 SAR Data Classification—A Case Study in the Mekong River Basin**. In: *Remote Sensing* 9.12, pp. 1–21

Copyright

Summary of content

This work focused on the use of CryoSat-2 *S*ynthetic *A*perture *R*adar (SAR) altimetry over rivers. Cryosat-2, which was launched in 2010, is the first altimeter satellite carrying a SAR altimeter which has a smaller along-track footprint and thus an increased along-track resolution. Especially for smaller rivers, this improves the accuracies of water level observations. However, even with this higher resolution and better accuracies a main challenge of inland altimetry remains: the identification of water and land measurements. The conventional approach by using land-water-masks fails for many small rivers due to the inaccuracies of these masks. This study introduced a classification approach for water identification in CryoSat-2 SAR data over the Mekong River Basin.

The classification was conducted with the unsupervised k-means clustering algorithm based on features derived from the multi-look SAR and the *R*ange *I*ntegrated *P*ower (RIP) waveform. The latter is only available for SAR altimetry and provides further inside to the reflectivity properties of the surface. The used features of the classification are summarised in **??**:

Table A.2: Features used for the classification

RIP features	Waveform features
Peakiness: p_{RIP}	p_{wf}
Standard deviation: std_{RIP}	Maximum power: max_{wf}
Width: w	Relative position of leading edge
Off-centre: off	
Symmetry: s	

Due to the divers topography in the Mekong Basin it was found to improved the classification results by dividing the basin in three regions according to their topography. In each region the k-means algorithm clustered the data points in 20 classes. In the downstream region the classification failed due to surrounding seasonal wetland of the river.

In the upstream and middle region three and six classes were identified as water classes respectively. The classification was able to identify rivers with a width as small as 20 m in the upstream region. Following to the classification, the water level of the river was estimated from the water observations. The derived water levels were validated with regard to the stable annual signal and compared to *Envi*ronmental *Sat*ellite (Envisat) water levels and CryoSat-2 water levels derived with a land-water-mask. This showed that the classification approach provides improved water levels. Especially in the upstream region the classification resulted in better and more water level observations than the land-water-mask.

Declaration of contribution

The content of this study was developed during a stay abroad of Eva Börgens at the Danish Technical University (DTU) with Karina Nielsen and Ole B. Andersen. The classification ideas were developed by Eva Börgens with the help of Karina Nielsen. The realisation of the classification and water level estimation together with their validation was done by Eva Börgens as well as the figure compilation. Denise Dettmering and Ole B. Andersen contributed to the discussion of the results. The majority of the manuscript was written by Eva Börgens with all co-authors contributing with comments and corrections. The overall own contribution of Eva Börgens is estimated to be **92%**.

Article

River Levels Derived with CryoSat-2 SAR Data Classification—A Case Study in the Mekong River Basin

Eva Boergens [1,*] [ID]**, Karina Nielsen** [2] [ID]**, Ole Baltazar Andersen** [2]**, Denise Dettmering** [1] [ID] **and Florian Seitz** [1] [ID]

[1] Deutsches Geodätisches Forschungsinstitut der Technischen Universität München (DGFI-TUM), Arcisstraße 21, 80333 Munich, Germany; denise.dettmering@tum.de (D.D.); florian.seitz@tum.de (F.S.)
[2] Division of Geodesy, DTU Space, National Space Institute, DK-2800 Kongens Lyngby, Denmark; karni@space.dtu.dk (K.N.); oa@space.dtu.dk (O.B.A.)
[*] Correspondence: eva.boergens@tum.de; Tel.: +49-89-23031-1263

Abstract: In this study we use CryoSat-2 SAR (delay-Doppler synthetic-aperture radar) data in the Mekong River Basin to estimate water levels. Compared to classical pulse limited radar altimetry, medium- and small-sized inland waters can be observed with CryoSat-2 SAR data with a higher accuracy due to the smaller along track footprint. However, even with this SAR data the estimation of water levels over a medium-sized river (width less than 500 m) is still challenging with only very few consecutive observations over the water. The target identification with land–water masks tends to fail as the river becomes smaller. Therefore, we developed a classification approach to divide the observations into water and land returns based solely on the data. The classification is done with an unsupervised classification algorithm, and it is based on features derived from the SAR and range-integrated power (RIP) waveforms. After the classification, classes representing water and land are identified. Better results are obtained when the Mekong River Basin is divided into different geographical regions: upstream, middle stream, and downstream. The measurements classified as water are used in a next step to estimate water levels for each crossing over a river in the Mekong River network. The resulting water levels are validated and compared to gauge data, Envisat data, and CryoSat-2 water levels derived with a land–water mask. The CryoSat-2 water levels derived with the classification lead to more valid observations with fewer outliers in the upstream region than with a land–water mask (1700 with 2% outliers vs. 1500 with 7% outliers). The median of the annual differences that is used in the validation is in all test regions smaller for the CryoSat-2 classification results than for Envisat or CryoSat-2 land–water mask results (for the entire study area: 0.76 m vs. 0.96 m vs. 0.83 m, respectively). Overall, in the upstream region with small- and medium-sized rivers the classification approach is more effective for deriving reliable water level observations than in the middle stream region with wider rivers.

Keywords: satellite altimetry; inland water; CryosSat-2 SAR; Mekong Basin; water level time series; classification; stack data

1. Introduction

River waters are crucial as suppliers of water for irrigation and fresh water for drinking. However, river floods can destroy crops, settlements, and infrastructure. For this reason, it is essential to monitor the water level of river systems. However, an increasing number of in situ gauges have been derelicted since the 1980s [1], or the data is not publicly available. Therefore, it is more and more important to close this data gap with satellite altimetry.

In recent years many studies have been published that apply satellite pulse-limited altimetry over rivers of various sizes (e.g., [2–7]). CryoSat-2, launched in 2010, is the first satellite carrying a delay-Doppler altimeter [8] that operates in three measuring modes: the classical pulse-limited low resolution (LR) mode, the delay-Doppler synthetic-aperture radar (SAR) mode, and the SAR interferometric (SARin) mode.

Compared to conventional radar altimeters, delay-Doppler SAR measurements have a higher along-track resolution and a smaller footprint. This improves the observation of water levels of inland water bodies like lakes (e.g., [9–11]) or rivers (e.g., [12,13]). The advantage of SAR altimetry observations is that they are especially effective for measuring smaller inland waters like rivers. However, CryoSat-2 has a long repeat time of 369 days compared to 35 days for Envisat and SARAL, and 10 days for Topex/Poseidon, Jason-1, Jason-2, and Jason-3. This restricts the estimation of water level time series over lakes and even more over rivers. The advantage of the long repeat time is the very dense spatial distribution of observations. This spatial distribution enables better river monitoring in the continuous progression. Unlike lakes, rivers can change their water levels rapidly over their course which makes a denser spatial distribution of observations desirable.

To derive water levels from lakes or rivers it is necessary to identify the water returns of the altimeter. A land–water mask can be used for this purpose, like the mask provided by the World Wildlife Fund (https://www.worldwildlife.org/pages/global-lakes-and-wetlands-database). Such a mask is constant over time; therefore, it neither accounts for the seasonal variations of the water extent nor inter-annually shifting river and lake banks. Extracting dynamic land–water masks from optical remote sensing images is difficult in the tropics, which includes the study area of the Mekong Basin, since cloud-free optical data is only available during the dry season with low water level. Moreover, SAR images with sufficient spatial resolution are only available from the launch of Sentinel-1 in 2014. Although a high accuracy land–water mask is provided by the Mekong River Commission (http://portal.mrcmekong.org/map_service) for the study area with an accuracy of 30 m, this accuracy might not be sufficient for medium- and small-sized rivers. Additionally, the mask has no seasonal variations included.

Within this study, an innovative classification approach for SAR altimetry data is developed and validated, which is independent of the accuracy and availability of land–water masks. With this approach, reliable river levels, even for small and medium-sized rivers, are derived. Compared to classical approaches based on land–water masks, the number of valid measurements is increased and the water level precision is improved.

For the classical pulse-limited altimeter data, classification has been done successfully for the last decade worldwide (e.g., [14,15]). Even very small water areas in wetlands have been classified successfully with Envisat data by [16].

In these classifications, the shape of the waveform is used to discriminate between different reflecting surfaces. Also, CryoSat-2 SAR data has been classified based on the SAR waveform for lakes [11], lakes and rivers [17], or ice [18]. This study takes a step further and uses not only the waveform but also the range-integrated power (RIP) for a classification of the altimeter measurements in water and non-water returns over the Mekong River Basin in Southeast Asia. The RIP is only available for delay-Doppler SAR altimetry and gives additional insight to the reflective surface that the waveform alone could not provide [19].

The unsupervised *k-means* algorithm is employed for the classification [20] as not enough reliable training data is available for a supervised classification. The *k-means* algorithm is a widely used unsupervised clustering algorithm and has been used for altimetry classification before (e.g., [11]).

This paper is structured as follows: First, an introduction is given about the study area of the Mekong River Basin in Section 2, afterwards more information of the CryoSat-2 SAR data is given in Section 3. The classification and the used features are described in Section 4.1 followed by an explanation of the water level estimation in Section 4.2. The results and validations are presented in Section 5. These results are discussed in Section 6 and an outlook is given. The paper ends with

the conclusions in Section 7. An overview over all relevant processing steps of this study is given in Figure 1.
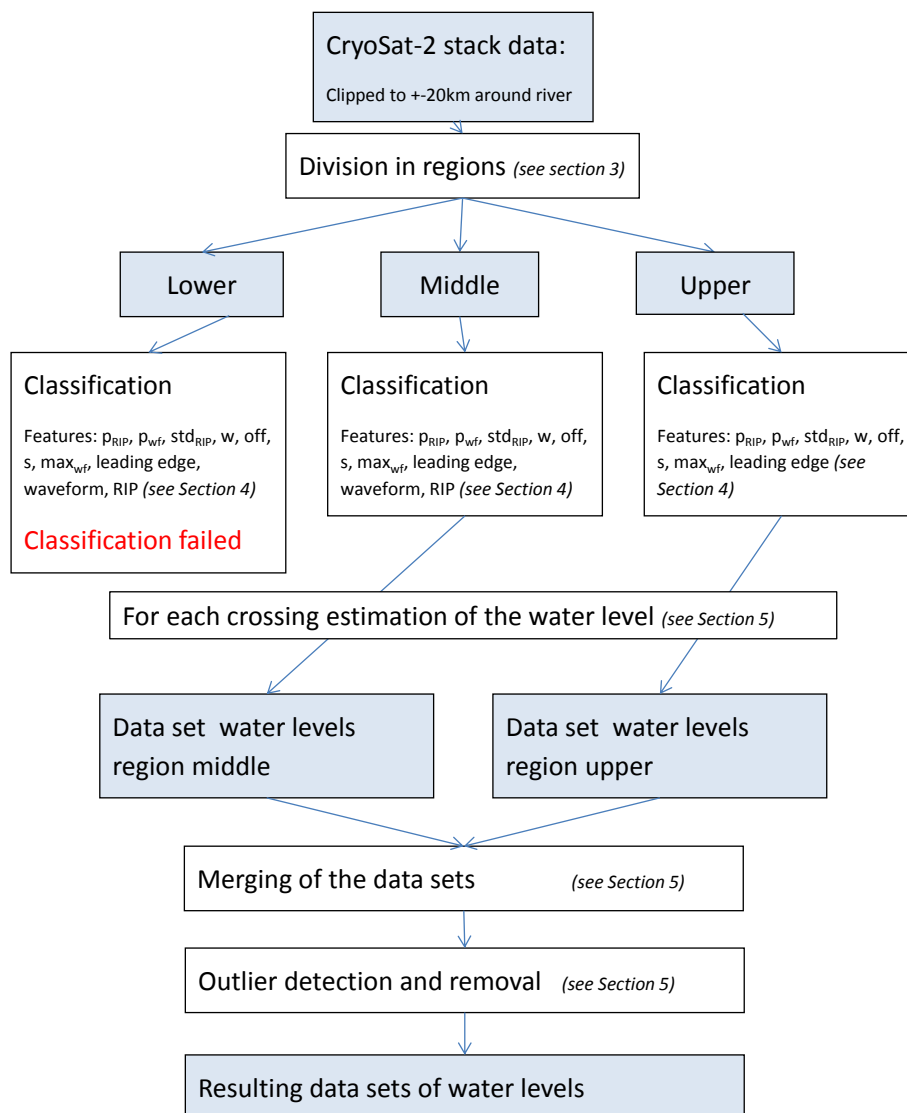

Figure 1. Processing steps used in this study for extracting water levels from the CryoSat-2 synthetic-aperture radar (SAR) data. RIP: range-integrated power.

2. Study Area

The Mekong River Basin in Southeast Asia (China, Myanmar, Thailand, Laos, Cambodia, and Vietnam) is investigated in this study, with a focus on the part of the basin south of the Chinese border. Further upstream the river gorge is too narrow for reliable altimeter observations. Downstream, the study area is limited by by the confluence with the Tonle Sap River from where the river is under a tidal influence. The tributaries, namely the large left bank side tributaries in Laos, are investigated as well. The hydrology of the Mekong Basin is primarily influenced by the precipitation on the Tibetan Plateau and the south-eastern monsoon [21].

In the Mekong River Basin the river width varies between 20 m to more than 2 km. Most of the tributaries and the upstream reach of the main river stream are less than 100- m-wide small rivers. The medium rivers, which are less than 500- m but more than 100- m-wide, are the main tributaries for

the upstream main river. In the downstream reach of the river, before it splits into the delta, the river has a width of over 2 km (see also Figure 2 for a map of the basin).

The Mekong River and its tributaries flow through different topographic regions (Figure 2). The main river upstream from Vientiane and the left bank tributaries in Laos are surrounded by mountainous areas with steep banks where the rivers have a greater slope and have a width smaller than 500 m or even less than 100 m. Downstream of Vientiane and up to the Mekong Falls the river widens and flows with less slope over the Khorat plateau. Below the Mekong Falls the river is surrounded by seasonal wetlands and widens to more than 1 km. For further processing we defined three overlapping data masks according to these regions (Figure 2). The regions are determined by the roughness of a topography model and the absolute height. Afterwards a margin around each subregion allows for an overlap.
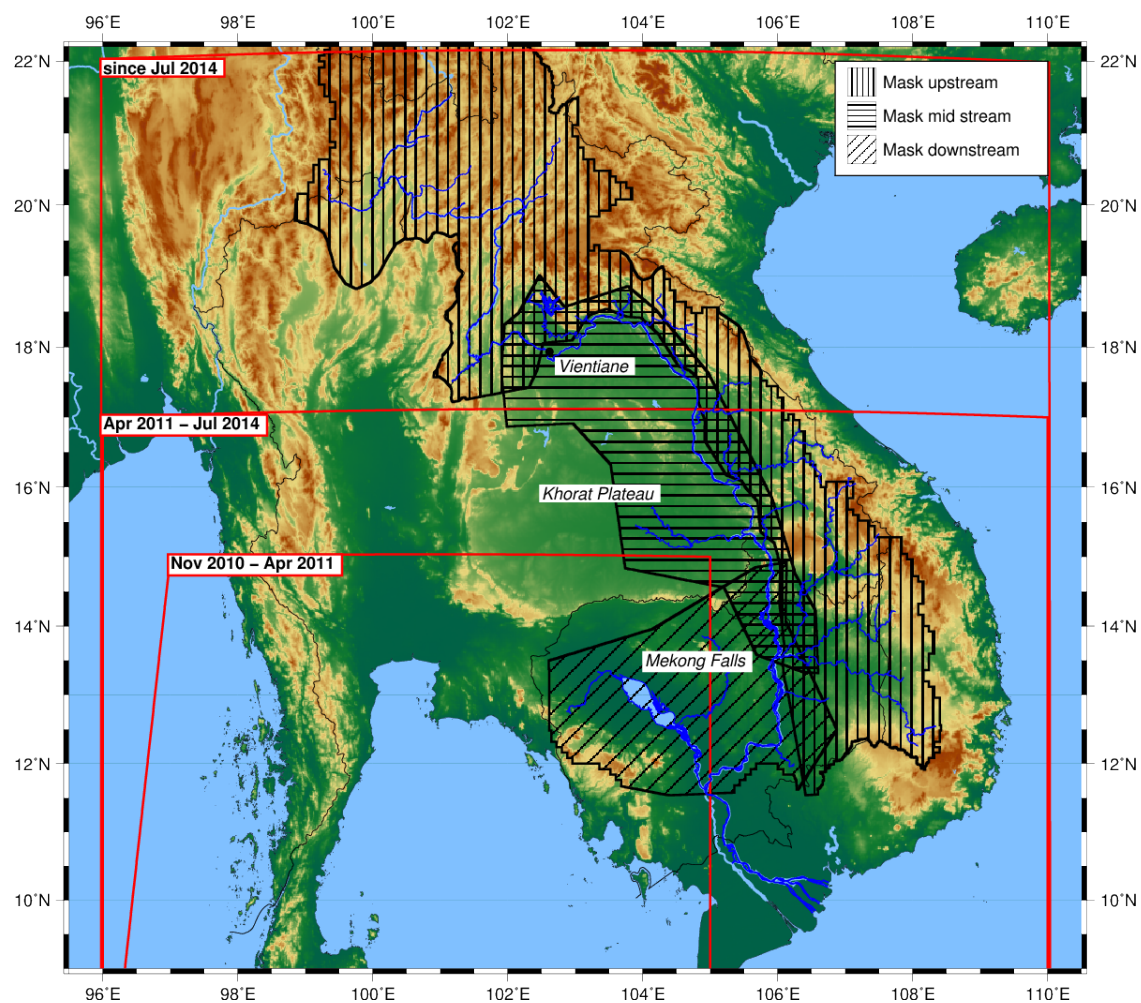

Figure 2. Map of the study area with the regional masks (black areas with different hachures) and the SAR mode mask with their validity period (red boxes).

3. Data

3.1. CryoSat-2 SAR Data

In this study we use delay-Doppler SAR altimeter data measured by CryoSat-2 between 2010 and 2016. CryoSat-2 measures in three different modes (LR, SAR, and SARIn mode), which are set in a geographical mask (https://earth.esa.int/web/guest/-/geographical-mode-mask-7107): The LRM is active mostly over the oceans and the interior of the ice sheets of Antarctica and Greenland, whereas the SAR mode measures over sea ice and other selected regions, and SARIn focuses mostly on glaciated

regions [22]. This mask has changed over the life time of the satellite. The entire study area of the Mekong River Basin has only been measured in SAR mode since July 2014 (see Figure 2 for the extent of the SAR mode mask). In SAR mode the along-track foot print size is reduced to 300 m while it remains at 14 km in the across-track direction [23].

The delay-Doppler SAR altimeter measures a point on the surface several times from different looking angles [24]. Unlike pulse limited altimetry, which is only able to measure the returning signal from the whole foot print, SAR altimetry discretizes the returning signal corresponding to 300-m-wide stripes of the footprint in along track direction. The signals from each of these stripes are recorded in the so-called single-look waveform. All single-look waveforms for the same surface area are collected in the stack matrix.

In Figure 3, two exemplary stack matrices are presented. The first (a) is measured over the Tonle Sap lake and the second (b) over a medium-sized river in the upstream region of the Mekong River. Each row is a single-look waveform. The integration of this matrix over all single-looks results in the multi-look SAR waveform (in Figure 3 with integration over each row of the stack) hereafter referred to as the waveform. The integration over the range bins results in the range-integrated power (RIP). In Figure 3 this corresponds to the integration over the columns. Detailed information on the delay-Doppler measurements is described in [8].

Here, we use the CryoSat-2 baseline C SAR Level 1b data provided by ESA GPOD SARvatore (https://gpod.eo.esa.int/) for the period 2010–2016. SARvatore is the official ESA platform for the dissemination of the CryoSat-2 level 1b SAR data. The data is processed on user request with different processing parameters. The most important data processing parameters of the data in this study are: the applied Hamming window, fft zero-padding, 20-Hz data, and stack data in the output file.
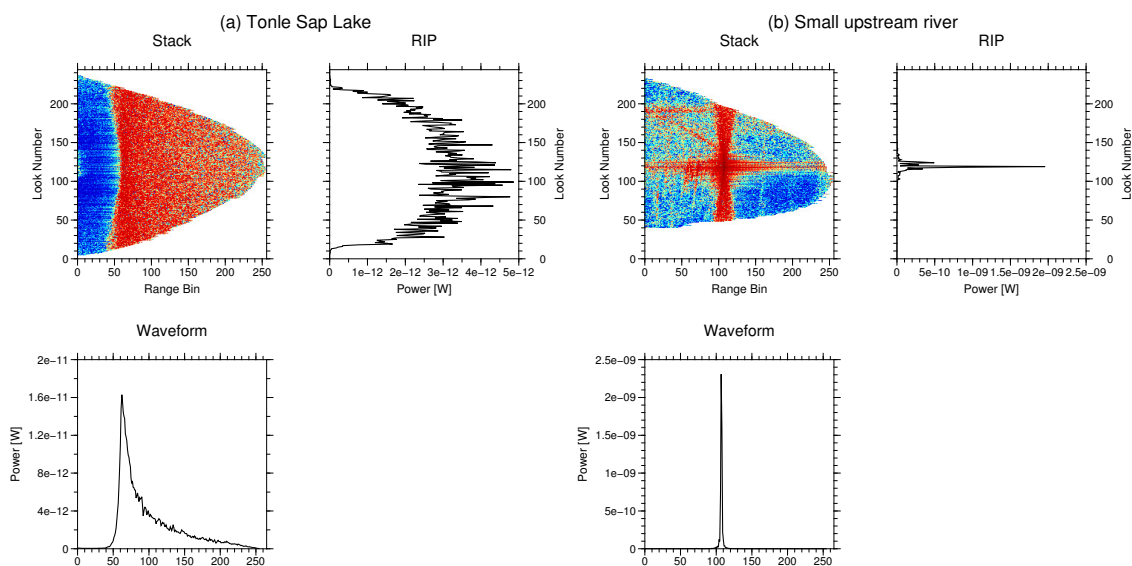

Figure 3. Two exemplary stack matrices with their RIP and waveform. The color of the stack plot indicates the power of the signal. The example on the left-hand side is measured over the Tonle Sap lake, the one on the right-hand side over a medium upstream river.

3.2. Envisat Data

Envisat water level observations are used for the validation in this study. The water levels are taken from the DAHITI database [4]. DAHITI uses a throughout outlier detection in combination with a Kalman filter approach to derive reliable water level time series for lakes and rivers. More information on the processing strategy is available in [4]. The Envisat water level time series in the Mekong Basin has a temporal resolution of 35 days, even though data gaps may occur for some cycles. For small tributaries, a correction for the Hooking effect is applied additionally in [5].

3.3. In Situ Data

For validation, in situ gauge data is used which is provided by the Mekong River Commission (http://ffw.mrcmekong.org/). The gauge data has a daily temporal resolution but the time series ends with 2012. No absolute height of the gauge is provided.

Additionally, we use a river polygon which is also provided by the Mekong River Commission (http://portal.mrcmekong.org/map_service). The polygon was derived from aerial images and topographic maps. The accuracy of the river mask is ~30 m, but no information about the seasonality of the polygon is given.

4. Methods

4.1. Classification Approach

For the medium and small rivers in our study area of the Mekong basin no reliable land–water mask is available. Thus, a classification by means of the *k-means* algorithm is performed to extract the water measurements.

The *k-means* algorithm [20] is an unsupervised method to cluster the data on the basis of different features. For the land–water classification a set of features derived from the CryoSat-2 stack data over the intermediate step of the waveform and the RIP is used. The features are summarized in Table 1. The features derived from the waveform are the *maximum power*, the *peakiness*, and the *position of the leading edge*. It is well known that waveforms of water reflections have a higher power than those of land reflections. Medium, and to a greater degree small, water bodies have smooth mirror-like surfaces which can only be measured by signals emitted close to nadir. This leads to a very peaky waveform and RIP with a high power. Following [25] the peakiness p_wf is calculated with

$$p_\mathrm{wf} = \frac{\max(\mathrm{wf}_i)}{\sum\limits_i \mathrm{wf}_i}, \tag{1}$$

where wf is the waveform and wf_i the power of the *i*th bin.

Table 1. Features used for the classification.

RIP Features	Waveform Features
Peakiness: p_RIP	p_wf
Standard deviation: std_RIP	Maximum power: max_wf
Width: w	Relative position of leading edge
Off-center: off	
Symmetry: s	

To estimate the relative *position of the leading edge* in the waveform, the waveform is retracked using an improved threshold retracker with a threshold of 50% on the best sub-waveform [26]. The on-board tracking system always tries to hold the leading edge of the main reflection at the nominal tracking point. This is not always possible and leads to a deviation of the leading edge from the nominal tracking point. Over wider rivers the tracking system can manage to keep the leading edge close to the tracking point. In Figure 4 (left panel), one exemplary waveform with its features *maximum power* and *position of the leading edge* is shown (the *peakiness* cannot be displayed).

Features based on the RIP are the *peakiness* p_RIP, the *standard deviation* std_RIP, the *width*, the *off-center*, and the *symmetry*. Water reflections over large water bodies result in a overall smoother RIP than water

reflections over small water bodies that in turn have a smoother RIP than land reflections(see Figure 3). This smoothness is measured with a standard deviation feature std_{RIP}. The std_{RIP} is then

$$std_{\text{RIP}} = \sqrt{\frac{1}{N}\sum_i (\text{RIP}_i - mean(\text{RIP}))^2}, \tag{2}$$

where RIP_i is the ith entry of the RIP and N the number of looks in the RIP, usually 246.
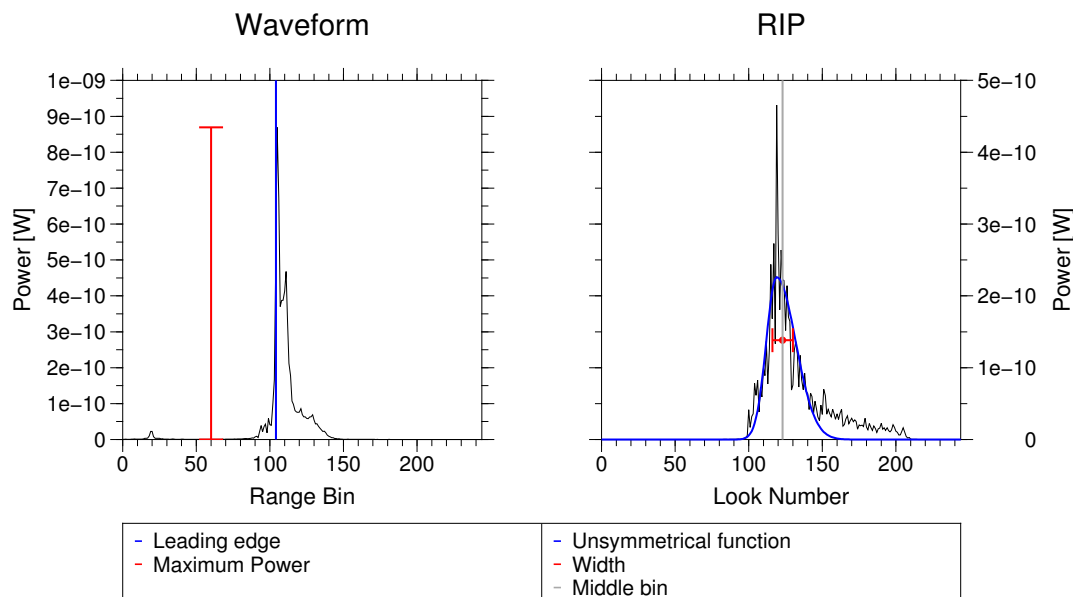
Figure 4. One example of a waveform and the corresponding RIP with some of their derived features.

As mentioned before, small and medium inland waters with a smooth surface only reflect the signal back to the satellite at near nadir. Therefore, the RIP is both very peaky and narrow. The width w is derived with:

$$w = \frac{\left(\sum_i \text{RIP}_i^2\right)^2}{\sum_i \text{RIP}_i^4}. \tag{3}$$

The off-center feature off describes the deviation of the main reflection from the nadir point. It should be close to zero for measurements of water, whereas land measurements are more disturbed and often show the maximum return in the side lobes. We measure the off-center feature off as the difference between the middle look of the RIP and the mean point of the RIP which is calculated with:

$$off = \frac{246}{2} - \frac{\sum_i i\text{RIP}_i^2}{\sum_i \text{RIP}_i^2}. \tag{4}$$

A positive off value indicates that the majority of the returning power was detected before the satellite passed the nadir position, a negative value vice versa.

The last feature is a measure of the symmetry of the RIP s. For an ideal smooth water reflection, like a small lake, the RIP should be perfectly symmetrical. However, for a sloped target, such as a river, the reflection depends on the relative orientation between the satellite and the water surface. The reflection is stronger when the satellite looks on a water surface that is sloped towards it. A positive s indicates

a water surface sloped towards the approaching satellite. This effect leads to an unsymmetrical RIP. To quantify this, an unsymmetrical exponential function $\overline{\text{RIP}}$ is fitted to the RIP with

$$\overline{\text{RIP}}_i = \begin{cases} a \exp\left(\frac{(i-b)^2}{2c_1^2} \right), & \text{if } i < b \\ a \exp\left(-\frac{(i-b)^2}{2c_2^2} \right), & \text{if } i \geq b. \end{cases} \tag{5}$$

Here, a is the amplitude of the exponential function, b the look where the function reaches its maximum, and c_1 and c_2 are the two decay parameters. The *symmetry* feature is then

$$s = c_1 - c_2. \tag{6}$$

Figure 4 (right-hand side), displays an RIP with the feature w marked. The off-center feature off is too small to be visible in this example, but the symmetry, or the lack thereof, is clearly showing.

Additional to these eight features, both the whole waveform and the whole RIP are used as features. Each bin is then considered as a single feature. The waveform needs to be shifted so that the leading edge is positioned on the nominal tracking point. We found that including waveform and RIP as features only improves the results for the middle region and does not change them in the upstream regions. Therefore, the upstream region is classified without waveform and RIP as features. Since the features span different orders of magnitude, it is necessary to normalize the feature set. All of these features were chosen according to their sensitivity for the posed problem of water classification in the Mekong River Basin and independently from each other. More features were tested but discarded because they were either not sensitive for the classification or highly correlated to one of the used features.

The *k-means* algorithm is used to cluster the data on the basis of the above features in 20 classes. An unsupervised clustering algorithm is applied because no reliable training data is available. The *k-means* algorithm assumes normally distributed features with equal variance, which we ensured and tested by the normalization of the features.

The number of classes depends on the application and variation in the input features. An estimate for the number of classes can be done with knowledge of the classified data. In our study case, a look at the spatial distribution of the features tells us that only two classes, land and water, are not sufficient as altimeter measurements of land can be very diverse (this holds also for water measurements, but they are less diverse than land). The diversity of the returning waveform and RIP can be explained by the reflective properties of e.g., land, water, vegetation. With this it can be concluded that at least 10 classes are needed. We tested the classification and validated resulting water levels for several numbers of classes (10, 15, 20, 30) and found similar results for all with the results of 20 classes slightly superior.

Each of the clusters is defined by their centroid which are the mean features of all points in this cluster. New data is classified by grouping it to the closest centroid. Here, the clustering is done on one randomly drawn third of the data. The residual two-thirds of the data are then classified into the cluster classes. The clustering is not done on the whole data set due to computational efficiency. The repeatability of the clustering and classification will be validated in Section 5. After the classification, it is determined which classes represent water and land returns. This was done by visual inspection of the mean waveform and RIP for each class and the locations of the observations in each class related to the approximate location of the river known from the land–water mask (see Section 3).

As described in Section 2 the Mekong Basin is divided into different regions: upstream, middle, and downstream. We classify each of the regions separately as they are too diverse in the reflectivity properties of the water bodies to be classified together. Additionally, the classification is done only on altimeter data not further away than 20 km from the river polygon due to computational efficiency (the polygon can be seen in Figure 2).

4.2. Water Level Estimation Approach

4.2.1. Altimetric Water Levels

The classification results in a set of measurements considered as water returns. From these measurements the water level at each crossing of the satellite track with a river in the Mekong River Basin is determined. A river polygon is employed to locate all crossings in the river basin (see Section 3). We used all measurements less than 5 km away from the river crossing that were classified as water and retracked the SAR waveforms with an improved threshold retracker with 50% threshold [26]. The retracked range is corrected for dry and wet tropospheres, ionospheres, solid Earth and pole tides, and geoid undulation. To ensure consistency for both the Envisat and CryoSat-2 data, the same corrections are used. Instead of using a median or mean over all classified measurements, we search for a horizontal line in the heights, which is assumed to represent the water surface. It is still possible that some of the water-classified measurements do not represent the river surface and need to be excluded from the water level computation (across-track of nadir effects or water bodies surrounding the river). These outliers do not necessarily have to be at the margin of the river but can also be located in the middle due to islands or sandbanks in the river. This can restrict the use of an along-track standard deviation of the heights for outlier detection.

To find the line of equal water height, a histogram of the water levels with Doane bins [27] is used. Doane bins are more suitable for small (less than 30) non-normally distributed data sets than the classical Sturge bins [28]. The Doane bin method not only uses the number of data points to estimate the number of bins and thus bin size, but the shape of the distribution is incorporated with a skewness parameter as well. The range of the data in the data set is indirectly considered in the Doane bins. If a horizontal line is present in the heights, one of the bins is distinctively larger, e.g., contains more observations, than the others and collects the heights of nearly equal water level. The median of the heights in this bin is then taken as water level. If less than five height points are classified as water, the median of the heights is taken as the water level. The advantage of this approach is that it is better suited for rivers wider than 1 km with islands and sandbanks that cause outliers in the heights. However, in many cases this histogram approach or only taking the median of all observations delivers similar results.

4.2.2. Outlier Detection

In spite of careful data selection through the classification and in the height retrieval, some of the water levels have to be considered as outliers. The height retrieval with a horizontal line only prevents outliers if more than five observations are labeled as water observations. In particular, along the small and medium-sized rivers many crossings have less than five observations. A considerable number of crossings have only one observation. The long repeat time of the CryoSat-2 satellite of 369 days complicates the detection of outliers. Unlike altimetric water levels of short repeat time missions, such as Envisat and the Jasons, we do not have a water level time series at a location which can be investigated for outliers by the estimation of and the comparison to an annual signal.

To find the CryoSat-2 outliers we make use of the said repeat time of 369 days. With the knowledge of the very stable annual signal of the Mekong River one can assume that two measurements of the same CryoSat-2 track 369 days apart should measure a similar height [21]. Based on this, a water level is considered as an outlier if the mean difference to all other heights of the same pass is larger than 7 m; the choice of threshold will be discussed below. This is only applicable if other water level measurements of the same track exist. Due to the changing mode mask (see Section 3) some regions are only measured in the last two years. To overcome this, a second outlier detection is applied which compares the water level with water levels of other tracks that are close in space and season (day of the year). To this end, we used all measurements that were less than 10 km away along the river and less than 30 days of the year apart. If the water level was different by more than 10 m from the distance weighted mean water level of all these points, it was considered as an outlier.

The thresholds for the outlier detection were chosen as a conservative upper bound. It is expected that there is an average water level difference of 40 to 60 cm in the five days during the rising water season, but it could be as high as 4 or 5 m [29]. Additionally, some inter-annual changes in the flood season can be expected, and the slope of the river has to be considered which is has a median value of 30 cm/km for the Mekong River. Of the three thresholds used for the outlier detection the difference of 7 m w.r.t. the year is the most sensitive for the later result. The time and distance weighted mean in the second part of the outlier detection limits the sensitivity of the other threshold.

4.2.3. Merging of the Overlap Regions

From the classification we derive a set of heights for each of the different geographical regions which have a certain overlap (see Figure 2 and Section 2). In this overlap, for the same crossing two water levels were computed. Therefore, it has to be decided which height shall be used. To resolve this, we use the distance-weighted mean water level as in the outlier detection (see Section 4.2.2). The water level that is closest to this mean water level is applied.

5. Results and Validation

We applied the described methodology for the classification and water level determination on CryoSat-2 SAR data in the Mekong River Basin. In this section, both the results of the classification and the water level determination are presented and validated.

5.1. Results of the Classification

After the clustering and classification of the CryoSat-2 measurements in the Mekong Basin we select the classes of water returns. In the upstream region we identify three and in the middle region six out of 20 classes as water classes. In the downstream region the rivers are surrounded by seasonal wetland, which makes it difficult to distinguish water return related to the river from the surroundings. Therefore, the downstream region will not be investigated further.

In Figure 5 the mean waveform and mean RIP of some classes are shown (note the different power axes). The classes displayed are selected to best represent all 20 classes for the upstream and middle region. As can be seen, the shape of the mean waveform and mean RIP of water classes in the upstream region reappear in the middle region, but not as water classes. In the middle region small lakes or paddy fields have the same signature as the river upstream. This observation leads to the decision to classify the two regions separately. Some classes have very similar mean waveforms and RIPs (e.g., second water class and first land class in the middle region) but are either classified as water or as land. In this case the maximum power is the important discriminant between the classes. In the upstream region not all stacks over land are 'full', i.e., not every single-look recorded the returning power. This leads to strongly distorted RIPs as shown for the third land class. All mean waveforms and RIPs are displayed in Appendix A for the interested reader.

In Figure 6, a section of the river network in the upstream region with the results of the classification is shown. The course of the river is well depicted, however, not every crossing of the satellite track with the river water is identified. At some crossings no water reflection of the river is measured since the river is too narrow. On the other hand, some points classified as water are not close to the given polygon (blue line). However, the topography model (HydroSHEDs, as presented in Lehner et al. [30]) shown in the background indicates river valleys in the three circled areas. Therefore, one can assume that the classification is able to find rivers that are so small (down to 20 m width) that they are not present in the high-resolution river polygon provided by the MRC. Figure 7 shows the classification for one exemplary track in the upstream region. The measurements classified as water (red dots) line up to a nearly constant water level at all crossings of the satellite track with the river.
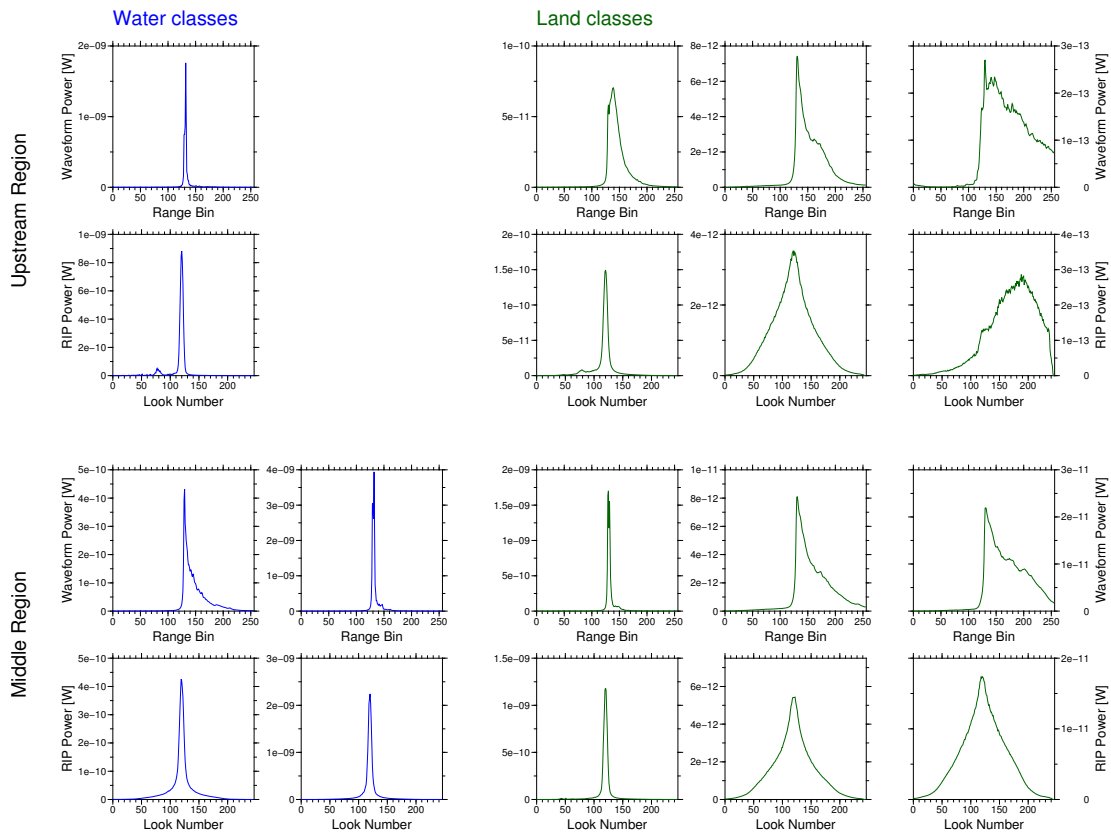
Figure 5. The mean waveforms and RIP of some selected classes; the waveforms and RIP above each other belong to the same class.
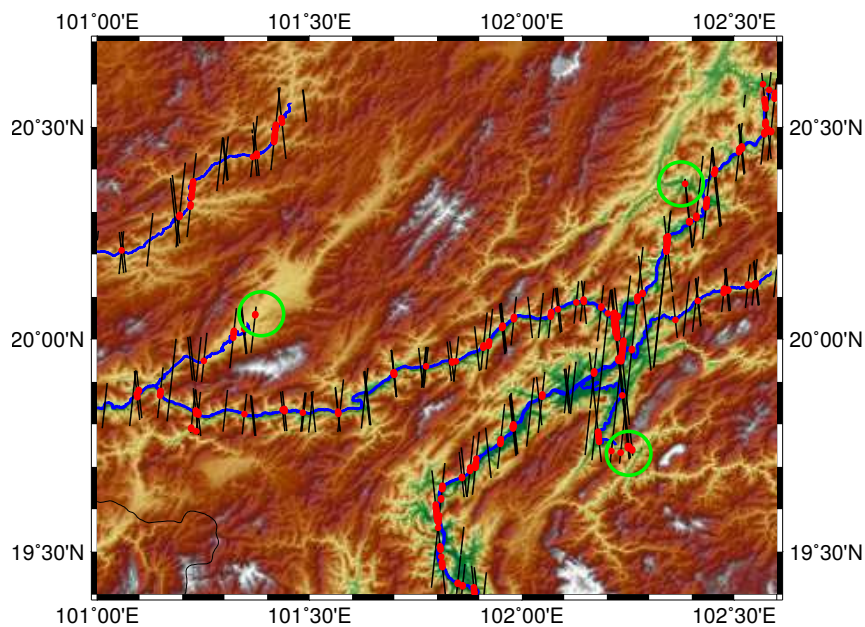

Figure 6. An example of the classification. The red dots are classified as water measurements, and black lines are the land-classified measurements. The three circles indicate areas where water was detected in river valleys which are not included in the river polygon. The background shows the HydroSHEDs topography model.
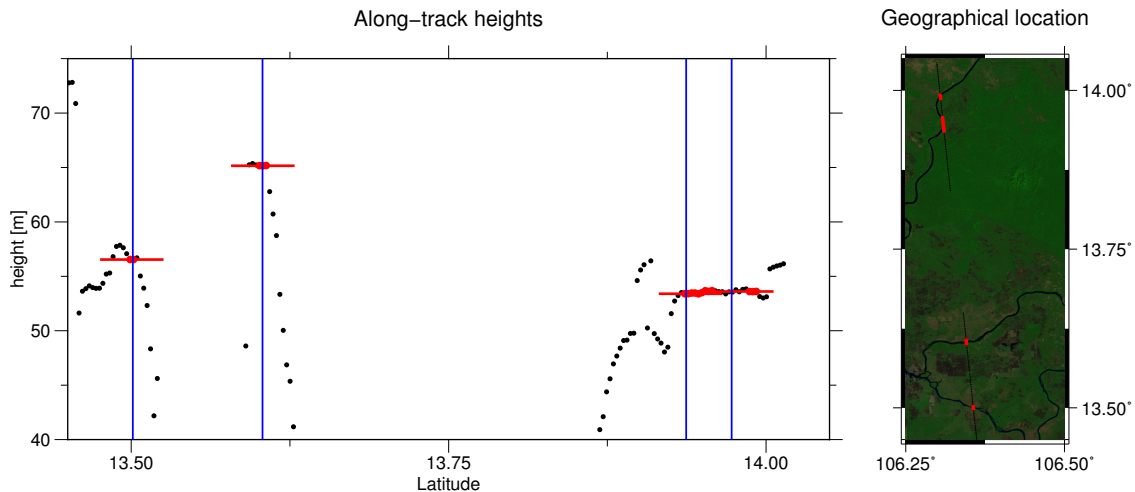
Figure 7. Heights along one track which crosses a river at four locations. The map on the right side shows the geographical surroundings with the background as a Landsat-8 scene where the rivers are well visible. The black dots are all retracked heights with the red dots indicating which measurements were classified as water. The blue vertical lines show the location of the crossing of the track with the river polygon and the horizontal lines are the estimated water level at each crossing.

5.2. Resulting Water Level

In the entire Mekong Basin we estimate water levels at more than 2000 crossings, which means approximately one measurement every 4 km along the main river (compared to 50 km for Envisat). The water level was not measured at every crossing. As mentioned before, at some crossings the river was so small that a reliable measurement could not be made in every pass, and some other water levels were discarded during outlier detection. Furthermore, at some crossings the classification failed to identify the water. However, we are still able to retrieve at least some measurements from rivers as narrow as 20 m. In Figure 8 all measured heights at all dates are presented in a map, which shows the overall topography of the river network well but cannot show details like seasonal variations.

For one track the heights and the classification are displayed in Figure 7 with a Landsat map of the river network and the surrounding area. In this track four water crossings are found where the two most northern ones are very close together with a difference of the water level of 20 cm. There the river meanders under the track which causes two crossings close together. The two southern crossings belong to two different rivers which explains the large height difference. It is visible that only few measurements are used to estimate the water level at each crossing. Approximately 180 water levels (or 8%) are estimated by just one measurement, with the majority in the upstream region. Hence, the outlier detection is more important in this area. In the upstream region, the outlier detection removes 113 of 1740 water level observations; all of them are detected by the comparison with surrounding water level measurements. The comparison with water levels of the same pass reveals only 37 of the 113 outliers. In the middle region only 13 of 529 observations are rejected as outliers: 10 by the comparison with surrounding observations, 9 by the comparison with the same pass, and 6 by both outlier detections.

For crossings with more than one water measurement we can calculate the standard deviation of the measurements used for water level estimation. More than 85% of the water levels have a standard deviation of less than 0.5 m.
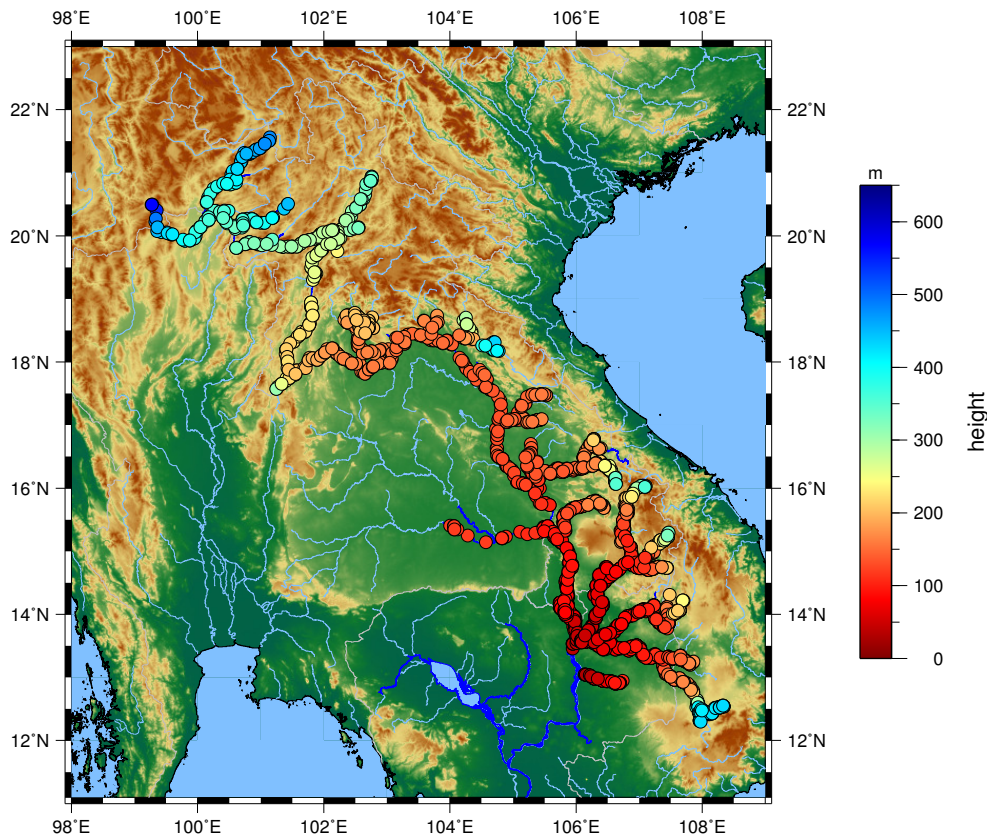
Figure 8. Resulting water levels in the Mekong River Basin.

5.3. Validation

In this section both the classification and the water levels are validated. We test and validate the repeatability of the classification with cross-validation. The altimetric water levels cannot be validated against in situ gauge data without an absolute height reference as is common for short repeat time missions because no time series can be built from CryoSat-2 data without reducing the unknown topography of the river. Therefore, we validate the resulting water levels with respect to the stable seasonal signal and compare these results with the performance of Envisat water levels and CryoSat-2 data extracted with a land–water mask in the same validation.

5.3.1. Validation of the Classification

The classification is validated with a cross-validation. To this end, we cluster the data in a first step. The resulting classes are considered as the 'true' classes. In the second step only parts of the data are clustered with the other parts classified in this second clustering. The cross-validation compares the resulting classifications of the two steps.

Table 2 summarizes the results of the cross-validation; water and non-water classes are distinguished. The overall accuracy is 97.9%. This cross-validation shows that the classification is stable and does not change with the data subset used for the clustering.

Table 2. Results of the cross-validation. The first classification is a clustering on the whole data set, and the second classification is based on clustering on a subset of data with classification of the residual data set.

| | | *Second Classification* | |
		Water	**No Water**
First Classification	**Water**	7321	205
	No water	423	22,660

5.3.2. Validation of Water Levels

Unlike water level time series measured by short repeat time missions, CryoSat-2 measurements cannot be validated against the time series of in situ gauges without reducing the topography as done by [12]. The Mekong River and its tributaries have topography that is too complex to allow for reliable reduction. Besides this, the temporal overlap between the CryoSat-2 data and the gauge data is only about 1.5 years or even less (April 2011 until December 2012).

To validate the water levels we use the nearly one-year repeat time of CryoSat-2. We investigate the differences between two subsequent tracks at the same river crossing. A histogram of the differences is shown in Figure 9a. Table 3 displays the median, mean, and standard deviation of these differences for the merged results as well as for the two regions (upstream and middle) separately. The results of the validation are compared to a validation with in situ gauge data, Envisat data, and CryoSat-2 data with a land–water mask.
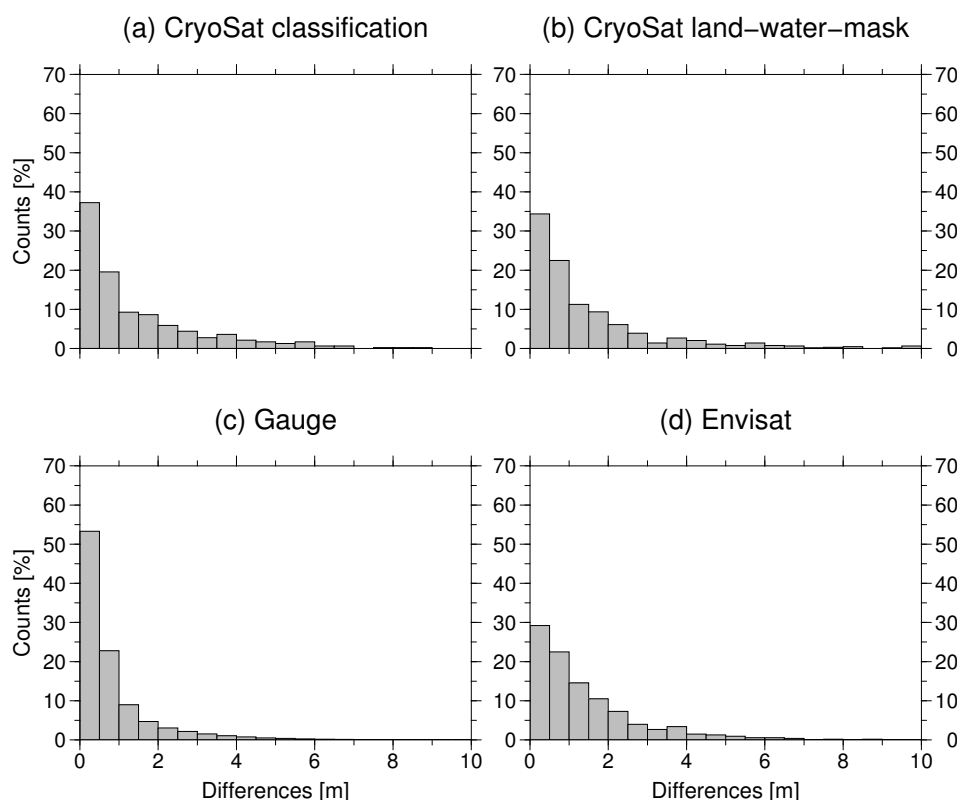

Figure 9. Histogram of the differences of height measurements 369 days apart for CryoSat-2 water levels with classification, CryoSat-2 water levels inside the land–water mask, gauge water level, and Envisat water level.

For this validation, we take the differences between gauge measurements that are 369 days apart and Envisat measurements where the day of the year has a less than 5-day difference. The gauges give a measure of how stable the annual signal is in the Mekong Basin, i.e., a benchmark on how small the differences between the water levels could be. The Envisat observations are the most commonly used data for inland waters with a pulse-limited altimeter. The comparison to the water levels which are derived from CryoSat-2 by simply averaging measurements inside the land–water mask allows for evaluation of the benefits of the classification approach. The land–water mask water levels underwent the same outlier detection as used on the results of the CryoSat-2 classification for better comparability. The median of the differences in Table 3 for the CryoSat-2 classification results are in both the upstream and the middle stream region better than the ones from the Envisat results. In the upstream region the improvements of the CryoSat-2 classification results compared to the Envisat results are more apparent than in the middle region where the validation results are more similar. However, the CryoSat-2 classification results have a higher standard deviation in the upstream regions, and thus larger differences than the Envisat results. The land–water mask approach for CryoSat-2 in the upstream region has even larger differences, which can also be seen in Figure 9. In the middle region no large differences between the validation of the two CryoSat-2 approaches are to be seen. The land–water mask approach yields to more valid water level observations in the middle region but at the same time also a higher number of outliers in both regions (see Table 4).

Table 3. Analysis of the differences of height measurements 369 days apart for the whole study area, only the upstream region, and only the middle stream region.

	Median (m)	Mean (m)	Standard Deviation (m)
Whole study area			
CryoSat-2 classification	0.76	1.43	1.59
CryoSat-2 land–water mask	0.83	1.86	4.55
Gauge	0.45	0.82	1.09
Envisat	0.96	1.42	1.44
Upstream region			
CryoSat-2 classification	0.79	1.54	1.70
CryoSat-2 land–water mask	0.85	2.00	5.44
Gauge	0.42	0.72	1.05
Envisat	1.01	1.46	1.49
Middle region			
CryoSat-2 classification	0.76	1.15	1.10
CryoSat-2 land–water mask	0.84	1.55	1.87
Gauge	0.54	1.00	1.14
Envisat	0.81	1.26	1.26

Table 4. Comparison of the two approaches for CryoSat-2 water levels in terms of absolute number of water levels and number of outliers.

	Upstream Region		Middle Region	
	No. of Water Levels	% of Outliers	No. of Water Levels	% of Outliers
Classification approach	1703	2	520	2
Land–water mask approach	1534	7	1364	4

6. Discussion

In the results and validation section above we demonstrated the advantages and limitations of the classification approach for CryoSat-2 SAR data over the Mekong Basin. Compared to CryoSat-2 water levels extracted with a fixed land–water mask, the classification approach yields water levels with a higher quality according to the used measures with fewer outliers. The difference between the two approaches is most pronounced in the upstream region with rivers as small as 20 m in width. However, the land–water mask approach yields more water levels in the middle region. This reveals the opportunity that SAR altimetry provides for rivers in the Mekong Basin which are too small to be reliably identified in optical (e.g., Landsat, resolution: 30 m) or SAR (e.g., Sentinel-1, resolution: 10 m) images. As shown in Section 5.1 and Figure 6 the classification of SAR altimetry is able to identify rivers which are not visible in the land–water mask derived from satellite images. On the other hand, the classification fails to identify all crossings with a river, which leads to data gaps in the water level measurements. Some of the undetected rivers are very small and shadowed by surrounding river gorges. At other crossings the returning signal is too noisy and disturbed to be identified correctly even by visual inspection.

The better performance of the classification approach in the upstream part of the river is probably caused by the feature selection which is more focused on the reflective properties of small water bodies. The main drawback of the classification approach is its failure in the downstream area. The classification is not able to discern between river water and water in seasonal wetland regions. This problem can only be solved by using a high-resolution seasonal land–water mask that could be derived from Sentinel-1 or 2 data for example.

The existence of outliers after the classification process indicates a certain amount of misclassification. Some of these might be related to reflections from river banks, concrete areas, or other flat regions causing river-like waveforms. Moreover, water surfaces close to the river (such as paddy fields) can provoke outliers.

The inevitable outlier detection is challenging due to the long-repeat orbit of CryoSat-2 preventing the application of the usual virtual station concept. In this study, the outlier detection approach exploits the stable annual water level cycle within the Mekong Basin. Hence, this method is not transferable to other river systems with less stable annual signals. The second outlier detection approach of this study relies on a certain density of water level observations along the river. Without any observation close by a water level cannot be checked to be an outlier.

The validation inherits the problems of the outlier detection as no direct comparison with in situ gauge data is possible. As the gauge data has no absolute reference, not even the absolute height of CryoSat-2 water levels in the vicinity of a gauging station can be validated.

Using CryoSat-2 over rivers improves the knowledge for the river topography, as with this mission the spatial distribution of water level observations is much denser than with any prior satellite altimetry mission (as can be seen in Figure 8). Even small tributaries are observed successfully with CryoSat-2 SAR, which allows monitoring of the entire river network. However, this high spatial resolution entails a sparse repeat time and thus, precludes the application of the classical virtual station concept for data screening, interpretation, and validation.

Nevertheless, using the derived CryoSat-2 data set—in combination with short repeat altimetry mission results—for building a mathematical water level model (as done in [31]) or for assimilation in hydrological models [32] will certainly improve our knowledge of the water regime in the Mekong region.

7. Conclusions

We demonstrate in this study the advantages of CryoSat-2 SAR altimetry data for measuring rivers in the Mekong Basin identified by a classification which is independent of an accurate land–water mask. The classification uses features derived not only from the waveform but also from the RIP. The RIP contains more information about the reflecting surface than the waveform on its own can

provide. This improves the classification and allows us to identify even very small rivers with a width as small as 20 m. In fact, the classification works better on medium and small rivers than on large rivers. The cross-validation of the classification shows that it is stable and repeatable. However, we were not able to use this classification to isolate the river in the downstream region where the Mekong River is surrounded by seasonal wetlands.

The classification in water and land measurements is used to derive water levels at the crossings of the CryoSat-2 track with a river in the whole Mekong Basin. Overall, more than 2000 water levels are measured, after outlier detection. However, it is not possible to derive a water level at every crossing. The altimeter is not able to measure a water return at every possible river crossing due to too-small rivers or overly-disturbed returns. Additionally, some measured water levels are discarded in the outlier detection.

The water levels are validated using the 369-day return time of CryoSat-2 and the very stable annual signal in the basin. The same validation is performed on Envisat water levels, gauge measurements, and by using a precise land–water mask on CryoSat-2 data. In particular, for small rivers in the upstream region the classification improves the water level determination compared to the use of a land–water mask: The median differences between consecutive passes in the upstream region are 0.79 m compared to 0.85 m for the land–water mask approach. The reduction of the standard deviation by a factor of four is even more significant. Moreover, the number of outliers is significantly smaller for the classification approach than for the land–water mask approach, with only 2% for the classification but 5.6% for the CryoSat-2 land–water mask.

Compared to Envisat water levels the CryoSat-2 water levels are of higher quality in the whole river basin due to the smaller footprint of the SAR compared to pulse-limited altimeter on Envisat. The median differences for Envisat are as high as 1.01 m in the upstream region, and 0.96 m for the whole basin (CryoSat-2 classification 0.76 m).

The classification of CryoSat-2 data allows to exploit the full along-track resolution of the data set. Therefore, it is possible to observe the water levels of rivers as small as 20 m that are usually not correctly mapped in land–water masks. Moreover, due to the dense spatial resolution of CryoSat-2 most of the smaller tributaries are observed, which is not possible with the short repeat missions Envisat, SARAL, or Jason-2 and Jason-3. Information on the water level variations for all rivers within the basin helps to further understand the hydrology of the river network.

The resulting water levels of this study will be used in combination with other altimetric water levels following the ideas of [31] to build basin-wide multi-mission water level time series. With CryoSat-2 data we will be able to significantly improve the spatial resolution of the water level observations and better close the data gap between the end of the Envisat mission and the launch of the SARAL mission. Since the launch of Sentinel-3A in February 2016, SAR altimetry data with a short repeat time of 27 days has been available. This enables testing of the transferability of the application and validation of the proposed classification approach based on a new data set.

Author Contributions: Eva Boergens developed the method, conducted the data analysis, and wrote the majority of the paper. Karina Nielsen helped with the development of the method and validation. Ole B. Andersen and Denise Dettmering contributed to the discussion of the method and results and the writing of the manuscript. Florian Seitz supervised the research and contributed to manuscript writing and organization.

Conflicts of Interest: The authors declare that they have no conflict of interest.
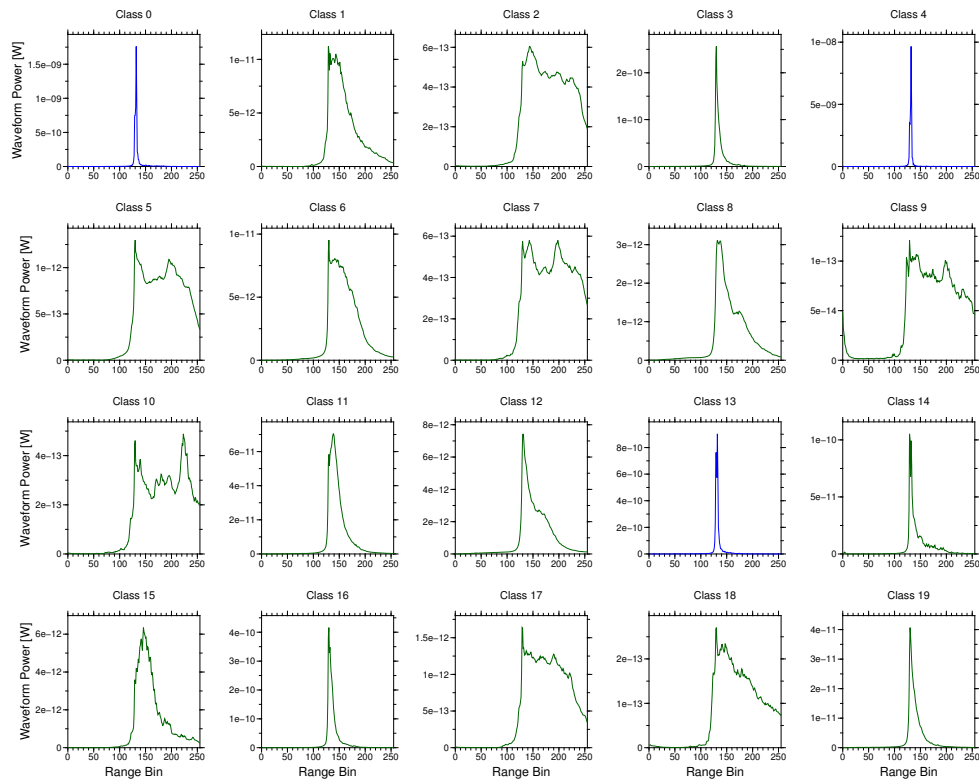
Appendix A. Mean Waveforms and RIPs

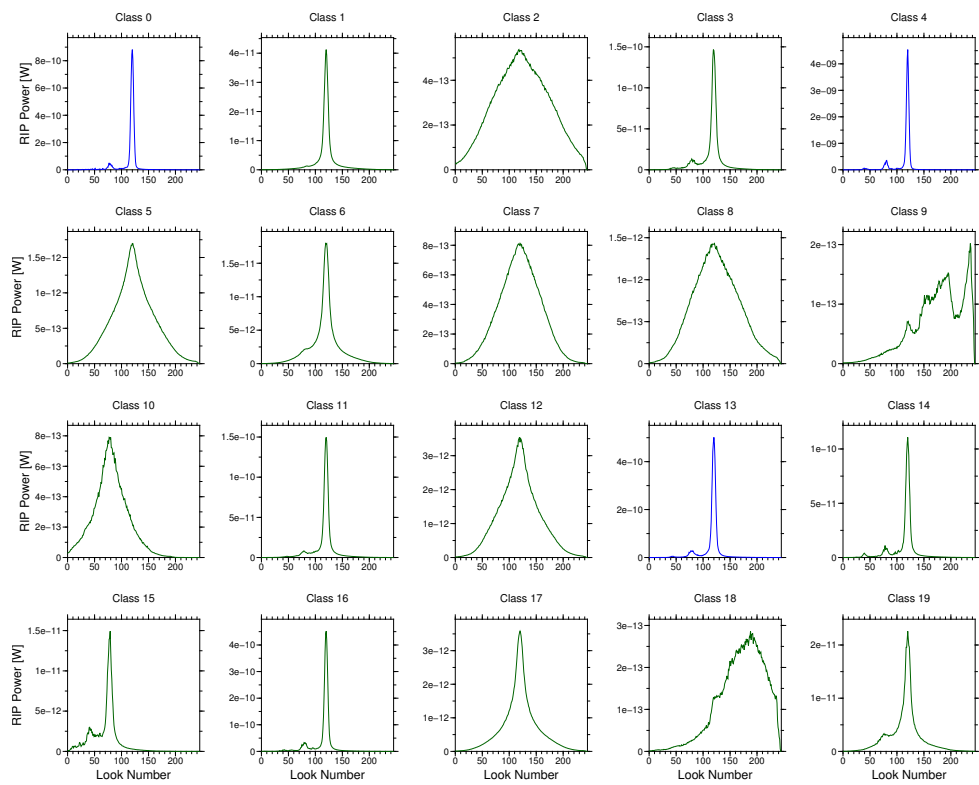**Figure A1.** Upstream region mean waveforms. Water classes: 0, 4, 13.

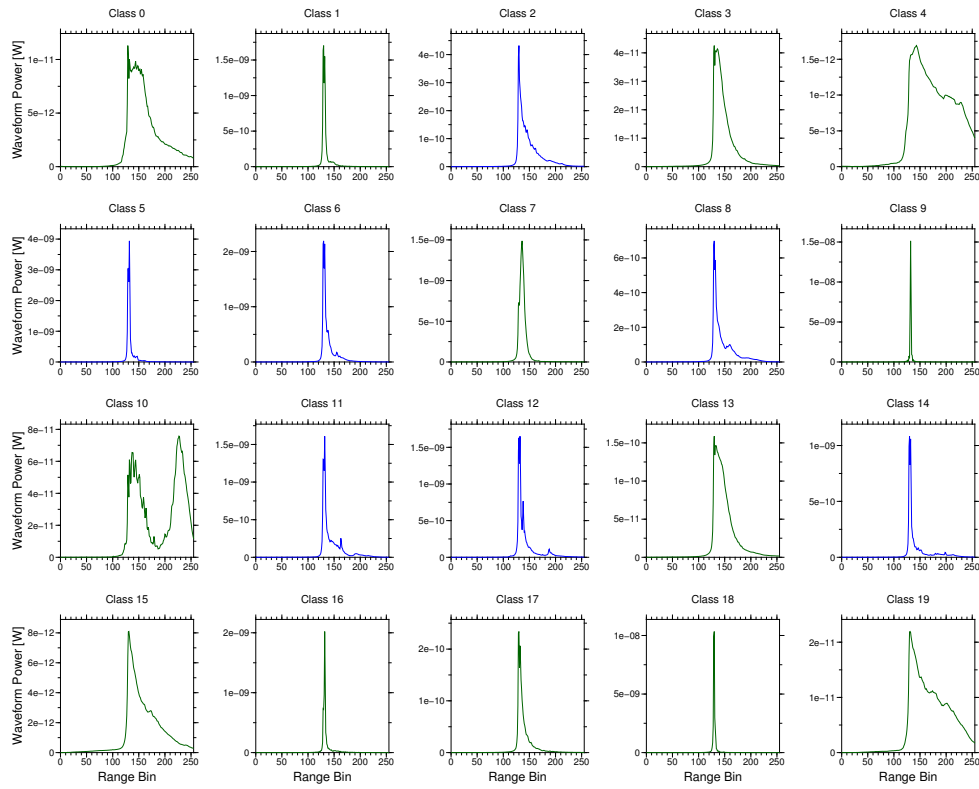**Figure A2.** Upstream region mean RIPs. Water classes: 0, 4, 13.

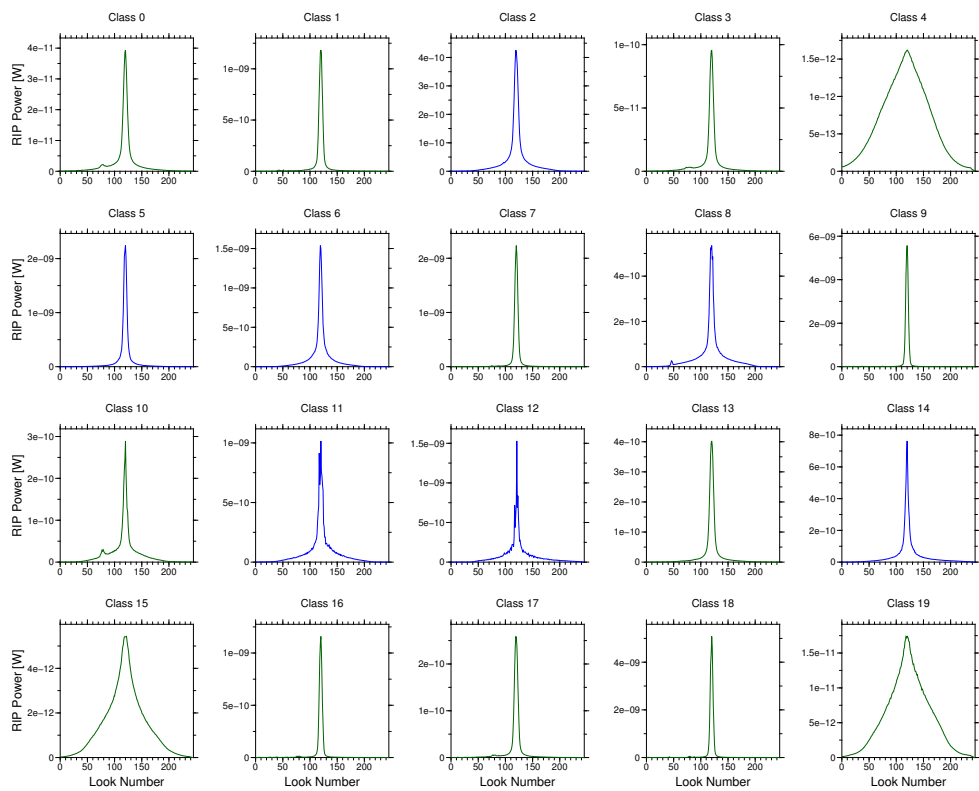**Figure A3.** Middle region mean waveforms. Water classes: 2, 5, 6, 8, 11, 12, 14.

Figure A4. Middle region mean RIPs. Water classes: 2, 5, 6, 8, 11, 12, 14.

References

1. Global Runoff Data Center. *Long-Term Mean Monthly Discharges and Annual Characteristics of GRDC Stations*; Technical Report; Federal Institute of Hydrology: Koblenz, Germany, 2013.
2. Birkett, C.M. Contribution of the TOPEX NASA radar altimeter to the global monitoring of large rivers and wetlands. *Water Resour. Res.* **1998**, *34*, 1223–1239.
3. Santos da Silva, J.; Calmant, S.; Seyler, F.; Rotunno Filho, O.C.; Cochonneau, G.; Mansur, W.J. Water levels in the Amazon basin derived from the ERS-2 and ENVISAT radar altimetry missions. *Remote Sens. Environ.* **2010**, *114*, 2160–2181.
4. Schwatke, C.; Dettmering, D.; Bosch, W.; Seitz, F. DAHITI—An innovative approach for estimating water level time series over inland waters using multi-mission satellite altimetry. *Hydrol. Earth Syst. Sci.* **2015**, *19*, 4345–4364.
5. Boergens, E.; Dettmering, D.; Schwatke, C.; Seitz, F. Treating the Hooking Effect in satellite altimetry data: A case study along the Mekong River and its tributaries. *Remote Sens.* **2016**, *8*, 91.
6. Frappart, F.; Do Minh, K.; L'Hermitte, J.; Cazenave, A.; Ramillien, G.; Le Toan, T.; Mognard-Campbell, N. Water volume change in the lower Mekong from satellite altimetry and imagery data. *Geophys. J. Int.* **2006**, *167*, 570–584.
7. Biancamaria, S.; Frappart, F.; Leleu, A.S.; Marieu, V.; Blumstein, D.; Desjonquères, J.D.; Boy, F.; Sottolichio, A.; Valle-Levinson, A. Satellite radar altimetry water elevations performance over a 200 m wide river: Evaluation over the Garonne River. *Adv. Space Res.* **2016**, *59*, 1–19.
8. Raney, R.K. The delay/doppler radar altimeter. *IEEE Trans. Geosci. Remote Sens.* **1998**, *36*, 1578–1588.
9. Nielsen, K.; Stenseng, L.; Andersen, O.B.; Villadsen, H. Validation of CryoSat-2 SAR mode based lake levels. *Remote Sens. Environ.* **2015**, *171*, 162–170.
10. Kleinherenbrink, M.; Lindenbergh, R.C.; Ditmar, P.G. Monitoring of lake level changes on the Tibetan Plateau and Tian Shan by retracking Cryosat SARIn waveforms. *J. Hydrol.* **2015**, *521*, 119–131.
11. Göttl, F.; Dettmering, D.; Müller, F.L.; Schwatke, C. Lake level estimation based on CryoSat-2 SAR altimetry and multi-looked waveform classification. *Remote Sens.* **2016**, *8*, 1–16.
12. Villadsen, H.; Andersen, O.B.; Stenseng, L.; Nielsen, K.; Knudsen, P. CryoSat-2 altimetry for river level monitoring—Evaluation in the Ganges-Brahmaputra River basin. *Remote Sens. Environ.* **2015**, *168*, 80–89.
13. Bercher, N.; Dinardo, S.; Lucas, B.M.; Fleury, S.; Picot, N. A review of cryosat-2/siral applications for the monitoring of river water levels. *ESA Living Planet* **2013**, *2013*, 1–7.
14. Berry, P.A.M.; Garlick, J.D.; Freeman, J.A.; Mathers, E.L. Global inland water monitoring from multi-mission altimetry. *Geophys. Res. Lett.* **2005**, *32*, 1–4.
15. Desai, S.; Chander, S.; Ganguly, D.; Chauhan, P.; Lele, P.; James, M. Waveform Classification and Water-Land Transition over the Brahmaputra River using SARAL/AltiKa & Jason-2 Altimeter. *Indian Soc. Remote Sens.* **2015**, *43*, 475–485.
16. Dettmering, D.; Schwatke, C.; Boergens, E.; Seitz, F. Potential of ENVISAT Radar Altimetry for Water Level Monitoring in the Pantanal Wetland. *Remote Sens.* **2016**, *8*, 596.
17. Villadsen, H.; Deng, X.; Andersen, O.B.; Stenseng, L.; Nielsen, K.; Knudsen, P. Improved inland water levels from SAR altimetry using novel empirical and physical retrackers. *J. Hydrol.* **2016**, *537*, 234–247.
18. Armitage, T.W.K.; Davidson, M.W.J. Using the interferometric capabilities of the ESA CryoSat-2 mission to improve the accuracy of sea ice freeboard retrievals. *IEEE Trans. Geosci. Remote Sens.* **2014**, *52*, 529–536.
19. Wingham, D.J.; Francis, C.R.; Baker, S.; Bouzinac, C.; Brockley, D.; Cullen, R.; de Chateau-Thierry, P.; Laxon, S.W.; Mallow, U.; Mavrocordatos, C.; et al. CryoSat: A mission to determine the fluctuations in Earth's land and marine ice fields. *Adv. Space Res.* **2006**, *37*, 841–871.
20. MacQueen, J. Some methods for classification and analysis of multivariate observations. *Proc. Fifth Berkeley Symp. Math. Stat. Probab.* **1967**, *1*, 281–297.
21. Mekong River Commission. (Ed.) *Overview of the Hydrology of the Mekong Basin*; Mekong River Commission: Phnom Penh, Cambodia, 2005.
22. ESA. *CryoSat-2 Geographical Mode Mask*; ESA: Paris, France, 2016.
23. Scagliola, M. *CryoSat Footprints*. 2013. Available online: https://earth.esa.int/documents/10174/125271/CryoSat_Footprints_TN_v1.1.pdf/2a5d996b-8b77-4d1c-ae7b-fbf93848c35d;jsessionid=B1FF8C50A1B0F2A0879F6FA028844644.eodisp-prod4040?version=1.0 (accessed on 23 November 2017).

24. Cullen, R.A.; Wingham, D.J. CryoSat Level 1b Processing Algorithms and Simulation Results. In Proceedings of the 2002 IEEE International Geoscience and Remote Sensing Symposium, Toronto, ON, Canada, 24–28 June 2002; pp. 1762–1764.

25. Laxon, S.W. Sea-Ice Altimeter Processing Scheme at the EODC. *Int. J. Remote Sens.* **1994**, *15*, 915–924.

26. Gommenginger, C.; Thibaut, P.; Fenoglio-Marc, L.; Quartly, G.; Deng, X.; Gómez-Enri, J.; Challenor, P.; Gao, Y. Retracking altimeter waveforms near the coasts. In *Coastal Altimetry*; Benveniste, J., Cipollini, P., Kostianoy, A.G., Vignudelli, S., Eds.; Springer: Berlin, Germany, 2011; pp. 61–101.

27. Doane, D.P. Aesthetic frequency classifications. *Am. Stat.* **1976**, *30*, 181–183.

28. Sturges, H. The choice of a class interval. *J. Am. Stat. Assoc.* **1926**, *21*, 65–66.

29. Mekong River Commision. *Annual Mekong Flood Report 2008*; Mekong River Commission: Phnom Penh, Cambodia, 2009.

30. Lehner, B.; Verdin, K.; Jarvis, A. New global hydrography derived from spaceborne elevation data. *Eos* **2008**, *89*, 93–94.

31. Boergens, E.; Buhl, S.; Dettmering, D.; Klüppelberg, C.; Seitz, F. Combination of multi-mission altimetry data along the Mekong River with spatio-temporal kriging. *J. Geodesy* **2017**, *91*, 519–534.

32. Schneider, R.; Nygaard Godiksen, P.; Villadsen, H.; Madsen, H.; Bauer-Gottwein, P. Application of CryoSat-2 altimetry data for river analysis and modelling. *Hydrol. Earth Syst. Sci.* **2017**, *21*, 751–764.

P-4: Observing Water Level Extremes in the Mekong River with Multi-Mission Altimetry

E. Boergens, D. Dettmering, and F. Seitz (2018): **Observing Water Level Extremes in the Mekong River with Multi-Mission Altimetry**. In: *Remote Sensing*. in review

Copyright

This publication is submitted to Remote Sensing, an open access MDPI journal.

Summary of content

Water level observations of single-mission altimetry are temporally limited by the repeat time of the missions and only available at fixed locations along the river, which are called *V*irtual *S*tations (VSs). Thus, they are often insufficient to quantify the extent of a flood or its extreme events in a river basin. Most of the extreme flood events have a duration shorter than the repeat time of *Envi*ronmental *Sat*ellite (Envisat) or *S*atellite with *Ar*gos and *Al*tiKa (SARAL) with 35 days and are therefore not observed by these missions. However, the temporal and spatial resolution of all available altimeter missions since 2008 is sufficiently dense to observe the full flood extent. In this study, water level observations from multiple altimeter missions in the Mekong River Basin, both from the main stream and tributaries, were combined into one multi-mission time series with *U*niversal *K*riging (UK).

Unlike the *O*rdinary *K*riging (OK) method used in P-2, UK did not require a constant mean over the data. For multi-mission altimetry, this allowed the incorporation of altimetric water levels from *l*ong-*r*epeat *o*rbit (LRO) or *n*on-*r*epeat *o*rbit (NRO) missions such as CryoSat-2, SARAL DP, and Envisat EM. While the mean water level of VSs of the *s*hort-*r*epeat *o*rbit (SRO) missions could be derived from the mean of the time series, this was not possible for LRO or NRO missions. Reducing the mean water level with a topography model is usually not feasible due to the inaccuracy of these models. With water level observations from LRO or NRO missions additional spatial samples compared to SRO altimetry can be acquired. The topography, or mean water level, along the river was modelled with an unknown linear combination of known functions

$\{f_0(\boldsymbol{x})...f_l(\boldsymbol{x})\}$—in this study B-Splines of degree 3 were used for the functions. This led to the functional model for the water level $Z(\boldsymbol{s},t)$ observed at location $\boldsymbol{s}$ and at time t

$$Z(\boldsymbol{s},t) = \sum_{j=0}^{l} f_j(\boldsymbol{s})\beta_j + \delta(\boldsymbol{s},t) \tag{A.3}$$

with $\delta(\boldsymbol{s},t)$ being the stochastic signal, i. e. the water level variation.

Based on this model assumption, UK estimated the optimal prediction with the non-stationary covariance model from P-2. With this, data of SRO, LRO, and NRO missions were combined to a multi-mission time series at the locations of all available gauging stations along the Mekong River between 2008 and 2016.

The extreme events in this time-span, two floodings in 2008 and 2011 and two below average floods in 2015 and 2016, were well-observed by the multi-mission time series whereas close-by VSs time series were not able to quantify the extent of these events. However, even the multi-mission time series were not able to observe every small flash flood as the spatial and temporal resolutions of the data were not sufficient for such short termed events.

Declaration of contribution

The idea for this study was developed following the previous multi-mission approach with OK in order to incorporate the long-repeat orbit mission CryoSat-2. Denise Dettmering helped discussing and developing the idea of UK for the Mekong River Basin. The realisation of the UK approach was done by Eva Börgens as well as the figure compilation. Denise Dettmering contributed to the analysis and discussion of the results. The lead of the manuscript writing had Eva Börgens but all co-authors helped with comments and corrections.

The data computation in DAHITI was done with the support of Christian Schwatke (see acknowledgements); the non-repeat orbit missions were processed by Johannes Lucke under Eva Börgens's supervision (see acknowledgements); Michael Schmidt helped with the development of the B-splines for the topography (see acknowledgements). The overall own contribution of Eva Börgens is estimated to be **95%**.

Observing Water Level Extremes in the Mekong River with Multi-Mission Altimetry

Eva Boergens [1],*, Denise Dettmering [1] and Florian Seitz [1]

[1] Deutsches Geodätisches Forschungsinstitut der Technischen Universität München, Arcisstraße 21, 80333 Munich, Germany

* Correspondence: eva.boergens@tum.de, +49 89 / 23031 - 1263

Abstract: Single-mission altimetric water level observations of rivers are spatial and temporally limited, and are often unable to quantify the full extent of extreme flood events. Combining data from multiple altimeter missions into a multi-mission product increases the spatial and temporal resolution of the data. In this study, we combined water level data from multiple altimeter missions in the Mekong River Basin between 2008 and 2016 into one multi-mission water level time series with universal kriging. Universal kriging allowed the incorporation of altimetry data from long or non-repeat orbit missions, such as CryoSat-2. The covariance model used in universal kriging also enabled inclusion of data both from the main stream and tributaries. The multi-mission time series adequately reflected the general inter-annual flood behaviour and extreme floodings in 2008 and 2011. However, flash floods remained undetectable with multi-mission data.

1. Introduction

The Mekong River Basin in South-East Asia is well known for its high and stable annual floods [1]. Floods are essential to the livelihoods of riparians, providing irrigation to the paddy fields, other agricultural activities and seasonal fisheries [2]. Lower than average river levels in the flood season can lead to water shortages in the basin during the following dry season between December and May [3]. On the other side, severe floodings can destroy infrastructure and agriculture. Despite the need to monitor river stages to forecast floods and identify long-term changes, the availability of global in situ gauge data has decreased in the past decades [4].

An increasing number of studies have used satellite altimetry to measure river water levels independently from in situ observations with satellite altimetry [e.g. 5–7], so that small rivers (<100 m wide) can now be accurately observed [e.g. 8,9]. The launch of CryoSat-2 in 2010 increased the accuracy of water level observations of small rivers even further due to its Synthetic Aperture Radar (SAR) altimeter which has a smaller along-track footprint, compared to pulse limited altimetry. This technology has enabled higher measurement accuracy for small rivers less than 200 m in width [10,11].

Data from short-repeat missions such as Envisat, SARAL, Jason-2 and Jason-3 can be used to build water level time series at a given location (i.e. virtual station; VS). However, the spatial and temporal resolution of satellite altimetry datasets is limited by the orbit design of satellite altimetry missions. Since 2010, at least three altimeter missions have been available to simultaneously observe water levels. Each mission has specific limitations with respect to temporal and spatial resolution. Even with the 10-day temporal resolution of Jason-2 and Jason-3, many flooding events cannot be observed in a river basin. Most missions available since 2010 have long or non-repeat orbits, so

time series at VSs cannot be estimated. To overcome this problem, it is necessary to combine data from multiple altimeter missions into a multi-mission altimetry dataset. Multi-mission combination is already operational for lakes and reservoirs [7], where multiple altimeter missions and tracks are combined under the assumption that all measurements observe the same equipotential water surface.

Unlike for lakes and reservoirs, combining data along rivers requires knowledge of river topography, slope and flow velocity [10]. Tourian *et al.* [12] used multi-mission altimetry to create a water level time series at the Po River, based on estimated flow time between the VSs. Tourian *et al.* [13] used a Kalman filter with multi-mission altimetry to estimate discharge in the Niger River Basin. Multi-mission altimetry water level time series based on an ordinary kriging approach with spatio-temporal covariance estimation were presented by Boergens *et al.* [14] for the Mekong River. However, the approach did not allow inclusion of data from tributaries or from long or non-repeat orbit missions such as CryoSat-2.

This study use multi-mission altimetry to investigate flood seasons in the Mekong River Basin from 2008 to 2016. We assess whether water level time series obtained with multi-mission altimetry could reflect flooding or other extreme events in the Mekong River Basin. Data from all available altimeter missions since 2008 are collected for the main stream and tributaries and are combined with a universal kriging approach [15,16], extending the work of Boergens *et al.* [14]. Universal kriging has been employed in hydrology before to interpolate ground water tables [17,18] and precipitation levels [19]. Brus and Heuvelink [20] applied universal kriging to multiple environmental variables.

Unlike ordinary kriging, universal kriging does not rely on the assumption of a constant data mean [21], and thus a reduction in topography is not necessary for the combination of data of multiple altimeter missions. This is a necessity for the incorporation of altimetry data from long or non-repeat orbit missions such as CryoSat-2 or the extended mission of Envisat. Additionally, also data along the rivers tributaries are included in the multi-mission approach which further densifies the available data. This study inherits the covariance models from Boergens *et al.* [14] but new model parameter are estimated based on the extended data set.

2. Study Area

This work constitutes a case study of the Mekong River Basin in South-East Asia (Figure 1). We investigated the river reach between the Chinese border and the confluence with the Tonle Sap River in Phnom Penh, including its tributaries. The river channels of the northern reach in China are too steep to use satellite altimetry. Downstream of Phnom Penh, the Mekong widens into a delta with tidal influence.

The landscape in the river basin varies along the course of the river. North of Vientiane, the main river flows through a mountainous area with steep river gorges, and is only a few hundred metres wide. South of Vientiane, the main river flows over the Khorat Plateau with hilly landscapes, up to the Mekong Falls between Pakse and Stung Treng. The river is 1 km wide in this area. Downstream of the Mekong Falls, the river is surrounded by flat terrain and seasonal wetlands, and widens from 1 to 5 km. In Phnom Penh, the Tonle Sap river joins the Mekong River, and the Mekong opens up to a delta with a multitude of shifting channels and islands. From this point onwards, the river is under tidal influence. Most of the tributaries of the Mekong flow through hilly or mountainous topography, including the important left-bank tributaries in Laos. Only the right bank tributaries originating on the Khorat Plateau and the tributaries of the downstream flatlands flow through smooth landscape.

The hydrology of the Mekong is dominated by two major compartments[1,3]. The first compartment is called the Yunnan compartment and is governed by snow melt on the Tibetan Plateau. The discharge of this compartment governs the flow of the river up to Vientiane, and constitutes up to 30% of the average dry season flow of the Mekong Basin. The main flood of the Yunnan compartment occurs in August and September. South of Vientiane, the South-Eastern monsoon drives the hydrology of the Mekong and thus the monsoon compartment. The major left-bank tributaries in Laos, entering the main river between Vientiane and Stung Treng, are only governed by the monsoon

and provide 50% of the overall runoff of the Mekong River Basin. The monsoon lasts from mid-May to mid-October, defining the annual flood season during June and November, with its main peak in precipitation and water level in August. The central region around Pakse and the left-bank tributaries are exposed to an average annual precipitation of 2000 mm, with 500 mm falling on average in August.

The main flood of the two hydrological compartments is usually in phase, with the main flood peak occurring in August and September. The flood peak requires approximately one month to travel from the northern end of the study area to the southern end. The flood season of the Mekong River is exceptionally regular, with the onset of the flood varying by about two weeks among years[1].

Dams have recently been built along many of the tributaries of the Mekong River Basin to generate hydro-electrical power and regulate floods [2, chap. 4.2]. In the upper Mekong Basin in China, several dams are currently in operation, with further dams planned along the whole main stream. The locations of dams built before 2016 are shown in Figure 1. Simulation studies predict that dams on the main stream will increase dry season discharge and decrease wet season discharge[22]. A recent study has shown that this phenomenon is already occurring due to Chinese dams [23]. Dams along tributaries have a limited influence and do not alter the flow of the main river [2, chap. 3.1]. However, dams alter flow behaviour so that the relation between upstream and downstream water levels is unknown. Some dams were put in operation during the timeframe of this study, thus only data prior to the start of operations were used for rivers upstream of these dams. The right bank tributaries on the Khorat Plateau are dammed close to confluence with the main river, and are therefore not considered in this study.

In the Mekong Basin, the terms flood or flood season denote the annually recurring rise in water level and discharge, whereas flooding is an anomalously high flood and drought is an anomalously low flood.

3. Data

3.1. Altimetry Data

The multi-mission altimetry approach used in this study relies on data from altimeter missions with a short-repeat cycle, and data from missions with either long repeat times or non-repeat/drifting orbits. Missions with short repeat times include Envisat (2002–2010) and its successor in the same orbit SARAL (2013–2016), with repeat times of 35 days. This leads to a VS being located approximately every 70 km along the river. The altimeter missions of Jason-2 (2008–2016) and its successor Jason-3 (2016-present) have repeat times of only 10 days, leading to an even sparser spatial coverage. The long repeat or non-repeat missions of CryoSat-2 (2010–present), Envisat-EM (2010–2011) and SARAL-DP (2016–present) show very high spatial resolutions, but temporal resolution is limited to 369 days for CryoSat-2, while Envisat-EM and SARAL-DP have drifting orbits and therefore do not have repeat observations. CryoSat-2 uses two measuring modes (SAR and LRM) in the study area.

High-frequency data from missions with short-repeat times (Envisat, SARAL, Jason-2 and Jason-3) are processed in DAHITI (Database for Hydrological Time Series of Inland Waters) to create water level time series. DAHITI pre-processing [7]is also used to derive water level data from Envisat EM, SARAL DP and CryoSat-2 LRM high-frequency data. In this pre-processing method, water level is estimated from all altimetry observations of one overflight following outlier removal based on the along-track standard deviation. Water levels from CryoSat-2 SAR data are computed based on a classification approach [11]. For all missions, it is ensured that the same atmospheric and geophysical corrections (wet and dry troposphere, ionosphere, earth and pole tide, and geoid) and retrackers are used to create consistent data sets. To combine altimeter missions it is necessary to correct for radial orbit offsets, which can cause height difference between water level observations from different missions [24]. All data upstream from dams are discarded (see section 2).
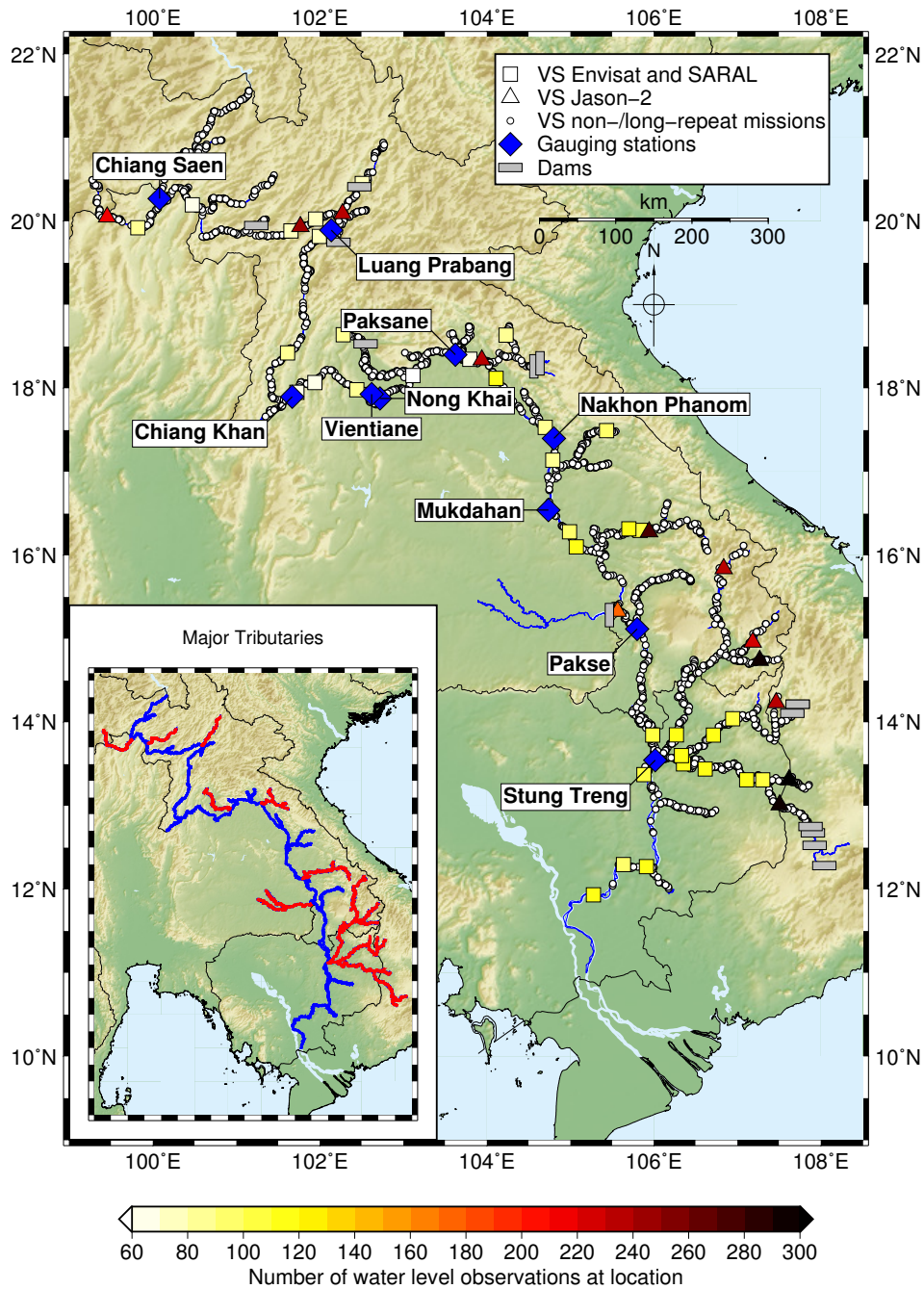
Figure 1. Map of the study area. The locations of altimetric water level observations are plotted, with colours indicating the number of observations at a location. For the long or non-repeat missions, the maximum number of observations is six (CryoSat-2). Dams considered in this study are indicated. The inlay map shows major tributaries in red.
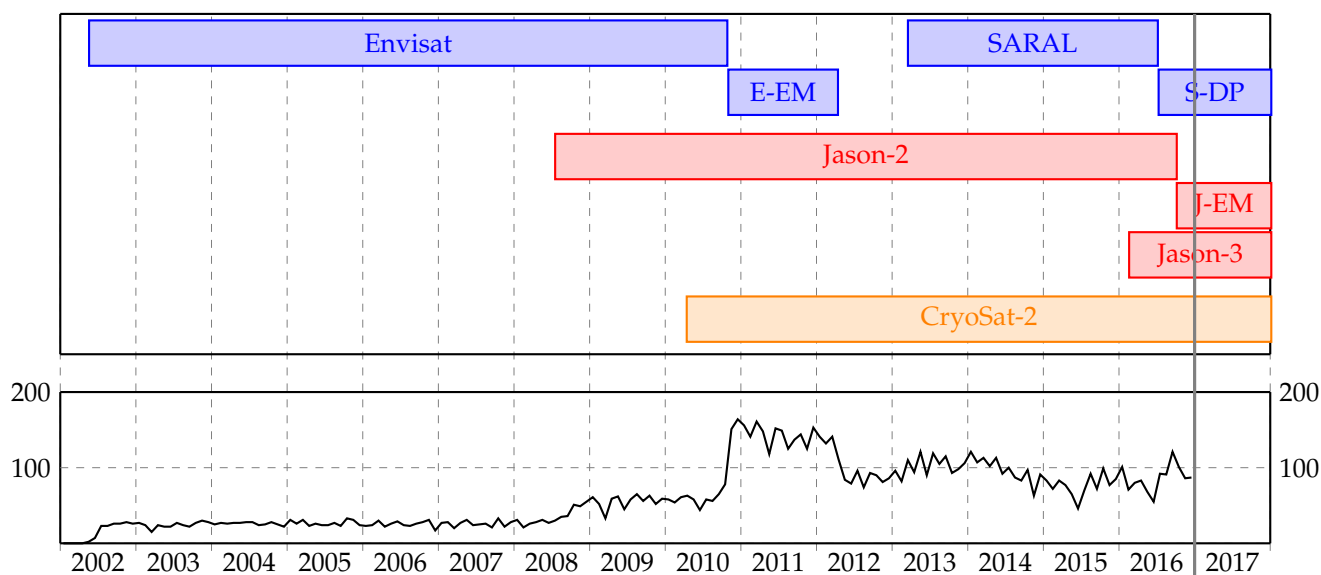
Figure 2. Temporal availability of altimetry missions. Data are used in this study until the end of 2016, as indicated by the grey vertical line. The lower panel shows the number of water level observations used in this study for each month.

Figure 2 shows the temporal availability of the different missions. The lower panel of this figure displays the number of water level measurements for each month available for this study. Figure 1 shows the spatial distribution of altimetry data along the river network. For the short-repeat missions the length of the water level time series is colour-coded.

Despite having 11,200 water level observations over all years in the study area, usable water level observations could not be derived for all locations and time points. For Envisat, only 35 out of 76 possible VSs are of acceptable quality. For SARAL, 26 out of 76 observations are used, and for Jason-2, 12 out of 26 observations are used. Several factors lead to the exclusion of data points. Topography can hinder the observation of water levels with satellite altimetry. For example, steep river gorges can hide the river from the altimeter radar, except in nadir. When a river is smaller than the along-track distance between two consecutive observations (e.g. ∼350 m for Envisat), the river cannot be observed. Complex terrain surrounding the river can limit the ability of the on-board tracker to shift its receiving window to the correct position to observe water levels [25]. In the case of SARAL, high atmospheric water content negatively affects the Ka-band altimeter [26].

3.2. In Situ Data

The results of the multi-mission altimetry approach are validated with in situ gauge data for the flood season provided by the Mekong River Commission (MRC, http://ffw.mrcmekong.org/). Gauge data with a daily resolution are extracted from the 1st of June to the 30th of November for the years 2008 to 2016. Locations and names of the gauging stations are shown in Figure 1.

4. Methods

4.1. Universal Kriging for Multi-Mission Altimetry Combination

This study employs an universal kriging method (UK) [e.g. 15,16,21] to link multi-mission altimetry data from different tributaries and streams of the river. Unlike the widely used ordinary kriging (OK) method, which was used in Boergens et al. [14] for multi-mission altimetry, UK does not require a constant mean over the data. In the case of multi-mission altimetry, this allows the

incorporation of altimetric water levels from long or non-repeat orbit missions such as CryoSat-2, SARAL DP and Envisat EM. While the mean water level of VSs of short-repeat orbit missions (Envisat, SARAL, Jason-2, Jason-2 EM and Jason-3) can be derived directly from the mean of the time series, this is not possible for long or non-repeat missions. A reduction of mean water levels with topography models is not feasible due to the inaccuracy of these models. Altimetry data from long or non-repeat orbit missions can be used to acquire additional spatial samples compared with only using short-repeat orbit altimetry. Unknown mean water levels or topography along the river are modelled with an unknown linear combination of known functions $\{f_0(\boldsymbol{x})...f_p(\boldsymbol{x})\}$. The water level $Z(\boldsymbol{s}, t)$ observed at location $\boldsymbol{s}$ and at time t can be formulated as:

$$Z(\boldsymbol{s}, t) = \sum_{j=0}^{p} f_j(\boldsymbol{s})\beta_j + \delta(\boldsymbol{s}, t). \tag{1}$$

Where $\delta(\boldsymbol{s}, t)$ is the variation in water level at a given location and w.r.t. the mean water level $\sum_{j=0}^{p} f_j \boldsymbol{s} \beta_j$ with the unknown parameter β_j. We use polynomial B-Splines with a spline degree of three for $f_j(\boldsymbol{s})$ [27,28]. The B-Spline B_i^r (ith of degree r) is recursively defined over the knots $t_j, j = 0, \ldots, r + k + 1$ by:

$$B_i^0(x) = \begin{cases} 1, & \text{if } t_i \leq x < t_{i+1} \\ 0, & \text{otherwise,} \end{cases} \tag{2}$$

$$B_i^r(x) = \frac{x - t_i}{t_{i+r} - t_i} B_i^{r-1}(x) + \frac{x_{i+r+1} - x}{x_{i+r+1} - x_{i+1}} B_{i+1}^{r-1}(x) \tag{3}$$

with $i = 0, \ldots, k$ and $r = 1, 2, 3$.
The kriging equation for the prediction of a water level at point $\boldsymbol{s}_0$ and time t_0 is

$$p(\boldsymbol{s}_0, t_0) = \sum_{i=1}^{n} \lambda_i Z(\boldsymbol{s}_i, t_i), \tag{4}$$

with the altimetric water level observations $Z(\boldsymbol{s}_i, t_i)$ at the locations $\boldsymbol{s}_i$ and time t_i and

$$\boldsymbol{\lambda} = (\lambda_1, \ldots, \lambda_n) = (\Sigma_U + \Sigma_{alti})^{-1} \boldsymbol{c}_U. \tag{5}$$

$\boldsymbol{c}_U$ and Σ_U respectively contain the covariances of all observations to the prediction point and the covariances among all observations. The word prediction is used in the kriging context as the result of the kriging approach.

Σ_{alti} includes the uncertainty weights of the data in the kriging approach (see De Marsily [29]). For more information on UK refer to Cressie [21].

To derive the covariance function between the observations required in kriging, we use the non-stationary spatio-temporal covariance model introduced in Boergens *et al.* [14], which allows the modelling of the inflow of tributaries and of different flow behaviours along the river. The covariance model consists of independent spatial and temporal components. The temporal component is an exponentially declining covariance model. The spatial component consists of two elements. The first element depends on the distance along the river, if the locations are connected. The second element relates the location of the sub-basins to each other. The river distance-related covariance is a non-stationary covariance model based on the flow between points. The details of the covariance functions and their parameter estimations can be found in Boergens *et al.* [14].

4.2. Comparison with Previous River Multi-Mission Altimetry Studies

Here, we discuss the differences between our universal kriging approach and three studies that have used multi-mission altimetry to investigate rivers: Tourian *et al.* [12], Boergens *et al.* [14], and Tourian *et al.* [13] (in the order of publication)

The multi-mission study by Tourian *et al.* [12] investigated altimetry data densification in the main stream of the Po River in Italy. Data from Jason-2, Envisat, SARAL and CryoSat-2 were used. Data combination was achieved with flow velocity between observations. Flow velocity was estimated at each VS using river slope and width. River slope was approximated from four in situ stations and river width was derived from Landsat 7 images. Auxiliary information were necessary to the combination of altimetry data, whereas our UK approach does not rely on in situ and Landsat 7 data sets.

The study by Boergens *et al.* [14] investigated the same study area as presented here, but multi-mission combination was conducted with ordinary kriging (OK). Boergens *et al.* [14] combined data for the main Mekong River from short-repeat orbit missions (Envisat, SARAL and Jason-2). To apply OK, it is necessary to remove the mean water levels of all data to obtain a constant mean. The UK approach in our study can handle non-constant means, thus the mean water level does not have to be removed. This allows the incorporation of water levels of missions with a long or non-repeat orbits. This results in a denser spatial distribution of the data and increased availability of data in 2011 and 2012, when only Jason-2 data was available. Including data of the major tributaries provides additional information on the flow of the river. At the Luang Prabang, Nakhon Phanom, Pakse and Kratie stations, the multi-mission time series obtained with OK were unable to quantify flood anomalies as precisely as our times series obtained with UK (see Section 5). The 2008 flood was not observed in the two upstream stations. Major flooding in 2002, which was even more severe than in 2008, was only partly captured by the OK time series.

In Tourian *et al.* [13], water levels from Jason-2, Envisat and SARAL were combined along the Niger River and two major tributaries in West Africa. Altimetric water levels were used to densify time series at in situ discharge stations [12]. At these stations, a discharge time series was estimated from the densified altimetric water level time series. A Kalman filter was employed to assimilate discharge time series of all in situ stations in a linear dynamic model. The stochastic model for the Kalman filter was assumed to be stationary over the whole river, as opposed to our non-stationary covariance model which allows for varying flow behaviours along the river. When converting water levels to discharge, the problem of topography along the river did not need to be addressed further, as in our study. In Tourian *et al.* [13], multiple scenarios regarding the two tributaries were tested (exclusion of tributaries; inclusion of one tributary in turn; inclusion of both tributaries; division of river in reaches). Dividing the river into hydrological reaches yielded the most accurate results when compared to in situ data. In our UK approach, river reaches do not need to be defined as the non-stationary covariance model integrates changing flows in the river. A direct comparison between the two studies is difficult due to the different study areas and different characteristics (water level vs. discharge) investigated.

5. Results and Validation

We use UK to predict time series during flood seasons in the years 2008 to 2016 at the locations of all gauging stations shown in Figure 1. It is possible to use any location along the river but the gauging stations are chosen for validation. The temporal resolution of the time series is set to five days based on mean data availability in the study area. The Mekong River Commission defines the flood season between June 1st to November 30th, which we use as the study time frame. The exact onset of the flood changes by up to 14 days over the years, but never occurs before June. The results of the UK method are only presented for the flood season because of two reasons. In situ data is only available for the whole year since 2013, therefore validation for the dry season in the years 2008 - 2012

is not possible. We aim to assess the ability of multi-mission altimetry to quantify extreme water levels, which only occur in the Mekong River during the flood season [1].

The UK approach is investigated under two situations. In Section 5.1 , we investigate and validate the predicted water level time series during the flood season. And in Section 5.2 we demonstrate the ability of the multi-mission altimetry time series to quantify extreme events.

5.1. Accuracy of Time Series and Consistency with In situ Data

To evaluate the influence of tributaries on results, we conduct three different estimations. Water level observations along tributaries may contain valuable information on the main river stream and increase data availability. However, observations of water levels in tributaries are less accurate due to their smaller size.

The three scenarios are:

- S-I: altimetry data for the whole river basin, including tributaries;
- S-II: altimetry data only for the main river stream;
- S-III: altimetry data on the main river stream and major tributaries (see the inlay in Figure 1).

The third dataset including only major tributaries constitute an intermediate scenario, as not all tributaries are equally important to the main river flow. Major tributaries in S-III are defined by their relative inflow to the total inflow of the river [3] (see Figure 1 for the major tributaries). In the second and third scenarios observations of tributaries are assigned a higher covariance factor than observations on the main stream in Σ_{alti} (see subsection 4.1).

In situ data from gauging stations are used to validate the UK time series. Results are shown in Table 1 with addtional validation results of the closest VS.Validation is performed with three performance measures: root mean square error (RMSE), coefficient of determination (squared correlation coefficient; R^2) and Nash-Sutcliffe model efficiency coefficient (NSE) [30]. RMSE measures absolute differences between gauge and altimetry time series, whereas the coefficient of determination is sensible to phase shifts between time series. The maximum value of NSE is one and a value of zero indicates that the UK time series predicts the in situ times series as well as the mean observed water level. NSE values below zero indicate that the altimetric time series is worse than the mean observed water level. Because of the higher temporal resolution and better data availability of Jason-2, we decide to use a Jason-2 time series instead of a closer Envisat and SARAL time series for the closest VS when the Jason-2 VS is less than 100 km away. Envisat and SARAL have a data gap in 2011 and 2012, whereas Jason-2 is available for the whole timeframe of the study. VS data is derived from DAHITI. At some stations (Chiang Khan and Chiang Saen), the closest VS only includes Envisat data as SARAL data quality is insufficient. In this case only floods in the years 2008 - 2010 are monitored by the VS.

At many stations, performances for all three data sets used in UK are similar. S-I show intermediate performance (RMSE range: 1.20 m - 1.67 m; ^{2} range: 0.66 - 0.88; NSE range: -0.97 - 0.77). S-II perform worst (RMSE range: 1.19 - 2.22 m; ^{2} range: 0.5 - 0.88; NSE range: -1.03 - 0.77), while S-III perform best (RMSE range: 1.05 - 1.75 m; R^2 range: 0.81 - 0.9; NSE range: 0.02 - 0.8). Correlations between the quality of the results and locations along the river are not significant. NSE values do not fall below 0.59 except for Chiang Saen and Paksane stations in S-II. The results of VSs are inferior to UK results, except at Pakse and Paksane stations, both measured by Jason-2. However, flood behaviour may change over a distance of 100 km between the gauge and the VS (see differences between Chiang Khan and Vientiane stations in 2008 in Figure 5). Four of the stations, including Chiang Saen and Paksane have a notable different behaviour which will be explained in more detail following. The time series of these stations (Chiang Saen, Paksane, Pakse and Stung Treng) are displayed in Figure 3. Differences between the gauge and altimetric time series are given below each station's time series in Figure 3.

Chiang Saen station (Figure 3 (a)) is the most northern gauging station included in this study. There we have fewer datapoints in the vicinity and lower data quality due to small rivers (<200 m in

width). The results of S-I and S-II are inferior to the results in S-III at this station. This indicates that along some of the nearby tributaries, erroneous water level observations degraded the time series. In contrast, major tributaries contribute important information for estimating water levels along the main river. Amplitude is overestimated in all scenarios, leading to low NSE values. Differences show similar behaviours among years, with decreasing positive differences before the flood peak and negative differences after the flood. This indicates a phase shift between the UK time series and gauge data, with the peak of the flood observed earlier in gauge data. The phase shift is probably caused by uneven data distribution around Chiang Saen station, with more data available downstream than upstream due to the limits of the study area. Thus, the estimated time series incorporates more downstream data which detects the flood later than the gauge time series. This biased data distribution shifts the estimated time series towards the values of downstream data.

At Paksane station the time series in S-II shows a distinct offset in 2011 (Figure 3 (b)). This may be caused by a single major outlier in the dataset. Because no tributaries are included, fewer data data are available for UK. Therefore a possible outlier could not be evened out by correct data. Unfortunately, if the flood is only measured by one altimetric observation, the UK approach could consider this value an outlier and remove it. This is most probably the case in 2008 and 2016, where S-II detected the flood peak more accurately.

The right bank tributary Nam Mun flows into the main stream a few kilometres upstream from Pakse. This tributary has a high yearly inflow in relation to the main river flow. However, we are unable to incorporate data from this river because the Pak Mun Dam blocks the Nam Mun 5 km upstream from the confluence. All data above this dam are unusable in UK as the covariance models employed cannot assess flow behaviour across a dam. Therefore the inflow of the Nam Mun cannot be incorporated into the estimation of the time series. In the Pakse station time series (Figure 3 (c)), only the S-I results accurately reflects the 2011 flood, while the other two scenarios show amplitudes that are too low. S-II and S-III show similar results but fail to quantify inter-annual variations in water levels, possibly due to lack of data from the Nam Mun tributary. Prior to 2011, few datapoints are available around Pakse as only one Jason-2 VS is situated close-by. With few datapoints, the UK approach can only predict the mean annual signal.

In Stung Treng, the largest of the left bank tributary system of Se Kong, Se San, and Sre Pok joins the Mekong River. In S-II, ignoring this tributary system negatively affects the time series (Figure 3 (d)). In S-I, minor tributaries are given the same weight as the Se Kong, Se San and Sre Pok system, degrading the resulting time series. In the differences a similar behaviour to the Chiang Saen station is visible, but reversed. Here the differences indicate a phase shift towards an earlier flood peak in the UK time series compared to the gauge time series. The effect is however less pronounced than at Chiang Saen station, as Stung Treng station is located further from the end of the study area.

The multi-mission approach is not always able to identify the main peak of the flood or flash floods. The main peak of the flood lasts for a few days to a month; flash floods are even shorter. The flood peak can only be observed in the multi-mission time series if a water level measurement is available in the vicinity. In Figure 4 in situ data at the gauging station Paksane is shown (heights colour coded). The available altimeter observations in the surrounding 200 km of Paksane station are shown as black crosses (Figure 3). No altimeter observations are available during the peak of the main flood (∼2013.60 - 2013.62), therefore the flood peak could not be observed in the multi-mission time series (Figure 3). The flash floods following the main flood occur rapidly and could not be detected in the time series (Figure 3 (b)).

5.2. Monitoring Extreme Events

The extent of the flood season is evaluated with a novel flood index, based on the mean differences in each year between the long-term annual signal and observed water level. The flood index f for the year y and the location s is defined as:

Table 1. Validation of the universal kriging (UK) time series against in situ gauge data. Validation of the closest Virtual Station (VS) is given at the end of the table for comparison. The parentheses following each station name indicate the distance between the gauge and the VS, and the name of the mission used to measure the VS (E = Envisat, S = SARAl and J2 = Jason-2). RMSE: Root Mean Square Error. R^2: coefficient of determination. NSE: Nash-Sutcliffe model efficiency coefficient.

|	All tributaries			Only main river			Major tributaries			Closest VS		
	RMSE [m]	R^2	NSE	RMSE [m]	R^2	NSE	RMSE [m]	R^2	NSE	RMSE [m]	R^2	NSE
Chiang Saen (72 km, E)	1.66	0.76	-0.97	1.69	0.73	-1.03	1.24	0.81	0.02	2.64	0.45	-8.86
Luang Prabang (-36 km, J2)	1.66	0.78	0.61	1.54	0.81	0.66	1.75	0.83	0.6	1.77	0.62	0.32
Chiang Khan (12 km, E)	1.39	0.84	0.63	1.34	0.85	0.65	1.05	0.9	0.8	3.27	0.45	-1.41
Vientiane (-22 km, E+S)	1.2	0.87	0.76	1.19	0.87	0.76	1.31	0.89	0.74	2.43	0.51	-0.43
Nong Khai (-56 km, E+S)	1.21	0.88	0.77	1.22	0.88	0.77	1.22	0.89	0.79	2.45	0.5	-0.44
Paksane (41 km, J2)	1.31	0.86	0.73	2.22	0.65	0.3	1.44	0.86	0.72	1.28	0.88	0.67
Nakhon Phanom (-19 km, E+S)	1.36	0.86	0.74	1.36	0.87	0.73	1.36	0.86	0.73	2.81	0.67	-1.17
Mukdahan (42 km, E+S)	1.23	0.88	0.77	1.46	0.83	0.67	1.31	0.87	0.73	2.06	0.55	-0.38
Pakse (-41 km, J2)	1.67	0.8	0.59	1.39	0.85	0.72	1.47	0.84	0.7	1.26	0.94	0.78
Stung Treng (18 km, E+S)	1.63	0.66	0.31	1.83	0.5	0.11	1.13	0.84	0.68	1.88	0.38	-0.69
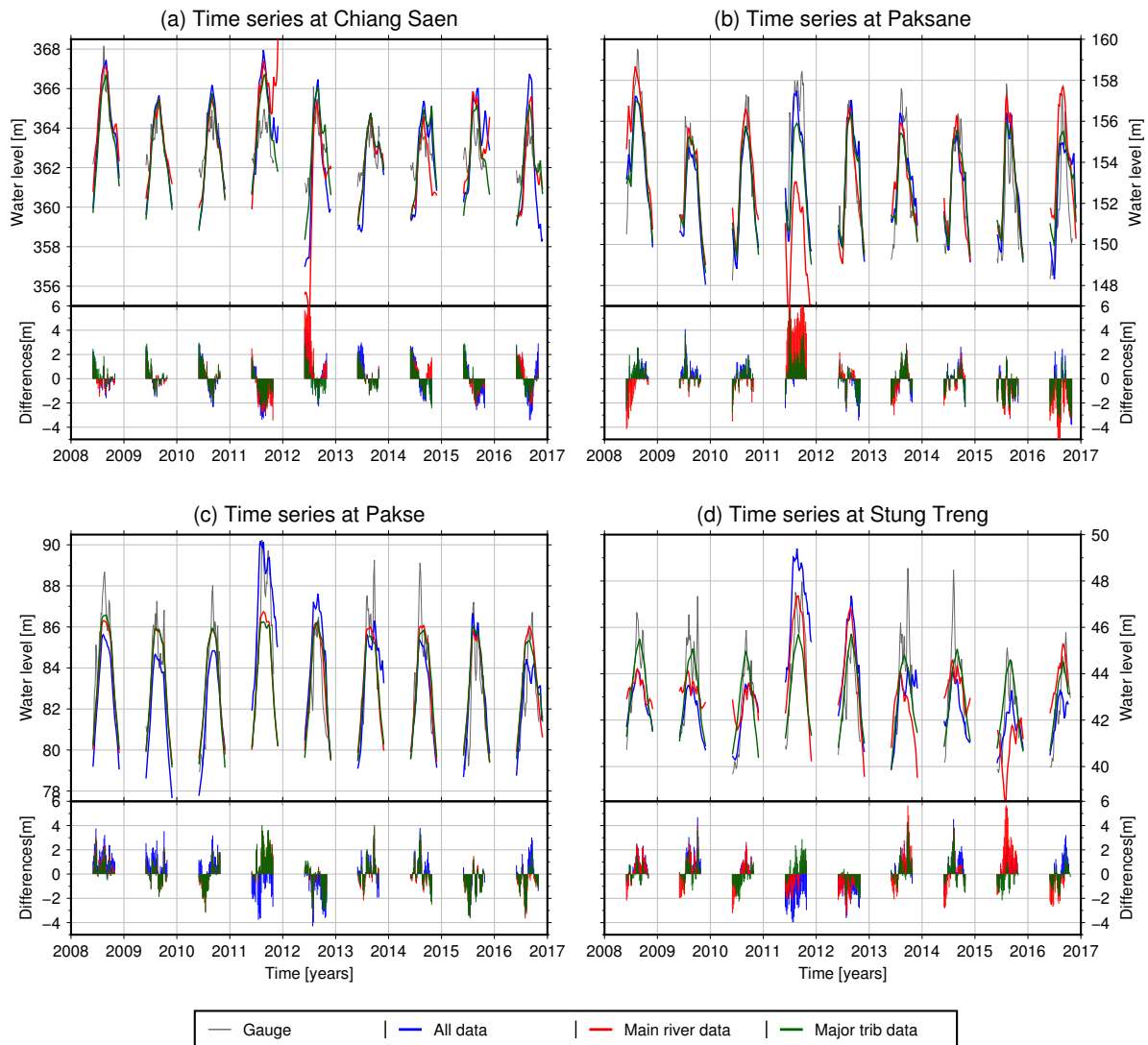
Figure 3. Resulting multi-mission altimetry time series at four stations. Differences between the gauge and altimetric time series (gauge-altimetry) are shown for each station.
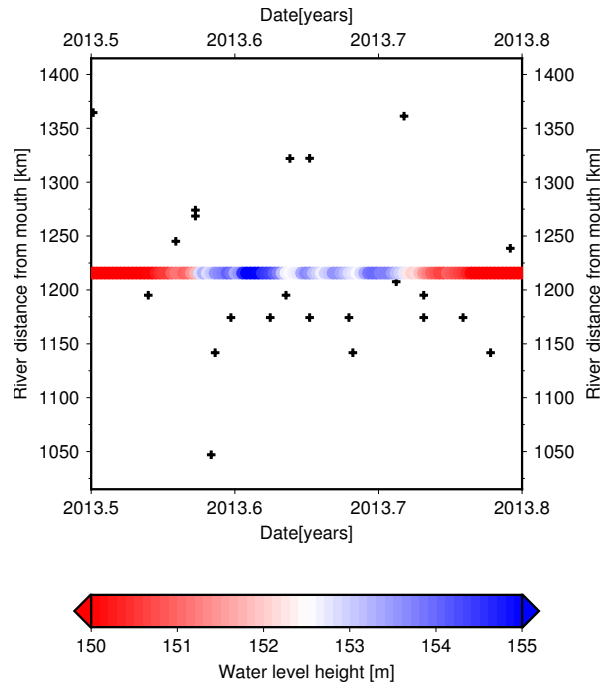
Figure 4. Water levels at Paksane gauging station in 2014. Surrounding altimetric water level observations are shown with black crosses. Flood peaks were not detected by any of the altimetric observations and thus could not be observed in the multi-mission time series.

$$f(\boldsymbol{s}, y) = \frac{1}{N} \sum_i Z(\boldsymbol{s}, d_i^y) - \overline{G(\boldsymbol{s}, d_i)}. \tag{6}$$

Where $Z(\boldsymbol{s}, d_i^y)$ are observed water levels at the location during the flood season in the year y; d_i^y is the ith day in the year y; and $\overline{G(\boldsymbol{s}, d_i)}$ is the long-term mean gauge reading over all years on a given day d_i.

Floods for each year and for each gauging station are evaluated with this flood index for the gauging data itself, the predicted five-day time series, and the nearest VS of a short-repeat altimetry mission. We use the same VSs as in the previous section. We only use results from S-III as these showed the highest performance in subsection 5.1. Gauge data are reduced to the same temporal resolution as the UK time series (five days). The long-term annual mean used for the index is calculated from gauge data and used for the altimetry-based flood indices as well.

For each year and station, the three flood indices (gauge, UK and VS) are shown in Figure 5. The first square is the flood index for the in situ gauge data and represents the ground truth. The names of the stations are given together with the distances to the closest VS . The coefficient of determination (R^2) between the gauge and UK flood indices is 0.79, and between gauge and VSs is 0.51.

The Mekong Basin was affected by two major flooding events during the study, in 2008 and 2011 (see also Figure 3). These extreme events are detected in both the gauge data and UK results. However, the extent of the flooding is underestimated by the UK time series. At Paksane station, flooding in 2011 is not detected in the UK time series. Only the Jason-2 VSs detect the floodings, whereas many of the Envisat/SARAL VSs fail to detect them. Anomalously low water levels in 2015 and 2016 are not detected by all UK time series, but are overestimated by some VSs. Medium flows are observed in 2009, but the VS close to Nakhon Phanom erroneously detected a flooding, and the VS close to Chiang Khan erroneously detected an exceptionally low flow.
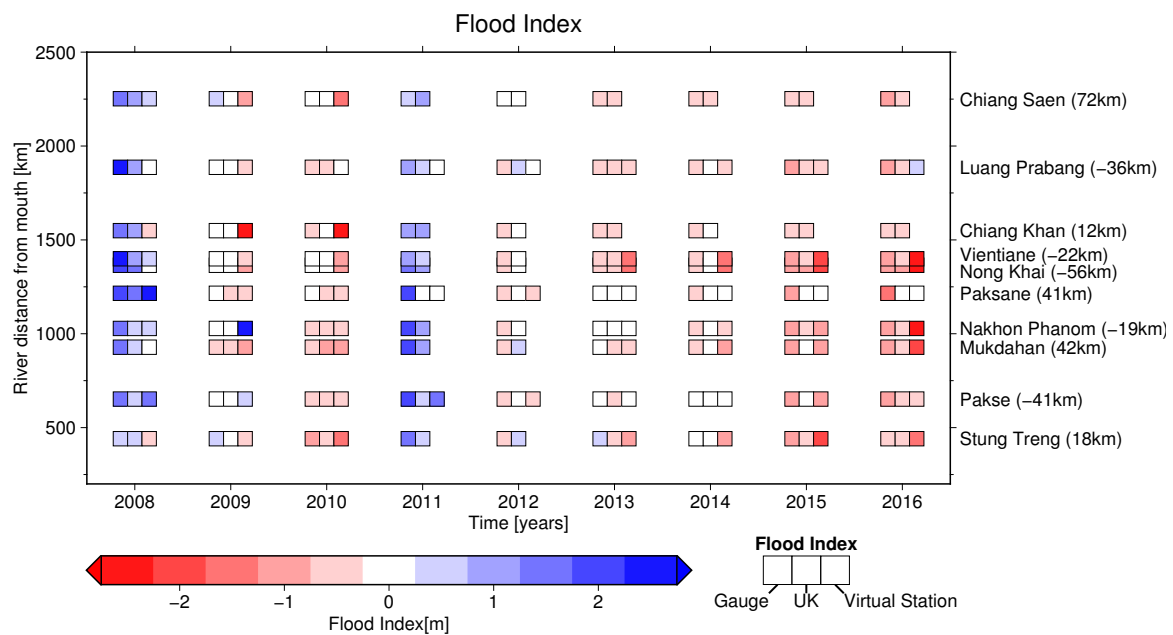
Figure 5. Flood index for all stations from gauge data, UK results and VSs.

5.3. Forecasting Extreme Events

6. Discussion

In the multi-mission altimetry approach used in this study, water levels are propagated along the Mekong River. However, water volume is not quantified despite representing more accurately the flow volume of the river. How well water level measurements and discharge correlate depends on the topography surrounding the river. The topography of deep river gorges can affect the amplitude of water levels even over distances of only 20 km [9]. This causes the overestimation of water level amplitude at Chiang Saen, as the gauge is located where the river gorge widens to a broader valley. This problem is pronounced in the river reach upstream of Vientiane, and in the upstream regions of the left-bank Laotian tributaries. A similar problem exists with the inclusion of tributaries. The water level of a tributary does not influence the water level in the main river with a one-to-one relationship. In the multi-mission approach, this is partly accounted for by down-weighting data from the tributaries. Overall, the inclusion of tributary data improves our results.

The multi-mission approach with only water level data improves data availability without relying on reliable in situ discharge data. The latter is needed to transfer water levels into discharge with a rating curve. Even without accounting for differences between water level and water volume, the multi-mission approach yields satisfying results.

7. Conclusion

This study demonstrates the potential of multi-mission altimetry for the observation of flood events along the Mekong River. Altimetric water levels are dispersed over the whole river basin, which allows for more continuous monitoring of the river independently from in situ gauging stations. With the proposed UK approach, altimetric data can be combined along the course of the main river. Observations from tributaries can also be included. Data from the tributaries, especially

the major ones, increase data availability and incorporate valuable information for determining water levels along the main river stream. As the mean water level of altimetric data does not need to be known, the approach can incorporate water levels from long or non-repeat missions such as CryoSat-2. The method is independent of auxiliary data modelling river flow, as the parameters of the covariance model are estimated from the data itself.

CryoSat-2 (SAR and LRM) has made a valuable contribution since 2010 by providing a denser spatial and temporal coverage of data along the Mekong River. This helps close the data gap between the end of the Envisat mission in 2010 and the launch of SARAL in 2013. With available data, we reach a spatial resolution of a few kilometres at a temporal resolution of up to five days.

Three scenarios are tested in the estimation of the multi-mission time series (all tributaries; only major tributaries; no tributaries). The scenario including only major tributaries, yield the best results, with RMSE values of 1.05 - 1.75 m, and coefficients of determination of 0.81 - 0.9. Single-mission altimetry with VSs only reaches RMSE values of 1.26 - 3.27 m and coefficients of determination of 0.38 - 0.94. These findings demonstrate the high predictive performance of multi-mission altimetry. In addition, higher temporal resolutions are achieved with multi-mission altimetry (five days) compared to single-mission altimetry (10 to 35 days).

Although the temporal and spatial resolutions of altimetric data are comparatively high, they are insufficient to detect every peak of the main flood. Flash floods often remain undetected, as the flood peak is too short to be measured in the vicinity of the station. With the launch of future and additional missions (Sentinel-3A, launched 2016, Sentinel-3B, planned for 2018, Jason CS, planned for 2020 and SWOT, planned for 2021) data availability will increase, and with it the ability to detect and predict flash floods.

Multi-mission altimetry allows the observation of changes during the flood season on a basin scale over multiple years. The floodings of 2008 and 2011 in the Mekong River Basin, as well as the two anomalous dry flood seasons in 2015 and 2016, are accurately detected by the multi-mission altimetry time series. Single mission altimetry may be able to observe floodings and droughts in a limited number of cases, but such basin-wide surveying would not be possible.

Theoretically, UK can be used to forecast water levels into the near future. But the available data quality and density is not sufficient for a reliable forecast so far. However, the flexibility of UK allows the incorporation of other data sets to estimate water levels, such as in situ gauge data and precipitation data. Daily in situ data are able to quantify water levels in detail but only at a few locations along the river. Precipitation is the main driver of floods in the Mekong Basin, but flow topography must be taken into account to accurately model its effects. Including such datasets should improve the abilities of UK to quantify floods and flash floods and especially improve the forecast abilities of the approach. Most importantly, flood forecasts based only on satellite data can be used in ungauged river basins where no reliable in situ data are available.

Author Contributions: Eva Boergens developed the method, conducted the data analysis and wrote the majority of the paper. Denise Dettmering helped with discussion of the method and results and writing the manuscript. Florian Seitz supervised the research and contributed to manuscript writing and organization.

Conflicts of Interest: The authors declare no conflict of interest.

Bibliography

1. Adamson, P.T.; Rutherfurd, I.D.; Peel, M.C.; Conlan, I.A. The Hydrology of the Mekong River. In *The Mekong*; Mekong River Commission, 2009; pp. 53–76.
2. Mekong River Commission. Mekong River Commission, State of the Basin Report 2010. Technical report, 2010, [arXiv:1011.1669v3].
3. Mekong River Commission., Ed. *Overview of the Hydrology of the Mekong Basin*; Mekong River Commission: Phnom Penh, Cambodia, 2005.
4. Center, G.R.D. Long-term mean monthly discharges and annual characteristics of GRDC stations. Technical report, Federal Institute of Hydrology, 2013.
5. Birkinshaw, S.J.; O'Donnell, G.M.; Moore, P.; Kilsby, C.G.; Fowler, H.J.; Berry, P.A.M. Using satellite altimetry data to augment flow estimation techniques on the Mekong River. *Hydrological Processes* **2010**, *24*, 3811–3825.
6. Santos da Silva, J.; Calmant, S.; Seyler, F.; Rotunno Filho, O.C.; Cochonneau, G.; Mansur, W.J. Water levels in the Amazon basin derived from the ERS- 2 and ENVISAT radar altimetry missions. *Remote Sensing of Environment* **2010**, *114*, 2160–2181.
7. Schwatke, C.; Dettmering, D.; Bosch, W.; Seitz, F. DAHITI - an innovative approach for estimating water level time series over inland waters using multi-mission satellite altimetry. *Hydrology and Earth System Sciences* **2015**, *19*, 4345–4364.
8. Maillard, P.; Bercher, N.; Calmant, S. New processing approaches on the retrieval of water levels in ENVISAT and SARAL radar altimetry over rivers: A case study of the São Francisco River, Brazil. *Remote Sensing of Environment* **2015**, *156*, 226–241.
9. Boergens, E.; Dettmering, D.; Schwatke, C.; Seitz, F. Treating the Hooking Effect in satellite altimetry data: A case study along the Mekong River and its tributaries. *Remote Sensing* **2016**, *8*, 91.
10. Villadsen, H.; Andersen, O.B.; Stenseng, L.; Nielsen, K.; Knudsen, P. CryoSat-2 altimetry for river level monitoring — Evaluation in the Ganges–Brahmaputra River basin. *Remote Sensing of Environment* **2015**, *168*, 80–89.
11. Boergens, E.; Nielsen, K.; Andersen, O.B.; Dettmering, D.; Seitz, F. River Levels Derived with CryoSat-2 SAR Data Classification - A Case Study in the Mekong River Basin. *Remote Sensing* **2017**, *9*, 1238.
12. Tourian, M.J.; Tarpanelli, A.; Elmi, O.; Qin, T.; Brocca, L.; Moramarco, T.; Sneeuw, N. Spatiotemporal densification of river water level time series by multimission satellite altimetry. *Water Resources Research* **2016**, *52*, 1140–1159.
13. Tourian, M.J.; Schwatke, C.; Sneeuw, N. River discharge estimation at daily resolution from satellite altimetry over an entire river basin. *Journal of Hydrology* **2017**, *546*, 230–247.
14. Boergens, E.; Buhl, S.; Dettmering, D.; Klüppelberg, C.; Seitz, F. Combination of multi-mission altimetry data along the Mekong River with spatio-temporal kriging. *Journal of Geodesy* **2017**, *91*, 519–534.
15. Delfiner, P.; Delhomme, J. Optimum interpolation by kriging **1975**.
16. Myers, D.E. Matrix formulation of co-kriging. *Journal of the International Association for Mathematical Geology* **1982**.
17. Kumar, V. Optimal contour mapping of groundwater levels using universal kriging - A case study. *Hydrological Sciences Journal* **2007**.
18. Gundogdu, K.S.; Guney, I. Spatial analyses of groundwater levels using universal kriging. *Journal of Earth System Science* **2007**.
19. Kastelec, D.; Košmelj, K. Spatial Interpolation of Mean Yearly Precipitation using Universal Kriging. *Metodološki zvezki* **2002**.
20. Brus, D.J.; Heuvelink, G.B.M. Optimization of sample patterns for universal kriging of environmental variables. *Geoderma* **2007**.
21. Cressie, N.A.C. *Statistics for spatial data*; New York : J. Wiley,, 1993.
22. Lauri, H.; De Moel, H.; Ward, P.J.; Räsänen, T.A.; Keskinen, M.; Kummu, M. Future changes in Mekong River hydrology: Impact of climate change and reservoir operation on discharge. *Hydrology and Earth System Sciences* **2012**, *16*, 4603–4619, [arXiv:gr-qc/9809069].

23. Liu, K.T.; Tseng, K.H.; Shum, C.; Liu, C.Y.; Kuo, C.Y.; Liu, G.; Jia, Y.; Shang, K. Assessment of the Impact of Reservoirs in the Upper Mekong River Using Satellite Radar Altimetry and Remote Sensing Imageries. *Remote Sensing* **2016**, *8*, 367.

24. Bosch, W.; Dettmering, D.; Schwatke, C. Multi-mission cross-calibration of satellite altimeters: Constructing a long-term data record for global and regional sea level change studies. *Remote Sensing* **2014**, *6*, 2255–2281.

25. Biancamaria, S.; Hossain, F.; Lettenmaier, D.P. Forecasting transboundary river water elevations from space. *Geophysical Research Letters* **2011**, *38*.

26. Schwatke, C.; Dettmering, D.; Börgens, E.; Bosch, W. Potential of SARAL/AltiKa for Inland Water Applications. *Marine Geodesy* **2015**, *38*.

27. Stollnitz, E.J.; DeRose, T.D.; Salestin, D.H. Wavelets for computer graphics: a primer, part 1. *IEEE Computer Graphics and Applications* **1995**, *15*, 76–84.

28. Schmidt, M.; Dettmering, D.; Seitz, F. Using B-Spline expansions for ionosphere modeling. In *Handbook of Geomathematics: Second Edition*; 2015; pp. 939–983.

29. De Marsily, G. Quantitative hydrogeology. Technical report, Paris School of Mines, Fontainebleau, 1986.

30. Nash, J.E.; Sutcliffe, J.V. River flow forecasting through conceptual models part I - A discussion of principles. *Journal of Hydrology* **1970**, *10*, 282–290.

Co-Authored publications

For the four co-authored publications only a short summary and authors' contributions are provided, but not the full text as they are not part of this thesis.

CP-1: Potential of SARAL/AliKa for Inland Water Applications

C. Schwatke, D. Dettmering, E. Börgens, and W. Bosch (2015a): **Potential of SARAL/ AltiKa for Inland Water Applications**. In: *Marine Geodesy* 38.sup1, pp. 626–643

This study investigated the abilities of *S*atellite with *Ar*gos and *Al*tiKa (SARAL) data to observe inland waters, lakes and rivers likewise. It was shown, that SARAL is more susceptible to precipitation or atmospheric water content. However, in dry conditions the water level time series quality were improved compared to *Envi*ronmental *Sat*ellite (Envisat) time series. Over the lakes the smaller footprint resulted in better water level observations closer to the land-water transition.

The study was led by Christian Schwatke including the compilation of the results and the majority of manuscript writing. Eva Börgens contributed first investigations of along-track heights of SARAL over lakes and rivers as well as the correlation between water level quality and atmospheric water content. All co-authors contributed to the manuscript writing.

CP-2: Potential of ENVISAT Radar Altimetry or Water Level Monitoring in the Pantanal Wetland

D. Dettmering, C. Schwatke, E. Boergens, and F. Seitz (2016): **Potential of ENVISAT Radar Altimetry for Water Level Monitoring in the Pantanal Wetland**. In: *Remote Sensing* 8.7, pp. 1–21

In this publication new methods were investigated to observe water level changes in the Pantanal wetland with Envisat observations. Different classification methods were tested for the identification of water surfaces below the satellite track. Together with an optimised retracking water level time series could be derived. The comparison of the altimetric time series against in situ gauge observations revealed the high agreement.

Denise Dettmering led the study including the computation of the water level time series and wrote the majority of the manuscript. Eva Börgens helped with the discussion of the methods and results. All co-authors contributed to the manuscript writing.

CP-3: Airborne Laser Scanning for calibration and validation of inshore satellite altimetry: A proof of concept

A. Zlinszky, E. Boergens, P. Glira, and N. Pfeifer (2017): **Airborne Laser Scanning for calibration and validation of inshore satellite altimetry: A proof of concept**. In: *Remote Sensing of Environment* 197, pp. 35–42

The ability to validate altimetric water level observations with airborne laser scanning was investigated in this study. The along-track water levels of three satellite overflights were compared to near concurrent LIDAR observations over Lake Balaton. The results showed that LIDAR can be used to calibrate and validate the altimetry data over inland water bodies.

András Zlinszky led the study, did the comparison between the data sets, and wrote the majority of the manuscript. Eva Börgens did the altimetry data processing and the figure compilation. Philipp Glira and Norbert Pfeiffer contributed the LIDAR data processing. All co-authors contributed to the manuscript writing.

CP-4: ALES+: Adapting a homogenous ocean retracker for satellite altimetry to sea ice leads, coastal and inland waters

M. Passaro, S. K. Rose, O. B. Andersen, E. Boergens, F. M. Calafat, D. Dettmering, and J. Benveniste (2018): **ALES+: Adapting a homogenous ocean retracker for satellite altimetry to sea ice leads, coastal and inland waters**. In: *Remote Sensing of Environment* 211, pp. 456–471

This study presented a new retracking algorithm: ALES+. This subwaveform retracker was a modification of the ALES retracker and adapted to changing sea states and slopes of trailing edges. Though designed for sea ice retracking, the study showed the good performance of the retracker for coastal and inland water applications as well. Thus, the retracker can consistently be used for all altimetry applications.

The ALES+ retracker was developed by Marcello Passaro who also led the study. Eva Börgens contributed the investigation of ALES+ for inland water bodies and wrote the corresponding section. All co-authors contributed to the discussion and manuscript writing.